The Dissertation Committee for Nariman Fathi Najafabadi certifies that this is the approved version of the following dissertation:

Modeling Chemical EOR Processes Using IMPEC and Fully Implicit Reservoir Simulators

Committee:

_____
Kamy Sepehrnoori, Co-Supervisor

_____
Mojdeh Delshad, Co-Supervisor

_____
Gary A. Pope

_____
Larry W. Lake

_____
Mark A. Miller

Modeling Chemical EOR Processes Using IMPEC and Fully Implicit Reservoir Simulators

by

Nariman Fathi Najafabadi, B.S; M.S.

Dissertation

Presented to the Faculty of the Graduate School of

The University of Texas at Austin

in Partial Fulfillment

of the Requirements

for the Degree of

Doctor of Philosophy

The University of Texas at Austin

August, 2009

The author dedicates this dissertation to his kind, supportive, intelligent and lovely wife,

Fatemeh Panahi.

Acknowledgements

The author would like to thank his supervising professors, Dr. Kamy Sepehrnoori and Dr. Mojdeh Delshad, for guiding and supporting him through his studies at The University of Texas at Austin.

Thanks to the faculty of the University of Texas at Austin, especially the members of my committee, for their efforts in educating me during the past six years.

Special thanks to my parents, Alinaghi Fathi Najafabadi and Zohreh Azarmgin for their support and guidance.

Thanks to the staff of the University of Texas at Austin, specially the staff of the Petroleum and Geosystems Engineering Department who have helped me during my studies. Special thanks to Cheryl, Roger and Joanna for their help and support.

Thanks to all of my friends at The University of Texas at Austin for sharing their happiness and sadness with me through these years and helping me in difficult situations.

Modeling Chemical EOR Processes Using IMPEC and Fully IMPLICIT Reservoir Simulators

Nariman Fathi Najafabadi, Ph.D.

The University of Texas at Austin, 2009

Supervisors: Kamy Sepehrnoori and Mojdeh Delshad

As easy target reservoirs are depleted around the world, the need for intelligent enhanced oil recovery (EOR) methods increases. The first part of this work is focused on modeling aspects of novel chemical EOR methods for naturally fractured reservoirs (NFR) involving wettability modification towards more water wet conditions. The wettability of preferentially oil wet carbonates can be modified to more water wet conditions using alkali and/or surfactant solutions. This helps the oil production by increasing the rate of spontaneous imbibition of water from fractures into the matrix. This novel method cannot be successfully implemented in the field unless all of the mechanisms involved in this process are fully understood. A wettability alteration model is developed and implemented in the chemical flooding simulator, UTCHEM. A combination of laboratory experimental results and modeling is then used to understand the mechanisms involved in this process and their relative importance.

The second part of this work is focused on modeling surfactant/polymer floods using a fully implicit scheme. A fully implicit chemical flooding module with comprehensive oil/brine/surfactant phase behavior is developed and implemented in general purpose adaptive simulator, GPAS. GPAS is a fully implicit, parallel EOS compositional reservoir

simulator developed at The University of Texas at Austin. The developed chemical flooding module is then validated against UTCHEM.

Table of Contents

List of Tables

List of Figures

Chapter 1: Introduction

As oil resources are depleted around the world, finding easy targets for primary oil recovery becomes more difficult. On the other hand, the demand for energy and crude oil increases rapidly. This calls for more efficient production of existing oil resources by conducting intelligent secondary and tertiary oil recovery methods. Chemical flooding processes can increase the recovery factor of existing oil reservoirs and help us with the current energy crises. Examples of classic chemical flooding processes are: polymer flooding, surfactant/polymer flooding and alkali/surfactant/polymer flooding. The above mentioned methods are well-studied for conventional (single porosity) sandstone reservoirs.

Chemically induced wettability alteration has been studied by many researchers during the past few years as one of the newly developed chemical flooding methods. This method can improve the oil recovery from Naturally Fractured Reservoirs (NFR) which are mostly carbonates. Most carbonate reservoirs are preferentially oil-wet. This decreases the secondary and tertiary oil recovery performance of such reservoirs to a great extent since the matrix does not spontaneously imbibe the injected aqueous phase. The injected aqueous phase is therefore produced through the fracture network without improving the recovery of the preferentially oil-wet fractured carbonates. A wettability alteration to more water-wet conditions can greatly improve the recovery efficiency of such reservoirs by improving the spontaneous imbibition of aqueous phase into the matrix and expulsion of the oleic phase into the fractures. The mechanisms involved in this process should be fully understood before it can be applied in the field. One of the goals of this work is to study these mechanisms and to model the wettability alteration process based on laboratory measurements. It is then desired to study the scale dependency of oil recovery by such methods to be able to infer the time required for oil recovery in field scale based on laboratory scale experiments.

One of the most important tasks in any chemical flooding project is its design and optimization in field scale. A robust chemical flooding design is the key to field scale chemical flooding success. A design is robust if it is not sensitive to reservoir heterogeneity and rock/fluid variations in the reservoir. Modeling of robust chemical flooding designs such as salinity gradient design requires comprehensive surfactant phase behavior modeling capability. On the other hand, optimization of field scale chemical floods requires a large computational capability where fully implicit formulation combined with parallel computation helps managing such optimizations more efficiently. Therefore, there is a need for a fully implicit, parallel chemical flooding simulator with comprehensive surfactant phase behavior. General Purpose Adaptive Simulator (GPAS) is a fully implicit, parallel, compositional EOS simulator developed at The University of Texas at Austin. A major contribution of this work is the development of a general and comprehensive chemical flooding module and its implementation in GPAS.

In Chapter 2, literature survey of the related topics is presented. Chapter 3 gives a brief introduction of UTCHEM, the implicit pressure explicit concentration (IMPEC) chemical compositional simulator of UT and discusses the development of its wettability alteration model. Chapter 4 is dedicated to validation of the wettability alteration model of UTCHEM and presents successful historymatching of two laboratory experiments involving wettability alteration. Scaleup methodology for wettability alteration of NFR is presented in Chapter 5 and UTCHEM is used to evaluate the importance of various recovery mechanisms in different matrix sizes. GPAS simulator is briefly introduced in Chapter 6 and the development of its fully implicit chemical flooding module with comprehensive surfactant phase behavior is explained in detail. The development of the new chemical flooding module of GPAS is validated in Chapter 7 by comparing results of similar cases to UTCHEM. Chapter 8 contains the summary and most important conclusions of the work presented in other chapters. It also contains the recommendations for future research.

Chapter 2: Literature Survey

Fluid flow in porous media and ultimate oil recovery from oil reservoirs is affected by several parameters, one of the most important of which is *wettability*. In this chapter an overview of the concept of wettability and its impacts on the reservoir performance are provided. Also, the concept of wettability alteration and its impacts on enhanced oil recovery methods (EOR) from naturally fractured reservoirs (NFR) are studied. The definition of EOR is then presented and some EOR processes are briefly discussed with more emphasis on NFRs.

The second part of this work is focused on development of a fully implicit, parallel chemical flooding module. Therefore a brief literature survey of fully implicit and parallel numerical simulation is presented along with a review of chemical flood modeling.

2.1 Wettability

Wettability is defined as "the tendency of one fluid to spread on or adhere to a solid surface in the presence of other immiscible fluids." Wettability is governed by the surface free energy of a substrate and by the wetting solution. The surface that has a higher free energy tends to be replaced by a liquid that has a lower surface energy, to reduce the total free energy of the system (Somasuundrara and Zhang, 2004).

Wettability is an important factor controlling phase trapping and multiphase flow because the most wetting fluid tends to occupy the smallest pores while the least wetting fluid distributes in the larger pores.

In a porous media, wettability is generally classified as either homogeneous or heterogeneous. In the homogeneous case, the entire rock surface has a uniform molecular affinity for either water or oil. On the other hand, heterogeneous wettability indicates

distinct surface regions that exhibit different affinities for oil or water. Homogeneous systems have three classifications: 1) strongly water wet, 2) strongly oil wet, and 3) intermediate wet. Two kinds of heterogeneous wettability are recognized: 1) mixed-wettability related to distinct and separate water-wet and oil-wet surfaces, which coexist in a porous medium, or 2) spotted, fractional, dalmatian or speckled wettability, which refers to continuous water-wet surfaces enclosing macroscopic regions of discontinuous oil-wet surfaces or vice versa (Radke, Kovsek and Wong, 1992; Anderson, 1986).

2.2 Wettability Measurement

The most popular methods of wettability measurements used in the petroleum industry are: 1) Contact angle measurement, 2) Amott wettability index and 3) United States Bureau of Mines or USBM method. Each of these methods is described below.

2.2.1 Contact Angle Measurement

Contact angle is the most universal measure of the wettability of surfaces. Early studies of wetting phenomena showed that the wetting properties of a solid are dominated by the outermost layer of molecules (Morrow, 1990).

Wetting could be described in terms of the spreading coefficient. The spreading coefficient, σ^{LSG}, is defined as follows for a liquid spreading on solid in the air:

$$\sigma^{LSG} = \gamma^{SG} - \gamma^{SL} - \gamma^{LG} \qquad \text{Eq.2.1}$$

where γ^{SG} , γ^{SL}, and γ^{LG} are solid/gas, solid/liquid and liquid/gas interfacial tensions, respectively. When σ^{LSG} is positive, spreading of the liquid occurs spontaneously. Since it is very difficult to determine γ^{SG} directly, Young's equation considers the equilibrium between force vectors at the Solid/Liquid/Gas interface:

$$\gamma^{SG} = \gamma^{SL} + \gamma^{LG}\cos(\theta) \qquad \text{Eq.2.2}$$

where θ is the angle of contact that the liquid/gas interface subtends with the solid/liquid interface (Fig. 2.1).

Figure 2.1 shows that contact angle, θ (between the denser fluid and the solid surface), which is a direct measure of the surface wettability. A contact angle of 0° indicates that the surface is totally hydrophilic, whereas an angle of 180° means that it is totally hydrophobic (Somasuundrara and Zhang, 2004). Different types of contact angles and spreading in an idealized system of polished surfaces/crude oil/brine, are illustrated in Fig. 2.2. Normally polished quartz crystals are used to represent sandstone reservoirs, and polished calcite crystals are used as representative of carbonate reservoirs.

To determine contact angles in a system of oil/brine/solid, two parallel mineral plates are submerged in brine and then a drop of oil is introduced between the plates. When the plates are moved relative to each other, advancing and receding conditions can be observed, water-advancing contact angles are reported as defining wettability because they are considered relevant to water flooding (Morrow, 1990).

Other techniques to measure contact angle include direct measurement based on projected or photographed images as well as indirect evaluations in which the angle is calculated from measured dimensions or measured mass of sessile drops (Somasuundrara and Zhang, 2004) (Fig. 2.3).

Because of many factors, such as surface roughness, presence of sharp edges in the formation, heterogeneity and composition of the rock and precipitation of hydrocarbon compounds on the rock surface, normally a range of contact angles coexist in a reservoir rock. Thus a single contact angle measured on a polished crystal can not be sufficient to determine the wettability of a reservoir rock. The situation gets even more complicated, if attention is paid to the difference between advancing and receding angles of an interface in the porous media. All of these facts put a big question mark on the validity of describing reservoir wettability by a simple equilibrium contact angle (Morrow, 1990).

2.2.2 The Amott Test

In this method, reservoir cores and reservoir fluids can be used. The Amott test is based on the fact that the wetting phase generally imbibes spontaneously into the core,

displacing the nonwetting phase. The average wettability is determined by the amount of oil or water spontaneously imbibed in a core sample compared to the same values when flooded. In this way the displacement-by-oil ratio can be calculated as the ratio of the water volume displaced by spontaneous oil imbibition alone, divided by the total water volume displaced by both oil imbibition and centrifugal (forced) displacement. A similar displacement-by-water ratio can be calculated (Morrow, 1990).

Several researchers (Morrow, 1990) use a modification of the Amott wettability test called the Amott-Harvey relative displacement index. This is defined as the displacement-by-water ratio minus the displacement-by-oil ratio. This parameter merges the two ratios into a single index, I, that ranges between +1 for complete water wet surfaces and –1 for complete oil wet surfaces. The system is defined to be water-wet when $0.3 \leq I \leq 1$, intermediate wet when $-0.3 < I < 0.3$ and oil-wet when $-1 \leq I \leq -0.3$(Morrow, 1990). A weakness of the Amott test is its failure to distinguish between important degrees of strong water-wetness, all of which will give an index of, or very close to, unity (Morrow, 1990).

2.2.3 The USBM Method

The US Bureau of Mines (USBM) wettability index test is based on the fact that the work required for the wetting fluid to displace the nonwetting fluid from the core is less than the work required for the opposite displacement, and the required work is proportional to the area under the capillary pressure curve. The index, W, is the logarithm of the ratio of the areas under centrifuge-measured capillary pressure curves for both increasing and decreasing wetting phase saturation. The index, W may vary from $-\infty$ (strongly oil wet) to $+\infty$ (strongly water wet) but generally it is between –1.5 and 1.0. The larger the absolute value of W, the greater the wetting preference. One of the weaknesses of this method is that it cannot recognize very strongly water wet systems.

2.3 Reservoir Wettability

Reservoir wettability is determined by complex interface boundary conditions acting within the pore space of sedimentary rocks. These conditions have a dominant effect on

interface movement and associated oil displacement. For many years it was believed that most of the reservoirs were very strongly water wet (Morrow, 1990; Anderson, 1986). The reason for this belief was that all of the researchers used to assume that water originally occupied the reservoir trap and while oil accumulated, water was kept in the finer pore spaces by capillary forces and as films on pore surfaces overlaid by oil. However more evidence about the effects of crude oil on wetting behavior has now led to wide acceptance of the idea that most reservoirs are at wettability conditions other than very strongly water wet. It has been inferred that mixed-wet conditions can be caused by destabilization of thin brine films coating the rock grain and that the adsorption of polar components such as resins and asphaltenes from the crude oil are involved in wettability reversal.

Cuiec (1984) cites many authors who have reported a high percentage of the reservoirs studied by them to be non-water wet. For instance, in the work of Treiber *et al.* (1971) it was found that out of 30 sandstone reservoirs, 15 were oil wet and two had neutral or intermediate wettability. Out of 25 carbonate reservoirs, 21 were found to be oil wet and two to have intermediate wettability. In all the reservoirs examined, 66% were oil wet, 7% neutral, and 27% water wet. These results were obtained using advancing contact angle measurements. These authors categorized a reservoir as water-wet if the contact angle was between 0° and 75°. Contact angles between 75° and 105° where deemed intermediate wet and contact angles between 105° and 180° where reported as oil wet. Chillingar and Yen (1983) also used contact angle measurements to evaluate wettability of 161 carbonate reservoirs with various lithology (limestone, dolomite limestone, dolomite and calcitic dolomite). They reported that 80% of these reservoirs where oil wet or strongly oil wet. The oil wet nature of some of these reservoirs was attributed to a bitumen coating. They deemed a reservoir as water wet if the measured contact angle was between 0 and 80 (8 reservoirs). Reservoirs with contact angles ranging from 80 to 100 were categorized as intermediate wet (12 reservoirs). Contact angles measured from 100 to 160 were reported as oil wet (65 reservoirs) and if the contact angle was larger than 160, the reservoir was deemed strongly oil wet (15 reservoirs).

2.4 Wettability Alteration

"Wettability alteration" is used in literature to address any change in the original wettability of a rock, either spontaneously or by EOR methods.

2.4.1 Spontaneous Wettability Alteration in Conventional Reservoirs

How is it that most of the reservoirs are found to be oil wet, if all of them were initially saturated with water? Adsorption of polar compounds from crude oil on the surface of reservoir rocks plays a critical role in determining the wetting properties of reservoir-rock surfaces. Most of the researchers believe that precipitation of heavy oleic compounds on the surface of the reservoir rocks is the reason for this change in wettability of the reservoirs from their initially water-wet state towards more oil-wet conditions (Anderson, 1986-1; Morrow, 1990; Al-Maamari and Buckley, 2000). Some investigators say that heavy compounds such as asphaltenes, resins, and high molecular weight hydrocarbons are responsible. Among them, asphaltenes are considered the primary wettability altering agents. Al-Maamari and Buckley (2000) conclude that instability of asphaltenes could cause asphaltene precipitation which results in alteration of wettability of the surface to oil-wet conditions.

Asphaltenes exist in colloidal suspensions in oil. These suspensions are caused by resins that are adsorbed onto the surface of asphaltenes, preventing the asphaltenes from flocculating due to the repulsive forces between the adsorbed resins and resin molecules in the solution. Asphaltenes are considered as the major portion of the surface-active components of the crude oil. Their molecular structure consists of aromatic, naphthenic groups and heteroatoms such as oxygen, sulfur, and nitrogen. This molecular structure has properties similar to that of surfactants and this is the reason that asphaltenes are strongly surface active. Reservoir rock surfaces are electrically charged and thus the polar segments of an asphaltene molecule are oriented towards the surface and the non-polar portions are pointed away from it, which makes the surface oil-wet. For instance, it has been reported that the wettability of Berea sandstone core is altered from its normal water-wet condition to neutral wettability because of the adsorption of asphaltenes and

resins on its surface (Kim *et al.*, 1990). Clementz (1982) found that adsorption of petroleum heavy ends can offer a benefit because the adsorbed layer can stabilize potentially damaging formation clay minerals against dispersion and subsequent migration. Also surfactant adsorption is reduced when the adsorbed layer is present on clay mineral surfaces.

Several researchers claim that oil induced changes in rock wettability from water wet to mixed wet could lead to a higher oil recovery (Jadhunandan and Morrow, 1992; Jain, Chattopadhyay and Sharmah, 2002). Jadhunandan and Morrow (1992) concluded that waterflood recovery from sandstone is optimum at close to neutral wettability ($I \approx 0.1$ or 0.3). Tie and Morrow (2005) reached to same conclusion for carbonate rocks. Others claim that wetting conditions other than strongly water wet are preferable (Morrow, Lim and Ward, 1986). Wang (1986) stated that during waterflood, a strongly water-wet core ceases to produce oil as soon as water breaks through, while a mixed-wet core continues producing oil for many pore volumes yielding very low residual oil saturation (S_{or}). He also showed that wettability of reservoir cores could be altered in both directions, i.e. strongly water-wet Berea sandstone could be made mixed-wet by aging with crude oil, and mixed-wet Loudon core could be made more water-wet using extraction with toluene. Caution should be used in judging the best wettability condition for oil recovery, since not only the amount of oil recovered, but also the rate of recovery is important from economics perspective. Salathiel (1973) reported that laboratory-prepared mixed-wet systems gave low residual oil saturations ($S_{or)}$, by extended waterflood. He also found that oil saturation continued to decline as long as water was injected into mixed-wet cores, while with the same oil in a water-wet core, the oil saturation quickly reached a constant value. He explained this phenomenon through the existence of strongly oil-wet paths that are connected in consolidated media and allow oil to flow continuously even at very low oil saturations. These strongly oil-wet paths are generated at those parts of the pore surfaces in contact with crude oil, while the remainder stays strongly water wet.

2.4.2 Wettability Alteration in Naturally Fractured Reservoirs

The impact of wettability on EOR recovery mechanisms in naturally fractured reservoirs is different compared with conventional oil reservoirs. Water wet conditions are considered favorable for oil recovery in naturally fractured reservoirs (Hatibogglu and Babadagli, 2004; Babadagli, 2003), since oil production from fractured reservoirs mostly occurs by spontaneous water imbibition and oil expulsion from the matrix into the fracture network (Chen *et al.*, 2000). Thus in the case of naturally fractured reservoirs, the tendency of the matrix (which contains almost all of the oil reserves) to imbibe water is very important for both ultimate oil recovery and the rate of recovery. Thomas (1987) concludes that for a low permeability water-wet fractured chalk, significant improvements in oil recovery can be obtained by water injection. This is completely different than the observation of Wang (1986) where he states that strongly water-wet cores cease to produce oil as soon as water breaks through. Austad (1997) studied spontaneous imbibition of water into low permeable chalk at different wettabilities using surfactants. He studied the effect of interfacial tension, core size, and wettability on the recovery of oil from cores, with and without surfactant. He observed good recoveries for water wet cores using brine, especially for short cores. He also found that it is possible to imbibe water into nearly oil-wet chalk using a cationic surfactant. To describe this process, he suggested that the surfactant turns the chalk more water-wet during the imbibition process.

Based on the observations of many researchers (Hatibogglu and Babadagli, 2004, Chen *et al.*, 2000; Thomas, 1987; Austad, 1997; Babadagli, 2003; Al-Hadherami and Blunt, 2000, Liu *et al*., 2008; Hirasaki *et al*., 2004), ultimate oil recovery from naturally fractured reservoirs increases as the wetting condition of the matrix is shifted towards more water wet conditions. Hence, it has recently been tried to alter the wettability of NFR towards more water-wet conditions. There are two major methods for wettability alteration. One is elevation of temperature or thermal procedures and the other is the use of surface active agents or surfactants. The second method of wettability alteration, namely surfactant injection, is the main scope of this work.

Al-Hadherami and Blunt (2000) examined thermal alteration in wettability and were able to change the wetting condition of a carbonate towards more water-wet conditions by elevation of temperature, resulting in enhanced water imbibition and more oil recovery. They concluded desorption of asphaltenes from rock surfaces was responsible for wettability alteration. Olsen (1991) observed an increase in oil production from oil-wet cores in core floods due to rise in temperature. He concluded that this was because of alteration of wettability towards more water-wet conditions. There are more examples of thermal induced wettability alteration in the literature, but it is beyond the scope of this work.

2.5 Effect of Wettability on Petrophysical Properties

Wettability of a rock controls the configuration distribution of fluids in the porous medium, which affects the petrophysical properties such as residual oil saturation, relative permeability and capillary pressure. These effects are briefly discussed.

2.5.1 Effect of Wettability on Residual Oil Saturation

Wetting phase has more tendencies to be in contact with the rock surface which results in distribution of this phase in smaller pores and as a thin film on the surface of bigger pores. This distribution makes the wetting phase less mobile than the non-wetting phase which is present in the larger pores, due to higher capillary forces (Hirasaki *et al.*, 2004). Figure 2.4 (Hirasaki *et al.*, 2004) shows the relationship between residual oil saturation and Amott-Harvey wettability index taken from three references. All the three references report the minimum residual oil saturation to be in neutral-wet conditions, i.e. Amott-Harvey coefficients of about zero. As seen in Fig. 2.4, as the rock tends towards more water-wetness, $I > 0$, and more oil-wetness, $I < 0$, residual oil saturation increases and these increases are almost mirror image of each other. In other words, if the Amott-Harvey coefficient of a rock is zero, then changing the wettability of the rock to more water-wet conditions such that $I = 0.3$, will increase the residual oil saturation of the rock almost the same as if the rock was made more oil-wet with $I = -0.3$.

2.5.2 Effect of Wettability on Relative Permeability

Distribution of the wetting phase in smaller pores, as mentioned above, makes the flow of this phase harder and this means lower relative permeability for the wetting phase at an equal saturation with the non-wetting phase (Anderson, 1987). Hence, generally it could be concluded that wettability of a phase and its relative permeability are reversely proportional, i.e. if wettability of a phase increases, its relative permeability would decrease. Craig (1971) gives some rules of thumb about the relative permeability curves for different wetting conditions. He states that generally initial water saturation of water-wet systems is higher than 20% to 25%, whereas it is less than 15% for oil-wet systems. Craig (1971) also gives a rule of thumb about the crossover point of water and oil relative permeabilities. He states that the crossover point occurs in water saturations more than 50% in water-wet systems and less than 50% for oil-wet systems. This could be described by the relative permeability endpoints of the two phases at different wetting conditions. In a strongly water-wet system, endpoint relative permeability to oil is high (normally near 1), but water relative permeability endpoint is low (0.15 to 0.3) which results in a crossover point at water saturations greater than 50%. In an oil-wet system, water relative permeability endpoint is generally greater (0.4 to 0.7) and oil relative permeability is less than unity, resulting in a crossover point at water saturations more than 50% (Hirasaki *et al.*, 2004).

2.5.3 Effect of Wettability on Capillary pressure and Capillary Desaturation Curves

Capillary pressure is defined as the pressure difference between the wetting and non-wetting phases. Lake (1989) claims that capillary pressure is due to high curvature in boundaries between different homogeneous phases. Young-Laplace equation could be used to relate capillary pressure to contact angle (which is a measure of wettability as described in Section 2.2.1), pore curvature, and interfacial tension as shown in Eq.2.3

$$P_c = \frac{2\sigma Cos(\theta)}{R} \qquad \text{Eq.2.3}$$

where P_c is the capillary pressure between the two phases, σ is interfacial tension between the two immiscible fluids, θ is contact angle and R is radius of the curvature where the pores are assumed to be cylinders. For the non-wetting phase to be able to enter a pore, its pressure should exceed the capillary entry pressure which is a function of the pore throat diameter. The smaller the pore throat diameter, the higher the capillary entry pressure is. In oil-wet reservoirs, since oil is distributed in smaller pores and capillary entry pressures are high for these pores, most of the oil is trapped and bypassed in water floods. One way of overcoming the capillary forces is to reduce the interfacial tension between the two phases, which would result a smaller capillary pressure as described in Eq.2.3. This could be done by surface active agents or surfactants.

Capillary pressure is normally defined as oil pressure minus water pressure (regardless of wettability conditions) in reservoir engineering, and plotted versus water saturation. Based on the wettability condition of the rock, such plots might have positive and negative values such as graphs shown by Craig (1971). Based on this definition of capillary pressure, if a rock is strongly water-wet, i.e. I ~ 1, then its spontaneous imbibition curve would only be positive and residual oil saturation would be achieved at zero capillary pressure. If the rock is intermediate or neutral wet, then it would have less tendencies to imbibe water spontaneously and oil saturation in that rock would be higher at the end of spontaneous imbibition compared to a strongly water-wet rock. In this case it would be possible to increase water saturation of the core by forced imbibition, which results in a capillary pressure curve with positive and negative portions. If the rock is oil-wet then it would have no tendency for imbibing water, resulting in negative capillary pressures. Examples of such capillary pressure data are found in Craig (1971).

Capillary number, N_c, introduced by Brownell and Katz (1949) is a dimensionless number resulting from the ratio of viscous to capillary forces. Up to a certain capillary number known as critical capillary number, N_{cc}, a phase is not mobilized. But eventually when $N_c > N_{cc}$, as this ratio increases, i.e. viscous forces overcome the capillary forces, more amount of each phase is mobilized and as a result of this, residual phase saturations

decrease. This effect could be shown in capillary desaturation curves (CDC), in which residual phase saturations are plotted against capillary number, N_c. If a rock is strongly water-wet, then N_{cc} of water is higher than N_{cc} of oil and it is easier to mobilize oil than water. This is the result of phase distributions and the fact that in a water-wet rock, water tends to occupy smaller pores. Obviously in an oil-wet rock this reverses because of the same reason. Figure 2.5 shows an good example of CDC curves for different fluids in Berea sandstone core presented by Pope *et al*. (1982). Mohanty (1983) shows the effect of wettability on oil capillary desaturation curves as presented in Fig. 2.6. The shape and characteristics of capillary desaturation curves depend also on rock types besides the wettability. This could be observed by comparing Figs. 2.6 and 2.7. Figure 2.7 (Kamath *et al*., 2001) shows oil capillary desaturation curves for three oil-wet to neutral-wet carbonates. The main observation is extremely lower (about three orders of magnitude) critical capillary numbers for carbonate rocks compared to the Berea sandstone with approximately same wettability condition. This different behavior could be due to different pore size and fluid distributions and different porosity, and permeability of the two rock types (Hirasaki *et al.*, 2004).

2.6 Surfactants Used for Enhanced Oil Recovery

Surfactants or surface active agents are usually large molecules with minimum one hydrophilic and minimum one hydrophobic portion. This dual nature enables surfactants to exist at the interface of water and other fluids (such as oil) and to reduce the surface energy.

Surfactant concentration has a strong effect on surfactant behavior. At low concentrations anionic surfactants, as described below, ionize to a cation and an anionic monomer if dissolved in aqueous phase (Akstinat, 1981). If the surfactant concentration is then increased, the lypophilic portions of the monomers start to aggregate and form micelles which might contain several monomers. After a certain concentration known as the *critical micelle concentration* (CMC), further increase in the surfactant concentration will only increase the micelle concentration. Figure 2.8 shows a schematic of surfactant monomer concentration versus total surfactant concentration (Lake, 1989). Other

parameters such as temperature, brine salinity, and hardness play a more critical role in surfactant/oil/brine phase behavior.

2.6.1 Classification of surfactants

Four groups of surfactants based on the polar portion are (Lake, 1989):

1. Anionics: The molecule is electrically neutralized with an inorganic metal cation. When dissolved in aqueous phase, the molecule is ionized into a cation and the anionic monomer. This group of surfactants has been used widely in oil industry for their good retention resistance, stability, and low cost.
2. Cationics: A positively charged polar portion results in a cationic surfactant. The molecules of these surfactants are electrically neutralized with an inorganic anion. This group of surfactants has not been widely used in chemical floods since they are easily adsorbed by negatively charged surface of interstitial clays.
3. Nonionics: These molecules exhibit surfactant properties due to electronegativity contrasts between their constituents. Nonionics are poorer surfactants compared to anionic surfactants but work much better in high salinities. This group of surfactants is recently used more extensively in chemical floods as primary surfactant.
4. Amphoterics: These surfactants exhibit properties of two or more groups of previously discussed surfactants and have not been used in chemical flooding.

2.6.2 Surfactant/Brine/Oil Phase Behavior

Conventionally the surfactant/oil/brine phase behavior is shown on a ternary diagram and usually the surfactant pseudocomponent is placed at the top apex, brine is placed at the lower left apex and lower right apex represents oil. The phase behavior is strongly controlled by salinity of the brine among other variables such as temperature and cosolvent concentration. Surfactants used in chemical flooding processes, typically exhibit good aqueous-phase solubility and poor oil-phase solubility at low brine salinities. Thus at low brine salinities, an overall composition in the two phase region will split into two phases: an excess oil phase and a water external microemulsion phase. The excess oil

phase is essentially pure oil and the microemulsion phase is consisted of brine, surfactant and some solubilized oil which is at the center of micelles. This phase environment is referred to as Winsor Type I system, a lower phase microemulsion or Type II(-) system. The last terminology is due to the fact that the system consists of two phases and the slope of the tie lines in the two phase region is negative (Winsor, 1954; Nelson and Pope, 1978; Lake, 1989). Figure 2.9 shows a schematic for phase behavior of a Type II(−) system.

At high brine salinities, surfactant solubility in the aqueous phase is drastically reduced due to electrostatic forces. Thus at high brine salinities, an overall composition in the two phase region will split into an oil external microemulsion phase and an excess brine phase. In this case the brine phase would essentially contain no surfactant and some of the brine phase is solubilized in the microemulsion phase at the center of the micelles. This system is referred to as a Winsor Type II, an upper microemulsion or a Type II(+) system (Winsor, 1954; Nelson and Pope, 1978, Lake, 1989) (Fig. 2.10).

At the brine salinities between the two extremes discussed above, there exists a third type of phase behavior in which three phases (a brine phase, a microemulsion phase and an oil phase) coexist. The microemulsion phase could be water or oil external depending on salinity and overall composition. This system is known as a Winsor Type III, a middle-phase microemulsion or a Type III system (Winsor, 1954; Nelson and Pope, 1978, Lake, 1989) (Fig. 2.11).

2.6.3 Phase Behavior and Interfacial Tension

Reed and Healy (1974) correlated the interfacial tension (IFT) and phase behavior of microemulsion systems. Figure 2.12 shows their correlation. In this figure σ_{32} and σ_{31} are interfacial tensions between the microemulsion/excess oil and microemulsion/excess brine respectively. As could be seen in this figure, σ_{32} decreases drastically as brine salinity increases and σ_{31} increases drastically as brine salinity increases. The salinity at the crossover point of these two interfacial tensions is called the optimum salinity and the interfacial tension of the whole system is minimized at this salinity. The IFT of the

system at the optimum salinity is normally about 1 μN/m which is good enough to reduce the capillary forces to negligible values and result in recovery of bypassed and trapped oil saturations.

2.7. Enhanced Oil Recovery

Willhite (1986) defines enhanced oil recovery as any process that helps recover more oil from a reservoir than what the reservoirs can produce by its own energy. This is a very general definition and includes gas injection for maintenance of pressure and waterflooding. Lake (1989) defines EOR as a process that recovers oil from a reservoir by injection of materials not normally present in the reservoir. This definition is more specific and excludes the above mentioned processes. Three categories can be specified for EOR processes based on the second definition: thermal oil recovery, miscible flooding and chemical flooding. The later is the subject of this study. Several chemical flooding processes are defined and discussed below.

2.7.1. Polymer Flooding

Polymer flooding is probably the simplest chemical EOR process. The main objective in a polymer flood is to improve the efficiency of the flood by decreasing water mobility (Sorbie, 1991). This is done by injection of water soluble polymers that increase water viscosity and therefore decrease water mobility. This decrease in water mobility can also help preventing viscous instability at the polymer/oil bank front. As water viscosity increases its fractional flow decreases and this increases the displacement sweep efficiency. The permeability reduction effects of polymer reduce the effective permeability of the high permeability channels and improve the areal sweep efficiency. Recent studies have shown that increasing the injected mass of polymer results in better mobility control and sweep efficiency which results in more profitability (Anderson *et al.*, 2006).

Two types of polymers have been used for field applications: polysaccharides and partially hydrolyzed polyacrylamides (HPAM). Recent advances in polymer technology have increased the limits of polymer flooding to a great extent. Levitt and Pope (2008)

have presented polymers with high viscosities at high salinities (up to 170,000 ppm NaCl with greater than 17,000 ppm $CaCl_2$ present). They have also shown that if calcium concentration can be kept below 200 ppm, polyacrylamide polymers can be used up to 100 °C. Levitt and Pope (2008) also suggest that for higher concentrations of calcium at high temperatures, sodium metaborate or copolymers such as sodium 2-acrylamide-2-methylpropane sulfate (AMPS) could be used to increase the calcium tolerance.

Huh and Pope (2008) have shown that polymer floods are capable of reducing the residual oil saturation to values lower that residual oil saturation to waterfloods, provided the polymer flood is used as a secondary recovery mechanism, i.e. a waterflood is not performed prior to the polymer flood.

The above mentioned findings may stretch the application range for polymer flooding.

2.7.2. Alkaline Flooding

In this chemical EOR process an alkaline agent is injected into a reservoir. The classic reason for injection of alkali in the past was to create some in-situ soap (surfactant) from the acidic components of the crude oil which then would help lowering the interfacial tension (IFT) between the oil and water and help mobilizing the trapped oil. When an alkaline agent is injected into a reservoir, the hydroxide anions reduce the concentration of hydrogen in the aqueous phase. This helps in solubilization of some of the acidic components of the oil in the aqueous phase and generation of in-situ soap.

Besides the above mentioned application of alkaline flooding, recently researchers have focused on wettability alteration effects of some alkalis. A large portion of world's oil reserves are contained in carbonate formations (Roehl and Choquette, 1985) most of which are naturally fractured. The fracture network has much higher permeability compared to the matrix. Most of these carbonate reservoirs are mixed-wet to preferentially oil-wet (Downs and Hoover, 1989). The combination of the low matrix permeability and the preferentially oil-wt nature of carbonate formations result in poor primary oil recovery factors in such reservoirs. Waterflooding of these formations is not

efficient due to very small tendency for imbibition of the injected aqueous solution by the oil-wet matrix. To improve the oil recovery from such formations, it is required to improve the rate of imbibition of the injected aqueous phase into the matrix. One way of achieving this goal is by alteration of the wettability of the matrix rock towards more water-wet conditions. Many researchers have recently studied the imbibition rate of aqueous solutions into preferentially oil-wet carbonate rocks. Hirasaki and Zhang (2004) and Adibhatla and Mohanty (2008) have studied oil recovery from such formations using a combination of anionic surfactants (propoxyl ethoxyl sulfates) and an alkali (sodium carbonate). They concluded that at ultra-low IFTs achieved by the anionic surfactants, the oil can be recovered by virtue of buoyancy and wettability alteration. Zhang *et al*. (2008) have shown that an alkali such as sodium carbonate is capable of drastically reducing the contact angle of an oil droplet on both quartz (SiO_2) and calcite ($CaCO_3$). On the quartz surface (Fig. 2.13) the initial contact angle of 130° was reduced to 105° after 25 hours of aging in a 4.8% Na_2CO_3 solution. The wettability alteration effects of the alkali were even more on the calcite surface (Fig. 2.14) where the initial contact angle of 120° was reduced to 75° after 25 hours. This significant change in the wetting characteristics of the carbonate surfaces can increase the imbibition rate of the injected aqueous solutions into the matrix rock of fractured carbonates and increase the recovery factor to a great extent. A complete definition of wettability and contact angle is given earlier in this chapter.

2.7.3. Surfactant/Polymer Flooding

This chemical EOR method is probably the most widely studied and used process after polymer flooding up to this day. A surfactant or a group of surfactants and other chemicals such as cosolvents are designed and tailored for the rock fluid system of the target reservoir. The chemicals are injected into the reservoir as a finite slug that also contains polymer for mobility control. This chemical slug is then pushed towards the production wells by a polymer drive. The surfactant slug helps recovering the oil in two important ways: oil solubilization and oil mobilization. The former is the result of creation of a microemulsion phase. Microemulsions are thermodynamically stable phases containing surfactants, aqueous electrolytes and oleic components. Oil mobilization is the

result of IFT reduction by the surfactant(s). The mobilization process will be discussed in the following sections.

The most important advantage of surfactant/polymer process over polymer flooding is recovery of the residual oil. Although polymer flooding may have a lower residual oil saturation compared to waterfloods (Huh and Pope, 2008), it is not capable of reducing residual oil saturation to values close to zero. Surfactant/polymer floods on the other hand are capable of reducing the residual oil to low values (Osterioh and Jante, 1992; Wang *et al*., 2008). In fact, in many lab tests recoveries very close to 100% OOIP are reported (Delshad, 1990; Zhao *et al*., 2008; Flaaten *et al*., 2008). For a successful surfactant/polymer flood in the field, besides the choice of chemicals suitable for the specific properties of the target reservoir there are other important steps to be taken. The most important of these steps is design and optimization of the flood in the field scale. This is when numerical simulation plays a crucial role for design and optimization of chemical floods. The development of a fully implicit, parallel chemical flooding module is the subject of Chapter 6. Design and optimization of chemical floods in field scale are discussed in the following chapters.

2.7.3.1 Surfactant/Polymer Flood Simulators

There are very few reservoir simulators that have capability of modeling surfactant/polymer floods. Examples include commercial simulators of ECLIPSE 100, CMG-STARS and UT developed simulators of UTCHEM, GPAS, and UTCOMP. A brief description of the capability of some of these codes is presented here.

ECLIPSE 100

ECLIPSE simulator models polymer viscosity as function of polymer concentration and salinity and shear rate generally by input of tables by user specifying polymer viscosity as a function of the above mentioned parameters. Polymer adsorption and permeability

reduction effects of polymer can also be modeled using ECLIPSE (ECLIPSE Technical Documentation, 2008).

Surfactant model of ECLIPSE is fully implicit and it is limited to Winsor Type I (Winsor, 1954) floods where the surfactant is only present in an aqueous external ME phase. Relative permeability curves in ECLIPSE are functions of capillary number using a table that describes the transition of relative permeability curves as function of $\log_{10}$ of capillary number. Capillary pressure is scaled with IFT and as IFT is reduced due to presence of surfactant, the capillary pressure is reduced. ECLIPSE also models surfactant adsorption on the rock surface (ECLIPSE Technical Documentation, 2008).

UTCHEM

Polymer viscosity in UTCHEM is modeled as a 3rd order parabolic function of polymer concentration. Effects of salinity (both anions and cations) and temperature on polymer viscosity are modeled. Correlation presented by Meter and Bird (1964) is used for modeling effect of shear rate on polymer viscosity with an effective shear rate calculated for the porous medium. Polymer adsorption, permeability reduction effects of polymer and the inaccessible pore volume by polymer is also modeled in UTCHEM (UTCHEM Technical Documentation).

Surfactant/oil/brine phase behavior as function of salinity (anions and cations), temperature and co-solvent concentration is modeled using Hand's rule (Hand, 1939). IFT can be calculated in two ways: using Huh's correlation (1979) modified by Hirasaki (1981) and Delshad *et al*. (1996) or using the correlation introduced by Healy and Reed (1974) and corrected by Hirasaki (1981). Surfactant adsorption and the consequent reduction of pore volume are modeled in UTCHEM. ME viscosity as a function of ME composition is calculated in UTCHEM (UTCHEM Technical Documentation).

GPAS

The first chemical flooding module of GPAS was published by John *et al*. (2005). This development was based on a hybrid approach where the material balance equation of the hydrocarbon components and water were solved implicitly and then the material balance equation of the aqueous components such as surfactant, polymer and salt were solved explicitly. This implementation had two important shortcomings from the formulation point of view:

1. The volume of the oil dissolved in the microemulsion (ME) phase was neglected.
2. The volume of the surfactant was neglected in the volume constraint equation.

These two problems lead to inaccurate results specially when the height of binodal curve is small and/or the amount of injected surfactant is large in which case the volume of the oil solubilized in the ME phase is significant and cannot be neglected. Another important limitation of this development was its limitation to model only Type I or Type II(-) oil/brine/surfactant phase behavior where an excess oleic phase is in equilibrium with a ME phase. In 2007 Han *et al*. published a fully implicit chemical flooding module of GPAS which removed the two formulation limitations of the hybrid model (i.e. the volume of oil in the ME was considered and the volume of surfactant was taken into account in the volume constraint). But the limitation of the phase behavior to only two phase regions was not removed.

2.7.4. Alkaline/Surfactant Flooding

As mentioned above, the resources locked in naturally fractured carbonates are enormous and can have a huge effect on the energy security if unlocked. Hirasaki and Zhang (2004) and Adibhatla and Mohanty (2008) have used anionic surfactants to reach ultra low IFTs. Since the surface of carbonate rocks are normally positively charged in low pH, they have used alkalis such as sodium carbonate to reduce the adsorption of anionic surfactants to the carbonate surface. This is possible since carbonate surface becomes negatively charged in the presence of sodium carbonate. Hirasaki and Zhang (2004) suggest that the trapped oil in carbonate rocks is held in place by capillarity and wettability. Thus if capillary forces are diminished by ultra low IFTs and wettability is

modified to more water-wet conditions, the trapped oil can be produced. They show by conventional imbibition cell test experiments that in the absence of capillary forces and by the help of wettability alteration, the trapped oil in an originally oil-wet core can be produced under gravity drainage. Kumar *et al*. (2005) proposed that the wettability of carbonate surfaces is controlled by adsorption of asphaltenes. They found that anionic surfactants could remove the adsorbed asphaltenes and induce partial water-wetness. Adibhatla and Mohanty (2008) have also studied the oil recovery from carbonate rocks using anionic surfactants and alkaline solutions. They conclude that the surfactant lowers the IFT and alters the wettability as it diffuses into the matrix, enabling gravity to drain the oil upwards. They claim that the oil recovery rate increases as matrix permeability increases, fracture height or spacing decreases and the wettability alteration properties of the surfactant increases. They have also found that oil recovery is not necessarily enhanced by increasing the surfactant concentration and this is due to the fact that neither IFT reduction, nor wettability alteration are linearly correlated with surfactant concentration. Adibhatla and Mohanty (2008) named this oil recovery mechanism as "Surfactant-Aided Gravity Drainage."

In Chapter 4 of this work, one of the experiments performed by Hirasaki and Zhang (2004) is modeled to shed some light on the mechanisms involved in oil recovery from fractured oil-wet carbonates.

2.7.5. Oil Recovery Methods for NFRs

Some researchers have suggested use of non-ionic and cationic surfactants for modifying the wettability and enhancing the water imbibition rate in NFRs (Austad and Milter, 1997; Austad *et al.*, 1998; Standes and Austad, 2000). They have performed their studies on oil-wet chalk cores and used non-ionic and cationic surfactants to prevent adsorption of surfactants to positively charged chalk surface. Since the cationic surfactants do not reduce IFT to ultralow values, capillary imbibition of the aqueous phase would still be the dominate recovery mechanism. Chen *et al*. (2000) have also used nonionic surfactants for enhancement of spontaneous imbibition and Spinler *et al*. (2000) evaluated 46 different commercially available surfactants to improve spontaneous imbibition of chalk

samples. Austad *et al.* (2005 and 2007) proposed seawater injection as an improved oil recovery method for chalk formations and proposed a chemical model for wettability modification effects of seawater on chalk surface. They observed that neutral/moderately water-wet chalk surface becomes more water-wet in contact with seawater. The explanation was that the positively charged chalk surface becomes oil-wet by adsorption of negatively charged carboxylic acids present in the crude oil. Free divalent cations (Ca^{2+} active at low temperatures and Mg^{2+} active at high temperatures) present in seawater are claimed to attract the carboxylic acids and separate them from the chalk surface. This results in a water-wet surface that promotes spontaneous imbibition of aqueous phase, increasing the oil recovery. This recovery method will not be studied in this work.

2.8 Scale Dependency of EOR Methods for NFRs

Many of the EOR processes mentioned in Section 2.7 are tested in laboratory scale before going to pilot or commercial scale operations. A very important issue is then determination of the efficiency of these processes in field scale. In other words, does the recovery efficiency change from laboratory to field scale? How do different recovery mechanisms scale with reservoir size? Here two methods are specified to infer the performance of certain recovery mechanisms in field scale from their performance in laboratory scale. The first method discussed in Section 2.8.1 is based on dimensionless study of the system. The second method is based on numerical simulation where the results of a laboratory experiment are matched with an adequate numerical model. Then the matching parameters can be used to study the effect of reservoir size on different recovery mechanisms.

2.8.1 Dimensionless Analysis of Laboratory Experiments

Dependency of the results of laboratory experiments on reservoir size can be specified using dimensionless recovery curves or dimensionless recovery times. Laboratory alkali and surfactant floods have shown a great potential in increasing oil recovery for reservoirs that are naturally fractured with low permeability mixed-wet matrix rocks. Fractured, mixed-wet formations usually have poor waterflood performance because the

injected water tends to flow in the fractures and spontaneous imbibition into the matrix is generally insignificant. Surfactants or alkalis have successfully been used to change the wettability and enhance oil recovery by increased imbibition of the water into the matrix rock. The oil recovery mechanisms using surfactant/alkali mixtures are enhanced imbibition and buoyancy due to combined effects of reduced interfacial tension, reduced mobility ratio, and wettability alteration. An important question is that how do these recovery mechanisms scale with reservoir size?

Many researchers have made attempts to scale up imbibition test results from laboratory scale to field scale using a dimensionless time for imbibition. There are two major categories amongst these proposed scaling groups: most of them, assume that the main mechanism for oil production is capillary imbibition. Correlations proposed by Mattax and Kyte (1961), Cuiec *et al.* (1990), Kazemi *et al*. (1992), Zhang *et al.* (1996), Ma *et al.* (1997) and Babadagli (2001), fall into this category. All of these researchers claim that the imbibition time scales with the square of some measure of the length of the matrix blocks. There is another category of scaling groups which assumes that the main mechanism controlling the imbibition is buoyancy. In this category, the correlation proposed by Cuiec *et al.* (1990) (Eq.2.4) could be mentioned, which dictates that imbibition time scales with matrix block size. Some researchers such as Hirasaki and Zhang (2004) and Adibhatla and Mohanty (2006) claim that when a surfactant solution designed to lower the IFT to ultra low values is used for enhancement of the imbibition process the mechanisms are different. At early times, capillary imbibition is the dominant force but once IFT is reduced to ultra low values the gravity forces dominate the recovery process.

Cuiec *et al.* (1990) proposed a reference time based on the gravity forces (the ratio of viscous to gravity forces) as follows:

$$t_g = \frac{\mu_o L}{\Delta\rho g k} \qquad \text{Eq.2.4}$$

where t_g is the gravity reference time, μ_o is oil viscosity, k is absolute permeability, L is the length of the rock sample and $\Delta\rho$ is density difference between oil and water. If

gravitational and buoyancy forces are dominating the imbibition process, then dividing the experimental time with this reference time would result in one recovery curve for all the cases regardless of the matrix rock size.

Li and Horne (2006) introduced a generalized dimensionless time including almost all of the parameters present in an imbibition process for cocurrent flow except the wettability shift. Their dimensionless time is based on an analytical solution of the flow equations (Darcy's law) and reads as

$$t_d = c^2 \frac{k_e P_c \left(S_{wf} - S_{wi} \right)}{\phi \mu_e L_a^2} t \qquad \text{Eq.2.5}$$

where t_d is dimensionless time, c is the ratio of gravity to capillary forces, S_{wf} is the wetting phase saturation at the front, k_e^* is effective permeability of the two phases at S_{wf}, P_c^* is the capillary pressure at S_{wf}, μ_e is the effective viscosity of the two phases, S_{wi} is initial wetting phase saturation, ϕ is the porosity, L_a is the characteristic length of the core and t is experimental time. They introduce an effective mobility for the experiment as follows:

$$M_e^* = \frac{k_e^*}{\mu_e} = \frac{M_w^* M_{nw}^*}{M_{nw}^* - M_w^*} \qquad \text{Eq.2.6}$$

where M_e^* is the effective mobility at S_{wf} and M_w^* and M_{nw}^* are wetting and non-wetting phase mobilities at S_{wf} respectively. As could be seen in Eq.2.5, Li and Horne (2006) claim that the dimensionless time scales with reciprocal of length squared. Figure 2.15 shows resulting recovery curves for several experiments when the dimensionless time is used.

Ma *et al.* (1997) have proposed an equation for calculation of the characteristic length based on core geometry and boundary conditions. Li and Horn (2006) used the following equation proposed by Ma *et al.*:

$$L_c = \sqrt{\frac{V_b}{\sum_{i=1}^{n} \frac{A_i}{l_{A_i}}}} \qquad \text{Eq.2.7}$$

where L_c is the characteristic length, V_b is bulk volume of the core, A_i is any surface open to imbibition, l_{Ai} is the distance from A_i to the no flow boundary and n is number of surfaces open to imbibition. The characteristic length for the field is the distance between fracture faces. Therefore, the dimensionless time required to reach maximum recovery is inversely proportional to the square of fracture spacing.

Ma *et al*. (1997) proposed a dimensionless number for the rate of imbibition as follows:

$$t_D = t\sqrt{\frac{k}{\phi}}\frac{\sigma}{\sqrt{\mu_w \mu_o}}\frac{\cos(\theta)}{L_c^2} \qquad \text{Eq.2.8}$$

where t_D is dimensionless time, t is time, k is rock permeability, ϕ is porosity, σ is interfacial tension, μ_w and μ_o are water and oil viscosities, θ is the contact angle, and L_c is the characteristic length specified in Eq.2.7.

Hognesen *et al*. (2004) tested the dimensionless time correlation developed by Li and Horne (2006) for their imbibition experiments in carbonate rocks performed for a wide range of experimental conditions of interfacial tension, permeability, initial water saturation, core height and diameter, temperature, and sulfate concentration. All the parameters were scaled very well when the normalized oil recovery was plotted versus dimensionless time once the height of the core was used as the shape factor. They concluded that gravitational forces were significant oil recovery mechanisms in their experiments.

2.8.2 Scale Dependency of Recovery Mechanisms used for NFRs Using Numerical Modeling

Adibhatla *et al.* (2005) developed a simulator that incorporated variation of IFT and wettability as the results of surfactant diffusion and imbibition into a matrix rock. Numerical model successfully matched the results of their lab scale experiments. A simulation study was then carried out using the parameters that matched the lab scale experiment to model larger fracture blocks. Their results indicated that it takes over 100 years to recover about 60% oil from a 10m by 10m matrix block compared to 30 days in

the lab scale core. They concluded that the oil production decreases as the matrix block height increases or surfactant alters wettability to a lesser degree, or permeability decreases.

The time dependence of imbibition process and upscaling of the laboratory imbibition test results was also addressed by Stoll *et al.* (2008) using a 1D model to simulate numerous imbibition experiments. Their results indicated that the imbibition in the absence of buoyancy forces is very slow and diffusion-limited after the wettability alteration. Consequently, the wettability alteration of oil-wet fractured carbonates is not economically feasible unless there is a faster transport mechanism such as forced imbibition with viscous or buoyancy forces. Stoll *et al.* (2008) calculations indicated that the time scale of diffusion scales with length of sample squared. Therefore, it would take about 200 years before the same recovery is obtained from a meter scale matrix block compared to 100 days in one cm core plug.

Although laboratory experiments are essential, it is impossible to predict the performance of these complex processes with only laboratory experiments. Reservoir simulation is required to scale up the process from laboratory to field conditions and to understand and interpret the data. Without detailed and mechanistic simulations it is very unlikely that a cost-effective process can be developed and applied economically. The predictive simulations of such complex processes will reduce the risk of failure of the field projects.

2.9 Modeling Aspects of Wettability Alteration in NFRs

As mentioned in Section 2.7.4, chemicals such as alkali and/or surfactants are capable of changing the wettability of matrix formation towards more water wet conditions and improve the rate of imbibition of the injected aqueous phase into the matrix. This increases the oil recovery from NFRs with preferentially oil wet formations (Hirasaki and Zhang, 2004, Adibhatla and Mohanty, 2008). Some researchers have modeled the wettability alteration effects of alkali or surfactant mixtures to better understand such processes.

Castillo (2003) modeled the wettability alteration of alkali or surfactants in UTCHEM using the effect of wettability on petrophysical properties such as relative permeability and capillary pressure. In this model the user can specify the initial and altered wetting conditions of the rock. This is done by specifying water and oil relative permeability and water-oil capillary pressure tables for each wettability condition as input. Time dependent wettability alteration is modeled using an input threshold value for a tracer concentration representing the alkali or surfactant concentration in each gridblock. The injected surfactant advances in the reservoir and when its concentration is greater than a threshold value specified as an input parameter, the tables for altered wetting conditions are used.

Anderson (2006) used the model developed by Castillo (2003) and Fathi Najafabadi (2005) to study the effect of wettability on the oil recovery from NFRs. He was able to successfully model many published core floods that involving chemically induced wettability alteration.

Adibhatla *et al*. (2005) developed a 3D numerical simulator with the capability of modeling wettability alteration effects of surfactants. This simulator is finite-volume and can model flow of two phases and four components using fully implicit scheme. Residual phase saturations, relative permeability and capillary pressure curves in this model are functions of IFT and wettability. Contact angle is used in this model as a representation of the wetting state of each phase and residual phase saturations are interpolated based on their contact angle (Adibhatla *et al*. 2005). They were able to match oil recovery from alkali surfactant imbibition tests with this numerical simulator.

ECLIPSE simulator has also a wettability alteration model. The change in the wettability of the rock by adsorption of surfactant on the rock surface is modeled using two relative permeability tables for two extreme wetting conditions and interpolating between them using a weight factor, *F* (ECLIPSE Technical Documentation, 2008).

Delshad *et al*. (2006) used the wettability alteration model of UTCHEM (Fathi Najafabadi, 2005) to model an imbibition cell test published by Hirasaki and Zhang (2004). The matching parameters were then used to study the effect of wettability alteration in pilot scale.

Fathi Najafabadi *et al*. (2008) used the wettability alteration model of UTCHEM (Fathi Najafabadi, 2005) to model a dynamic chemical flood laboratory experiment performed on a fractured block at UT Austin. This experiment contained three parts; a waterflood followed by alkali flood for enhancing the wettability towards more water-wet conditions and an alkali surfactant flood for reducing the residual oil in the matrix. All three parts of this experiment were modeled and very good match between the recorded experimental recovery curves and the simulated curves was obtained. They concluded that a small viscous gradient can improve the recovery from NFRs to a great extent and static imbibition cell tests are not representative of dynamic conditions of the reservoir.

Delshad *et al*. (2009) used the models published by Delshad et al. (2006) and Fathi Najafabadi et al. (2008) to study the effect of matrix size on the recovery rate from NFRs. They concluded that in static imbibition conditions where gravity is the dominant oil recovery mechanism (due to reduction of capillary pressure to ultra low values by surfactant), the oil recovery rate scales with the height of the matrix block.

2.10 Reservoir Simulation Using Fully Implicit Scheme

A brief description of the fully implicit scheme is presented here along with its advantages and disadvantages.

2.10.1 Definition of Fully Implicit Method

When a partial differential equation (PDE), such as material balance equation of a species in the reservoir, is solved numerically, the equation should be discretized both in space and time. To obtain the solution of the PDE in the next time level, the dependency on time could be treated at the present time level and if so, the formulation is called explicit in time. If the time dependency is treated at the next time level, then the formulation is

called fully implicit. One method for solving a system of non linear equations arising from discretization of the material balance and volume constraint equations in a reservoir simulation is the Newton's method described below.

2.10.2 Newton's Method for Solving Fully Implicit System of PDEs

In reservoir simulation, we use Newton's method for solving a system of non-linear equations arising from discretization of governing PDEs using an implicit method. Suppose that we have a non-linear system of equations given below

$$\underset{\sim}{f}\left(\underset{\sim}{X}\right) = 0, i = 1, 2, \ldots, n \qquad \text{Eq.2. 9}$$

where

$$\vec{X} = \left(\vec{x}_1, \vec{x}_2, ..., \vec{x}_n\right) \qquad \text{Eq.2. 10}$$

is a solution to Eq.2. 9. This exact solution at a new time level can be approximated by the solution at the previous time level as follows:

$$\underset{\sim}{X}^{k+1} = \underset{\sim}{X}^{k} + \delta\underset{\sim}{X}^{k} \qquad \text{Eq.2. 11}$$

The increment vector ($\delta\underset{\sim}{X}^{k}$) is obtained as follows:

$$\delta\underset{\sim}{X}^{k} = -\left[\underset{\sim}{f}'\left(\underset{\sim}{X}^{k}\right)\right]^{-1}\underset{\sim}{f}\left(\underset{\sim}{X}^{k}\right) = -J\left(\underset{\sim}{X}^{k}\right)^{-1}\underset{\sim}{f}\left(\underset{\sim}{X}^{k}\right) \qquad \text{Eq.2. 12}$$

where $J\left(\underset{\sim}{X}^{k}\right)$ is called the Jacobian of the system.

This method has a second-order convergence when the approximate solution is near the exact solution and converges after few iterations. The stability of the Newton's method is maintained even with large changes in dependant variables (Anthony *et al*., 1980).

2.10.3 Advantages and Disadvantages of Fully Implicit Scheme

Fully implicit methods are very stable and can tolerate much larger timesteps compared to explicit methods. On the other hand the computational over head of fully implicit methods are larger per timestep compared to explicit methods. Another disadvantage of fully implicit methods is the truncation error associated with large timestep sizes. It is also more difficult to implement high-order methods in fully implicit scheme to reduce

spatial truncation errors and this is also considered one of the disadvantages of the fully implicit method (Anthony *et al*., 1980).

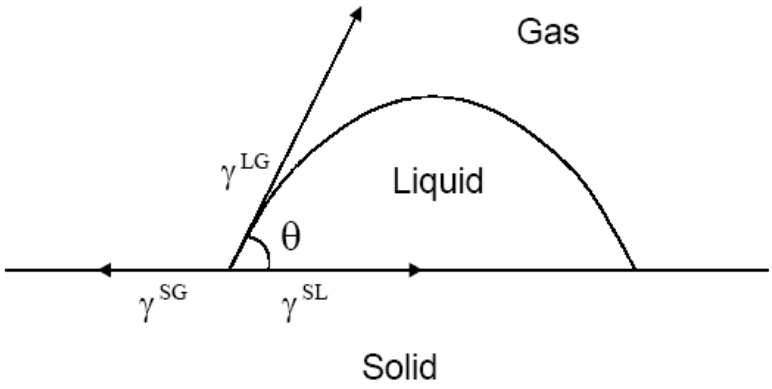

Figure 2.1: Interfacial tensions and contact angle.

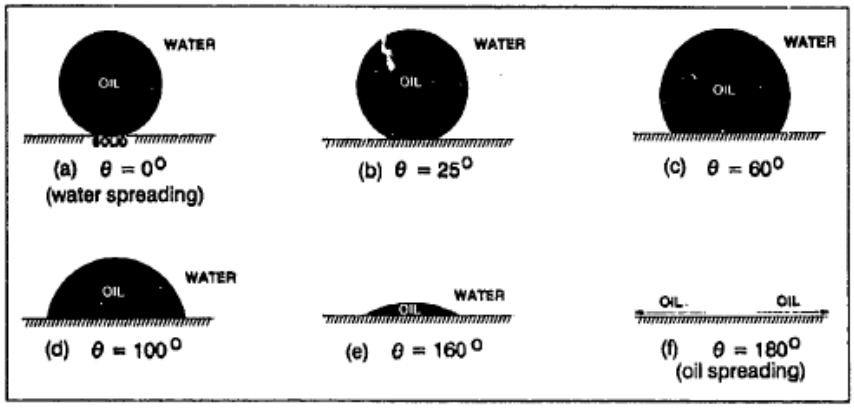

Figure 2.2: Idealized examples of contact angle and spreading (Morrow, 1990).

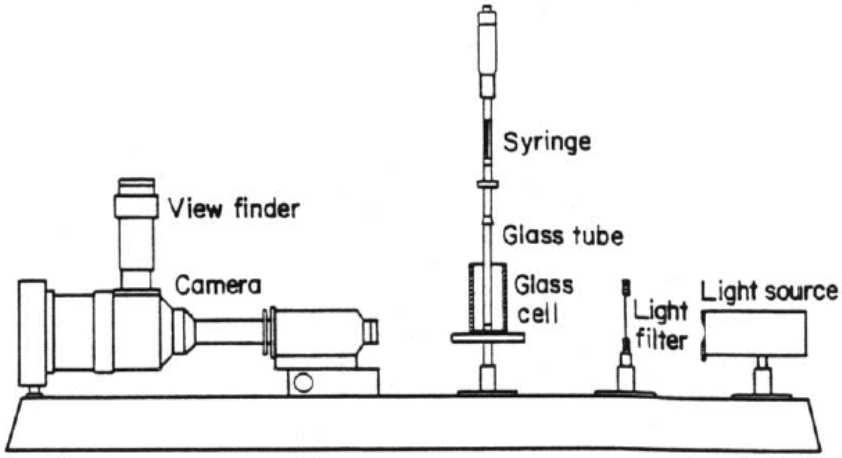

Figure 2.3: Schematic diagram of contact angle setup (Somasuundaran and Zhang, 2004).

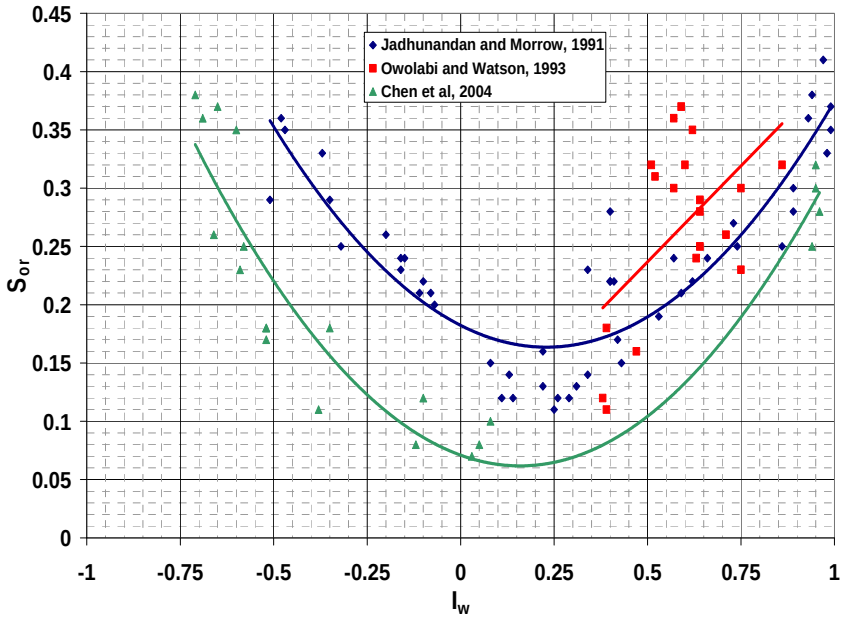

Figure 2.4: Effect of wettability on residual oil saturation (Anderson, 2006).

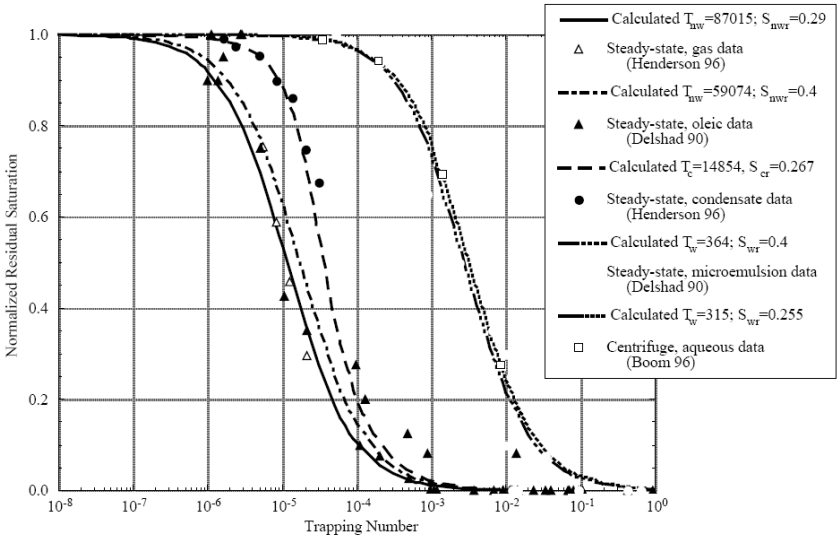

Figure 2.5: Capillary desaturation curves of different fluids in Berea sandstone (Pope *et al*., 2000). The curves are fits to the data using the dependency of residual phase saturations on trapping number (Eq.3.16).

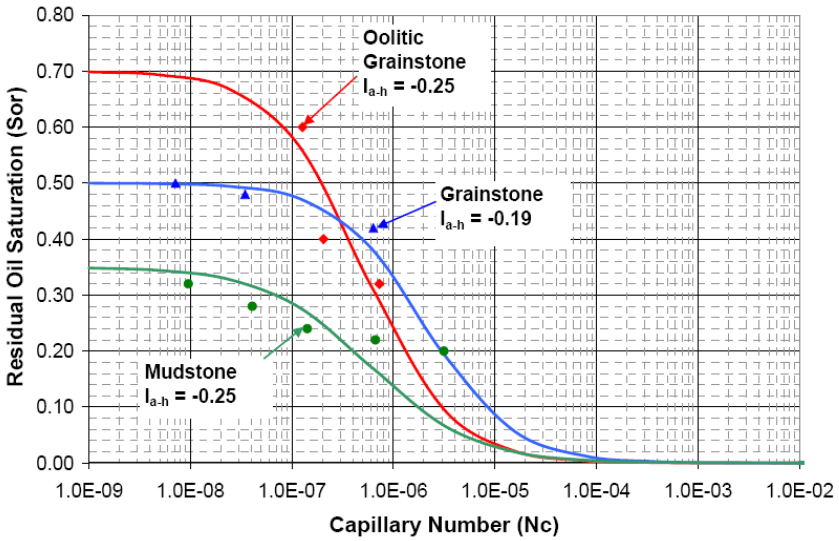

Figure 2.6: Effect of wettability on CDCs of Berea sandstone (Mohanty, 1983) Figure regenerated by Anderson (2006). The curves are fits to the data using the dependency of residual phase saturations on trapping number (Eq.3.16).

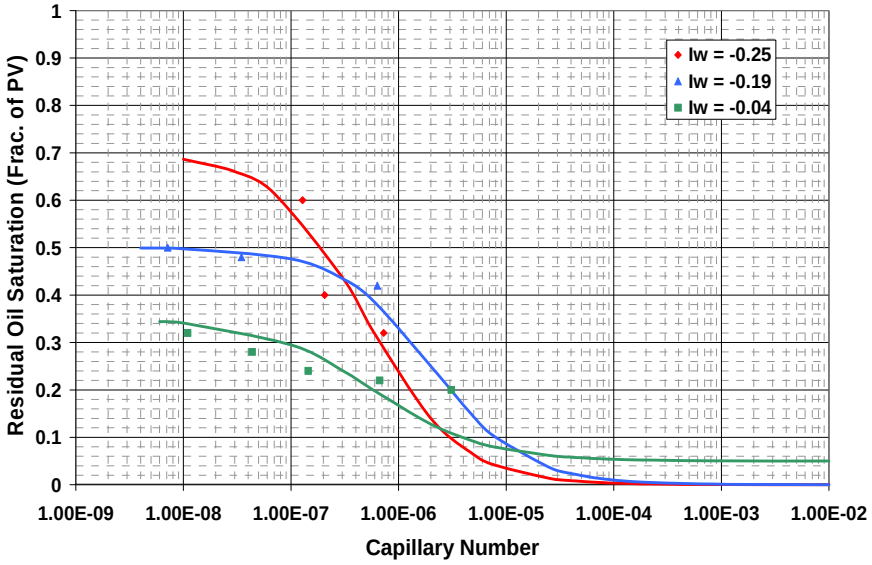

Figure 2.7: Effect of wettability on capillary desaturation curves for three carbonate rocks (Kamath *et al*., 2001). Figure regenerated by Anderson (2006). The curves are fits to the data using the dependency of residual phase saturations on trapping number (Eq.3.16).

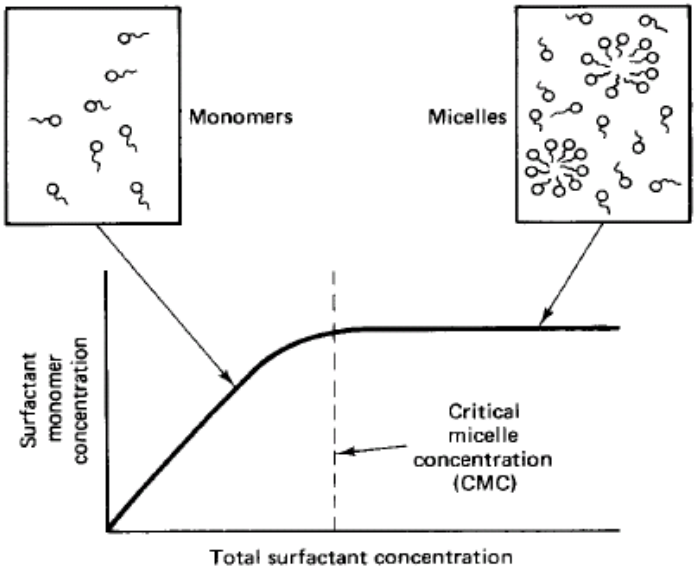

Figure 2.8: Schematic plot of surfactant behavior in aqueous phase, based on changes in surfactant concentration (Lake, 1989).

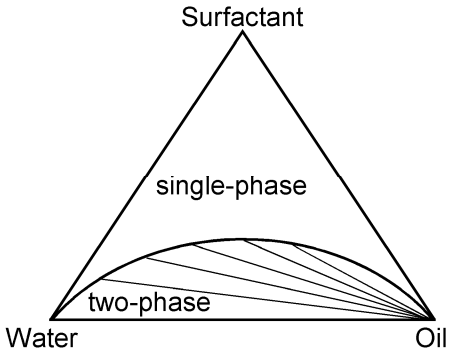

Figure 2.9: Type II(-) or Type I system illustration (Lake, 1989).

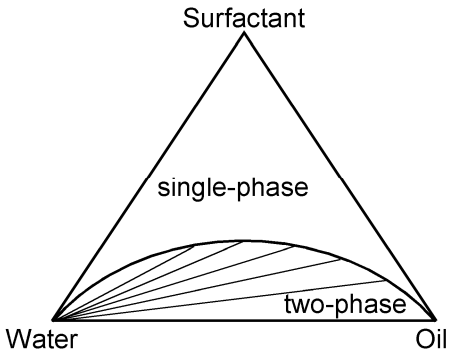

Figure 2.10: II(+) or Type II system illustration (Lake, 1989).

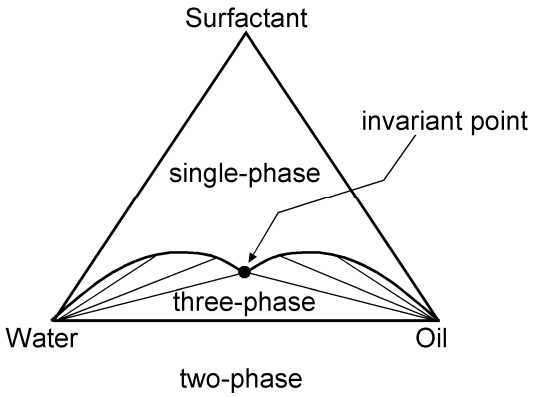

Figure 2.11: Type III system illustration (Lake, 1989).

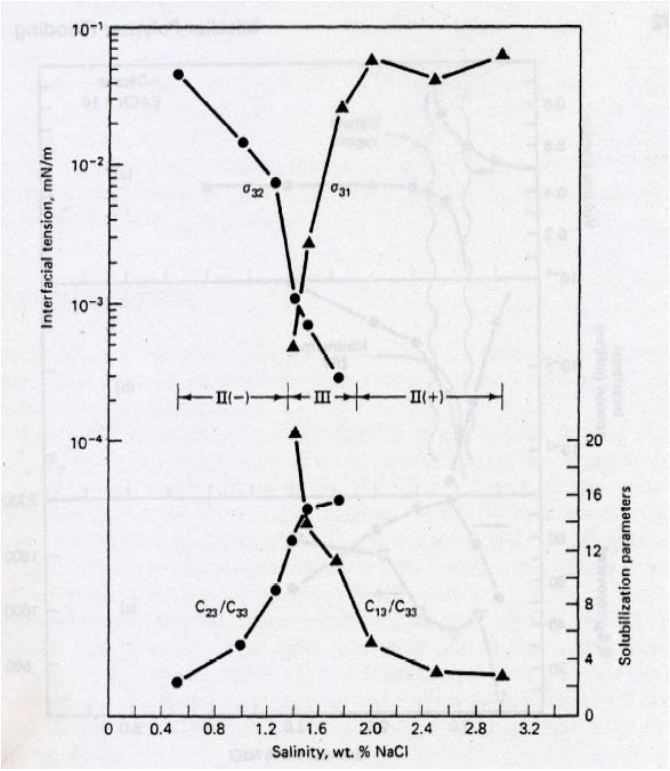

Figure 2.12: Optimal salinity is defined to be the salinity at which the water and oil solubilization ratios coincide which normally coincides with the salinity where oil-MW and MW-aqueous IFTs coincide (Healy and Reed, 1976).

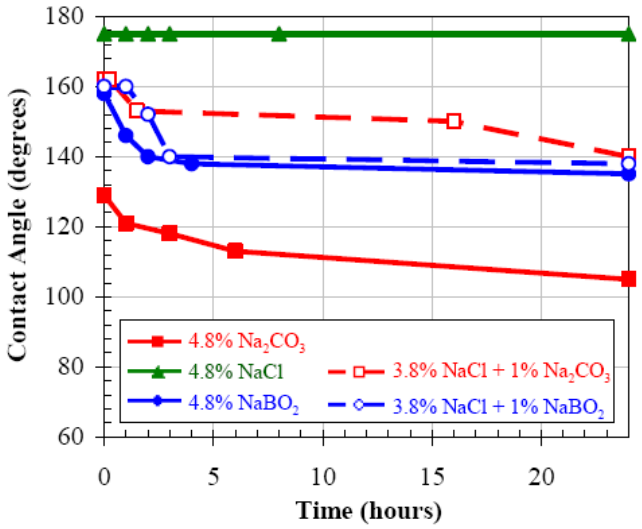

Figure 2.13: Contact angle data versus time using different alkalis on quartz plates (Zhang *et al*., 2008).

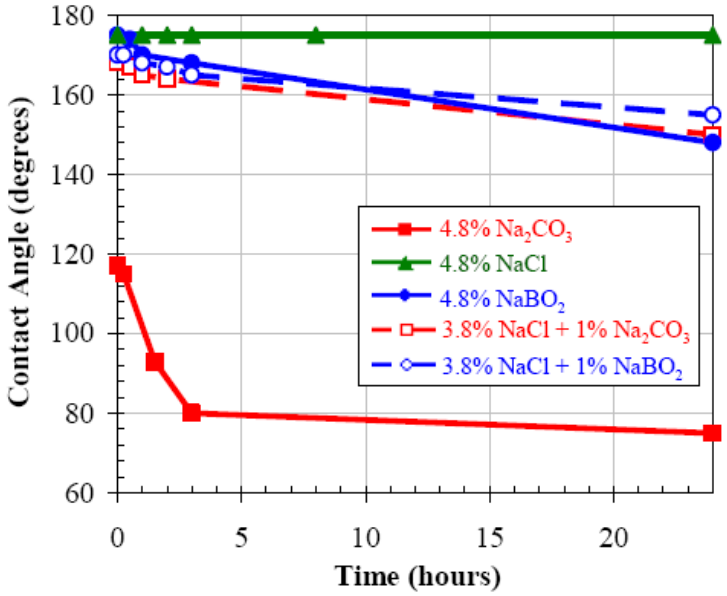

Figure 2.14: Contact angle data versus time using different alkalis on calcite plates (Zhang *et al*., 2008).

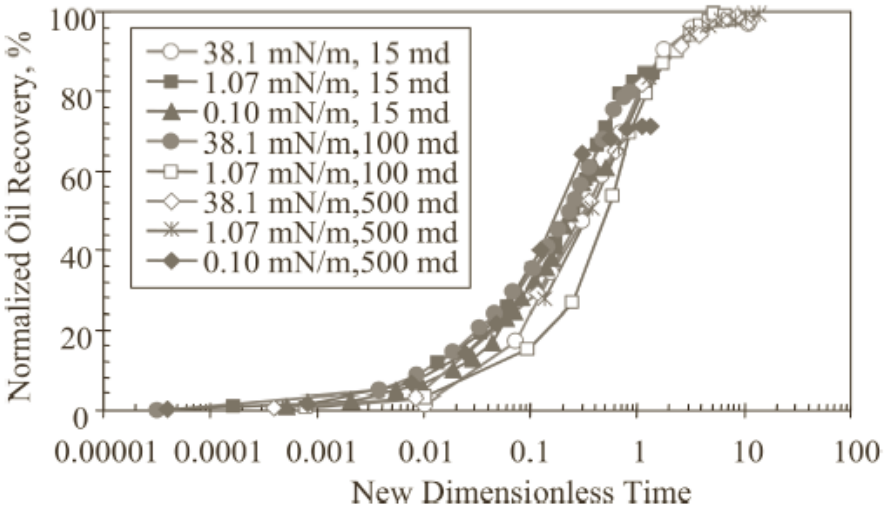

Figure 2.15: Use of the scaling factor proposed by Li and Horne (2006) yields similar oil recovery curves for imbibition tests with different rock/fluid properties.

Chapter 3: Implementation of Wettability Alteration Model in UTCHEM

3.1 Introduction to UTCHEM Simulator

The three-dimensional multiphase multicomponent chemical compositional simulator of The University of Texas, UTCHEM, is the result of an extensive research. (Satoh, 1984; Saad, 1989; Bhuyan, 1989; Delshad *et al*., 1996; Aldejain, 1989 and Liu *et al.*, 1994). The simulator is capable of accounting for complex surfactant/oil/brine phase behavior, petrophysical properties, chemical reactions, and heterogeneous porous media properties. It uses advanced concepts in high-order numerical accuracy and dispersion control. And can make up to four fluid phases (gas, aqueous, oleic, and microemulsion) and solid phases. Formation of microemulsion (ME) is only possible above the critical micelle concentration of the surfactant (CMC). ME is a thermodynamically stable mixture of water, surfactant, cosolvent, electrolytes, and oil. UTCHEM has many applications both in modeling enhanced oil recovery processes and enhanced remediation of contaminated aquifers, some of which are listed below (UTCHEM technical manual, 2000).

UTCHEM groundwater applications:

- NAPL spill and migration in both saturated and unsaturated zones
- Partitioning interwell test in both saturated and unsaturated zones of aquifers
- Remediation using surfactant/cosolvent/polymer
- Remediation using surfactant/foam
- Remediation using cosolvents
- Bioremediation
- Geochemical reactions (e.g., heavy metals and radionuclides)

UTCHEM oil reservoir applications:

- Waterflooding

- Single well, partitioning interwell, and single well wettability tracer tests
- Polymer flooding
- Profile control using gel
- Surfactant flooding
- High pH alkaline flooding
- Microbial EOR
- Surfactant/foam and ASP/foam EOR
- Formation damage

3.2 UTCHEM Formulation

The flow equations are solved by a block-centered finite difference scheme. The solution method used in UTCHEM is implicit in pressure and explicit in concentration. It is optional for the user to use One-, two-point upstream, and third-order spatial discretization, knowing that the third-order method is the most accurate. To increase the stability and robustness of the second-and third-order methods, a flux limiter that is total-variation-diminishing (TVD) has been added (Liu, 1993 and Liu *et al.*, 1994). The balance equations considered are as follows:

1. The mass balance equation for each species.
2. The overall mass balance on volume occupying components, i.e. water, oil, surfactant, co-solvent and air, which yields aqueous phase pressure. Adding the capillary pressure between the phases gives other phase pressures.
3. The energy balance equation.

Each of these equations is described briefly below. More complete description could be found in UTCHEM technical manual (UTCHEM technical manual, 2000).

3.2.1 Mass Conservation Equations

Few assumptions are made in developing the flow equations, the most important of which are the following:

1. There is local thermodynamic equilibrium except for tracers and dissolution of organic components
2. Porous medium and fluids are slightly compressible
3. Mixing is ideal
4. Dispersion is Fickian
5. Darcy's law applies.
6. No flow boundary conditions are assumed and no dispersive flux is allowed across the impermeable boundaries.

The mass conservation equation for component κ in terms of overall volume of component κ per unit pore volume is defined as

$$\frac{\partial}{\partial t}\left(\phi \tilde{C}_\kappa \rho_\kappa\right) + \vec{\nabla}\bullet\left[\sum_{\ell=1}^{n_p} \rho_\kappa \left(C_{\kappa\ell}\vec{u}_\ell - \vec{\tilde{D}}_{\kappa\ell}\right)\right] = R_\kappa \qquad \text{Eq.3.1}$$

where

$\tilde{C}_\kappa$ = overall volumetric concentration of component *k*, (L^3/L^3)

ρ_κ = density of component *k* , (m/L^3)

$C_{\kappa\ell}$ = concentration of component *k* in phase ℓ , (L^3/L^3)

$\vec{u}_\ell$ = volumetric flux of phase ℓ , (L/t)

$\vec{\tilde{D}}_{\kappa\ell}$ = dispersive flux of component *k* in phase ℓ , (L^2/t)

R_κ = total source/sink flow for component *k*, (m/L^3t)

ϕ = porosity, (L^3/L^3)

The overall volume of component κ , mentioned in Eq.3.1 is computed as follows for κ = 1 to n_c:

$$\tilde{C}_\kappa = \left(1 - \sum_{k=1}^{n_{cv}} \hat{C}_\kappa\right)\sum_{\ell=1}^{n_p} S_\ell C_{\kappa\ell} + \hat{C}_\kappa \qquad \text{Eq.3.2}$$

where

$\tilde{C}_\kappa$ = overall volumetric concentration of component κ , (L^3/L^3)

n_{cv}= total number of volume-occupying components

$\hat{C}_\kappa$ = adsorbed concentration of spices κ, (L^3/L^3)

n_p= number of phases

S_ℓ= saturation of phase ℓ, (L^3/L^3)

As described before, the dispersive flux is assumed to be Fickian and calculated as

$$\vec{\tilde{D}}_{\kappa\ell} = \phi S_\ell \vec{\vec{K}}_{\kappa\ell} \bullet \nabla C_{\kappa\ell} \qquad \text{Eq.3.3}$$

where

$\vec{\tilde{D}}_{\kappa\ell}$ = dispersive flux of component κ in phase ℓ, (L^2/t)

$\vec{\vec{K}}_{\kappa\ell}$ = dispersion tensor of spices κ in phase ℓ, (L^2/t)

The magnitude of the vector flux for each phase, $\vec{u}_\ell$ used in Eq.3.1 is computed as follows:

$$\left|\vec{u}_\ell\right| = \sqrt{\left(u_{x\ell}\right)^2 + \left(u_{y\ell}\right)^2 + \left(u_{z\ell}\right)^2} \qquad \text{Eq.3.4}$$

The phase flux using Darcy's law is

$$\vec{u}_\ell = -\frac{k_{r\ell}\vec{\vec{K}}}{\mu_\ell}\left(\vec{\nabla}P_\ell - \gamma_\ell \vec{\nabla}h\right) \qquad \text{Eq.3.5}$$

where

$\vec{\vec{K}}$ = permeability tensor, (L^2)

$k_{r\ell}$ = relative permeability of phase, ℓ (L^2/L^2)

μ_ℓ = viscosity of phase ℓ, (m/Lt)

γ_ℓ = specific weight of phase ℓ, (m/L^2t^2)

h = vertical depth, (L)

The source term in Eq.3.1 R_κ, is a combination of all rate terms for component κ:

$$R_\kappa = \phi \sum S_\ell r_{\kappa\ell} + \left(1-\phi\right) r_{\kappa s} + Q_\kappa \qquad \text{Eq.3.6}$$

where Q_κ is the injection or production rate for component κ per bulk volume, $r_{\kappa\ell}$ and $r_{\kappa s}$ are the reaction rates for component κ in phase ℓ and the solid phase *s*, respectively (Bhuyan, 1989, UTCHEM technical manual, 2000).

3.2.2 The Pressure Equation

A mass balance over all volume-occupying components yields the pressure equation. Darcy's law is substituted for the flux term of each phase and definition of capillary pressure is used. It is also noted that as stated in Eq.3.7, sum of concentrations of all of the components in each phase is equal to 1.

$$\sum_{\kappa=1}^{n_{cv}} C_{\kappa\ell} = 1 \qquad \text{Eq.3.7}$$

Then the pressure equation in terms of the reference phase pressure (phase 1) is

$$\phi C_t \frac{\partial P_1}{\partial t} + \vec{\nabla}\bullet\vec{\vec{K}}\bullet\lambda_{rTc}\vec{\nabla}P_1 = -\vec{\nabla}\bullet\sum_{\ell=1}^{n_p}\vec{\vec{K}}\bullet\lambda_{r\ell c}\vec{\nabla}D + \vec{\nabla}\bullet\sum_{\ell=1}^{n_p}\vec{\vec{K}}\bullet\lambda_{r\ell c}\vec{\nabla}P_{c\ell 1} + \sum_{\kappa=1}^{n_{cv}} Q_\kappa \qquad \text{Eq.3.8}$$

where

C_t = total system compressibility, (Lt^2/m)

D = depth, (L)

$\vec{\vec{K}}$ = permeability tensor, (L^2)

P_1 = pressure of phase 1, (Lt^2/m)

$P_{c\ell 1}$ = capillary pressure between the given phase ℓ and phase 1, (Lt^2/m)

Q_κ = source/sink flow for component κ per bulk volume. (L^3/L^3t)

$\lambda_{r\ell c}$ = relative mobility, (m/Lt)

λ_{rTc} = total relative mobility, (m/Lt)

The relative mobilities ($\lambda_{r\ell c}$ and λ_{rTc}) and total compressibility (C_t) in Eq.3.8 are calculated based on the following equations:

$$\lambda_{r\ell c} = \frac{k_{r\ell}}{\mu_\ell}\sum_{\kappa=1}^{n_{cv}} \rho_\kappa C_{\kappa\ell} \qquad \text{Eq.3.9}$$

$$\lambda_{rTc} = \sum_{\ell=1}^{n_p} \lambda_{r\ell c} \qquad \text{Eq.3.10}$$

$$C_t = C_r + \sum_{\kappa=1}^{n_{cv}} C_\kappa^o \tilde{C}_\kappa \qquad \text{Eq.3.11}$$

where

C_κ^o = component compressibility

C_r = rock compressibility

3.2.3 The Energy Balance Equation

Assuming that energy is only a function of temperature and energy influx in the reservoir happens only by advection and heat conduction, the energy balance equation would be in the following form:

$$\frac{\partial}{\partial t}\left[(1-\phi)\rho_s C_{vs} + \phi \sum_{\ell=1}^{n_p} \rho_\ell S_\ell C_{v\ell} \right] T + \vec{\nabla} \bullet \left[\sum_{\ell=1}^{n_p} \rho_\ell C_{p\ell} u_\ell T - \lambda_T \vec{\nabla} T \right] = q_H - Q_L \qquad \text{Eq.3.12}$$

where

T = Reservoir temperature

C_{vs} = Soil heat capacity at constant volume, (Q/Tm)

$C_{v\ell}$ = Phase ℓ heat capacity at constant volume, (Q/Tm)

$C_{p\ell}$ = Phase ℓ heat capacity at constant pressure, (Q/Tm)

λ_T = Thermal conductivity, (QL/tT)

q_H = Enthalpy source term per bulk volume, (Q/tL^3)

Q_L = Heat loss to overburden and underburden formations, (Q/tL^2)

3.2.3.1 Effect of Temperature on Surfactant Phase Behavior

The results of an extensive literature survey on the effect of temperature on surfactant phase behavior are presented in Appendix A. This appendix also contains the physical models used in UTCHEM for capturing the effect of temperature on rock/fluid system. The correlations used in UTCHEM are validated in this appendix and the resulting

conclusion is that these correlations do a great job in modeling the effect of temperature on rock/fluid properties (such as oil viscosity) and surfactant phase behavior.

3.3 Wettability Alteration Models

Waterfloods in naturally fractured reservoirs have usually very low performances, unless the reservoir formation is water-wet and has a high tendency for imbibing the injected water. Alkali/surfactants solutions have been used in mixed- and oil-wet formations to change the wetting state of matrix rock to more water-wet conditions, thus increasing the tendency of the matrix for imbibing the injected water and improve the oil recovery from naturally fractured reservoirs (Hirasaki and Zhang, 2004; Adibhatla and Mohanty, 2008). Reservoir simulation is required for scale up of the experimental results and feasibility study of chemical floods. Most of the commercial and academic reservoir simulators do not account for the wettability alteration effect of alkali/surfactants and thus can not model chemical floods accurately. It was decided to adopt UTCHEM, the University of Texas chemical compositional oil reservoir simulator, to model the effect of wettability alteration on relative permeabilities, residual saturations and capillary pressure in the matrix rock. This was accomplished in two steps. First a table lookup option was added to the simulator to allow input of two or more relative permeability and capillary pressure tables, each representing a wetting state of the rock. The appropriate table then was used based on the concentration of surfactant in each gridblock (Castillo, 2003). In the second approach, which is the subject of this work, two extreme wetting conditions, i.e. initial and final wetting conditions are considered. Each wetting state is represented by a set of relative permeability, capillary pressure and capillary desaturation curves. Relative permeability of each phase is then calculated by interpolating between these two extreme wettability conditions using a scaling factor, ω. These methods are described below.

3.3.1 Table Look up Option Using Tracers

The first approach to add the capability of modeling wettability alteration was the addition of a table lookup option. Using this option, the user can specify the initial and altered wetting conditions of the rock. This is done by specifying water and oil relative permeability and water-oil capillary pressure tables for each wettability condition as

input. Time dependent wettability alteration is modeled using an input threshold value for a tracer concentration representing the alkali or surfactant concentration in each gridblock. The injected surfactant advances in the reservoir and when its concentration is greater than a threshold value specified as an input parameter, the tables for altered wetting conditions are used (Castillo, 2003).

This method is a very simple way of modeling wettability alteration and has two limitations. First, the wettability alteration is a step function which may not be representative of what may happen in the reservoir. In reality, the change in the wettability may happen gradually not as a step function. The second limitation is that tracer component is used as the wettability modifier and therefore, all the other properties of surfactant such as interfacial tension reduction and oil mobilization are ignored. These properties of surfactants are important and help the improved oil recovery in naturally fractured reservoirs. A more general wettability alteration model was then developed and implemented in UTCHEM (Fathi, 2005).

3.3.2 Wettability Alteration Model Using Surfactants

This model is based on the effect of surfactant on relative permeability and residual saturation of each phase. Two extreme wetting conditions are assumed, original and final wetting conditions, and relative permeability of each phase in each gridblock is calculated for each extreme case. The relative permeability used for each gridblock, which is referred to as *actual* relative permeability, at each timestep is then obtained by interpolation between these two extreme values. The relative permeabilities are calculated using Corey-type exponential functions (Fathi, 2005; Delshad *et al*., 2006). The existing relative permeability model in UTCHEM is first discussed.

3.3.2.1 Relative Permeability Model in UTCHEM

Corey relative permeabilities are calculated for each gridblock as shown in Eq.3.13.

$$k_{r\ell} = k^{o}_{r\ell} S^{n_\ell}_{n\ell} \qquad \text{Eq.3.13}$$

where ℓ is water, oil or microemulsion phase, $k_{r\ell}^{o}$ is the relative permeability endpoint for phase ℓ , and n_ℓ is the Corey exponent of phase ℓ and $S_{n\ell}$ is the normalized saturation of phase ℓ calculated by Eq.3.14.

$$S_{n\ell} = \frac{S_\ell - S_{\ell r}}{1 - \sum_{\ell=1}^{n_p} S_{\ell r}} \qquad \text{Eq.3.14}$$

where S_ℓ is the saturation of phase ℓ and $S_{\ell r}$ is the residual saturation of phase ℓ. As mentioned before, in addition to the wettability alteration effect, surfactants also reduce the interfacial tension between the oil and aqueous phases and mobilize the oil. This effect is modeled by means of a dimensionless group called *trapping number*, which is a combination of *capillary number* and *bond number* (Eq.3.15) and can adequately model the combined effect of viscous, capillary, and buoyancy forces in three dimensions (Delshad, 1990; Delshad *et al.*, 1994; Jin, 1995, UTCHEM technical manual, 2000).

$$N_{T_\ell} = \frac{\left| -\vec{\vec{K}} \cdot \vec{\nabla} \Phi_{\ell'} - \vec{\vec{K}} \cdot \left[g\left(\rho_{\ell'} - \rho_\ell\right) \vec{\nabla} h \right] \right|}{\sigma_{\ell\ell'}} \qquad \text{Eq.3.15}$$

As the surfactant enters a gridblock, interfacial tension is reduced and trapping number is increased. Interfacial tension reduction and oil mobilization effect of surfactants, affects the residual phase saturations, endpoint relative permeabilities and exponents. Mobilization effect on residual phase saturations is modeled in UTCHEM as follows (Delshad *et al.*, 1986; UTCHEM technical manual, 2000):

$$S_{\ell r} = S_{\ell r}^{high} + \frac{S_{\ell r}^{low} - S_{\ell r}^{high}}{1 + T_\ell N_{T_\ell}} \qquad \text{Eq.3.16}$$

where $S_{\ell r}^{high}$ and $S_{\ell r}^{low}$ are residual saturations of phase ℓ at high and low capillary numbers respectively (given as input parameters), T_ℓ is the input trapping parameter of phase ℓ and N_{T_ℓ} is trapping number of phase ℓ Mobilization effects on endpoint relative permeabilities are modeled by Eq.3.17 (Delshad *et al.*, 1986; UTCHEM technical manual, 2000).

$$k_{r\ell}^{o} = k_{r\ell}^{o^{high}} + \frac{S_{\ell'r}^{low} - S_{\ell'r}}{S_{\ell'r}^{low} - S_{\ell'r}^{high}}\left(k_{r\ell}^{o^{high}} - k_{r\ell}^{o^{low}}\right) \qquad \text{Eq.3.17}$$

$k_{r\ell}^{o^{high}}$ and $k_{r\ell}^{o^{low}}$ represent the endpoint relative permeability of phase ℓ at low and high capillary numbers respectively. $S_{\ell'r}$, $S_{\ell'r}^{low}$ and $S_{\ell'r}^{high}$ correspond to the residual saturations of the conjugate phase. Equation 3.18 shows the relative permeability exponents as a function of capillary number (Delshad *et al.*, 1986; UTCHEM technical manual, 2000).

$$n_{\ell} = n_{\ell}^{low} + \frac{S_{\ell'r}^{low} - S_{\ell'r}}{S_{\ell'r}^{low} - S_{\ell'r}^{high}}\left(n_{\ell}^{high} - n_{\ell}^{low}\right) \qquad \text{Eq.3.18}$$

where n_{ℓ}^{low} and n_{ℓ}^{high} represent the Corey exponents for low and high capillary numbers respectively specified as input parameters.

Another important parameter that is affected by both wettability and IFT, is capillary pressure. In UTCHEM, capillary pressure is modeled as follows:

$$P_c = C_{pc}\frac{\sigma_{om}}{\sigma_{ow}}\left(1 - S_{\ell}\right)^{E_{pc}} \qquad \text{Eq.3.19}$$

where C_{pc} and E_{pc} are user defined endpoint and exponents and σ_{om} and σ_{ow} denote oil/ME and oil/water IFTs respectively.

3.3.2.2 Code Modifications to Model Wettability Alteration

Section 3.3.2.1 explains the case when only one wetting state is defined for the entire simulation period. To model wettability alteration, two sets of relative permeability, capillary pressure, and capillary desaturation curves are required corresponding to each wetting state. The existing one-dimensional arrays $S_{r\ell}$, $k_{r\ell}^{o^{low}}$, n_{ℓ}^{low}, P_c and T_{ℓ} were changed into two dimensional arrays with the first dimension being equal to the number of gridblocks and the second dimension equal to 2 for the two extreme wetting conditions. Two flags were defined to assist the user in using this option. The first flag, *IWALT*, indicates if wettability alteration is used (*IWALT = 1*) or not (*IWALT = 0*) and the second flag (*IWALF*) enables the user to choose the method of interpolation of

relative permeabilities and capillary pressure based on the two extreme wetting conditions. In each time step, relative permeability of each phase is calculated for each extreme wettability condition using Eqs.3.13 through 3.18 as described above. The *actual* relative permeability and capillary pressure of the gridblock ($k_{r\ell}^{actual}$ and P_c^{actual}) are then obtained by interpolation between these two extreme values based Eqs.3.20 and 3.21 respectively.

$$k_{r\ell}^{actual} = \omega_1 k_{r\ell}^{final} + (1-\omega_1) k_{r\ell}^{original} \qquad \text{Eq.3.20}$$

$$P_c^{actual} = \omega_2 P_c^{final} + (1-\omega_2) P_c^{original} \qquad \text{Eq.3.21}$$

where ω_1 and ω_2 are the interpolation scaling factors for relative permeability and capillary pressure respectively and *final* and *original* indicate values corresponding to the two extreme wetting states, i.e. final and initial wettability states, respectively.

In this work three options are provided for determination of the scaling factors, ω_1 and ω_2. If the flag for interpolation is equal to zero (*IWALF=0*) then ω_1 and ω_2 are specified by the user as a constant input parameter. Wettability alteration occurs if the concentration of surfactant is above CMC in each gridblock. If *IWALF = 1*, scaling factors ω_1 and ω_2 are calculated based on Eq.3.22:

$$\omega_1 = \omega_2 = \frac{\hat{C}_{surf}}{C_{surf} + \hat{C}_{surf}} \qquad \text{Eq.3.22}$$

where $\hat{C}_{surf}$ and C_{surf} represent the adsorbed and total fluid surfactant concentration respectively. This equation was used since it is known that surfactants can alter the wettability of the rock by adsorbing on the rock surface (Chillingar and Yen, 1983; Anderson, 1986; Lake, 1989; Al-Maamari and Buckley, 2000). Therefore a relationship between the amount of surfactant adsorbed on the rock surface and the state of wettability alteration of the rock is proposed here. It is obvious that ω should be in the range of zero to one and this equation satisfies this condition. Also, it should be noted that when the surfactant slug reaches a gridblock, total surfactant concentration in that gridblock starts to increase until it reaches a maximum that could be less than or equal to the injected

surfactant concentration and then eventually it starts to decrease when the slug passes through the gridblock. At the same time, as the surfactant slug reaches the gridblock, the amount of surfactant adsorbed by the gridblock increases and reaches a maximum after a while and since the adsorption is modeled as an irreversible process here, the adsorbed concentration remains at that maximum once the surfactant slug passes the gridblock. To a monotonic change with time, the value calculated by Eq.3.22 in each time step is compared with the value from the previous time step and the larger value is stored so that the historical maximum of ω_1 and ω_2 for each gridblock is used in the interpolation.

FORTRAN subroutine *TRAP* which calculates the relative permeability and capillary pressure curves as a function of trapping number (Eqs.3.13 through 3.18) is called twice, calculating the relative permeability and capillary pressure curves of each extreme wetting condition. Then *WETMODEL* subroutine is called where the relative permeability and capillary pressure curves are calculated using Eq.3.20 and Eq.3.21 depending on the value of *IWALF* flag.

3.3.3 Wettability Alteration Model Using Other Wettability Modifiers

The wettability alteration model discussed in Section 3.3.2 (Fathi, 2005) is further generalized to wettability modifiers other than surfactants such as pH, salinity, alkali.

When alkali is the wettability alteration agent, *IWALF=2* can be used which models the alkali as a tracer and when its concentration is greater than a constant threshold value, relative permeability and capillary pressure curves are interpolated using constant values of ω_1 and ω_2 provided by the user.

If wettability is assumed to be a function of salinity for low salinity waterflood applications, then *IWALF=3* is used. The scaling factors ω_1 and ω_2 are obtained from Eq.3.23 based on the salinity of the gridblock:

$$\omega_1 = \omega_2 = \frac{C_{51}^o - C_{51}}{C_{51}^o - C_{5inj}} \qquad \text{Eq.3.23}$$

where C_{51}^{o} is the initial salinity of the gridblock at the beginning of the simulation (eq/L), C_{51} is the salinity of the gridblock at any timestep (eq/L) and C_{5inj} is the injected salinity (eq/L). It should be noted that this equation is based on the assumption that initial reservoir salinity is greater than injected salinity and in fact the lower salinity of injected water is the cause of wettability alteration. This simple correlation for salinity needs to be validated against laboratory experiments.

The input flag *IWALF* is equal to 4 (*IWALF=4*) allows wettability alteration as a function of pH. The user would provide a pH limit as an input parameter and if the pH of a gridblock was greater than the provided value, the final wetting relative permeability and capillary pressure curves are used instead of the initial wetting curves. The gridblock values of pH are calculated using the geochemical options of UTCHEM.

Chapter 4: Validation of Wettability Alteration Model of UTCHEM

For validation of the implemented wettability alteration model described in Chapter 3, two laboratory experiments are modeled using the modified code. The first experiment is a static imbibition cell test conducted by Hirasaki and Zhang (2004) and the second is a dynamic fracture block experiment conducted at UT Austin (Fathi *et al*., 2008). Anderson (2006) gives the modeling procedure for the imbibition cell test. The match obtained by Anderson (2006) is improved in this work and later used to study the effect of matrix block size on the oil recovery (Chapter 5). This chapter gives full description of the matching procedure and obtained results for each experiment. More important than the above, this chapter summarizes some interesting insights obtained from the modeling of the experiments.

4.1 Modeling Wettability Alteration in a Static Imbibition Cell Test

4.1.1 Description of the Experiment

Hirasaki and Zhang (2004) used formation brine, crude oil and core samples of a dolomite formation (Yates field) to conduct several imbibition cell tests. This formation is preferentially oil-wet (Yang and Wadleigh, 2000) and Hirasaki and Zhang (2004) tested many alkaline/surfactant solutions to find the best design for the rock/fluid combination of the target reservoir. Since the carbonate formations are positively charged at low pH values, the adsorption of anionic surfactants used by Hirasaki and Zhang (2004) is very high at low pH values. To solve this problem they used an alkali (sodium carbonate) to increase the pH. They report that addition of the alkali changed the surface charge of the carbonates at high pH values and reduced surfactant adsorption to a great extent. Anderson (2006) modeled several experiments performed at Rice University besides the specific experiment discussed in this chapter. The results of some of these modeling are included in the final DOE report submitted by Hirasaki *et al*. (2004).

In this work, an attempt was made to improve the history match of one of the experiments as a validation of the wettability alteration model of UTCHEM. Table 4.1 summarizes the core and fluid properties of the experiment. The core sample was oil flooded to residual water saturation and aged for 24 hours at 80 °C. Oil recovery was measured by placing the oil-saturated core in an imbibition cell test filled with either formation brine or alkaline/ surfactant solution (Fig. 4.1). The surfactant solution was a mixture of 0.025 wt% CS-330 (C_{12}-3EO-sulfate) and 0.025 wt% TDA-4PO-sulfate (C_{13}-4PO-sulfate) with 0.3 M sodium carbonate added to reduce the surfactant adsorption.

The driving forces include capillary pressure and buoyancy. Spontaneous imbibition did not occur when partially oil saturated dolomite core samples were placed in a cell test filled with brine for one to two weeks (Fig. 4.1). This is another confirmation of the preferentially oil-wet nature of the matrix core. The formation brine was then replaced with the alkaline/surfactant solution. There was significant spontaneous imbibition when the brine was replaced by the alkaline/surfactant solution. The buoyancy driven gravity drainage was reported to be the dominant recovery mechanism rather than counter current capillary imbibition. This was supported by the appearance of oil on the top of the core rather than the sides of the core. The initial oil saturation was 0.68. The experimental cumulative oil recovery was about 44% of the original oil in place (OOIP) as shown in Fig. 4.2. The oil was recovered in about 138 days.

4.1.2 Modeling Approach

A 3D numerical model was set up to simulate the experiment and validate the wettability alteration model. A homogeneous Cartesian grid with 7x7x7 gridblocks was set up to simulate both the rock and fluids in the cell surrounding the core. A 5x5x5 portion of the middle grids was given petrophysical properties representing the rock (Table 4.2) and the remaining gridblocks were given properties representing the imbibition cell (i.e. porosity of one, permeability of 1,000 D, and zero capillary pressure). Figure 4.3 shows a vertical cross section through the center of the model. This figure shows the initial surfactant concentration for the imbibition simulation where the blue region (zero initial surfactant

concentration) is the “rock gridblocks” and the red region (0.05% initial surfactant concentration) is the “non-rock gridblocks.”

Table 4.1 shows the porosity, permeability, and initial oil saturation and Table 4.2 gives the relative permeability and capillary pressure parameters of the rock gridblocks obtained from matching the experiment. The difficulty of this simulation model is that it does not have any wells to induce flow, the convective fluxes are extremely small, and there are extreme property changes between rock and non-rock gridblocks.

Figure 4.4 shows the capillary desaturation curves that result from the parameters of Table 4.2. One should note that, it is harder to mobilize the oil if the rock is oil-wet since the CDC curve of the oil is more to the right in this case which means that the IFT needs to be reduced to lower values (higher trapping numbers) in order to mobilize the oil. The oil CDC is shifted to the left when the system becomes water-wet resulting in easier mobilization of the oil (Fig.4.4).

Figure 4.5 shows the relative permeability exponents obtained from the match (Table 4.2) as trapping number increases based on Eq.3.17. Based on Fig. 4.5, the relative permeability end point is lower for the wetting phase. This is in agreement with the findings of literature as mentioned in Chapter 2. The wetting phase tends to be in contact with the rock surface and thus occupies the smaller pores. This limits the mobility of the wetting phase and results in lower relative permeability endpoints for that phase.

Figure 4.6 shows the relative permeability exponents (Table 4.2) as a function of trapping number as described by Eq.3.18. The relative permeability exponents obtained by matching the experiment are also consistent with the findings in the literature; if a phase is the wetting phase, then it has a high relative permeability exponent which means that it would have a low relative permeability at each value of normalized saturation based on Eq.3.13 since normalized saturation is bounded by 0.0 and 1.0.

Figures 4.7, 4.8 and 4.9 show the actual relative permeability curves generated by the input of Table 4.2 for each of the water and oil phases at three different trapping numbers. In each of these figures, the relative permeability curves are given for three wetting conditions: water-wet, oil-wet and mixed-wet. The mixed-wet curves are resulting from interpolation between the water-wet and oil-wet curves using ω_1=0.5 (option of *IWALF*=0). It is interesting to observe the shift in the relative permeability curves as trapping number increases. At low trapping number of 10^{-7} (Fig. 4.7), the relative permeability curves are curved with high residual phase saturations. As the trapping number increases (Figs. 4.8 and 4.9), the curvature of the relative permeability curves decreases. This is due to the fact that based on Fig. 4.6, the relative permeabilities become straight lines (a value of 1.0 is used for Corey exponent at high trapping number) as trapping number increases. The relative permeabilities increase as trapping number increases for entire range of water saturation (Figs 4.7, 4.8, and 4.9). This is due to the increase in the relative permeability endpoint as a function of trapping number as described in Fig. 4.5.

Capillary forces are the main reason for trapping of the oil in the core plug at its initial preferentially oil-wet condition (Hirasaki and Zhang, 2004). Figure 4.10 shows the capillary pressure curves obtained from the input parameters of Table 4.2 for the initial and final wetting states and for wettability alteration using ω_2=0.5. The resulting capillary pressure curve from the wettability alteration model is mixed-wet with positive and negative values. This curve shows a zero capillary pressure at water saturation of 0.52.

An initial simulation was run to determine the oil recovery based on an assumption that the wettability is not altered from the original oil-wet conditions. This simulation only models the effect of surfactant and soap on interfacial tension reduction and oil mobilization. Surfactant concentration in gridblocks representing the oil-wet core initially increases primarily due to an effective molecular diffusion and impacts the onset of oil being produced from the core but very little impact on final oil recovery. An effective molecular diffusion/dispersion of 6.5×10^{-5} ft^2/d was used in the simulation. Based on

published data of Lam and Schechter (1987) and others, the expected surfactant molecular diffusion would be several magnitudes smaller than was simulated. Therefore, the value presented here can be described as a pseudo diffusion/dispersion coefficient.

Once the surfactant concentration within a gridblock exceeds the critical micelle concentration, microemulsion is formed, interfacial tension is reduced, and capillary pressure is reduced to zero. This process allows for slow imbibition of surfactant solution and oil displacement. The results are given in Fig. 4.11 where the maximum oil recovery is about 24% OOIP with at least an order of magnitude slower imbibition rate compared to the experimental results. Based on this result, it is clear that additional mechanisms are taking place to enhance the oil recovery.

Next, the enhanced simulator was used to model combined interfacial tension reduction and wettability alteration effects of surfactant/alkali solution on oil recovery. It was assumed that the final wettability condition was water-wet with relative permeability and capillary pressure parameters as shown in Table 4.2. The option of IWALF=0 (wettability alteration based on surfactant concentration with user defined constant scaling factors) was used for modeling this experiment and both of the interpolation scaling factors for this simulation were assumed to be a constant value of 0.5. A fairly good agreement between the simulated and experimental oil recoveries are obtained as shown in Fig.4.11. The distribution of surfactant concentration and oil saturation are given in Figs. 4.12 and 4.13 after 10 days of imbibition. There is a good agreement between the surfactant concentration and oil saturation as shown in Figs. 4.12 and 4.13. The rock gridblocks with higher surfactant concentration have lower oil saturation. These two figures also indicate the role of gravity in the oil recovery from the core plug. The rock gridblocks in the lower parts of the core have smaller oil saturations due to gravity drainage of the oil. The result with wettability alteration gives a much better agreement with the laboratory data than the case without wettability alteration. The simulation with wettability alteration has a faster response to oil production and a higher cumulative oil recovery. This is due to the increase in oil relative permeability and initial change in capillary

pressure from negative to positive during the wettability alteration process. Therefore, more surfactant solution is imbibed into the rock gridblocks displacing more oil before the interfacial tension reduction decreases the capillary pressure to zero. Alteration of the wettability towards more water-wet conditions increased the mobility of the oil and its final recovery and recovery rate as shown in Fig. 4.11. Successful modeling of this experiment validates the wettability alteration model and its implementation in UTCHEM for the spontaneous imbibition test.

Chapter 5 presents results of scale up study based on this experiment.

4.2 Modeling Wettability Alteration in a Fractured Block

The Fractured Block experiment was performed at The University of Texas at Austin in the Petroleum and Geosystems Engineering Department. The experiment was carried out by Dr. Q. P. Nguyen and his Post Doctoral Fellow, J. Zhang. This section describes the details of the experiment and the details and steps taken in modeling it using the enhanced UTCHEM simulator with the wettability alteration model.

After modeling the experiment, the matching parameters are used to investigate the effect of various design and reservoir parameters on oil recovery. Chapter 5 gives the results of scale up study using the conditions of this experiment.

4.2.1 Experimental Description and Results

The experiment was designed to aid in a better understanding of mechanisms occurring in flow of fluids such as alkali and surfactant in naturally fractured formations. The experiment can also improve our understanding of the relative importance of capillary, viscous, and buoyancy forces. Alkali agent was used as a wettability modifier and surfactant solution was used to lower the interfacial tension and enhance oil recovery by oil emulsification (Fathi *et al*., 2008).

The matrix rock used in this study was Texas cream limestone. The crude oil was McElroy oil and the alkali was sodium metaborate. Oil viscosity and density at 30 °C are 10 Pa.s and 843.8 kg/m^3 respectively.

Nine Texas cream cores of 3″ x 1″ x 1″ were placed together following the pattern shown in Fig. 4.14. Each of these blocks was cut precisely to the mentioned dimensions from a larger block of outcrop. The composite fractured block was 9″ long, 3″ wide, and 1″ high and was placed horizontally as shown in Fig. 4.14. The fracture aperture was not constant and measurable and was much less than 1 mm Two end caps were designed to distribute injected fluids uniformly over the entire end face of the block (Fig. 4.14). The entire rock-end cap assembly was coated with epoxy to ensure fixed placement of the cores and consistent fracture aperture during the experiment. The core was then saturated with crude oil as follows. First the block outlet was closed and the air from the setup was evacuated for 3 hours. An under-pressure of smaller than -13 psi was obtained. The setup maintained its under-pressure even after the vacuuming was stopped for preparation of the saturation stage. This indicated that the setup was free of any leaks. Crude oil and water were then injected at a constant volumetric fraction of 95% oil and 5% water. The block outlet remained closed during the injection until the pressure inside the block was higher than atmospheric pressure as indicated by a pressure transducer. The injection was then continued with the open outlet for 7 days and oil and water were produced. The production volumetric ratio was different than that of the injection for a transient period (about three days) and after that the system reached the steady state and the injected and produced ratios were identical. The experimental setup was flipped every half a day to eliminate any gravity segregation. The pore volume of the rock was 120 ml, determined by measuring its mass change before and after oil saturation. Material balance methods are more precise compared to volumetric calculations. Due to variable fracture apertures and unknown matrix heterogeneity, there is a relatively large uncertainty in the pore volume calculated by volumetric methods. Using a matrix porosity of 0.3 and fracture aperture of 1 mm, one can calculate the pore volume of the setup to be 133 ml which is close to the value obtained by material balance method. It should be noted that the

porosity of the matrix rock may not be uniformly 0.3 and the fracture aperture is variable and much less than 1 mm at some points. Therefore the pore volume obtained by material balance is more reliable and was used in the modeling. The block then underwent the aging process with crude oil at 40ºC for 3 weeks. It was cooled down to room temperature before starting the first fluid injection stage.

Figure 4.15 shows the oil recovery for the three different fluid injection steps. Injection of 4.8 wt% NaCl solution at 5 ml/hr resulted in an ultimate recovery of about 15% OOIP. As shown in Fig. 4.15, during the first few hours of waterflood, no oil was produced from the setup. This delay was due to the volume of the tube connecting the fracture block setup to the sample collection unit. This was not properly communicated to the modeling group at the time of modeling of the experiment. Next, water containing 1 wt% sodium metaborate ($NaBO_2$) and 3.8 wt% NaCl injected at the same rate mobilized additional 15% OOIP. The producing oil cut was reduced to zero at the end of the alkaline flood. A mixture of alkali/surfactant was then injected at the same flow rate, rendering incremental recovery of 6% OOIP (Figure 4.15). The surfactant solution contained 1.5 wt% PetroStep®S-1 and 0.5 wt% PetroStep®S-2, 2 wt% secondary butanol as co-solvent, 1 wt% sodium metaborate, and 3.8 wt% NaCl. This surfactant formulation formed a microemulsion with the crude oil which exhibits an IFT of 0.0008 mN/m. It is important to note that the pressure gradient was around 0.8 psi/ft throughout the experiment. This pressure gradient corresponds to the pressure difference at the inlet and outlet of the setup.

4.2.2 Modeling the Fractured Block Experiment

The main assumptions for modeling this experiment are as follows:

- During the waterflood, the flow is dominated by capillary pressure. The initial mixed-wet nature of the rock creates both positive and negative capillary pressure. The negative capillary pressure traps a large amount of oil in the matrix.
- After the introduction of alkali solution, the wettability of the matrix rock is altered towards water-wet conditions and this causes a shift in the petrophysical

properties such as relative permeability and capillary pressure. Capillary pressure becomes positive and oil is expelled under capillary and viscous forces.

- During the alkali/surfactant flood, the IFT is reduced to ultra low values causing the following changes in petrophysical properties:
    - Residual saturations of oil, water, and microemulsion decrease
    - Relative permeability curves becomes more linear for all three phases
    - Capillary pressure diminishes

4.2.2.1 Base Case Simulation Model

A 3D discrete fracture model consisting of 6 fractures was used (Fig. 4.16). Two of these fractures are parallel and four are perpendicular to the flow direction. The end caps were modeled as fractures and the injection and production wells were placed in these openings to model the same conditions as the experiment. The matrix gridblock size was 1/3″ x 1/3″ x 1/3″. Fracture aperture was 1 mm (0.039372"). Third order finite difference method (Liu *et al.*, 1994) is used in these simulations that reduces the numerical dispersion to a great extent and eliminate the instabilities caused by abrupt changes in grid size. Sensitivity of the results to the matrix block size is presented later. Fracture gridblocks are assumed to have a porosity of 1 as opposed to 0.298 for matrix blocks (based on laboratory material balance). Fracture permeability was used as a matching parameter since the fracture aperture was not measured precisely and was variable throughout the setup. A uniform and isotropic matrix permeability of 3.36×10^{-14} m^2 (34 md) was used based on laboratory measurements. Figure 4.16 shows the 3D view of the permeability distribution in the base case simulation model. A uniform initial saturation was assumed based on the measured values. Table 4.3 summarizes the base case simulation parameters.

4.2.2.2 Modeling the Waterflood Part of the Experiment

As mentioned above, waterflood part of the experiment is dominated by capillary forces and a correct estimation of capillary pressure and relative permeability is essential for

modeling of this part. Based on laboratory measurements the initial wetting state of the rock was mixed-wet. This is essential information for choosing the initial relative permeability and capillary pressure curves. Fracture relative permeability curves are expected to be higher and more linear compared to those for the matrix. Residual saturations in the matrix were assumed to be higher than those in the fractures. Since the waterflood experiment is governed by capillary forces, a reasonable estimate of initial capillary pressure endpoint is essential. The fracture capillary pressure is assumed to be zero. To get an initial estimate of the matrix capillary pressure, Carman-Kozeny correlation (Eq.4.1) and a cylindrical tube capillary pressure (Eq.2.3) were used.

$$R = \sqrt{\frac{8k}{\phi}} \qquad \text{Eq.4.1}$$

where k is the permeability, ϕ is the porosity, and R is the average pore throat radius. Eq.4.1 gives an average pore throat radius of 0.95 μm for matrix blocks. Using an oil/water IFT of 30 mN/m (based on laboratory measurements using the ring method) and a contact angle of 86º, capillary pressure of 0.6 psia is obtained using Eq.2.3. It should be noted that this is only an initial guess on the endpoint value of the capillary pressure curve. The capillary pressure curve is one of the most important and uncertain matching parameters in this study and the final curve obtained from the history matching is shown in Fig. 4.17.

Table 4.4 summarizes the relative permeability and capillary pressure parameters and Fig. 4.17 shows the resulting relative permeability and capillary pressure curves used for modeling the waterflood experiment. These curves represent the initial mixed-wet state of the matrix rock. Figure 4.18 indicates an excellent match of waterflood oil recovery data. This figure captures the initial time of the experiment where no oil production is observed. It also gives a reasonable match of the oil recovery and oil recovery rate (slope of the recovery curve) at all times during the waterflood.

The negative capillary pressure (Fig. 4.17) is the main reason for holding oil in place and the plateau oil recovery at the end of the waterflood (Fig. 4.18). As water saturation

increases in a gridblock, the capillary pressure decreases until it reaches zero at the water saturation of 0.41. This is referred to as the critical water saturation where the capillary pressure sign changes at this saturation. The water saturation would still increase as the viscous pressure gradient forces more water into the gridblock, but from then on, the capillary pressure would become negative and grow more negative as water saturation increases. Eventually the gridblock reaches a point where the viscous pressure gradient of water is as large as the existing negative capillary pressure and causes the oil production to cease. Figures 4.19 and 4.20 show oil saturation and pressure profiles viewed from the top in the middle layer during the waterflood. The following observations were made:

- The capillary imbibition of the injected water occurs uniformly across the simulation domain. To illustrate this phenomenon, the oil saturation distribution after 1.9 days of static (no viscous pressure gradient) imbibition simulation with the same model parameters is presented in Fig. 4.21. It should be noted that the range of the color scale has been modified in this figure to better visualize the saturation gradient. The white parts of the graph fall out of the visualized range.
- Pressure gradient decreases with time.
- The water saturation front moves much slower in the matrix compared to the fractures.
- There is a significant difference between oil saturation in matrix cells on either side of a fracture perpendicular to the flow direction. This is due to directions of imbibition and viscous forces. For the cells on the left of the fracture, the imbibition happens in the opposite direction of the bulk flow but for the cells on the right of the fracture these two phenomena happen in the same direction. As a result the oil saturation of the cell on the right side of the fracture is higher compared to the cell on the left.
- After 1.9 days (0.7 PV) of waterflood, water saturation becomes nearly uniform and at critical water saturation and the remaining oil is held in the matrix by the capillary forces (Fig. 4.19).
- In Fig. 4.19, the oil saturation in the fractures (especially the ones in Y direction or perpendicular to flow direction) is higher than that of matrix. This may be

explained by two phenomena, one an artifact of the experimental setup and one an artifact of numerical simulation. The viscous gradient pushes the oil forward and to the boundaries of the setup due to the presence of two high conductivity fractures in the direction of flow (X direction). Since the fractures in the Y direction are dead ends, the only way for transport of material from these fractures is transportation in the X direction (the viscous gradient in the Y direction pushes towards the dead end). This causes accumulation of oil transported from the X direction fractures in Y direction fractures and this is an artifact of the experimental setup. Another factor causing this accumulation is an artifact of numerical simulation and is related to transmissibility calculations. Figure 4.22 shows that for the range of saturations in the matrix blocks for matrix cells at initial wetting state, oil relative permeability is much lower than water relative permeability. On the other hand Fig. 4.23 shows that for the same range of saturations, oil relative permeability is comparable to water relative permeability in the fractures. This means that due to upstream waiting of transmissibilities, transport of oil from the matrix into the fractures is easy and transport of oil from the fractures into the matrix is hard. So the oil is accumulated in the fractures and oil saturation in the fractures increases.

- The experiment was conducted under a low pressure gradient of less than 1 psi/ft and the simulation pressure gradient is in agreement with the experimental data (Fig. 4.20). This along with the close match of oil production indicates that the numerical model captures the basic mechanisms involved in the waterflooding experiment of the mixed-wet fractured block.

4.2.2.3 Modeling the Alkali Flood Part of the Experiment

In order to produce the trapped oil in the matrix at the end of the waterflood, one needs to overcome the capillary forces responsible for trapping the remaining oil in the matrix. One approach is to change the wetting state of the rock towards more water-wet conditions using a wettability modifying agent such as an alkaline solution. A water-wet rock exhibits a positive capillary pressure and can imbibe water spontaneously. The

relative permeability curves become more favorable in a water-wet rock where water mobility decreases whereas oil mobility increases. Sodium metaborate was used in this work to alter the wettability towards more water-wet conditions.

To model the alkaline flood part of the experiment, the previous relative permeability and capillary pressure curves are preserved and assumed to correspond to initial wetting state of the rock. A second set of relative permeability and capillary pressure curves representing the altered wetting state are introduced. The wettability alteration model is used and the *IWALF=2* option is activated. This option models the wettability alteration based on concentration of a tracer which is assumed to be the wettability alteration agent. The values of the scaling factors are assumed to be $\omega_1=\omega_2=0.5$. **Table 4.5** gives the water-wet relative permeability and capillary pressure parameters. Figure 4.22 compares matrix relative permeability curves for initial and final wettability conditions. The initial wetting curves (solid curves in Fig. 4.22) cross at a water saturation of 0.34 whereas the final wetting curves cross at a water saturation of 0.60. Another important difference between the two curves is the endpoint relative permeabilities. The oil endpoint of the initial wetting (mixed-wet) is smaller compared to the final wetting (water-wet) and visa versa for the water endpoints. These are consistent with the fact that at water-wet conditions the mobility of the oil increases. Figures 4.23 and 4.24 give the fracture relative permeability and matrix capillary pressure curves respectively. A Comparison of Figs. 4.22 and 4.23, indicates that the fracture relative permeability curves have smaller curvature and higher endpoints for each phase and wetting state compared to the matrix curves. This honors the fact that fluid flow in the fractures is much easier than the matrix due to the nature of the fractures. It should also be noted that we do not assume straight line relative permeability curves for the fractures at low capillary numbers (Fig. 4.23). This honors the fact that the fractures are not ideal slits and the relative permeability curves may not be straight lines due to the roughness of the fracture walls which creates a tortuous pore space. Figure 4.25 shows a very good match obtained for the water and alkaline flood part of the experiment using the relative permeability and capillary pressure curves of Figs. 4.22, to 4.24. Figure 4.26 shows the quality of the match for the

alkali flood part of the experiment for a better comparison. This match is considered very good since the oil recovery and oil recovery rate are estimated by the numerical model to a great extent at each time during both the water and alkali flood stages.

Figures 4.27 and 4.28 show the oil saturation distribution in the middle layer of the model during the alkaline flood and the corresponding normalized alkaline concentration, respectively. The color scale of Fig. 4.27 is chosen to be the same that of Fig. 4.19 for consistency. It is clearly seen that the oil is swept from the regions flooded by the alkali. We assume zero physical dispersion and molecular diffusion for the alkali at this point. The sensitivity of the simulation results to molecular diffusion is presented later in the Section 4.2.3.4. The gridblocks near the boundaries and farther from the fractures, which are not swept by the alkali, still have high remaining oil saturation. Most of the injected alkali is produced quickly from the X direction fractures and very small portion is forced into the matrix blocks by viscous forces (Fig. 4.28). As a result of this, at the end of alkali flood (after 1.68 PVs of alkali injection) only about 1/3 of the matrix blocks have been effectively flooded by alkali (Fig. 4.28C). Therefore, it is the best practice to start the alkali flood at the early stages of the secondary recovery from naturally fractured rocks in order to take advantage of the small capillary gradients due to mixed-wet or intermediate wetting state of the rock and push as much alkali as possible into the matrix for a more effective wettability alteration and oil recovery. The sensitivity of oil recovery to injection scenario is presented later in this chapter.

Figure 4.29 gives the pressure profiles which indicate a very low pressure gradient compared to those observed during waterflood simulations (Fig. 4.20). The color scale of Fig. 4.29 is kept the same as that of Fig. 4.20 for consistency.

4.2.2.4 Modeling the Alkali/Surfactant Flood Part of the Experiment

Although the alkali leads to an additional 15% oil recovery after the waterflood by virtue of the wettability alteration of the matrix, it cannot reduce the IFT and produce the

trapped oil held in place by capillary forces. At the end of alkali flood a large amount of trapped oil is present in the matrix. Injection of a surfactant solution can reduce the oil/water IFT and recover the residual oil by both solubilization and mobilization. Alkali is still injected in the surfactant solution for its original purpose of wettability alteration as well as to reduce surfactant adsorption and maintain the same salinity as the alkaline flood (1 wt% sodium metaborate, and 3.8 wt% NaCl) for consistency.

Laboratory measured surfactant phase behavior data were used to tune the surfactant phase behavior model in UTCHEM and obtain the simulation parameters. **Table 4.6** presents phase behavior input parameters.

The relative permeability and capillary pressure used in matching waterflood and alkaline flood were still representative for modeling the surfactant/alkali experiment. Therefore, matching parameters for the surfactant flood were capillary desaturation curves to model the impact of interfacial tension or more generally trapping number on relative permeability and capillary pressure (Eq.3.15) gives the definition of trapping number used in UTCHEM). Figure 4.30 shows the capillary desaturation curves (residual saturation as a function of trapping number) used to match the alkali/surfactant flood.

As surfactant reduces the oil/water IFT, trapping number (Eq.3.15) increases and residual phase saturations are mobilized as described by capillary desaturation curves of Fig. 4.30. Delshad *et al.* (2006) discuss the effect of trapping number on residual phase saturations and the way it is modeled in the UTCHEM simulator. Figure 4.31 shows the comparison of simulation results and experimental oil recoveries for all of the three stages of the experiment. Figure 4.32 shows the quality of the match obtained for the alkali/surfactant part of the experiment. As shown in this figure, the model can match the measured oil recovery to a great extent demonstrating that the numerical model captures the physics of the experiment. Figure 4.33 gives oil recovery results as a function of pore volumes fluid injected. As shown in this figure, about 3.15 PVs are injected into the fractured block during the whole experiment. This is close to what may happen in reality for a reservoir

and this makes the results much more interesting and practical. Figure 4.34 shows the oil saturation profile during alkali/surfactant flood. Figure 4.35 shows the normalized alkali concentration profiles where most of the fractured block is flooded with alkali by the end of the experiment. Figure 4.36 gives the surfactant concentration distribution. Comparison of Figs. 4.34 and 4.36 shows that the gridblocks swept by surfactant have lower oil saturations compared to those with no surfactant. After 1.2 PVs of surfactant injection, the surfactant has invaded a relatively small portion of the rock volume because of low mobility of viscous surfactant-rich microemulsion phase and large permeability contrast between the fracture and matrix. Figure 4.37 shows the oil pressure profiles indicating that high microemulsion viscosity (a maximum of 20 Pa.s compared to 10 and 1 Pa.s for oil and water respectively) causes a slightly higher pressure gradient compared to the alkaline flood (Fig. 4.29). These results indicate a very important aspect of surfactant flooding of naturally fractured formations and that is the need for mobility control. Similar to the surfactant flooding in conventional single porosity formations, we need a mobility control agent such as foam for improved sweep efficiency.

4.2.3 Sensitivity Studies

After history matching the experimental results and calibrating the model to represent the experiment, several sensitivity studies are performed. The goal of these studies is to examine the importance of key process design parameters including injection strategies, injection rate and fracture/matrix permeability ratio and simulation model parameters such as grid size and molecular diffusion.

4.2.3.1 Grid Refinement

Although UTCHEM has a higher order numerical scheme that minimizes the numerical dispersion (Liu *et al.*, 1994), we still performed a grid refinement study to ensure that the grid sizes are adequate for the chemical flooding simulations. Gridblock sizes were reduced from 1/3" x 1/3" x 1/3" in the base case simulation to 1/6" x 1/6" x 1/6". Figure 4.38 compares the results with those of the base case and laboratory. The difference between the base case and the mesh refinement case was relatively small.

The finer mesh predicts a slightly smaller final oil recovery compared to the base case (Fig. 4.38). This may appear to be counter intuitive since smaller grid sizes means smaller numerical dispersion which results in sharper fronts and higher oil recoveries. It is important to notice that the above conclusion is only relevant for conventional single porosity and permeability reservoirs and may not be true for fractured reservoirs. The main problem with fractured systems is vast permeability contrast between the fractures and matrix which limits transportation of injected fluids into the matrix. Coarser grids (more numerical dispersion) help in this case and make this transport easier. Hence, in simulation of fractured reservoirs the finer the grid is the lower the recovery will be obtained.

4.2.3.2 Injection Scenario

We explored different injection scenarios and compared the results with oil recovery obtained in the laboratory experiment. Figure 4.39 compares the oil recovery results for (1) alkaline flooding with no pre-waterflood (AF only), (2) alkaline/surfactant flooding from the beginning (ASF only), and (3) Alkaline flood from the beginning followed by alkaline/surfactant flooding with no pre-waterflood (AF + ASF). If alkali is injected from the beginning of the experiment, the initial oil recovery is much higher compared to the results of the base case (Fig. 4.39). The reason is obvious; the sooner the alkali is injected, the sooner the wetting state of the rock is altered to water-wet and the sooner the trapped oil is expelled from matrix to fractures. Injection of alkali/surfactant solution from the beginning would result in a faster recovery and greater final oil recovery compared to the base case (about 9% OOIP). The incremental oil is about 11%OOIP compared to the alkali only flood (AF). These results need to be further evaluated for economic feasibility of each process for field scale operations.

4.2.3.3 Injection Scenario

Several simulations were performed with different fracture permeability than that used in the base case. It is expected that as fracture/matrix permeability contrast increases, the residence time of the injected fluid in the reservoir decreases as well as the performance of the flood. Figure 4.40 shows that the slope of the recovery curve increases as the fracture/matrix contrast decreases.

4.2.3.4 Effective Molecular Diffusion Coefficient

In the base case, the molecular diffusion coefficients of both surfactant and alkali were assumed to be zero. A simulation was performed where a relatively large effective molecular diffusion coefficient of 9.3×10^{-5} ft^2/day was used for both surfactant and alkali. Figure 4.41 shows that molecular diffusion has very negligible effect on the oil recovery.

4.2.3.5 Injection Scenario

The laboratory experiment was performed with constant rate injection and constant pressure production. The sensitivity of the results to injection rate is studied by changing the injection rate to half, twice, 5 times, and 10 times the original experimental flow rate. For the purpose of comparison, the pore volumes injected were the same as the experiment in order to maintain similar chemical mass. Figures 4.42 and 4.43 show similar final oil recovery despite the injection rate used. The higher injection rates, however, reduce oil recoveries of water and alkaline flood due to shorter residence times. The waterflood part of the experiment is dominated by capillary forces. The capillary forces also dominate the flow in cells affected by alkali and undergone the wettability alteration during the alkali flood. The residence time is very important in capillary dominated flow since more residence time means more time for capillary imbibition to occur which results in higher oil recoveries. The surfactant flood appears to be more effective as injection rate increases but this is the result of higher remaining oil saturation after the alkaline flood.

4.3 Summary and Conclusions

1. Sequential injection of water, alkaline, and surfactant/alkaline in a mixed-wet fractured carbonate block was performed. High waterflood residual oil saturation was drastically reduced by injection of sodium metaborate as a wettability modifier.
2. Residual oil saturation remained after the alkali injection was further reduced by injection of a surfactant solution due to ultra-low interfacial tension and oil mobilization.
3. Experimental results were successfully modeled using UTCHEM with a wettability alteration model.
4. A combination of ultra low interfacial tension of surfactant solution and wettability alteration of sodium metaborate has a great potential in recovering significant bypassed oil from mixed wet fractured carbonates. The main recovery mechanisms are wettability alteration, interfacial tension reduction, emulsification, and oil mobilization.
5. In a field application, it is very important to inject the chemicals before the critical water saturation is reached. The reason is the lack of any considerable gradient for transport of the chemicals into the matrix after the viscous forces are balanced with negative capillary forces.
6. Dynamic laboratory experiments and modeling are required to evaluate chemical floods for naturally fractured reservoirs. Imbibition cell experiments are not representative of the field operations and lack the viscous forces that may play a critical role in the design of field applications and scale up studies from laboratory to field scale.

Table 4.1: Core Properties of Imbibition Experiment performed by Hirasaki and Zhang (2004)

Diameter (in)	1.5
Length (in)	3
Porosity (%)	24
Permeability (md)	122
Brine	5.815 g/l NaCl
Crude oil viscosity, cp	19
Initial oil saturation	0.68
Aging	24 hr at 80 °C
Time in brine (days)	8
Oil recovery in brine (%OOIP)	0
Surfactant	CS-330+ TDA-4PO
Surf. conc (wt%)	0.025+0.025
Na_2CO_3 (Molar)	0.3
Time in surf (days)	138
Oil recovery in surf (%OOIP)	44
Remaining oil saturation	0.38

Table 4.2: Relative Permeability and Capillary Pressure Parameters (Imbibition Cell Test Simulation)

	Oil-Wet		**Water-Wet**	
	Oil	**Water**	**Oil**	**Water**
Residual saturation	0.28	0.12	0.25	0.12
Endpoint relative permeability	0.80	0.56	1	0.26
Relative permeability exponent	3.3	1.4	1.3	3
Trapping parameters (T_ℓ)	1,000	20,000	1,500	200
Capillary pressure endpoint (C_{PC})	-15		7	
Capillary pressure exponent (E_{PC})	6		2	
Wettability scaling factor (ω)	0.5			

Table 4.3: Simulation input parameters for base case model of fracture block experiment

Simulation Parameters	**Matrix**	**Fracture**
Grid	31x11x3	
Grid size (m)	0.085	0.001
Porosity	0.298	1
Permeability (m^2)	3.36×10^{-13}	1.97×10^{-10}
Initial water saturation	0.14	0.99
Flow rate (m^3/day)	5.66×10^{-6}	

Table 4.4: Relative permeability and capillary pressure parameters corresponding to initial wetting used for modeling the waterflood part of Fracture Block experiment.

Simulation Parameters	Matrix	Fracture
Residual water saturation	0.1	0.05
Residual oil saturation	0.4	0.35
Water rel. perm. endpoint	0.3	0.4
Oil rel. perm. endpoint	0.4	0.6
Water rel. perm. Exponent	2	1.5
Oil rel. perm. Exponent	3	1.8
Wettability	Mixed-wet	Mixed-wet
Positive capillary pressure endpoint (psia)	0.3	0
Negative capillary pressure endpoint (psia)	-0.43	0
Capillary pressure exponent	3	0
Water saturation at zero capillary pressure	0.41	0

Table 4.5: Water-wet relative permeability and capillary pressure parameters used for modeling the wettability alteration caused by the alkali in Fracture Block experiment.

Simulation Parameters	Matrix	Fracture
Residual water saturation	0.2	0.1
Residual oil saturation	0.2	0.05
Water rel. perm. endpoint	0.2	0.3
Oil rel. perm. endpoint	0.7	1
Water rel. perm. Exponent	2.5	2
Oil rel. perm. Exponent	2	1.5
Wettability	Water-wet	Water-wet
Capillary pressure endpoint (psia)	0.3	N/A
Capillary pressure exponent	3	N/A

Table 4.6: Surfactant phase behavior parameters for modeling alkali/surfactant flood part of the Fracture Block experiment based on laboratory measurements

Height of binodal curve at zero salinity (vol. frac.)	0.037
Height of binodal curve at optimum salinity (vol. frac.)	0.035
Height of binodal curve at twice optimum salinity (vol. frac.)	0.038
Lower effective salinity limit for Type III phase behavior (eq/lit. water)	0.77
Upper effective salinity limit for Type III phase behavior (eq/lit. water)	1.15

Figure 4.1: Illustration of the imbibition cell test experiment performed by Hirasaki and Zhang (2004). The core plug on the left is placed in brine and no oil is recovered even after 2 weeks. The right core plug is placed in alkaline/surfactant solution and almost immediately oil recovery is initiated.

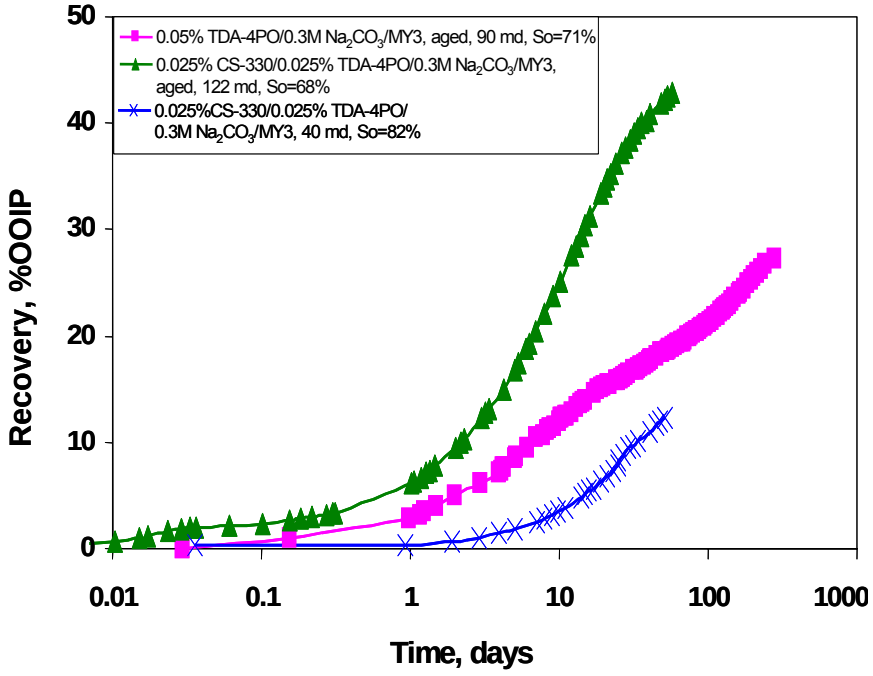

Figure 4.2: Imbibition cell test oil recovery results by Hirasaki and Zhang (2004). The green curve (triangle symbols) is modeled for validation of UTCHEM.

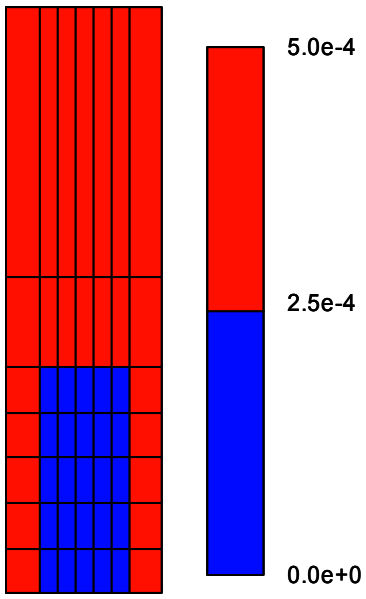

Figure 4.3: Initial surfactant concentration (Volume fraction) for the imbibition test model.

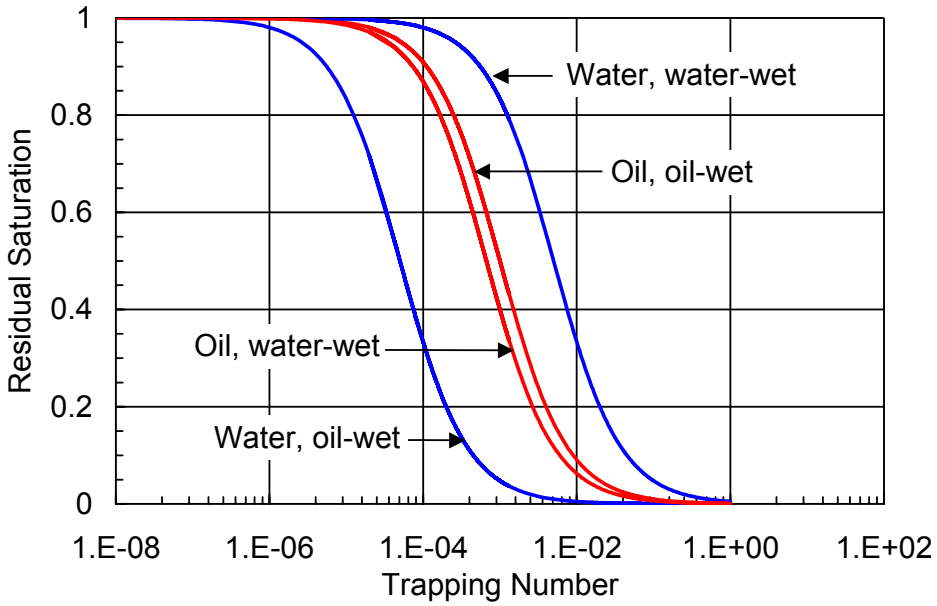

Figure 4.4: Capillary desaturation curves used in the simulation.

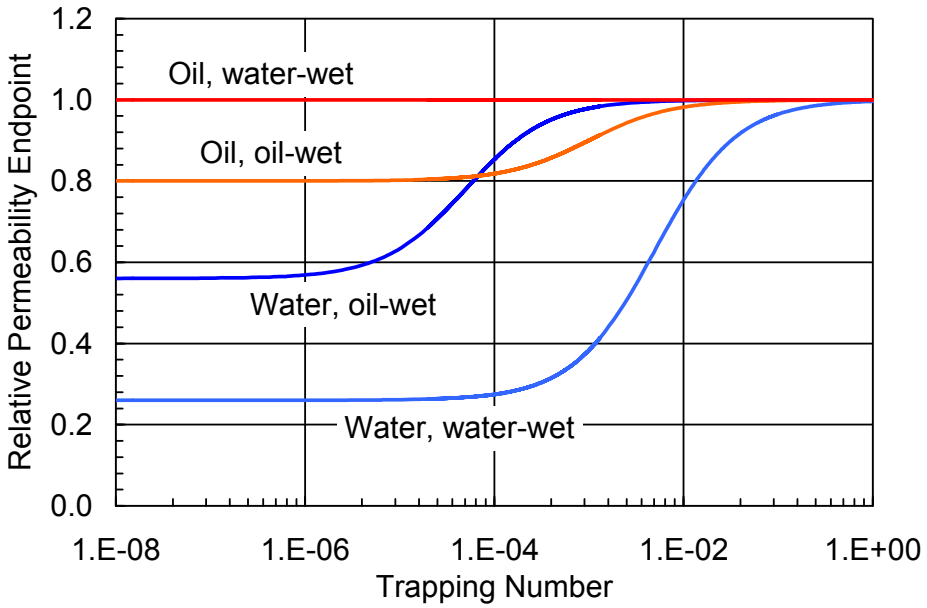

Figure 4.5: Endpoint relative permeability as a function of trapping number used in the modeling of the imbibition cell test experiment.

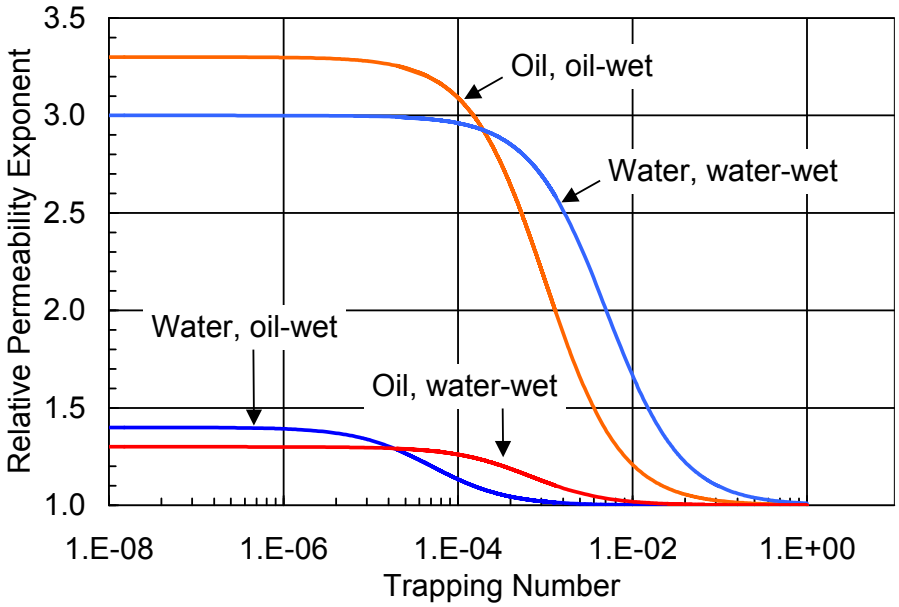

Figure 4.6: Relative permeability exponents as a function of trapping number used in the modeling of the imbibition cell test experiment.

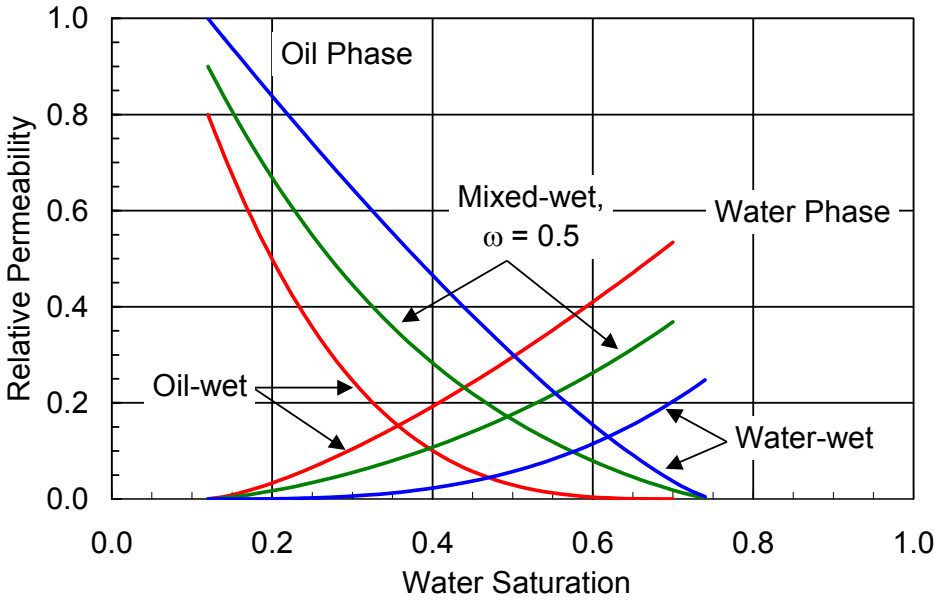

Figure 4.7: Calculated relative permeability curves for different wetting conditions at low trapping number of 10^{-7}.

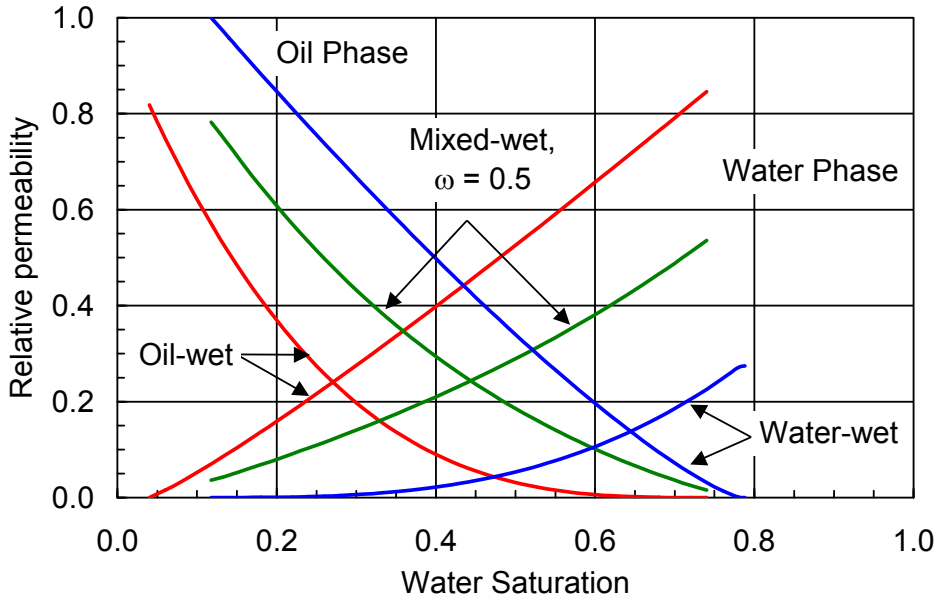

Figure 4.8: Calculated relative permeability curves for different wetting conditions at trapping number of 10^{-5}.

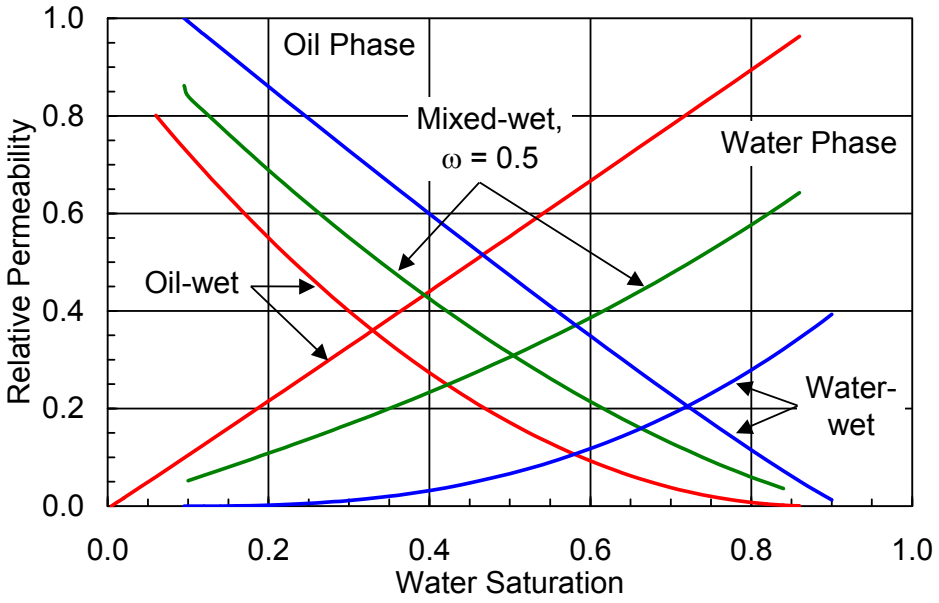

Figure 4.9: Calculated relative permeability curves for different wetting conditions at trapping number of 10^{-3}.

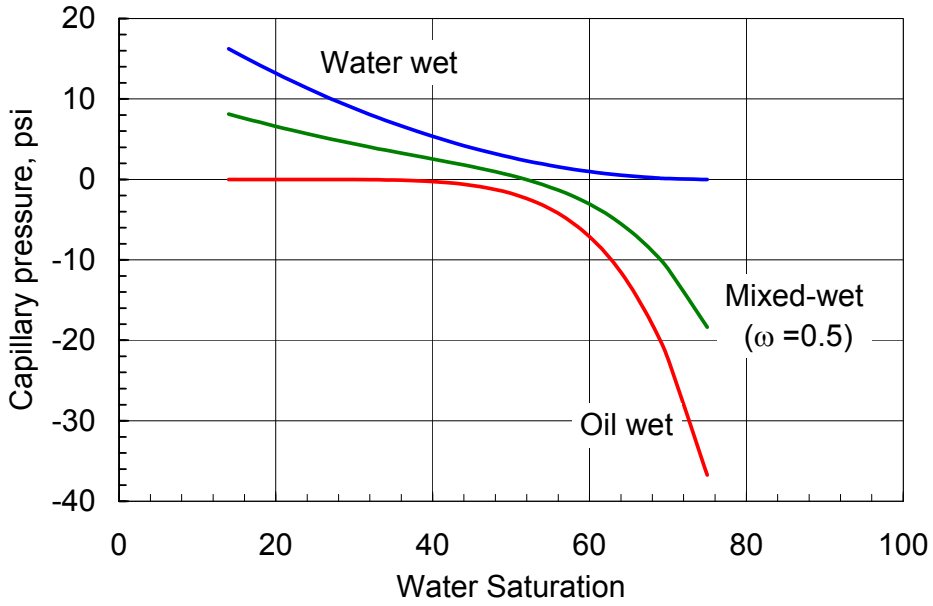

Figure 4.10: Calculated capillary pressure curves for different wetting conditions.

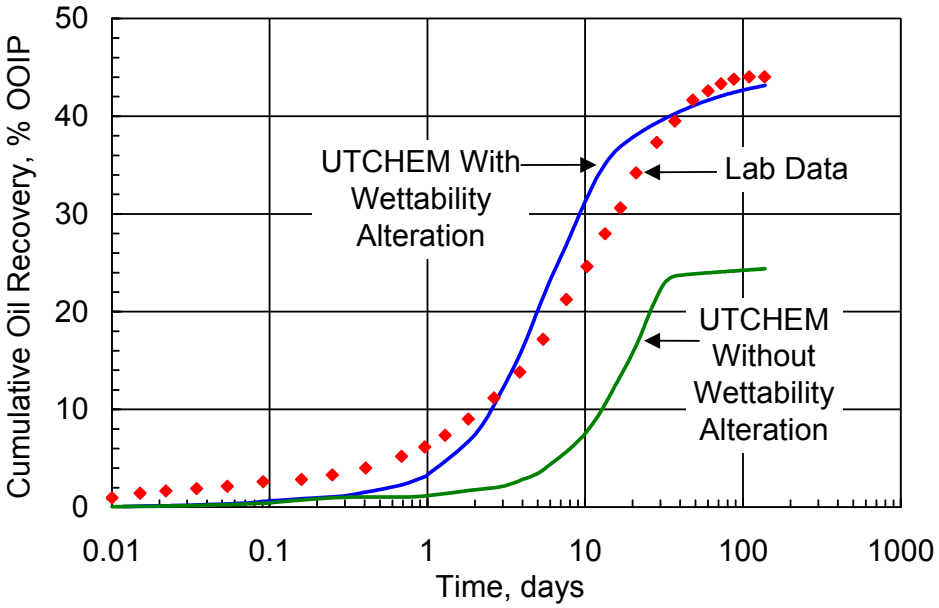

Figure 4.11: Comparison of simulated and laboratory imbibition oil recovery.

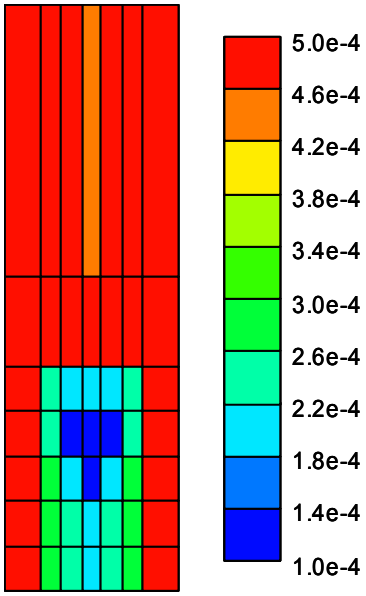

Figure 4.12: Surfactant concentration (volume fraction) after 10 days of imbibition.

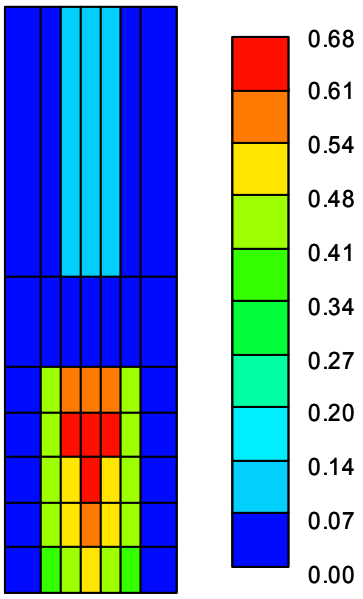

Figure 4.13: Oil saturation distribution after 10 days of imbibition.

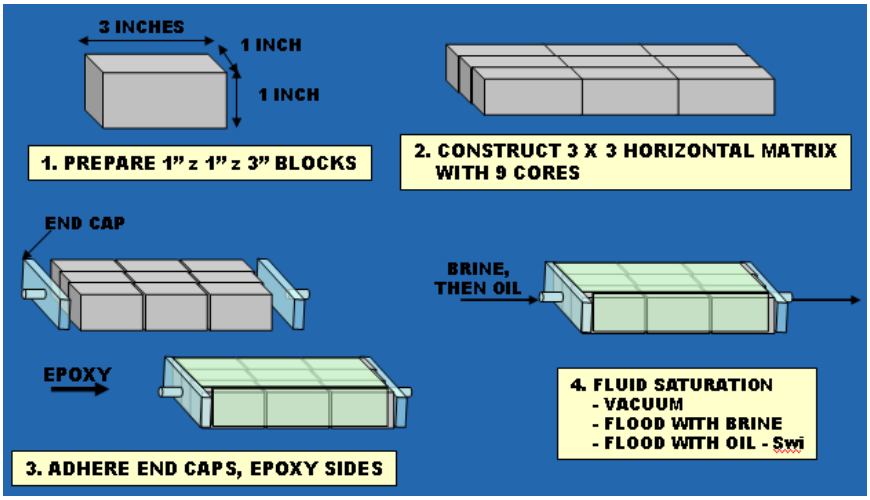

Figure 4.14: Fractured block setup preparation and the schematic of the final setup.

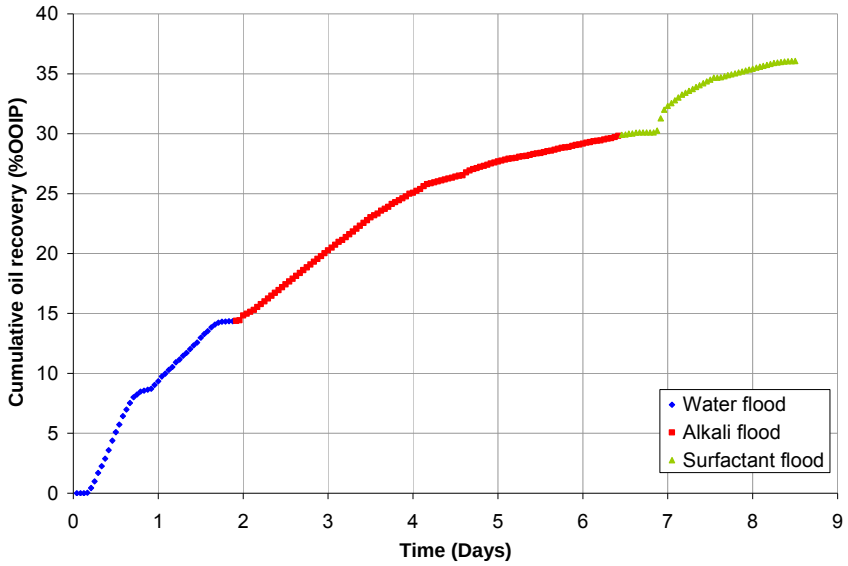

Figure 4.15: Laboratory measured oil recovery curve.

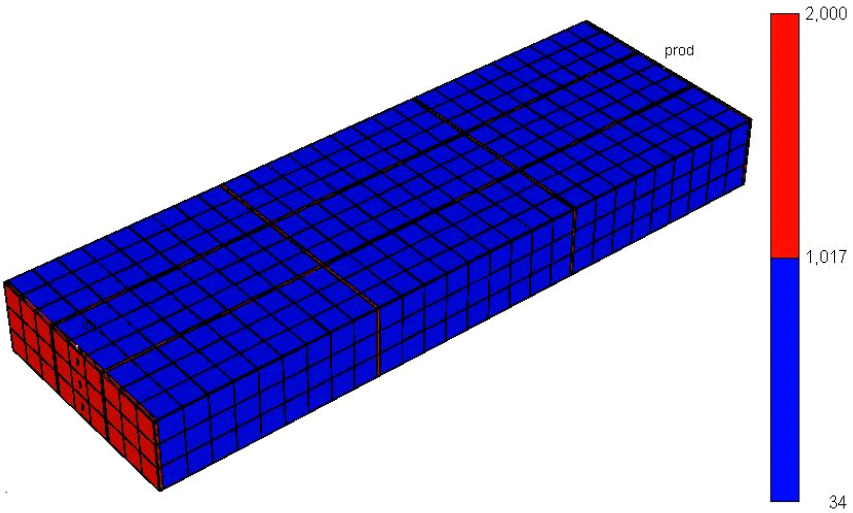

Figure 4.16: 3D view of permeability (md) distribution in the base case simulation model.

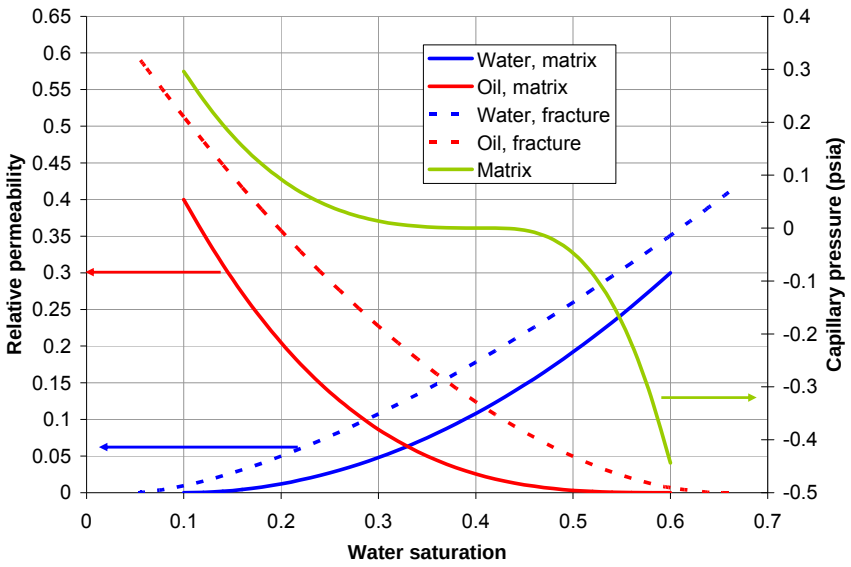

Figure 4.17: Relative permeability and capillary pressure curves used for modeling the waterflood part of the Fractured Block experiment (initial wetting, mixed-wet).

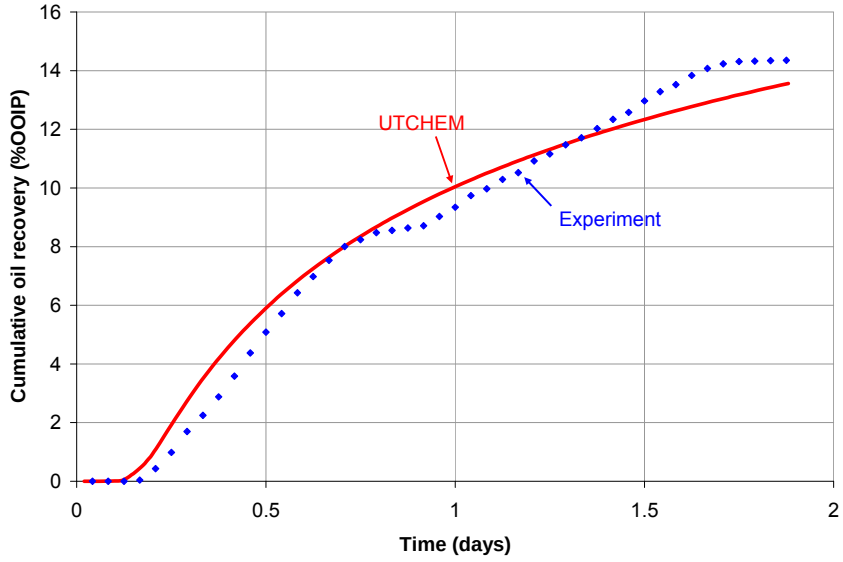

Figure 4.18: Comparison of laboratory and simulated waterflood oil recovery.

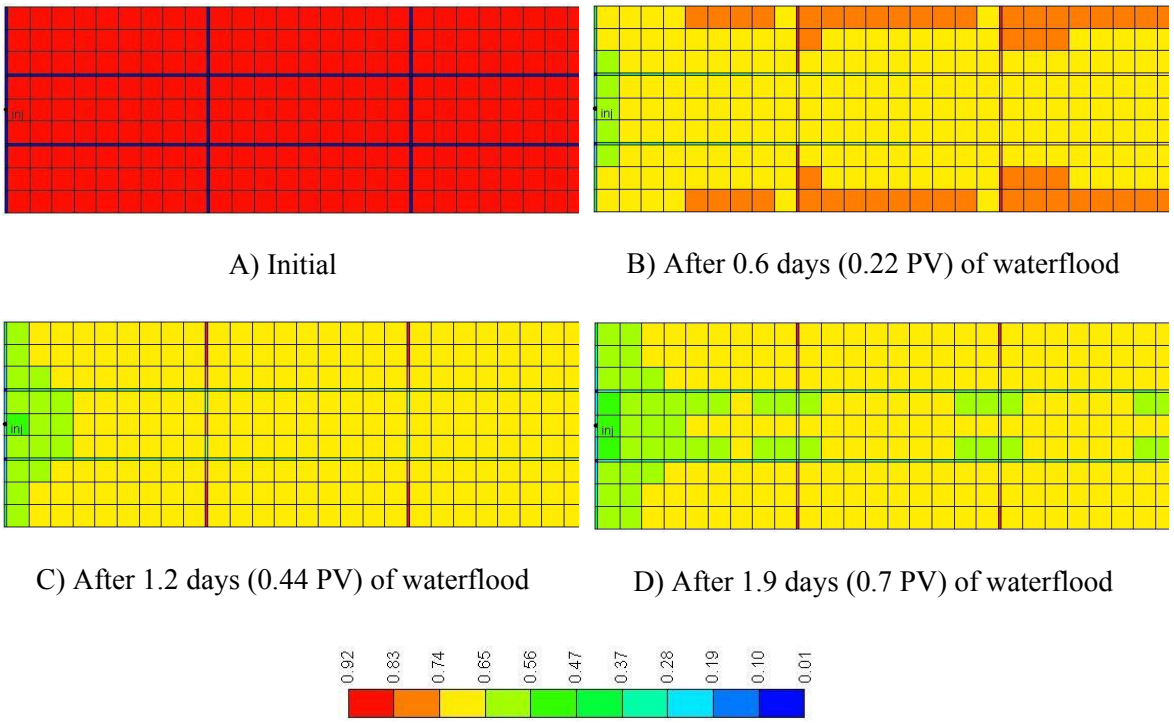

Figure 4.19: Oil saturation profiles in the middle layer during the waterflood.

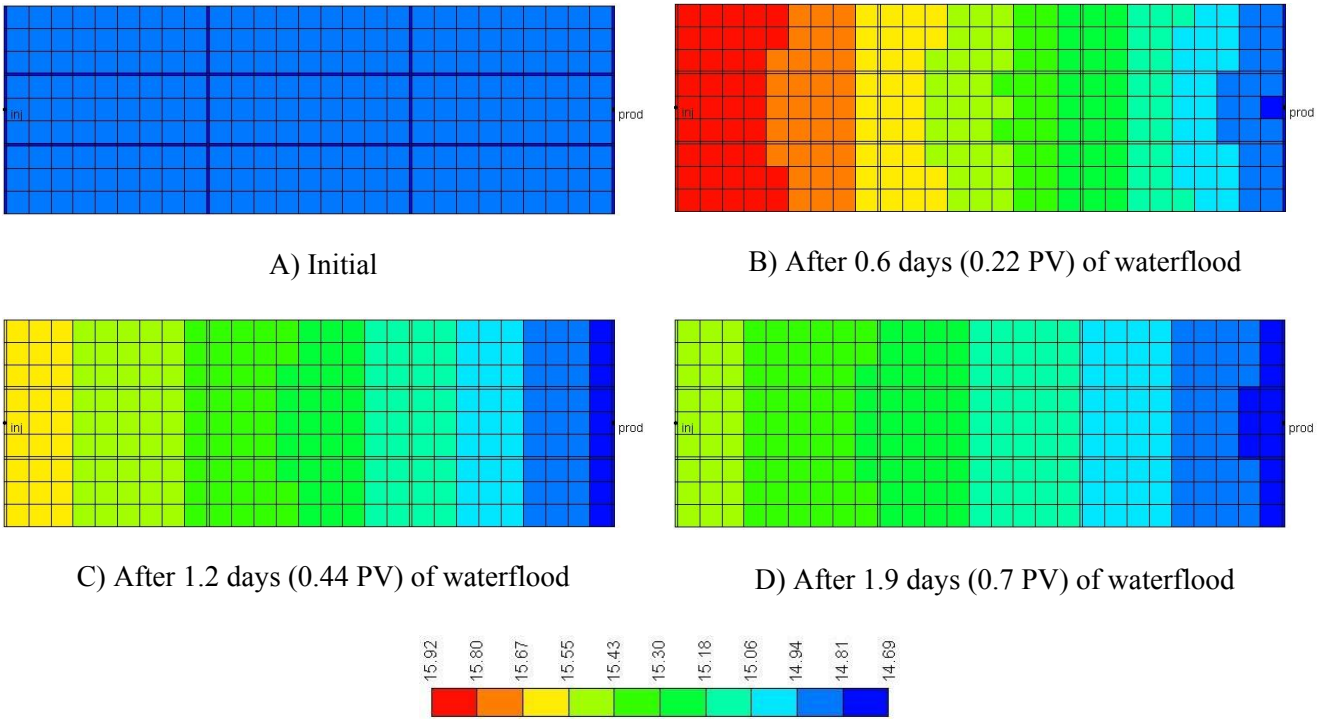

Figure 4.20: Oil pressure profiles in the middle layer during the waterflood.

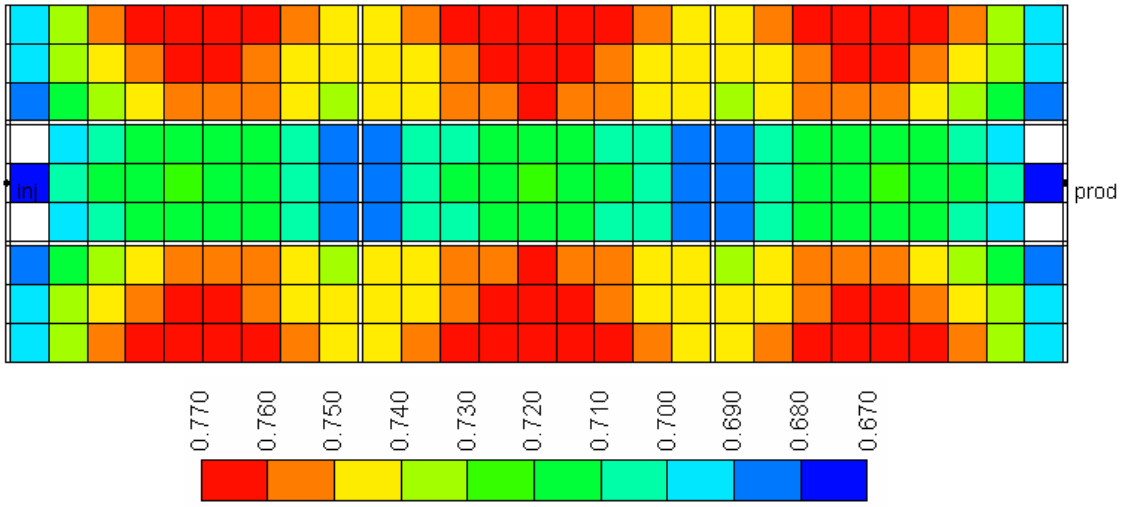

Figure 4.21: Oil saturation distribution in the middle layer after 1.9 days of pure capillary imbibition (no viscous forces). White cells fall out of the visualization range.

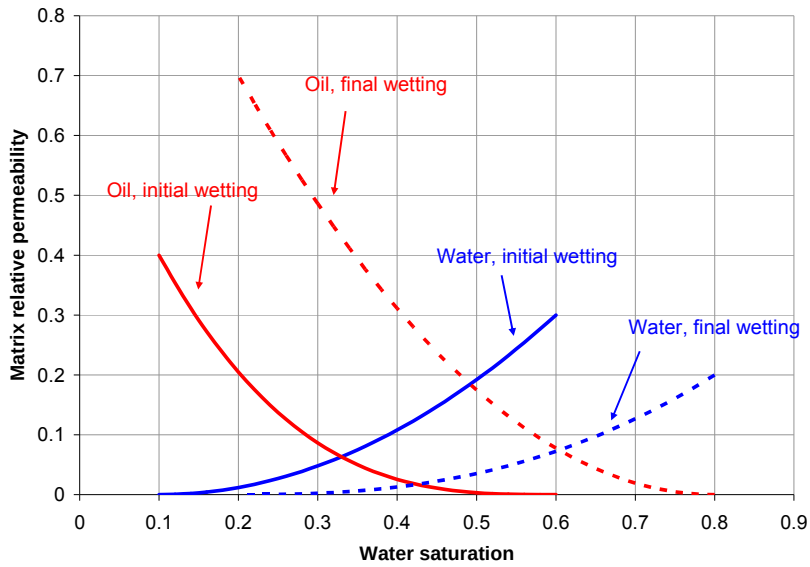

Figure 4.22: Matrix relative permeability curves for initial and final wetting states.

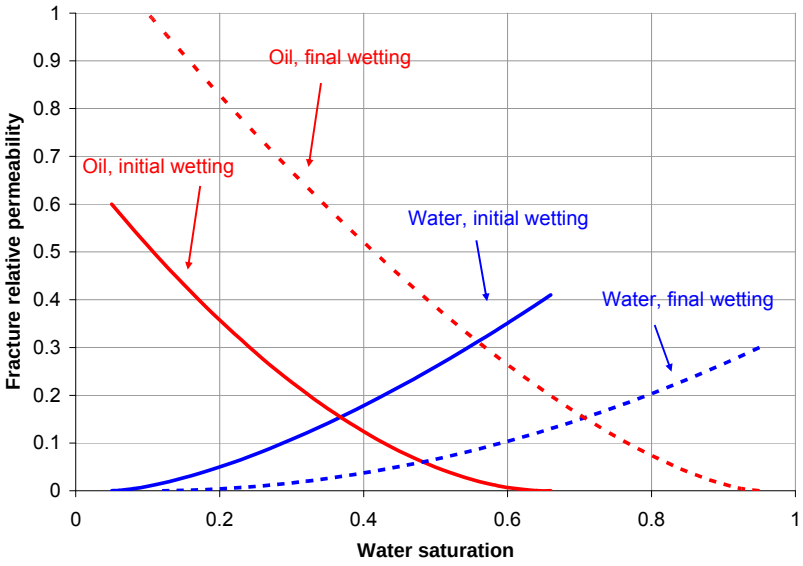

Figure 4.23: Fracture relative permeability curves for initial and final wetting states

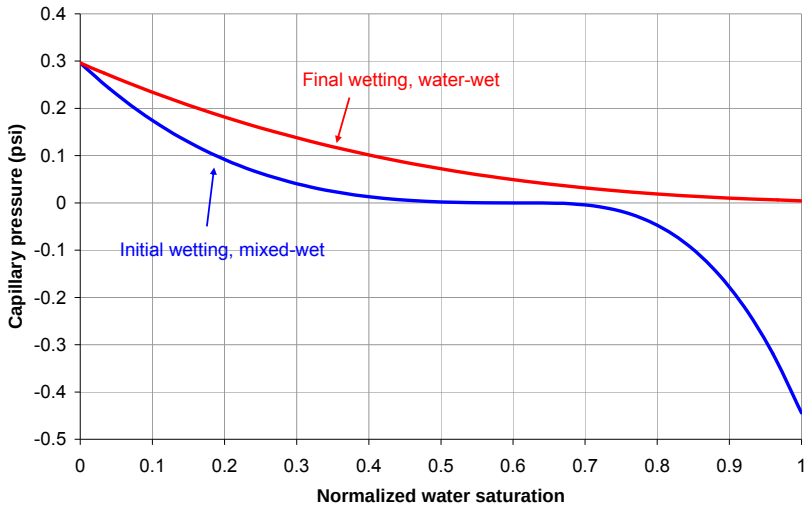

Figure 4.24: Matrix capillary pressure curves for initial and final wetting states.

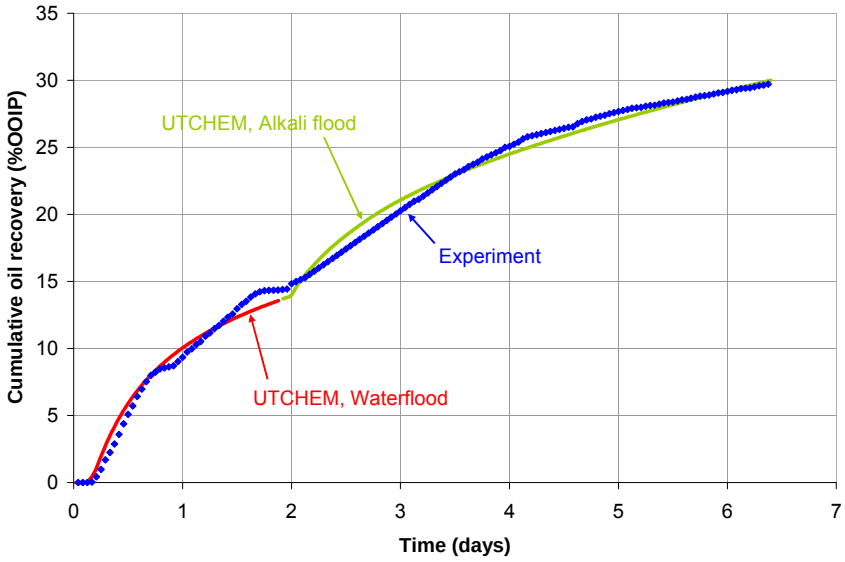

Figure 4.25: Comparison of experimental and simulated oil recoveries for the waterflood and alkali flood part of the Fractured Block experiment.

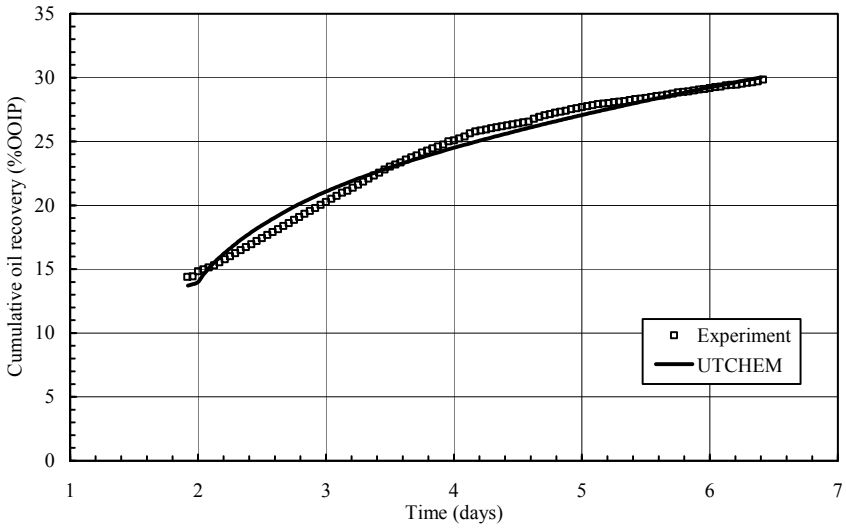

Figure 4.26: The quality of the match between the model and experiment for alkali flood part of the Fractured Block experiment.

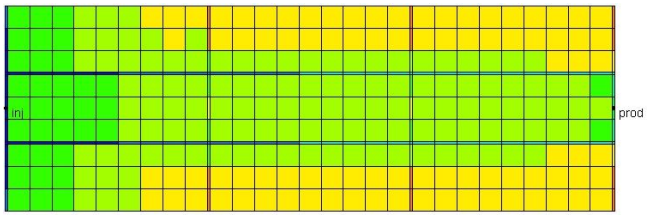

A) After 1.4 days (0.52 PV) of alkali flood

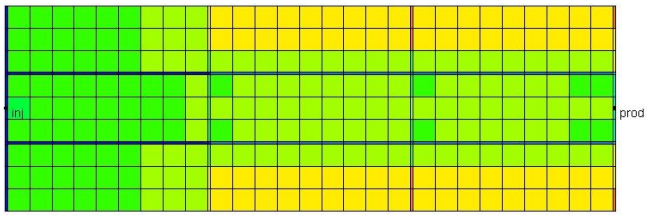

B) After 2.8 days (1.04 PV) of alkali flood

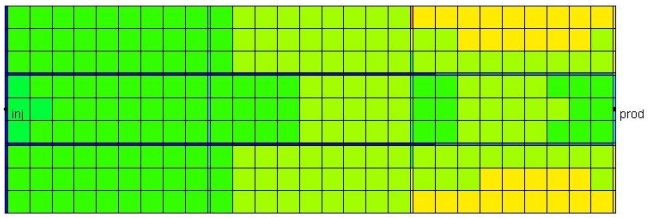

C) After 4.5 days (1.68 PV) of alkali flood

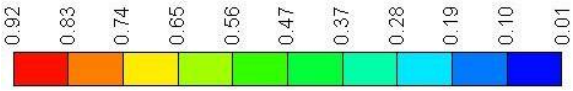

Figure 4.27: The oil saturation distribution in the middle layer during the alkali flood

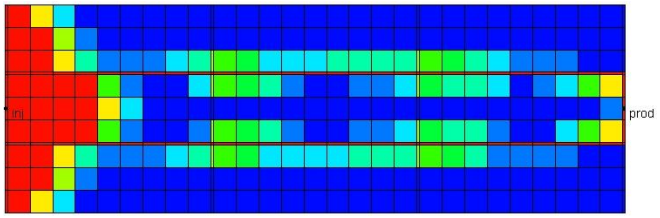

A) After 1.4 days (0.52 PV) of alkali flood

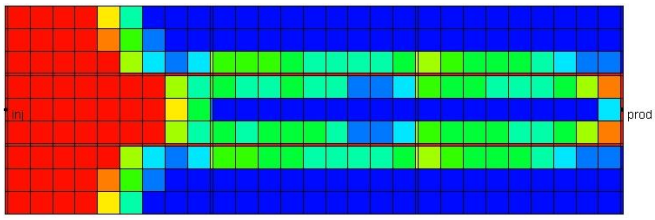

B) After 2.8 days (1.04 PV) of alkali flood

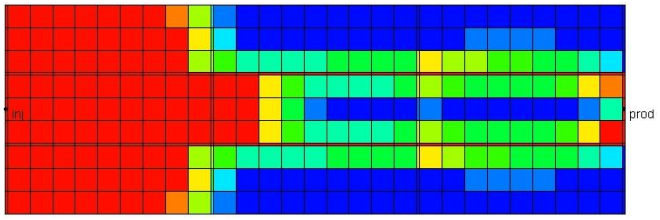

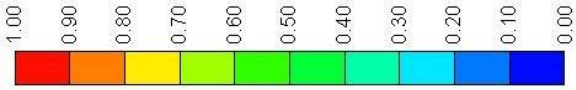

C) After 4.5 days (1.68 PV) of alkali flood

Figure 4.28: Normalized alkali concentration in the middle layer during the alkali flood.

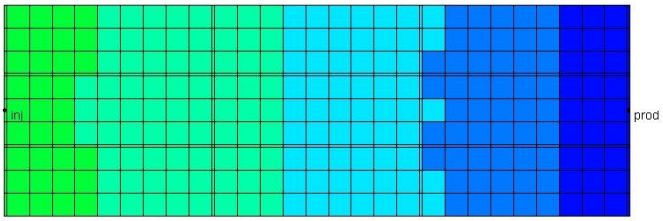

A) After 1.4 days (0.52 PV) of alkali flood

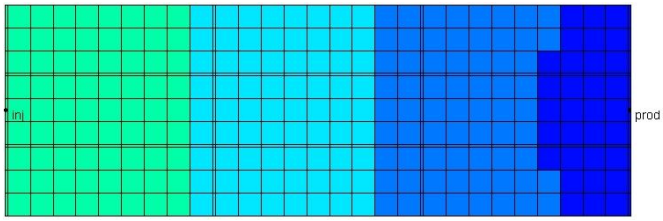

B) After 2.8 days (1.04 PV) of alkali flood

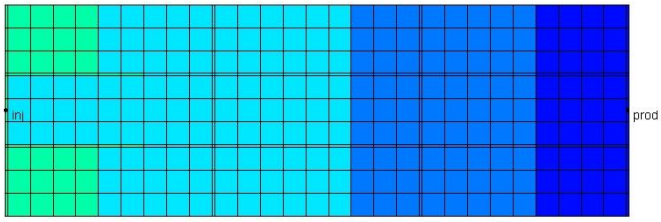

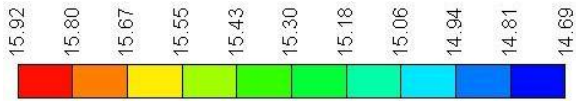

C) After 4.5 days (1.68 PV) of alkali flood

Figure 4.29: Pressure profiles (psia) in the middle layer during the alkali flood.

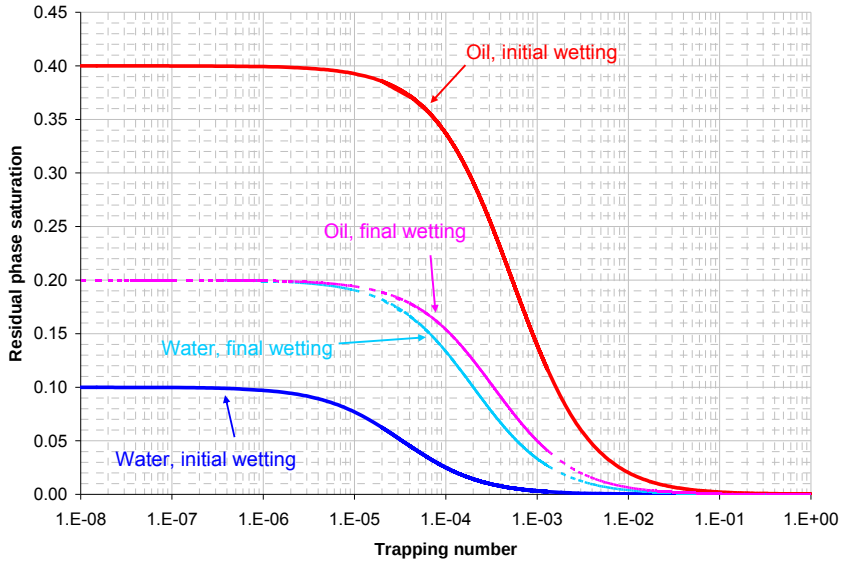

Figure 4.30: The capillary desaturation curves for initial and final wetting states used to match the alkali/surfactant part of the Fractured Block experiment.

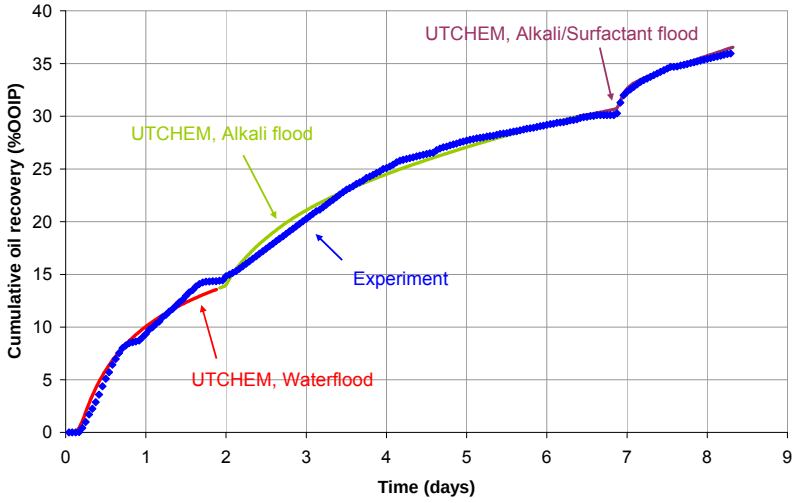

Figure 4.31: The quality of the match obtained for all three stages of the Fractured Block experiment.

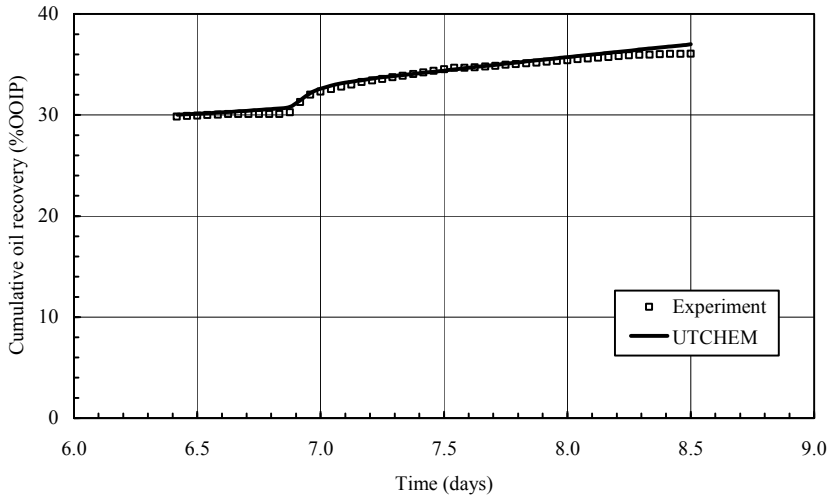

Figure 4.32: The quality of the match between the simulation and laboratory measurements for the alkali/surfactant part of the Fractured Block experiment.

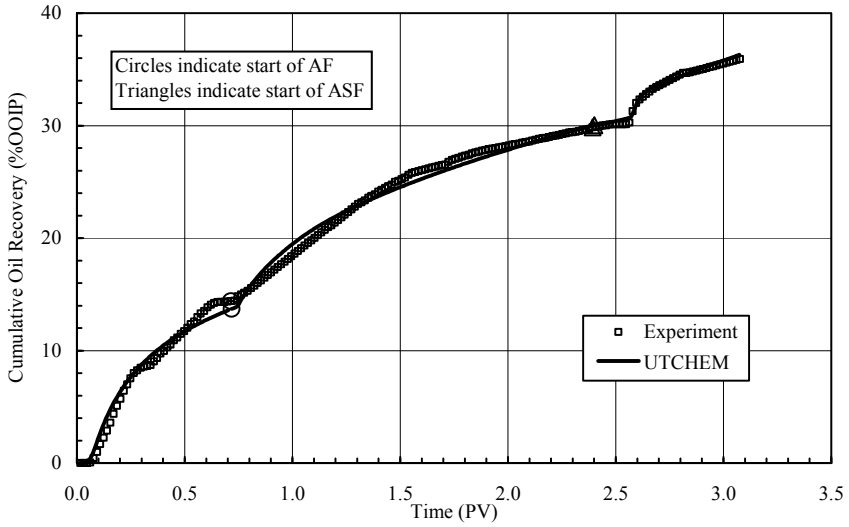

Figure 4.33: Comparison of simulation and laboratory recovery curves in pore volumes injected. (AF stands for alkali flood and ASF stands for alkali/surfactant flood).

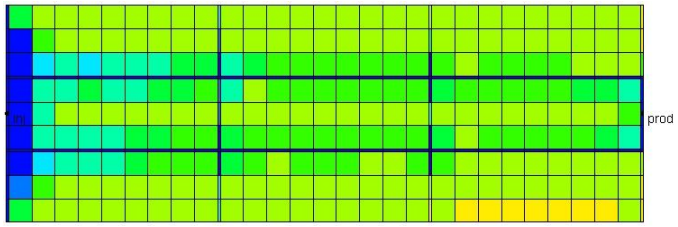

A) After 0.6 days (0.4 PV) of alkali/surfactant flood

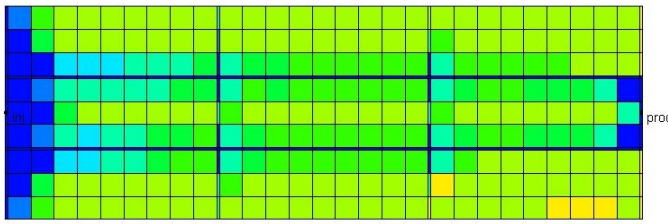

B) After 1.2 days (0.8 PV) of alkali/surfactant flood

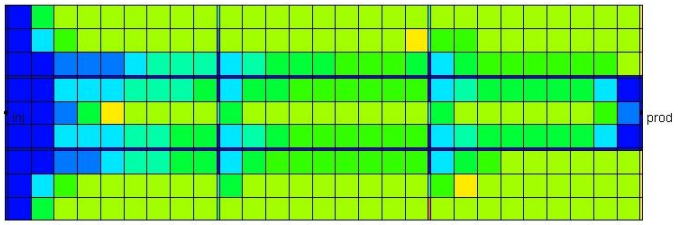

C) After 1.8 days (1.2 PV) of alkali/surfactant flood

Figure 4.34: Simulated oil saturation profiles in the middle layer of the setup during the alkali/surfactant flood.

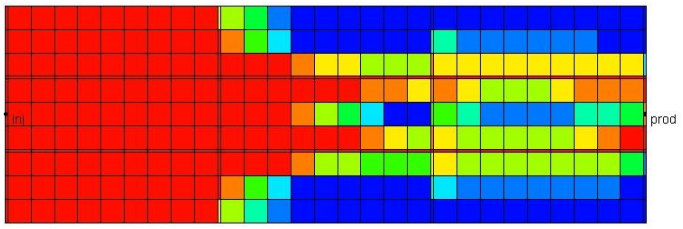

A) After 0.6 days (0.4 PV) of alkali/surfactant flood

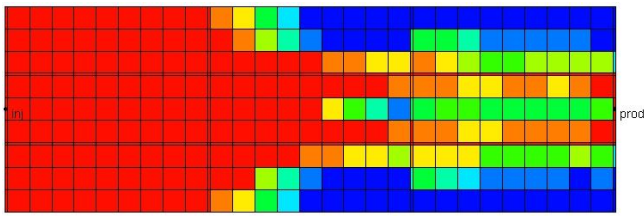

B) After 1.2 days (0.8 PV) of alkali/surfactant flood

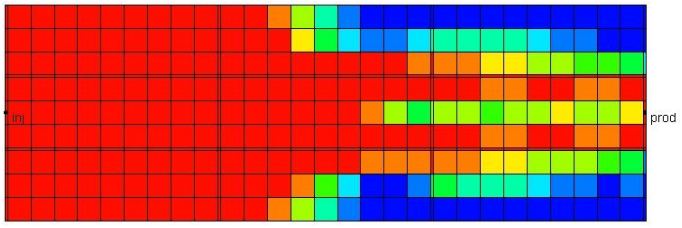

C) After 1.8 days (1.2 PV) of alkali/surfactant flood

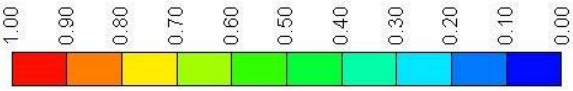

Figure 4.35: Simulated normalized alkali concentration profiles in the middle layer for the alkali/surfactant flood.

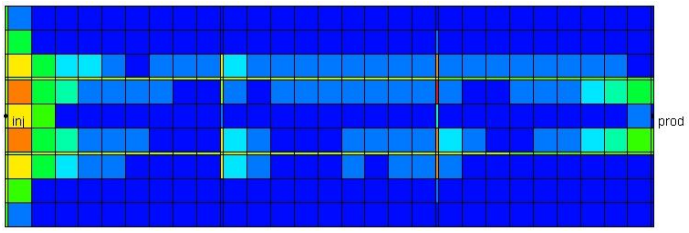

A) After 0.6 days (0.4 PV) of alkali/surfactant flood

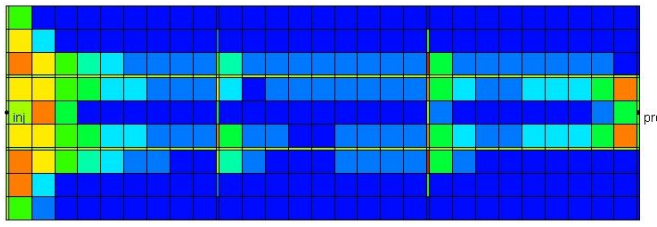

B) After 1.2 days (0.8 PV) of alkali/surfactant flood

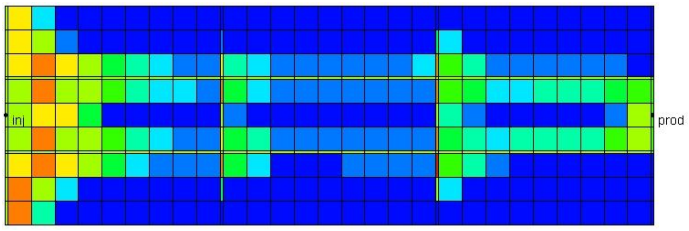

C) After 1.8 days (1.2 PV) of alkali/surfactant flood

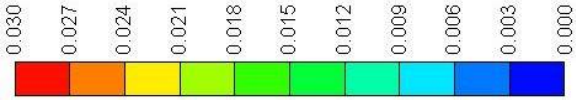

Figure 4.36: Simulated surfactant concentration (Vol. %) profiles in the middle layer for the alkali/surfactant flood.

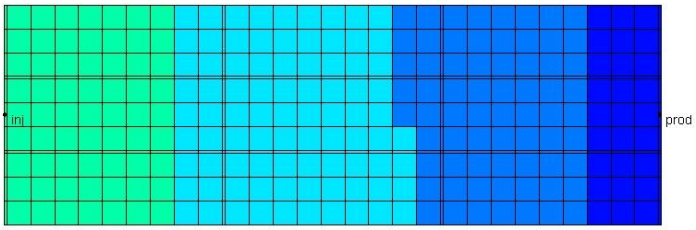

A) After 0.6 days (0.4 PV) of alkali/surfactant flood

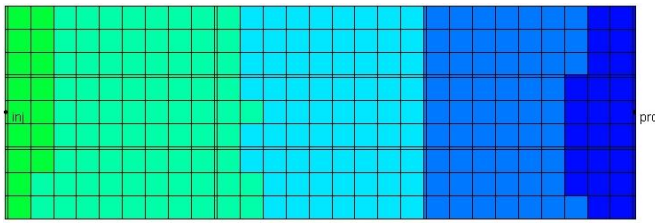

B) After 1.2 days (0.8 PV) of alkali/surfactant flood

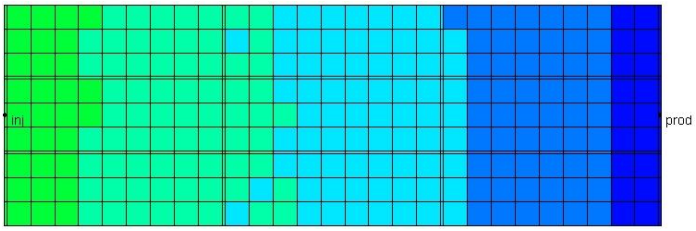

C) After 1.8 days (1.2 PV) of alkali/surfactant flood

Figure 4.37: Simulated pressure profiles in the middle layer for the alkali/surfactant flood.

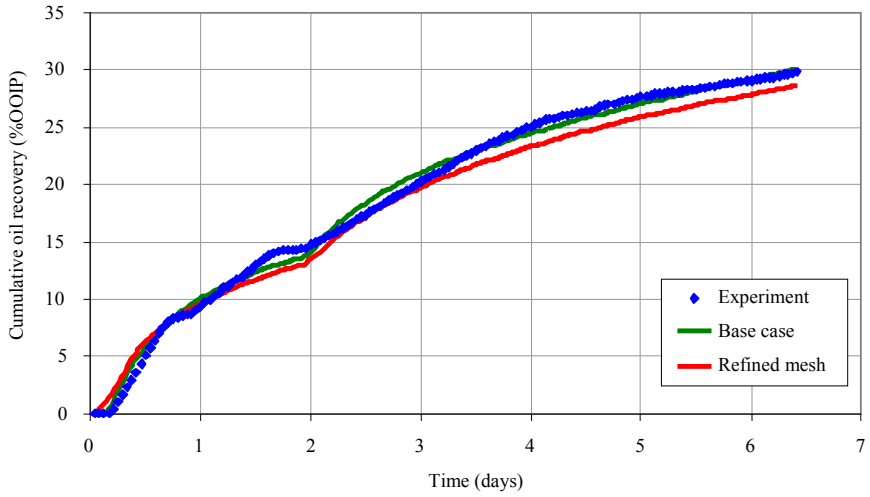

Figure 4.38: Effect of mesh refinement on simulation results of the Fractured Block modeling.

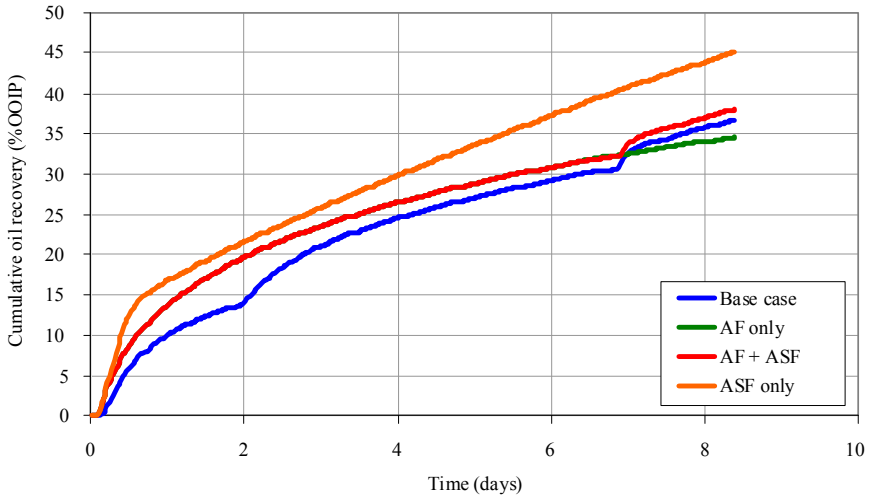

Figure 4.39: Simulated oil recovery for different injection scenarios compared to the base case injection.

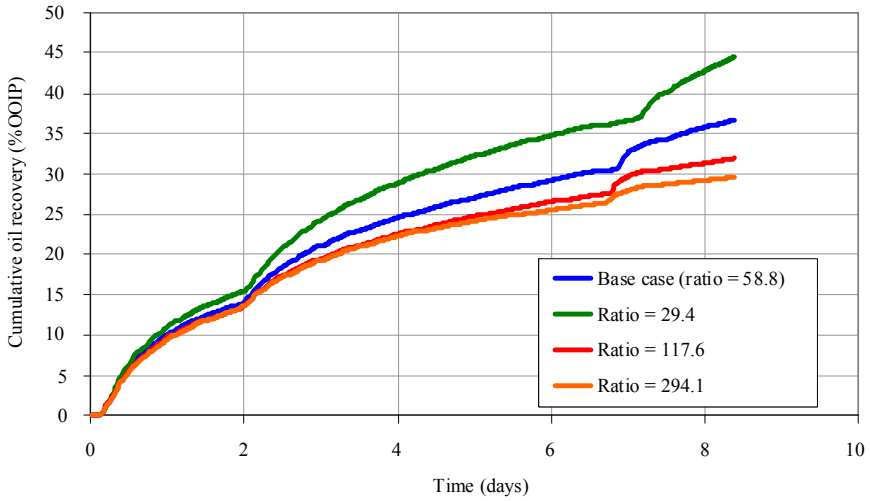

Figure 4.40: simulated oil recovery sensitivity to fracture/matrix permeability ratio.

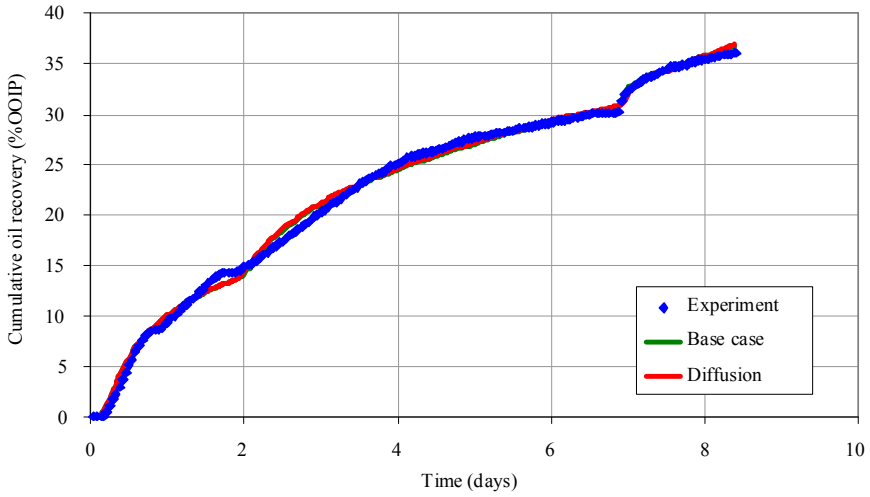

Figure 4.41: Sensitivity of simulated oil recovery to molecular diffusion.

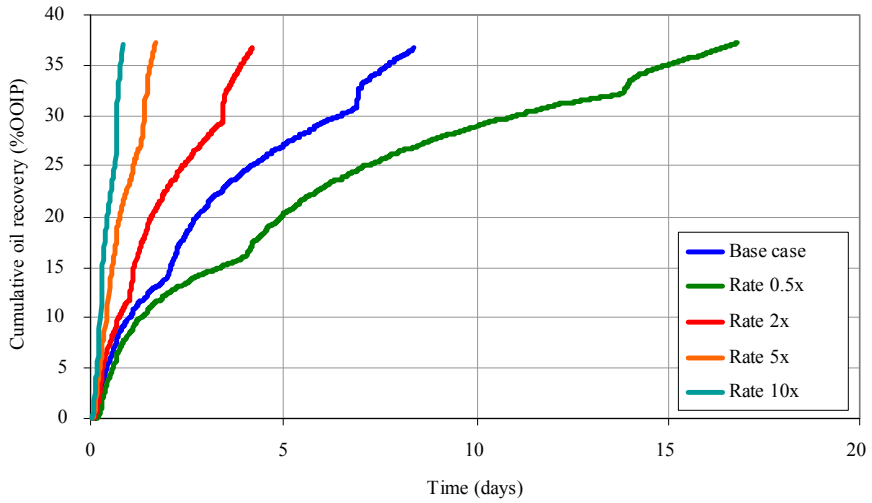

Figure 4.42: Sensitivity of simulated oil recovery to injection rate (constant rate injection, constant pressure production).

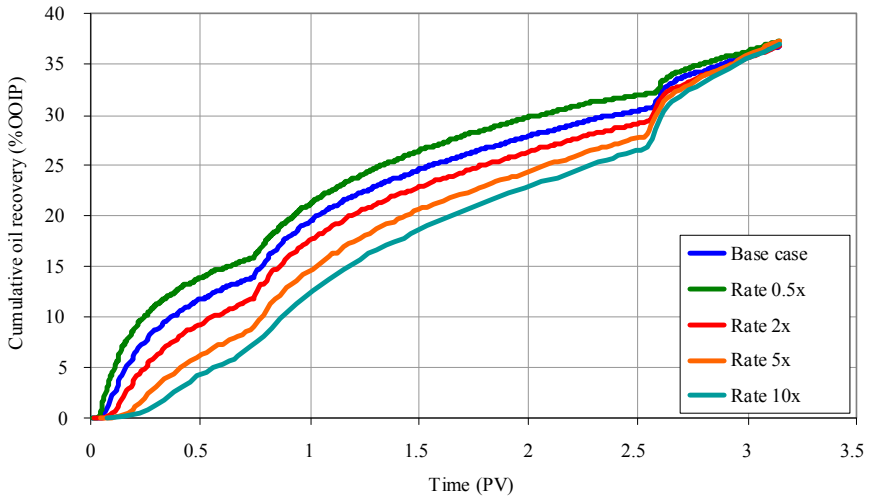

Figure 4.43: Sensitivity of simulated oil recovery to injection rate (Results of Fig. 4.42 plotted versus injected pore volumes).

Chapter 5: Scale Up Methodology for Wettability Modification in Fractured Carbonates

5.1 Introduction

Laboratory alkali and surfactant floods have shown a great potential in increasing oil recovery for reservoirs that are naturally fractured with low permeability mixed-wet matrix rocks. Fractured, mixed-wet formations usually have poor waterflood performance because the injected water tends to flow in the fractures and spontaneous imbibition into the matrix is generally insignificant. Surfactants or alkalis have successfully been used to change the wettability and enhance oil recovery by increased imbibition of the water into the matrix rock. The oil recovery mechanisms using surfactant/alkali mixtures are enhanced imbibition and buoyancy due to combined effects of reduced interfacial tension, reduced mobility ratio, and wettability alteration.

Although laboratory experiments are essential, it is impossible to predict the performance of these complex processes with only laboratory experiments. Reservoir simulation is required to scale up the process from laboratory to field conditions and to understand and interpret the data. Without detailed and mechanistic simulations it is very unlikely that a cost-effective process can be developed and applied economically. The predictive simulations of such complex processes will reduce the risk of failure of the field projects. A compositional chemical reservoir simulator (UTCHEM) with wettability alteration capability is used for this study. This chapter focuses on the scale up simulations of two different oil recovery experiments in carbonate rocks using chemicals for wettability modification. Several imbibition rate scaling groups are tested in an attempt to scale the lab results to larger field scale matrix blocks (Delshad *et al*., 2009).

5.2 Scale Up of the Imbibition Cell Test Experiment

The laboratory alkaline/surfactant imbibition experiment reported by Hirasaki and Zhang (2004) is used for the scale up study. This is a static imbibition cell experiment as described in Section 4.1.1. The approach taken for modeling of the experiment is presented in Section 4.1.2.

The effect of matrix block size on oil recovery is investigated keeping the same simulation model properties as those obtained by history match of the imbibition cell test presented in Table 4.1 and Table 4.2. Preserving all of the simulation parameters obtained from modeling the experiment (such as grid size, relative permeability and capillary pressure curves, etc.) will ensure that the scaled model is representative of the same conditions as that of the experiment. The scale up is performed to investigate the effect of matrix height and volume separately. First several simulations are performed increasing the height as much as 5 ft which is 20 times larger than that of the lab core of 0.25 ft while keeping the area of the model the same as that of the experiment. The increase in height is preformed by adding more layers to the model keeping the grid size the same as that of the lab model. In a separate set of simulations, the volume of the block is increased as much as 125 times the core bulk volume. This is done by increasing the number of gridblocks in all three directions while keeping the grid size the same as that of the experiment. The modeling results for the effect of matrix height are shown in Fig. 5.1 where the time of oil recovery to reach the same recovery of 44% as the lab core increases significantly as the block height increases.

The top surface and four side surfaces of the core are open to imbibition similar to the experimental set up. The characteristic length based on Eq.2.7 is as follows for this case:

$$L_c = \frac{hx}{\sqrt{8h^2 + x^2}} \qquad \text{Eq.5.1}$$

where h is the height of the core and x is its lateral dimension. Figure 5.2 shows the effect of matrix height on the characteristic length (Eq.5.1). As shown in this figure, the characteristic length does not change a lot as the matrix height is increased to even 20

times as large as the experiment (5 ft). The simulation times for different matrix heights are normalized by the corresponding L_c^2. The recovery curves should merged to one curve if the imbibition recovery time scales with the inverses of characteristic length as both Ma *et al*. (1995) and Li and Horne (2006) suggested. However, the recovery curves did not converge when the simulation time was scaled using L_c^2 (Fig. 5.3). Figure 5.4 shows the results of Fig. 5.1 plotted against the dimensionless time proposed by Li and Horne (2006) (Eq.2.13). As shown in this figure, not only their dimensionless time does not bring the results closer, it diversifies the results. This indicates that the experiment of the Hirasaki and Zhang (2004) was not dominated by capillary imbibition. Another reason for the poor performance of this dimensionless time could be the fact that the characteristic length proposed by Ma *et al*. (1995) (Eq.2.7) for this case (Eq.5.1) does not vary to a great extent as the matrix area is kept constant and matrix height is increased as shown in Fig. 5.2.

Next the height of the matrix was used as a characteristic length and the simulation time was divided by the height of matrix in each simulation. Figure 5.5 shows the results of this analysis. As shown in this figure, the recovery curves for different matrix heights tend to aggregate to a single curve when the simulation time is divided by the height of the matrix. The gravity time (t_g) of Eq.2.4 was then tried to scale the simulation times obtained with different matrix height. Figure 5.6 presents the oil recovery as a function of simulation times normalized by t_g where the oil recovery curves are collapsed to nearly one curve. This is an indication of a gravity dominated flow where the dominant mechanism is the buoyancy. The theoretical calculations confirmed the significance of buoyancy-driven gravity drainage under the low interfacial tension condition of the experiment. This is consistent with the findings of Hirasaki and Zhang (2004) and Adibhatla and Mohanty (2006).

The volume of the block was then increased by as much as 125 times the lab core. Figure 5.7 shows the effect of increasing the bulk volume of the setup on calculated characteristic length proposed by Ma *et al*. (1995) based on Eq.5.1. This figure indicates

that a relatively large range of the characteristic lengths are covered in this case. The simulated cumulative recoveries are shown in Fig. 5.8. Increasing the volume of the matrix increases the time required for recovering the same amount of oil as that of the experiment (44% OOIP). To see if the characteristic length proposed by Ma et al. (1995) works for this case, the simulation times for each case are divided by L_c^2. Figure 5.9 shows these results and once again one can see that the recovery curves do not aggregate when divided by L_c^2. Since in this case the characteristic length covers a relatively large range of values, the divergence of the recovery curves can only be due to the fact that the experiment is not dominated by capillary imbibition.

The height of the matrix is tested then as a characteristic length and the results are shown in Fig. 5.10. The recovery curves for different cases fall on top of each other when the simulation time is divided by matrix height (Fig. 5.10). The simulation times are then normalized by the gravity time (t_g) and the oil recovery curves for different matrix block volumes collapse to essentially one curve (as shown in Fig. 5.11), re-emphasizing the fact that the buoyancy was a dominant mechanism in this case.

The recovery times computed for different matrix block sizes in Fig. 5.12 indicate that if the reservoir conditions were the same as the ones used in the experiment then to attain the same oil recovery as the lab core it takes about 7.5 years for the block size of 0.67 m wide x 1.5 m high and 15 years for the block size of 1.37 m wide by 3 m high. Therefore, the imbibition time increases proportional to the height of the block size. These results are consistent with those of Adibhatla *et al*. (2005). They specify that it takes 10 years for 1 m wide x 1 m high block and 100 years for 10 m wide x 10 m high block to reach the same oil recovery indicating that the time scales with the height of the core.

5.3 Scale Up of the Fractured Block Experiment

Section 4.2.1 gives the description of the Fractured Block experiment and Section 4.2.2 gives a detailed explanation of the modeling procedure. The same simulation parameters obtained from modeling the experiment are used to study the effect of matrix block size on oil recovery. These parameters can be found in Table 4.3 through Table 4.6.

Only one matrix block (as shown in Fig. 5.13) is modeled for the scale up study to reduce the computation time and to be able to keep the same grid resolution to minimize the numerical dispersion. The single matrix block is surrounded by several fractures depending on the scale up scenario of enlarging the area, height or volume. To maintain comparable viscous forces to the experiment, pressure constraint injection and production wells are used with the same pressure gradient of the experiment. Same pore volumes of water, alkaline, and surfactant/alkaline are injected as those of the experiment. The height of the matrix is increased as much as ten times keeping the area the same as the experiment with sealed left and right hand side faces. The reason for sealing the left and right faces is to isolate the effect of matrix height on the oil recovery. The block area is increased as much as 81 times keeping the height the same as the experiment. The top and bottom of the matrix are sealed in this case to isolate the effect of matrix area on oil recovery. The volume of the matrix block is increased as much as 64 times the experiment with all faces open to flow. Injection and production wells are placed in the fractures at the back and front of the matrix block along the longer face of the matrix. For the purpose of comparison, a single matrix block as the lab size is also simulated for each case referred to as the "Base" in the figures. Figures 5.14 through 5.16 show the oil recoveries for height, areal, and volume scale up where the oil recovery increases with larger block sizes because of longer residence times.

An attempt was made to scale the results using Eq.2.4 and Eq.2.7. The simulated alkali flood oil recovery curves for larger block thicknesses collapsed to nearly one curve when Ma's dimensionless time (t_D) was used as shown in Fig. 5.17. The injection times and oil recoveries of waterflood are subtracted for these analyses. Simulation results for larger block areas are plotted versus t_D in Fig. 5.18. The results indicate that the larger block sizes recover oil faster as a result of viscous gradient that is not accounted for in Ma's dimensionless time. The gravity reference time (t_g) gave very poor scaling for this case.

Figure 5.18 shows that even a small viscous gradient aided in recovery of oil from larger matrix blocks. Due to the complexity of the experiment in using alkali for wettability alteration and surfactant for reducing interfacial tension, each flood was dominated by different magnitudes of gravity, capillary, and viscous forces. A new dimensionless time is required to adequately scale the results of this experiment by taking different recovery mechanisms into account.

5.4 Summary and Conclusions

1. The imbibition cell test results were dominated by the buoyancy driven gravity drainage.
2. A published dimensionless time based on gravity was able to successfully scale the imbibition oil recovery results with increased height and volume of matrix block consistent with the laboratory observation. The reason for this is the dominance of gravity in this experiment.
3. The imbibition times increased linearly with the length scale for the static imbibition experiment. This is also due to the dominance of gravity rather than capillary forces.
4. The scaling of imbibition experiments showed that the rate of imbibition and oil recovery were much faster under the low IFT conditions compared to diffusion-dominated high IFT experiments reported in the literature. The ultra low IFTs reduce the capillary forces and result in dominance of buoyancy forces which accelerates the oil recovery process.
5. The fractured block experimental conditions was used for the scale up study and the results indicated that even a small viscous gradient aided in recovery of oil from larger matrix blocks.
6. Due to the complexity of the fractured block experiment in using alkali for wettability alteration and surfactant for reducing interfacial tension, each flood was dominated by different magnitudes of gravity, capillary, and viscous forces.
7. A new dimensionless time is required to adequately scale the results of the fractured block experiment by taking into account different recovery mechanisms.

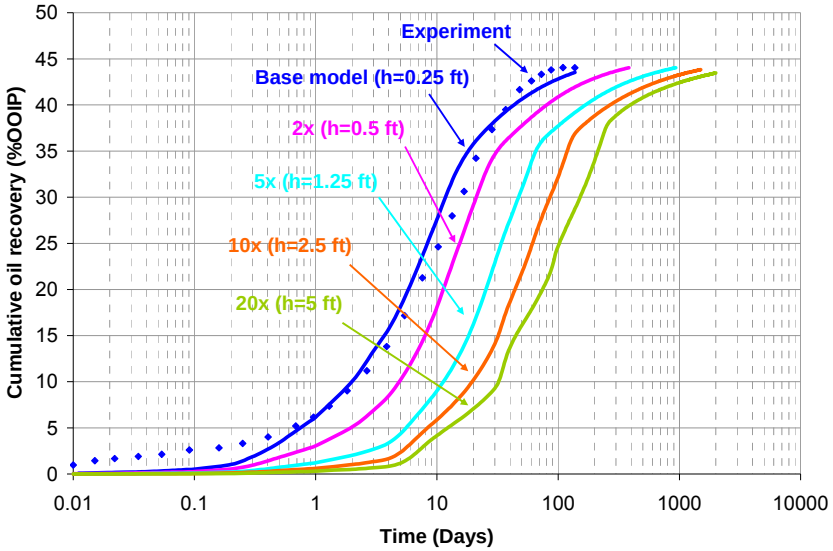

Figure 5.1: Effect of core height on oil recovery based on imbibition cell experiment.

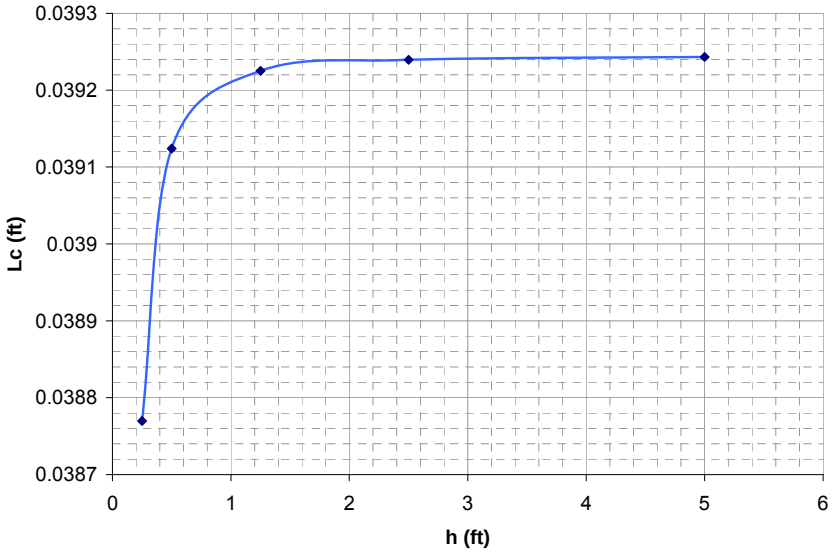

Figure 5.2: Effect of matrix height on characteristic length for the imbibition cell test.

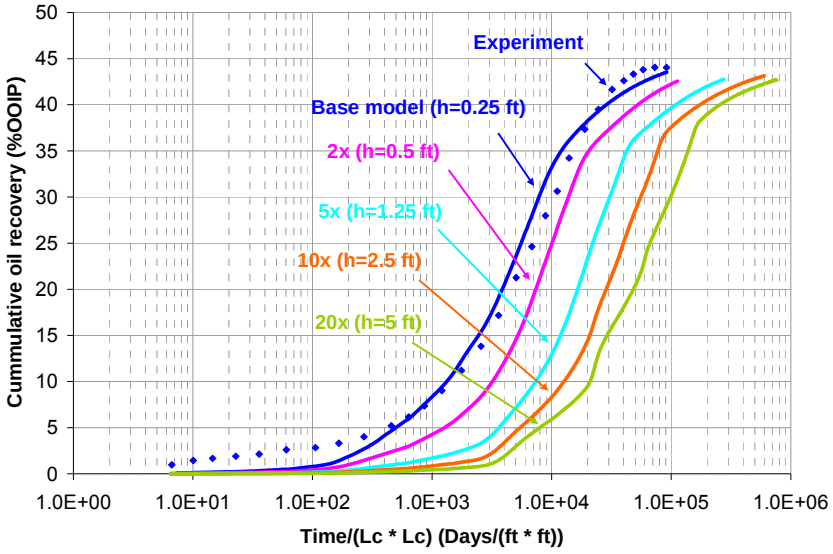

Figure 5.3: Results of Fig. 5.1 plotted versus simulation time divided by L_c^2.

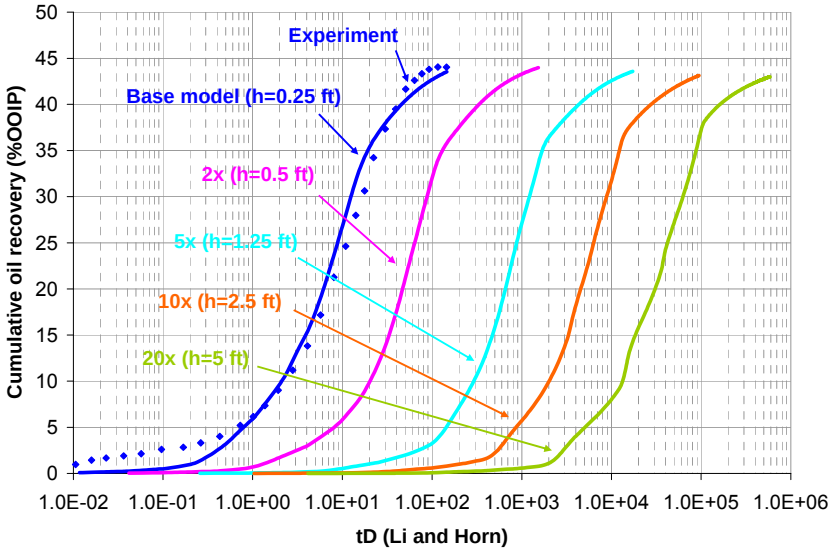

Figure 5.4: Results of Fig. 5.1 plotted versus dimensionless time proposed by Li and Horne (2006).

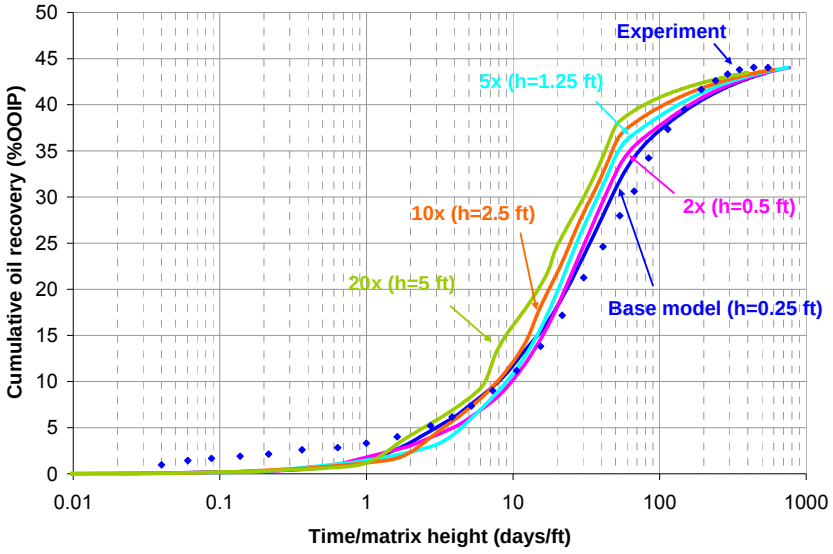

Figure 5.5: Results of Fig. 5.1 plotted versus simulation time divided by matrix height.

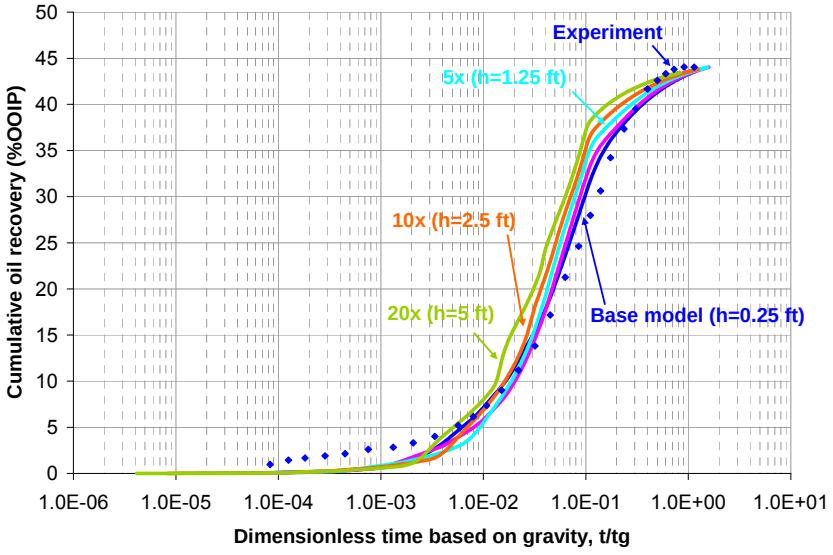

Figure 5.6: Oil recovery vs. dimensionless time based on gravity for effect of matrix height on oil recovery (Results of Fig. 5.1 plotted vs. dimensionless time based on gravity proposed by Cuiec *et al*., (1990)).

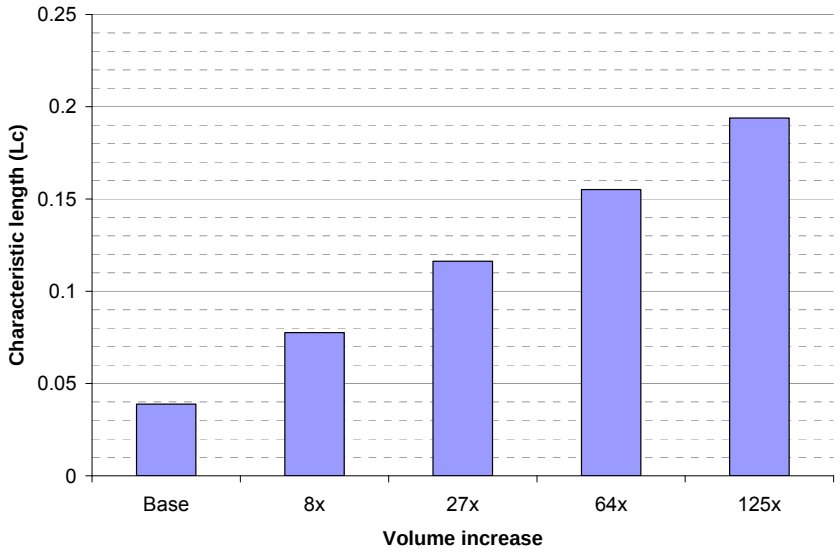

Figure 5.7: Effect of increasing the volume of the matrix on characteristic length for Hirasaki and Zhang (2004) imbibition cell test based on Eq.5.1.

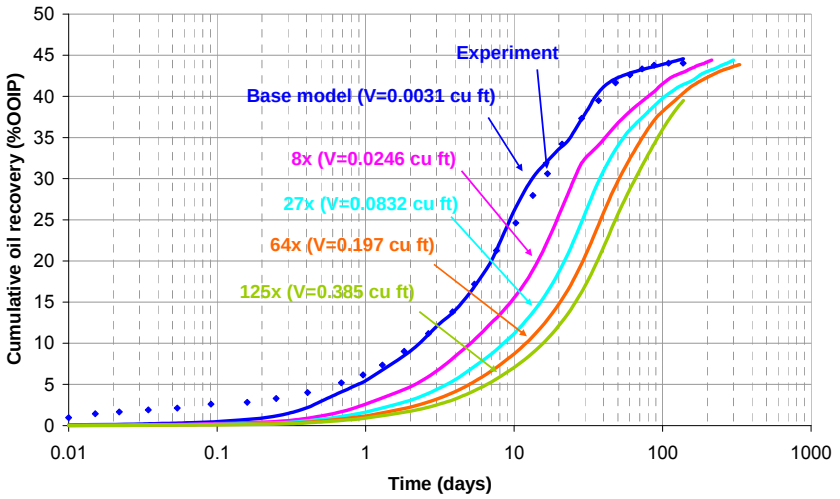

Figure 5.8: Effect of matrix bulk volume on oil recovery based on imbibition cell test experiment.

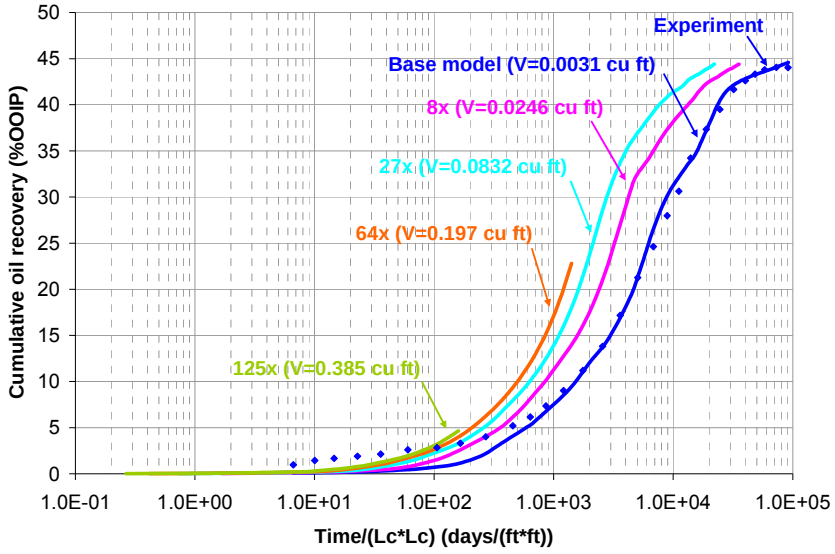

Figure 5.9: Results of Fig. 5.8 plotted versus simulation time divided by L_c^2 proposed by Ma *et al*. (1995).

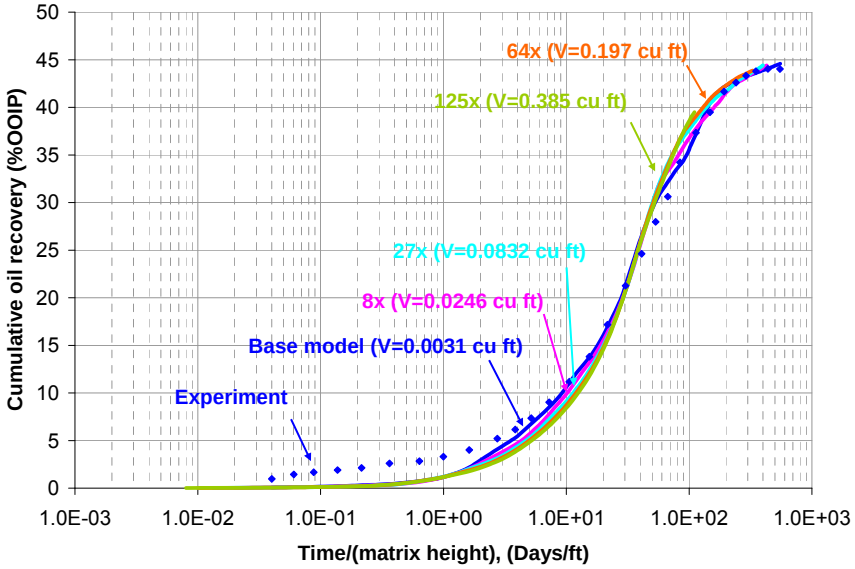

Figure 5.10: Results of Fig. 5.8 plotted versus simulation time divided by height of the matrix.

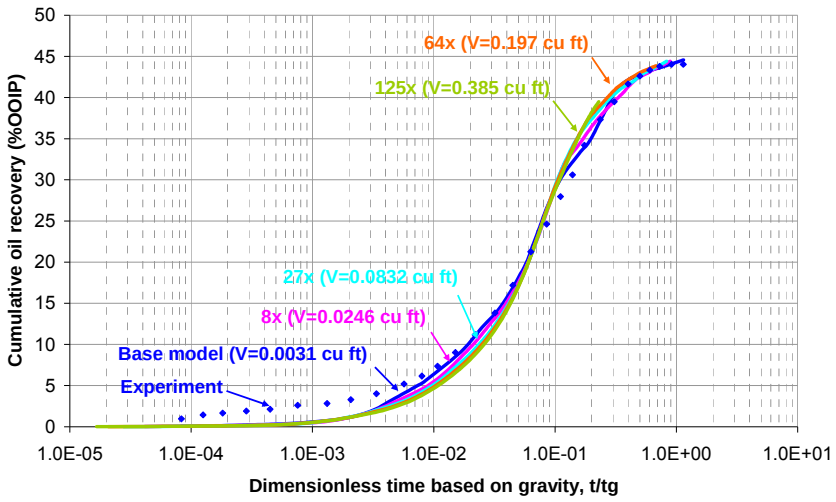

Figure 5.11: Oil recovery vs. dimensionless time based on gravity for effect of matrix bulk volume on oil recovery (Results of Fig. 5.8 plotted vs. dimensionless time based on gravity proposed by Cuiec *et al*., (1990)).

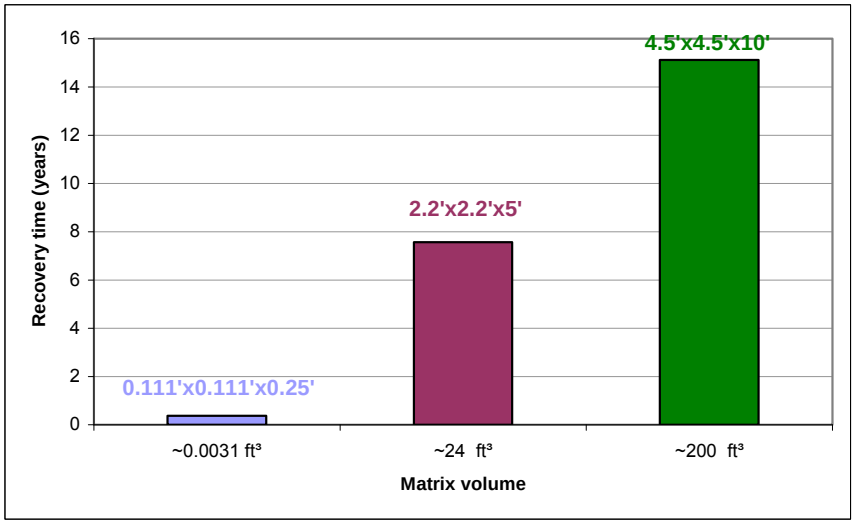

Figure 5.12: Recovery time vs. matrix bulk volume based on imbibition cell test results.

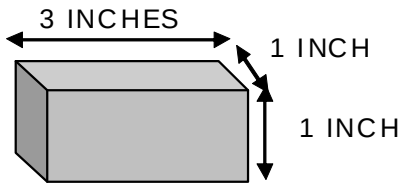

Figure 5.13: A single block of the Fractured Block experiment used for scale up simulations.

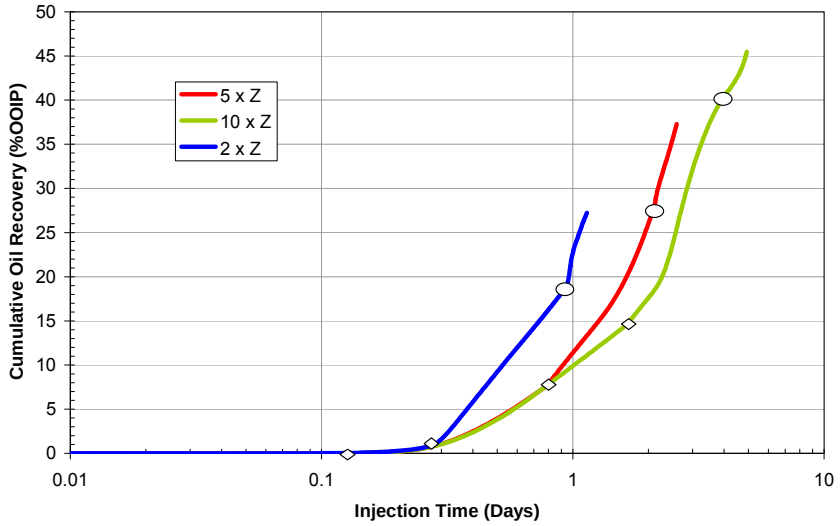

Figure 5.14: Effect of matrix height on oil recovery from the Fractured Block experiment (diamonds show the beginning of alkali flood and ovals show the start of alkali/surfactant flood).

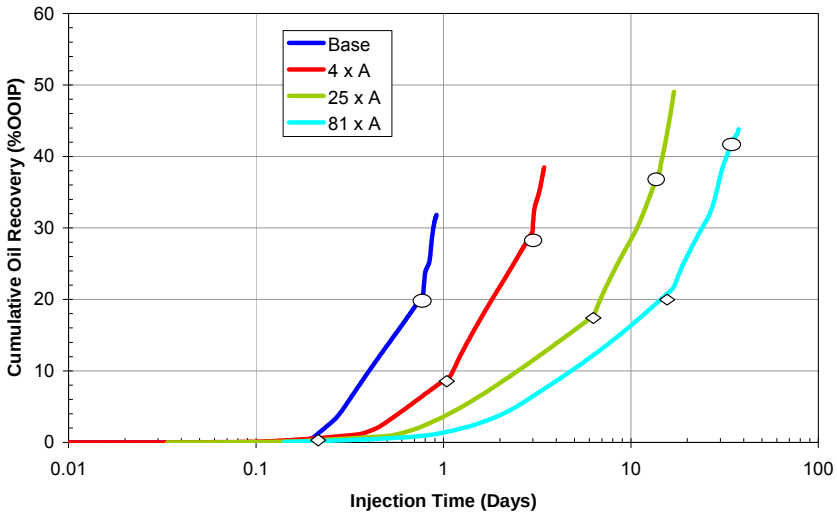

Figure 5.15: Effect of matrix area on oil recovery from the Fractured Block experiment (diamonds show the beginning of alkali flood and ovals show the start of alkali/surfactant flood).

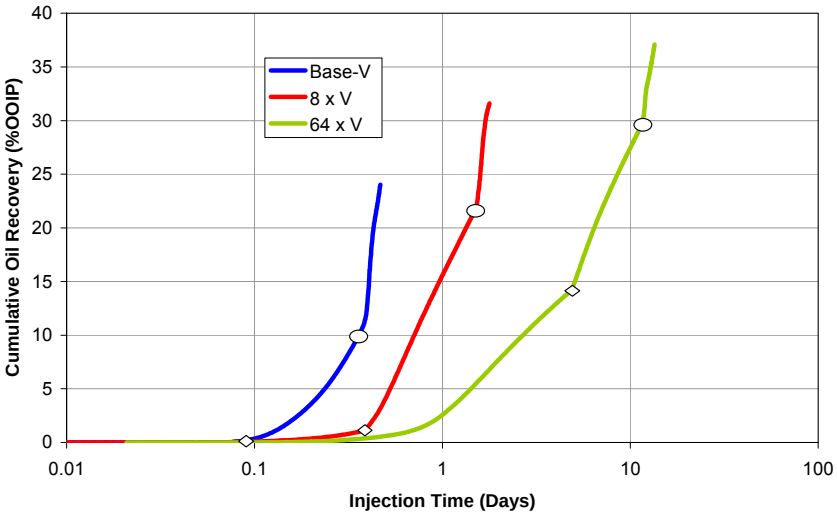

Figure 5.16: Effect of matrix volume on oil recovery from the Fractured Block experiment (diamonds show the beginning of alkali flood and ovals show the start of alkali/surfactant flood).

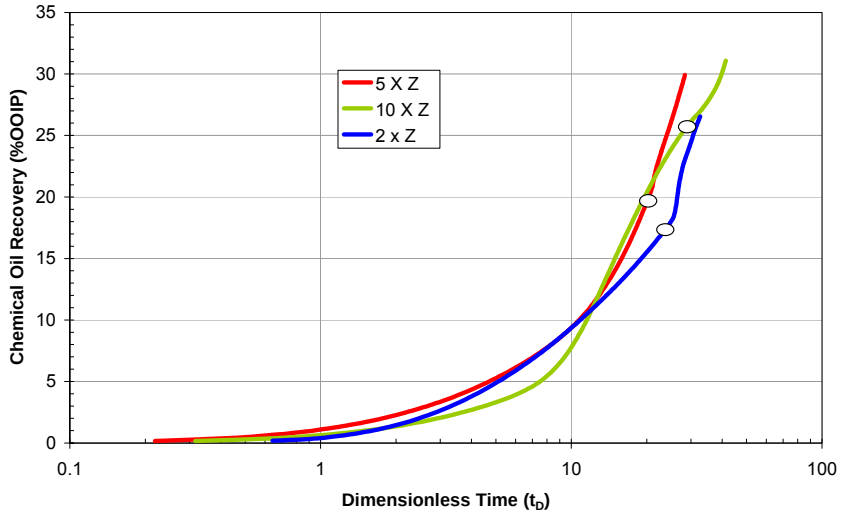

Figure 5.17: Dimensionless time by Ma *et al*. (1995) used for scaling the effect of matrix height on oil recovery.

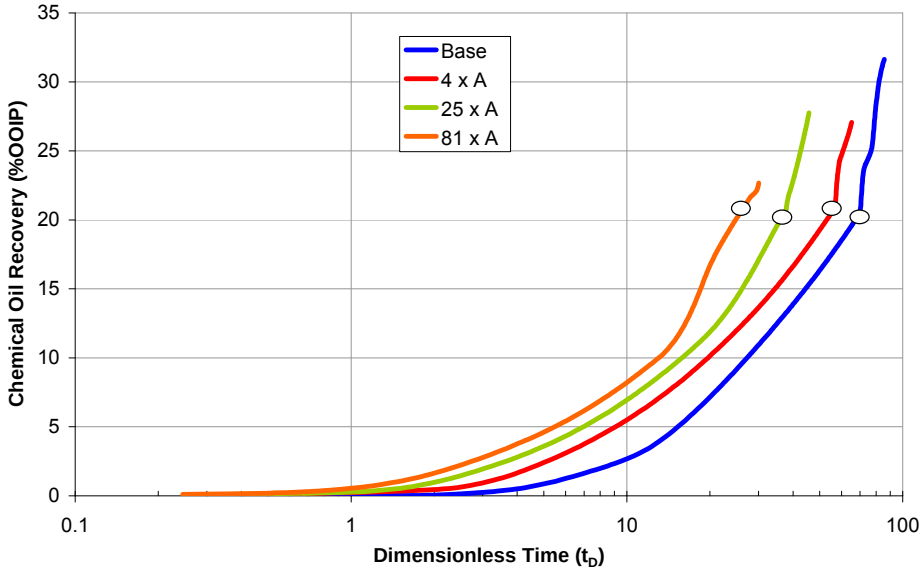

Figure 5.18: Dimensionless time by Ma et al. (1995) used for scaling the effect of matrix area on oil recovery.

Chapter 6: Chemical Flooding Module of GPAS

6.1 Introduction to GPAS

General purpose adaptive reservoir simulator (GPAS) is a fully implicit, parallel reservoir simulator developed at The Department of Petroleum and Geosystems Engineering in The University of Texas at Austin (Wang *et al*., 1997; Parashar *et al*., 1997; Wang *et al*., 1999; John *et al*., 2005; Marcondes *et al*., 2005 and Han *et al*., 2007). This simulator has corner point and unstructured grid options in addition to structured Cartesian grid (Marcondes *et al*., 2008). A list of physical modules is as follows:

1. Equation of state (EOS) compositional module. This module uses Peng-Robinson EOS to model miscible floods such as gas injection (Wang *et al*., 1999).
2. Chemical flooding module which is the focus of this study and models the injection of chemicals (surfactant and polymer) to recover the oil (Han *et al*., 2007 and Fathi Najafabadi *et al*., 2009). In this chapter a detailed explanation of this module is presented.
3. Thermal flooding module which uses the energy balance to model thermal flooding processes such as steam injection (Varavei and Sepehrnoori, 2009).
4. Dual-porosity module for modeling NFRs (Naimi-Tajdar *et al*., 2007 and Tarahhom *et al*., 2009).
5. Geomechanics module for modeling the effect of stress and strain on porosity and permeability (Pan *et al*., 2007 and Pan *et al*., 2009).
6. Asphaltene precipitation module for modeling the effect of asphaltene precipitation (Fazelipour *et al*., 2008).
7. Wellbore module for modeling the fluid flow in the wellbore (Pourafshary *et al*., 2008).

Figure 6.1 shows the structure of GPAS. The IPARS framework handles input of simulation parameters and parallel computation. It also allocates the memory required for

the global arrays. The gridding and discretization of the governing equations is then performed as instructed by the user in the input file. Different physical models such as EOS compositional and chemical flooding are then called as instructed by the user in the input file.

6.2 Chemical Flooding Module of GPAS

The first chemical flooding module of GPAS was published by John *et al*. (2005). This development was based on a hybrid approach where the material balance equation of the hydrocarbon components and water were solved implicitly and then the material balance equation of the aqueous components such as surfactant, polymer and salt were solved explicitly. This implementation had two important shortcomings from the formulation point of view:

1. The volume of the oil dissolved in the microemulsion (ME) phase was neglected.
2. The volume of the surfactant was neglected in the volume constraint equation.

Another important limitation of this development was that the oil/brine/ surfactant phase behavior was limited to Type I (Winsor, 1954) where an excess oleic phase is in equilibrium with a ME phase.

In 2007, Han *et al*. published a fully implicit chemical flooding module of GPAS which removed the two formulation limitations of the hybrid model (i.e. the volume of oil in the ME was considered and the volume of surfactant was taken into account in the volume constraint) but this development was still limited to Type I phase behavior. The contribution of the current development is to overcome this limitation and implement a comprehensive surfactant phase behavior in the chemical flooding module of GPAS.

The importance of this development is in the need for a fast and effective reservoir simulator capable of modeling robust chemical flooding designs such as salinity gradient design. Robust designs are those that are not sensitive to rock and/or fluid variations in the reservoir. Usually this is achieved by inducing a gradient or taking advantage of a natural one that shifts the oil/brine/surfactant phase behavior with the goal of keeping the

injected chemical slug close to optimum conditions as long as possible. This will ensure that each pore swept by the surfactant goes through the optimum conditions and its residual oil is mobilized. To model such designs, one would need comprehensive surfactant phase behavior. This capability already exists in UTCHEM chemical flooding simulator. The development in GPAS has advantages of being fully implicit and parallel for commercial scale simulations.

This chapter discusses in detail the newly developed fully implicit chemical flooding module of GPAS with comprehensive phase behavior. The governing equations and their derivatives are presented as well as physical property and phase behavior models.

6.2.1 Model Assumptions

The following assumptions are made in the development of the chemical flooding module of GPAS:

1. Isothermal conditions are assumed.
2. No free gas is present.
3. Corner plait point formulation is assumed where the excess oleic phase is pure oil and the excess aqueous phase does not contain any surfactants and dissolved hydrocarbons.
4. Symmetrical binodal curve formulation is based on modified Hand's rule (Hand, 1939; Treybal, 1963).
5. Effect of divalent cations and alcohols on surfactant phase behavior is not modeled.
6. Polymer has no effect on surfactant phase behavior.
7. The effect of pressure on surfactant phase behavior is neglected.
8. No surfactant is present in the reservoir at initial conditions.
9. Physical dispersion and molecular diffusion are neglected.

6.2.2 Overview of the Chemical Flooding Module

The phase behavior calculation is the same as that in UTCHEM and is based on the empirical observation that equilibrium phase concentration ratios are straight lines on a

log-log scale (Hand, 1939; Treybal, 1963). Physical property models describing the flow and transport of surfactant and polymer species are the same as those in UTCHEM. The physical property models include surfactant phase behavior, interfacial tension, capillary desaturation, viscosity, adsorption, and relative permeability as a function of trapping number. Polymer properties include viscosity as a function of polymer concentration, salinity and shear rate, permeability reduction, inaccessible pore volume, and adsorption.

Material balance equations (Eqs.6.3 and 6.4 discussed in Section 6.2.3.2) are solved for n_c hydrocarbon components, n_a aqueous components and water. Thus, the total number of components during the chemical flood would be $n_c + n_a + 1$. The unknowns in a gridblock are the number of moles per pore volume of $n_c + n_a + 1$ components, N_i, plus aqueous phase pressure, P. Hence we need $n_c + n_a + 2$ equations per gridblock to evaluate the unknowns. These equations are the material balance equations for $n_c + n_a + 1$ components and a volume constraint equation. A detailed description of these equations is described in this chapter. The non-linear system of equations is solved numerically using Newton's method. The details are discussed below.

Figure 6.2 shows the flowchart of the chemical flooding module. In the first timestep it is assumed that there are no surfactants in the reservoir. The whole simulation is performed by Integrated Parallel Accurate Reservoir Simulator (IPARS) (Parashar *et al*., 1997) framework. Section 6.2.5 gives more details about the framework. A subroutine called INFLUID0 is called once by the framework at the beginning of the simulation. This subroutine calculates the molar densities and number of moles of each component per pore volume based on the user input. A subroutine called XSTEP is then called by the framework to calculate the solution of each timestep based on the previous timestep solution and the changes induced by injection and production wells.

As shown in Fig.6.2, the first subroutine called by XSTEP is PROPIN. In this subroutine the vector of unknowns of each gridblock at the previous timestep (denoted as $\vec{x}$) is assumed to be the solution at n^{th} Newton iteration (denoted as $\vec{x}^n$). Just for one time

before the Newton iteration starts, this $\vec{x}^n$ is assumed to be the solution to the Newton's iteration (denoted as $\vec{x}^{new}$). The XSTEP calls a subroutine called TRAPN to calculate the trapping number for each phase in each gridblock. PROP subroutine is then called by XSTEP where residual saturations, relative permeability curves, and viscosities are calculated. XSTEP then calls the XWELL subroutine where the flow rates and bottomhole pressures of each well are calculated. Then subroutines TRANSPORT and RESIDUALS calculate the residual of material balance equations for each component (Eq.6.5) and the residual of volume constraint equation (Eq.6.1) respectively. XSTEP checks for convergence of the solution, meaning that whether or not the residuals are close enough to zero. Based on the outcome of this check two routes may be taken. If the solution is converged, then the iteration stops and this solution vector $\vec{x}^{new}$ is declared as the true solution for the current timestep. Next, subroutines SURFACE and AVERAGE are called to calculate the flow rates at surface conditions and the average reservoir properties respectively. The loop for obtaining the solution for the next timestep is then started by calling the PROPIN subroutine (Fig.6.2).

On the other hand, if the solution is not converged, JACOBIAN subroutine is called by XSTEP to construct the Jacobian at $\vec{x}^{old}$ where $\vec{x}^{old} = \vec{x}^{new}$. After the calculation of the Jacobian matrix, the SOLVER subroutine is called to solve the linear system of equations using the PETSc linear solver (Balay *et al*., 1997) and obtain the new solution at the current Newton's iteration, $\vec{x}^{new}$. Section 6.3 describes the solution procedure in more details. After obtaining the new vector of unknowns, $\vec{x}^{new}$, the molar densities, mole fractions of each component in each phase, IFT and the new phase saturations are calculated in XIMPSURF subroutine. This subroutine uses the Hand's rule to calculate volumetric concentrations of the brine, oil and surfactant pseudo-components in each phase and converts them to mole fractions. The convergence is checked once again and the iteration is repeated until the solution converges.

6.2.3 Governing Equations

6.2.3.1 The Volume Constraint Equation

At each time, the sum of volume of all volume-occupying components should be the same as the pore volume. The total pore volume consists of the fluid volumes and the adsorbed surfactant volume and the volume occupying components are water, surfactant, and oleic components. This constraint is defined as follows:

$$R_V = \frac{N_{water}}{\xi_{water}} + \frac{N_{surf}}{\xi_{surf}} + \frac{1}{\xi_o}\sum_{i=1}^{n_c} N_i - 1.0 \qquad \text{Eq.6.1}$$

InEq.6.1, the molar density of oil component is assumed to be the same as one of oleic phase (ξ_o). The residual of volume constraint is only dependent on primary variables (or unknowns) at its own gridblock. The primary variables are $V = (N_1, \ldots, N_{n_c}, N_{n_{c+1}}, \ldots, N_{n_c+n_a}, P, N_{water})$ at new time level. Therefore, derivatives of the residual can be easily obtained as follows:

$$\frac{\partial R_V}{\partial V} = \begin{cases} \dfrac{1}{\xi_o} - \dfrac{1}{\xi_o^{\,2}}\dfrac{\partial \xi_2}{\partial V}\displaystyle\sum_{i=1}^{n_c} N_i \quad if \quad V = N_1, \ldots N_{n_c} \\ \dfrac{1}{\xi_{water}} \quad if \quad V = N_{water} \\ \dfrac{1}{\xi_{surf}} \quad if \quad V = N_{surf} \\ -\dfrac{N_{water}}{\xi_{water}^{\,2}}\xi_{water}{}^{o} c_{water}{}^{o} - \dfrac{N_{surf}}{\xi_{surf}^{\,2}}\xi_{surf}{}^{o} c_{surf}{}^{o} - \dfrac{1}{\xi_o^{\,2}}\dfrac{\partial \xi_2}{\partial V}\displaystyle\sum_{i=1}^{n_c} N_i \quad if \quad V = P \\ 0 \quad if \quad V = N_{poly}, \; N_{salt}, \; or \; N_{trac} \end{cases} \qquad \text{Eq.6.2}$$

6.2.3.2 Material Balance Equations

Since a complete oil/brine/surfactant phase behavior model as a function of salinity is considered in this work, up to 3 liquid phases may coexist. This leads to 5 different possibilities for phases depending on the concentration of surfactant, oil, and electrolytes:

1. Aqueous and oleic phases coexist.

2. ME and oleic phases coexist.
3. ME and aqueous phases coexist.
4. Three phases (aqueous, ME and oleic) coexist.
5. Single ME, oil, or water phase.

It should be noted that the gaseous phase is not currently considered in the chemical module. The aqueous and oleic components can partition into the ME phase. The surfactant is assumed to be only in the aqueous phase if its concentration is below critical micelle concentration (CMC) and only in the ME phase if its concentration is above CMC. It is also assumed that oleic components cannot partition into excess aqueous phase. Using these assumptions and neglecting physical dispersion, the material balance equation for any hydrocarbon component is as follows:

$$V_b \frac{\partial}{\partial t}\left(\phi N_i\right) - V_b \vec{\nabla} \bullet \left(\xi_2 \frac{\vec{\vec{k}}k_{r2}}{\mu_2} x_{i2} \left(\nabla P_2 - \gamma_2 \nabla D\right) + \xi_3 \frac{\vec{\vec{k}}k_{r3}}{\mu_3} x_{i3} \left(\nabla P_3 - \gamma_3 \nabla D\right) \right) = q_i \qquad \text{Eq.6.3}$$

$$i = 1 \quad to \quad n_c$$

where subscripts 2 and 3 refer to oleic and ME phases respectively. The number of hydrocarbon components is denoted as n_c.

The material balance equation for the aqueous components such as water, surfactant, salt, polymer, and tracer is described as follows:

$$V_b \frac{\partial}{\partial t}\left(\phi N_i\right) - V_b \vec{\nabla} \bullet \left(\xi_1 \frac{\vec{\vec{k}}k_{r1}}{\mu_1} x_{i1} \left(\nabla P_1 - \gamma_1 \nabla D\right) + \xi_3 \frac{\vec{\vec{k}}k_{r3}}{\mu_3} x_{i3} \left(\nabla P_3 - \gamma_3 \nabla D\right) \right) = q_i \qquad \text{Eq.6.4}$$

$$i = n_c + 1 \quad to \quad n_c + n_a + 1$$

where subscripts 1 and 3 refer to aqueous and ME phases, respectively. The number of aqueous components except water is denoted as n_a and water is last component denoted by n_c+ n_a+1.

Based on the above, the residual of the material balance equation for each component can be written as follows:

$$R_{m_i(I,J,K)} = \left[\frac{V_b}{\Delta t}\left(\left(\phi N_i\right)^{n+1} - \left(\phi N_i\right)^{n}\right)\right]_{(I,J,K)} + \left(F_{i(I+1/2,J,K)} - F_{i(I-1/2,J,K)}\right)^{n+1} + \left(F_{i(I,J+1/2,K)} - F_{i(I,J-1/2,K)}\right)^{n+1} + \left(F_{i(I,J,K+1/2)} - F_{i(I,J,K-1/2)}\right)^{n+1} - q_{i(I,J,K)} \quad \text{Eq.6.5}$$

where

$$\phi = \phi_r\left(1 + c_f\left(P - P^o\right)\right) \quad \text{Eq.6.6}$$

For Cartesian grids, the flux of each component is calculated over each of the faces of a gridblock if that face is open to flow. *I*, *J* and *K* indicate the position of the gridblock in the *x*, *y* and *z* directions respectively. The $F_{i(I+1/2,J,K)}$ in Eq.6.5 denotes the flux of component *i* in the x direction and between *I* and *I+1* gridblocks. These fluxes can be further expanded as follows:

$$F_{i(I+1/2,J,K)} = \begin{cases} T_{i2(I+1/2,J,K)} v_{2(I+1/2,J,K)} + T_{i3(I+1/2,J,K)} v_{3(I+1/2,J,K)} \\ (hydrocarbon - components) \\ T_{i1(I+1/2,J,K)} v_{1(I+1/2,J,K)} + T_{i3(I+1/2,J,K)} v_{3(I+1/2,J,K)} \\ (water - components) \end{cases} \quad \text{Eq.6.7}$$

$$F_{i(I-1/2,J,K)} = \begin{cases} T_{i2(I-1/2,J,K)} v_{2(I-1/2,J,K)} + T_{i3(I-1/2,J,K)} v_{3(I-1/2,J,K)} \\ (hydrocarbon - components) \\ T_{i1(I-1/2,J,K)} v_{1(I-1/2,J,K)} + T_{i3(I-1/2,J,K)} v_{3(I-1/2,J,K)} \\ (water - components) \end{cases} \quad \text{Eq.6.8}$$

$$F_{i(I,J+1/2,K)} = \begin{cases} T_{i2(I,J+1/2,K)} v_{2(I,J+1/2,K)} + T_{i3(I,J+1/2,K)} v_{3(I,J+1/2,K)} \\ (hydrocarbon - components) \\ T_{i1(I,J+1/2,K)} v_{1(I,J+1/2,K)} + T_{i3(I,J+1/2,K)} v_{3(I,J+1/2,K)} \\ (water - components) \end{cases} \quad \text{Eq.6.9}$$

$$F_{i(I,J-1/2,K)} = \begin{cases} T_{i2(I,J-1/2,K)} v_{2(I,J-1/2,K)} + T_{i3(I,J-1/2,K)} v_{3(I,J-1/2,K)} \\ (hydrocarbon - components) \\ T_{i1(I,J-1/2,K)} v_{1(I,J-1/2,K)} + T_{i3(I,J-1/2,K)} v_{3(I,J-1/2,K)} \\ (water - components) \end{cases} \quad \text{Eq.6.10}$$

$$F_{i(I,J,K+1/2)} = \begin{cases} T_{i2(I,J,K+1/2)} v_{2(I,J,K+1/2)} + T_{i3(I,J,K+1/2)} v_{3(I,J,K+1/2)} \\ (hydrocarbon - components) \\ T_{i1(I,J,K+1/2)} v_{1(I,J,K+1/2)} + T_{i3(I,J,K+1/2)} v_{3(I,J,K+1/2)} \\ (water - components) \end{cases} \quad \text{Eq.6.11}$$

$$F_{i(I,J,K-1/2)} = \begin{cases} T_{i2(I,J,K-1/2)} v_{2(I,J,K-1/2)} + T_{i3(I,J,K-1/2)} v_{3(I,J,K-1/2)} \\ (hydrocarbon - components) \\ T_{i1(I,J,K-1/2)} v_{1(I,J,K-1/2)} + T_{i3(I,J,K-1/2)} v_{3(I,J,K-1/2)} \\ (water - components) \end{cases} \quad \text{Eq.6.12}$$

where T_{ij} is chosen based on the upstream direction as follows:

$$T_{ij(I+1/2,J,K)} = \begin{cases} T_{ij(I,J,K)} & if \left(v_{j(I+1/2,J,K)} \geq 0 \right) \\ T_{ij(I+1,J,K)} & if \left(v_{j(I+1/2,J,K)} < 0 \right) \end{cases} \quad \text{Eq.6.13}$$

$$T_{ij(I-1/2,J,K)} = \begin{cases} T_{ij(I-1,J,K)} & if \left(v_{j(I-1/2,J,K)} \geq 0 \right) \\ T_{ij(I,J,K)} & if \left(v_{j(I-1/2,J,K)} < 0 \right) \end{cases} \quad \text{Eq.6.14}$$

$$T_{ij(I,J+1/2,K)} = \begin{cases} T_{ij(I,J,K)} & if \left(v_{j(I,J+1/2,K)} \geq 0 \right) \\ T_{ij(I,J+1,K)} & if \left(v_{j(I,J+1/2,K)} < 0 \right) \end{cases} \quad \text{Eq.6.15}$$

$$T_{ij(I,J-1/2,K)} = \begin{cases} T_{ij(I,J-1,K)} & if \left(v_{j(I,J-1/2,K)} \geq 0 \right) \\ T_{ij(I,J,K)} & if \left(v_{j(I,J-1/2,K)} < 0 \right) \end{cases} \quad \text{Eq.6.16}$$

$$T_{ij(I,J,K+1/2)} = \begin{cases} T_{ij(I,J,K)} & if \left(v_{j(I,J,K+1/2)} \geq 0 \right) \\ T_{ij(I,J,K+1)} & if \left(v_{j(I,J,K+1/2)} < 0 \right) \end{cases} \quad \text{Eq.6.17}$$

$$T_{ij(I,J,K-1/2)} = \begin{cases} T_{ij(I,J,K-1)} & if \left(v_{j(I,J,K-1/2)} \geq 0 \right) \\ T_{ij(I,J,K)} & if \left(v_{j(I,J,K-1/2)} < 0 \right) \end{cases} \quad \text{Eq.6.18}$$

where T_{ij} and v_j for each gridblock are obtained using the properties of that gridblock:

$$T_{ij(I,J,K)} = \left(\xi_j \frac{k_{rj}}{\mu_j} x_{ij} \right)_{(I,J,K)} \quad \text{Eq.6.19}$$

$$T_{ij(I+1,J,K)} = \left(\xi_j \frac{k_{rj}}{\mu_j} x_{ij} \right)_{(I+1,J,K)} \quad \text{Eq.6.20}$$

$$T_{ij(I-1,J,K)} = \left(\xi_j \frac{k_{rj}}{\mu_j} x_{ij} \right)_{(I-1,J,K)} \quad \text{Eq.6.21}$$

$$T_{ij(I,J+1,K)} = \left(\xi_j \frac{k_{rj}}{\mu_j} x_{ij} \right)_{(I,J+1,K)} \quad \text{Eq.6.22}$$

$$T_{ij(I,J-1,K)} = \left(\xi_j \frac{k_{rj}}{\mu_j} x_{ij} \right)_{(I,J-1,K)} \quad \text{Eq.6.23}$$

$$T_{ij(I,J,K+1)} = \left(\xi_j \frac{k_{rj}}{\mu_j} x_{ij} \right)_{(I,J,K+1)} \quad \text{Eq.6.24}$$

$$T_{ij(I,J,K-1)} = \left(\xi_j \frac{k_{rj}}{\mu_j} x_{ij} \right)_{(I,J,K-1)} \quad \text{Eq.6.25}$$

$$v_{j(I+1/2,J,K)} = -\widetilde{k}_{j(I+1/2,J,K)} \left(\left(P_j - \gamma_j D \right)_{(I+1,J,K)} - \left(P_j - \gamma_j D \right)_{(I,J,K)} \right) \quad \text{Eq.6.26}$$

$$v_{j(I-1/2,J,K)} = -\widetilde{k}_{j(I-1/2,J,K)} \left(\left(P_j - \gamma_j D \right)_{(I,J,K)} - \left(P_j - \gamma_j D \right)_{(I-1,J,K)} \right) \quad \text{Eq.6.27}$$

$$v_{j(I,J+1/2,K)} = -\widetilde{k}_{j(I,J+1/2,K)} \left(\left(P_j - \gamma_j D \right)_{(I,J+1,K)} - \left(P_j - \gamma_j D \right)_{(I,J,K)} \right) \quad \text{Eq.6.28}$$

$$v_{j(I,J-1/2,K)} = -\widetilde{k}_{j(I,J-1/2,K)} \left(\left(P_j - \gamma_j D \right)_{(I,J,K)} - \left(P_j - \gamma_j D \right)_{(I,J-1,K)} \right) \quad \text{Eq.6.29}$$

$$v_{j(I,J,K+1/2)} = -\widetilde{k}_{j(I,J,K+1/2)} \left(\left(P_j - \gamma_j D \right)_{(I,J,K+1)} - \left(P_j - \gamma_j D \right)_{(I,J,K)} \right) \quad \text{Eq.6.30}$$

$$v_{j(I,J,K-1/2)} = -\widetilde{k}_{j(I,J,K-1/2)} \left(\left(P_j - \gamma_j D \right)_{(I,J,K)} - \left(P_j - \gamma_j D \right)_{(I,J,K-1)} \right) \quad \text{Eq.6.31}$$

where

$$\widetilde{k}_{(I+1/2,J,K)} = \frac{2\Delta y_{(I,J,K)} \Delta z_{(I,J,K)} k_{x(I,J,K)} k_{x(I+1,J,K)}}{\Delta x_{(I+1,J,K)} k_{x(I,J,K)} + \Delta x_{(I,J,K)} k_{x(I+1,J,K)}} \quad \text{Eq.6.32}$$

$$\widetilde{k}_{(I-1/2,J,K)} = \frac{2\Delta y_{(I,J,K)} \Delta z_{(I,J,K)} k_{x(I,J,K)} k_{x(I-1,J,K)}}{\Delta x_{(I-1,J,K)} k_{x(I,J,K)} + \Delta x_{(I,J,K)} k_{x(I-1,J,K)}} \quad \text{Eq.6.33}$$

$$\tilde{k}_{(I,J+1/2,K)} = \frac{2\Delta x_{(I,J,K)}\Delta z_{(I,J,K)}k_{y(I,J,K)}k_{y(I,J+1,K)}}{\Delta y_{(I,J+1,K)}k_{y(I,J,K)} + \Delta y_{(I,J,K)}k_{y(I,J+1,K)}} \quad \text{Eq.6.34}$$

$$\tilde{k}_{(I,J-1/2,K)} = \frac{2\Delta x_{(I,J,K)}\Delta z_{(I,J,K)}k_{x(I,J,K)}k_{x(I,J-1,K)}}{\Delta y_{(I,J-1,K)}k_{x(I,J,K)} + \Delta y_{(I,J,K)}k_{x(I,J-1,K)}} \quad \text{Eq.6.35}$$

$$\tilde{k}_{(I,J,K+1/2)} = \frac{2\Delta x_{(I,J,K)}\Delta y_{(I,J,K)}k_{z(I,J,K)}k_{z(I,J,K+1)}}{\Delta z_{(I,J,K+1)}k_{z(I,J,K)} + \Delta z_{(I,J,K)}k_{z(I,J,K+1)}} \quad \text{Eq.6.36}$$

$$\tilde{k}_{(I,J,K-1/2)} = \frac{2\Delta x_{(I,J,K)}\Delta y_{(I,J,K)}k_{x(I,J,K)}k_{x(I,J,K-1)}}{\Delta z_{(I,J,K-1)}k_{x(I,J,K)} + \Delta z_{(I,J,K)}k_{x(I,J,K-1)}} \quad \text{Eq.6.37}$$

To obtain the residual of material balance equation (Eq.6.5) for each component, one needs to calculate the flow rate of that component in the injection and production wells. The flow rate of water, q_{water}, for a well on injection rate constraint is calculated based on the flow rate of water at surface conditions $q_{water}\big|_{surface}$, the productivity index (PI) of the gridblock, $\left(PI_t\right)_z$, and the sum of the productivity indices of all of the well blocks in that injector as follows:

$$q_{water(I,J,K)} = \frac{q_{water}\big|_{surface}\left(PI_t\right)_z}{\sum_{m=z_t}^{z_b}\left(PI_t\right)_m} \quad \text{Eq.6.38}$$

where PI of each gridblock, ,$\left(PI_t\right)_z$ is the sum of the PIs of all phases present in that gridblock:

$$\left(PI_t\right)_z = \sum_{j=1}^{3}\left(PI_j\right)_z \quad \text{Eq.6.39}$$

where the PI for each phase, $\left(PI_j\right)_z$, is calculated as follows:

$$\left(PI_j\right)_z = c_z\left(\frac{k_{rj}}{\mu_j}\right)_z \quad \text{Eq.6.40}$$

where

$$c_z = \frac{\sqrt{k_x k_y}\Delta z}{25.14872\ln\left(r_o/r_w\right)} \quad \text{Eq.6.41}$$

The derivatives of Eq.6.38 are obtained as follows:

$$\frac{\partial q_i}{\partial V} = \frac{q_{water}\big|_{surface}}{A^2}(A-a)\frac{\partial a}{\partial V} \qquad \text{Eq.6.42}$$

Eq.6.42

where

$$A = \sum_{m=z_t}^{z_b} (PI_t)_m$$

$$a = (PI_t)_z$$

$$\frac{\partial a}{\partial V} = c_z \sum_{j=1}^{3} \left(\frac{1}{\mu_j}\frac{\partial k_{rj}}{\partial V} - \frac{k_{rj}}{\mu_j^2}\frac{\partial \mu_j}{\partial V} \right)$$

The flow rate of other aqueous components for a constant rate injection well is calculated based on the water injection rate as follows:

$$q_{i(I,J,K)} = \begin{cases} c_{i,inj}\,(q_{water})_{(I,J,K)}\,\dfrac{\xi_{surf}}{\xi_{water}}\Big|_{surface} & if \quad i = surf \\ \dfrac{c_{i,inj}}{100}(q_{water})_{(I,J,K)}\,\dfrac{M_{water}}{M_{poly}} & if \quad i = poly \\ \dfrac{c_{i,inj}\,(q_{water})_{(I,J,K)}}{16.037\,\xi_{water}\big|_{surface}} & if \quad i = salt \quad or \quad tracer \end{cases} \qquad \text{Eq.6.43}$$

Derivatives of Eq.6.43 are calculated as below.

$$\frac{\partial q_{i(I,J,K)}}{\partial V} = \begin{cases} \dfrac{\partial q_{water}}{\partial V}\,c_{i,inj}\,\dfrac{\xi_{surf}}{\xi_{water}}\Big|_{surface} & if \quad i = surf \\ \dfrac{\partial q_{water}}{\partial V}\,\dfrac{c_{i,inj}}{100}\,\dfrac{M_{water}}{M_{poly}} & if \quad i = poly \\ \dfrac{\partial q_{water}}{\partial V}\,\dfrac{c_{i,inj}}{16.037\,\xi_{water}\big|_{surface}} & if \quad i = salt \quad or \quad tracer \end{cases} \qquad \text{Eq.6.44}$$

The source term for a constant bottomhole pressure injection well is

$$q_{i(I,J,K)} = \begin{cases} \dfrac{c_z}{1+c_{surf,inj}} \xi_{water}\big|_{inj} \left(\dfrac{k_{r1}}{\mu_1}\right)_z \left(P_{wf} - P_1\right)_z & if \quad i = water \\ c_{i,inj} \left(q_{water}\right)_{(I,J,K)} \left.\dfrac{\xi_{surf}}{\xi_{water}}\right|_{surface} & if \quad i = surf \\ \dfrac{c_{i,inj}}{100} \left(q_{water}\right)_{(I,J,K)} \dfrac{M_{water}}{M_{poly}} & if \quad i = poly \\ \dfrac{c_{i,inj} \left(q_{water}\right)_{(I,J,K)}}{16.037\, \xi_{water}\big|_{surface}} & if \quad i = salt \quad or \quad tracer \end{cases} \qquad \text{Eq.6.45}$$

Derivatives of the water injection rate for a pressure constraint well are as follows:

$$\frac{\partial q_{water}}{\partial V} = \begin{cases} \dfrac{c_z}{1+c_{surf,inj}} \xi_{water}\Big|_{inj} \left(P_{wf} - P\right)\left(\dfrac{1}{\mu_1}\dfrac{\partial k_{r1}}{\partial V} - \dfrac{k_{r1}}{\mu_1^2}\dfrac{\partial \mu_1}{\partial V}\right) & \left(V \neq P\right) \\ \dfrac{c_z}{1+c_{surf,inj}} \xi_{water}\Big|_{inj} \left[\left(P_{wf} - P\right)\left(\dfrac{1}{\mu_1}\dfrac{\partial k_{r1}}{\partial V} - \dfrac{k_{r1}}{\mu_1^2}\dfrac{\partial \mu_1}{\partial V}\right) - \dfrac{k_{r1}}{\mu_1}\right] & \left(V = P\right) \end{cases} \qquad \text{Eq.6.46}$$

The derivatives of injection rates of other components mentioned in Eq.6.45 are calculated below.

$$\frac{\partial q_{i(I,J,K)}}{\partial V} = \begin{cases} \dfrac{\partial q_{water}}{\partial V} c_{i,inj} \left.\dfrac{\xi_{surf}}{\xi_{water}}\right|_{surface} & if \quad i = surf \\ \dfrac{\partial q_{water}}{\partial V} \dfrac{c_{i,inj}}{100} \dfrac{M_{water}}{M_{poly}} & if \quad i = poly \\ \dfrac{\partial q_{water}}{\partial V} \dfrac{c_{i,inj}}{16.037\, \xi_{water}\big|_{surface}} & if \quad i = salt \quad or \quad tracer \end{cases} \qquad \text{Eq.6.47}$$

For a constant pressure production well the sink term and its derivatives would be:

$$\sum_{j=1}^{3} \left(\left(\xi_j x_{ij} PI_j\right)_z \left(P_{wf} - P_j\right)_z\right) \quad for \quad all \quad components \qquad \text{Eq.6.48}$$

$$\frac{\partial q_i}{\partial V} = \begin{cases} c_z \left(P_{wf} - P\right) \displaystyle\sum_{j=1}^{3} \frac{\partial}{\partial V}\left(\xi_j \frac{k_{rj}}{\mu_j} x_{ij}\right) & \left(V \neq P\right) \\ c_z \displaystyle\sum_{j=1}^{3} \left(\left(P_{wf} - P\right)\frac{\partial}{\partial V}\left(\xi_j \frac{k_{rj}}{\mu_j} x_{ij}\right) - \xi_j \frac{k_{rj}}{\mu_j} x_{ij}\right) & \left(V = P\right) \end{cases} \qquad \text{Eq.6.49}$$

6.2.3.3 Accumulation Term

The accumulation term in residual of material balance equations (Eq.6.5) is only dependant on primary variables at its own gridblock. Therefore its derivative is calculated as follows:

$$\frac{\partial}{\partial V}\left(\frac{V_b}{\Delta t}\left(\left(\phi N_i\right)^{n+1}-\left(\phi N_i\right)^{n}\right)\right)_{(I,J,K)}=\begin{cases}\left(\frac{V_b}{\Delta t}\phi^{n+1}\right)_{(I,J,K)} & if \quad V=N_i\\ \left(\frac{V_b}{\Delta t}\phi_r c_f N_i^{\,n+1}\right)_{(I,J,K)} & if \quad V=P\end{cases} \qquad \text{Eq.6.50}$$

6.2.3.4 Flux Term

The derivatives of flux term in residual of material balance equation (Eq.6.5) are more complicated because the flux term is dependent on primary variables at six neighbor gridblocks as well as those at its own gridblock. Here we derive the derivative of $F_{i(I+1/2,J,K)}$ for an aqueous component only i.e. the flux between (I,J,K) and (I+1,J,K) gridblocks. The derivatives of the remaining terms and the derivatives of flux for hydrocarbon components can be derived following similar procedures. Several indices are omitted for simplicity.

$$\begin{aligned}\frac{\partial}{\partial V}\left(F_{i(I+1/2)}\right)&=\frac{\partial}{\partial V}\left(T_{i1(I+1/2)}v_{1(I+1/2)}+T_{i3(I+1/2)}v_{3(I+1/2)}\right)\\&=\frac{\partial}{\partial V}\left(T_{i1(I+1/2)}\right)v_{1(I+1/2)}+\frac{\partial}{\partial V}\left(v_{1(I+1/2)}\right)T_{i1(I+1/2)}\\&\quad+\frac{\partial}{\partial V}\left(T_{i4(I+1/2)}\right)v_{3(I+1/2)}+\frac{\partial}{\partial V}\left(v_{3(I+1/2)}\right)T_{i3(I+1/2)}\end{aligned} \qquad \text{Eq.6.51}$$

If *I+1* gridblock is upstream cell, the above equation is rewritten as

$$
\begin{aligned}
&\frac{\partial}{\partial V}\left(T_{i1(I+1/2)}\right)v_{1(I+1/2)}+\frac{\partial}{\partial V}\left(v_{1(I+1/2)}\right)T_{i1(I+1/2)}\\
&+\frac{\partial}{\partial V}\left(T_{i3(I+1/2)}\right)v_{3(I+1/2)}+\frac{\partial}{\partial V}\left(v_{3(I+1/2)}\right)T_{i3(I+1/2)}\\
&\quad=\frac{\partial}{\partial V}\left(T_{i1(I+1)}\right)v_{1(I+1/2)}+\frac{\partial}{\partial V}\left(v_{1(I+1/2)}\right)T_{i1(I+1)}\\
&\qquad+\frac{\partial}{\partial V}\left(T_{i3(I+1)}\right)v_{3(I+1/2)}+\frac{\partial}{\partial V}\left(v_{3(I+1/2)}\right)T_{i3(I+1)}\\
&\quad=\frac{\partial}{\partial V}\left(\left(\xi_1\frac{k_{r1}}{\mu_1}x_{i1}\right)_{(I+1)}\right)v_{1(I+1/2)}+\frac{\partial}{\partial V}\left(v_{1(I+1/2)}\right)\left(\xi_1\frac{k_{r1}}{\mu_1}x_{i1}\right)_{(I+1)}\\
&\qquad+\frac{\partial}{\partial V}\left(\left(\xi_3\frac{k_{r4}}{\mu_4}x_{i3}\right)_{(I+1)}\right)v_{3(I+1/2)}+\frac{\partial}{\partial V}\left(v_{3(I+1/2)}\right)\left(\xi_3\frac{k_{r3}}{\mu_4}x_{i3}\right)_{(I+1)}
\end{aligned}
\qquad \text{Eq.6.52}
$$

where

$$
\begin{aligned}
&\frac{\partial}{\partial V}\left(\left(\xi_j\frac{k_{rj}}{\mu_j}x_{ij}\right)_{(I+1)}\right)\\
&=\begin{cases}
\dfrac{\partial\xi_{j_{(I+1)}}}{\partial V}\left(\dfrac{k_{rj}}{\mu_j}x_{ij}\right)_{(I+1)}+\dfrac{\partial k_{rj_{(I+1)}}}{\partial V}\left(\xi_j\dfrac{x_{ij}}{\mu_j}\right)_{(I+1)}+\\
\quad\dfrac{\partial x_{ij_{(I+1)}}}{\partial V}\left(\xi_j\dfrac{k_{ij}}{\mu_j}\right)_{(I+1)}-\dfrac{\partial\mu_{j_{(I+1)}}}{\partial V}\left(\xi_j\dfrac{k_{rj}x_{ij}}{\mu_j{}^2}\right)_{(I+1)} & \text{if}\quad V=V_{(I+1)}\\
0 \qquad\qquad \text{if}\quad \text{or}\quad V_I &
\end{cases}
\end{aligned}
\qquad \text{Eq.6.53}
$$

If *I* gridblock is upstream, then

$$
\begin{aligned}
&\frac{\partial}{\partial V}\left(T_{i1(I+1/2)}\right)v_{1(I+1/2)}+\frac{\partial}{\partial V}\left(v_{1(I+1/2)}\right)T_{i1(I+1/2)}\\
&+\frac{\partial}{\partial V}\left(T_{i3(I+1/2)}\right)v_{3(I+1/2)}+\frac{\partial}{\partial V}\left(v_{3(I+1/2)}\right)T_{i3(I+1/2)}\\
&=\frac{\partial}{\partial V}\left(T_{i1(I)}\right)v_{1(I+1/2)}+\frac{\partial}{\partial V}\left(v_{1(I+1/2)}\right)T_{i1(I)}\\
&\quad+\frac{\partial}{\partial V}\left(T_{i3(I)}\right)v_{3(I+1/2)}+\frac{\partial}{\partial V}\left(v_{3(I+1/2)}\right)T_{i3(I)} \qquad \text{Eq.6.54}\\
&=\frac{\partial}{\partial V}\left(\left(\xi_1\frac{k_{r1}}{\mu_1}x_{i1}\right)_{(I)}\right)v_{1(I+1/2)}+\frac{\partial}{\partial V}\left(v_{1(I+1/2)}\right)\left(\xi_1\frac{k_{r1}}{\mu_1}x_{i1}\right)_{(I)}\\
&\quad+\frac{\partial}{\partial V}\left(\left(\xi_3\frac{k_{r3}}{\mu_3}x_{i3}\right)_{(I)}\right)v_{3(I+1/2)}+\frac{\partial}{\partial V}\left(v_{3(I+1/2)}\right)\left(\xi_3\frac{k_{r3}}{\mu_3}x_{i3}\right)_{(I)}
\end{aligned}
$$

where

$$
\begin{aligned}
&\frac{\partial}{\partial V}\left(\left(\xi_j\frac{k_{rj}}{\mu_j}x_{ij}\right)_{(I)}\right)\\
&=\begin{cases}
\dfrac{\partial\xi_{j_{(I)}}}{\partial V}\left(\dfrac{k_{rj}}{\mu_j}x_{ij}\right)_{(I)}+\dfrac{\partial k_{rj_{(I)}}}{\partial V}\left(\xi_j\dfrac{x_{ij}}{\mu_j}\right)_{(I)}+\\
\quad\dfrac{\partial x_{ij_{(I)}}}{\partial V}\left(\xi_j\dfrac{k_{ij}}{\mu_j}\right)_{(I)}-\dfrac{\partial\mu_{j_{(I)}}}{\partial V}\left(\xi_j\dfrac{k_{rj}x_{ij}}{\mu_j^{\,2}}\right)_{(I)} & \text{if}\quad V=V_{(I)}\\
0 \qquad\qquad \text{if}\quad V=V_{(I)}\quad \text{or}\quad V_{(I+1)}
\end{cases} \qquad \text{Eq.6.55}
\end{aligned}
$$

6.2.3.4 Physical Properties

Physical properties such as molar density, relative permeability, viscosity, and mole fraction of each phase and their derivatives can be calculated based on values of dependent parameters in the following order:

$$\tilde{C}_1, C_1, \tilde{C}_2, C_2, \tilde{C}_3, C_3$$
$$\downarrow$$
$$C_{SE}$$
$$\downarrow$$
$${C_3}^f, {C_4}^f$$
$$\downarrow$$
$${N_{surf}}^f, {N_{poly}}^f$$
$$\downarrow$$
$$C_3$$
$$\downarrow$$
$$C_{11}, C_{12}, C_{13}, C_{21}, C_{22}, C_{23}, C_{31}, C_{22}, C_{33}$$
$$\downarrow$$
$$C_{43}, C_{41}, C_{51}, C_{53}$$
$$\downarrow$$
$$R_{23},\ R_{13}$$
$$\downarrow$$
$$\xi_j$$
$$\downarrow$$
$$N_{oil,3}, N_{T,3}, x_{ij}$$
$$\downarrow$$
$$\sigma_{13}, \sigma_{23}, N_{T_j}, S_j, S_{jr}, k_{rj}$$
$$\downarrow$$
$$\mu_j$$

Overall and Fluid Concentrations

Oil/brine/surfactant phase behavior is calculated using the total fluid concentration of oil, brine and surfactant pseudocomponents. The total fluid concentrations are calculated from the overall and adsorbed surfactant concentrations.

The overall concentration of water in each gridblock is calculated as follows:

$$\widetilde{C}_1 = \frac{N_{water}}{\xi_{water}} \qquad \text{Eq.6.56}$$

where

$$\xi_{water} = \xi^o_{water}\left(1 + c^o_{water}\left(P - P^o\right)\right) \qquad \text{Eq.6.57}$$

The derivatives of overall water concentration are then calculated as follows:

$$\frac{\partial \widetilde{C}_1}{\partial N_i} = \begin{cases} \dfrac{1}{\xi_{water}} & if \quad i = water \\ 0 \quad if \quad i \neq water \end{cases} \qquad \text{Eq.6.58}$$

$$\frac{\partial \tilde{C}_1}{\partial P} = -\frac{N_{water}}{\xi_{water}^2}\left(\xi_{water}^o c_{water}^o\right) \qquad \text{Eq.6.59}$$

$$\frac{\partial \tilde{C}_1}{\partial P} = -\frac{N_{water}}{\xi_{water}^2}\left(\xi_{water}^o c_{water}^o\right) \qquad \text{Eq.6.59}$$

The total in-fluid concentration of water is calculated as follows:

$$C_1 = \left(\frac{N_{water}}{\xi_{water}}\right)\frac{1}{1-\hat{C}_3} \approx \left(\frac{N_{water}}{\xi_{water}}\right) \qquad \text{Eq.6.60}$$

where $\hat{C}_3$ is the adsorbed surfactant concentration. Since the adsorbed surfactant concentration is normally very small compared to the pore volume, the derivatives of fluid concentration of water C_1 could be assumed to be the same as those of its overall concentration, $\widetilde{C}_1$. Overall concentration of oil and its derivatives are calculated as follows:

$$\widetilde{C}_2 = \frac{1}{\xi_o}\sum_{i=1}^{n_c} N_i \qquad \text{Eq.6.61}$$

$$\frac{\partial \widetilde{C}_2}{\partial N_i} = \begin{cases} \dfrac{1}{\xi_o}\left(1 - \dfrac{1}{\xi_o}\dfrac{\partial \xi_o}{\partial N_i}\sum_{i=1}^{n_c} N_i\right) & if \quad for \quad hydrocarbons \\ 0 \quad for \quad aqueous \quad components \end{cases} \qquad \text{Eq.6.62}$$

$$\frac{\partial \tilde{C}_2}{\partial P} = -\frac{1}{\xi_o^2}\frac{\partial \xi_o}{\partial P}\sum_{i=1}^{n_c} N_i \qquad \text{Eq.6.63}$$

$$\frac{\partial \tilde{C}_2}{\partial P} = -\frac{1}{\xi_o^2}\frac{\partial \xi_o}{\partial P}\sum_{i=1}^{n_c} N_i \qquad \text{Eq.6.63}$$

The same assumption as above is made for oil. Therefore, derivatives of C_2 are the same as those of $\widetilde{C}_2$.

$$C_2 = \left(\frac{1}{\xi_o}\sum_{i=1}^{n_c} N_i\right)\frac{1}{1-\hat{C}_3} \approx \left(\frac{1}{\xi_o}\sum_{i=1}^{n_c} N_i\right) \qquad \text{Eq.6.64}$$

Similarly one can calculate the overall concentration of surfactant and its derivatives. The derivatives of the total fluid concentration of surfactant are presented later in this chapter.

$$\widetilde{C}_3 = \frac{N_{surf}}{\xi_{surf}} \qquad \text{Eq.6.65}$$

where

$$\xi_{surf} = \xi^o_{surf}\left(1 + c^o_{surf}\left(P - P^o\right)\right) \qquad \text{Eq.6.66}$$

$$\frac{\partial \tilde{C}_3}{\partial N_i} = \begin{cases} \dfrac{1}{\xi_{surf}} & if \quad i = surf \\ 0 & if \quad i \neq surf \end{cases} \qquad \text{Eq.6.67}$$

$$\frac{\partial \tilde{C}_3}{\partial P} = -\frac{N_{surf}}{\xi^2_{surf}}\left(\xi^o_{surf} c^o_{surf}\right) \qquad \text{Eq.6.68}$$

The overall concentration of polymer in wt% is calculated as follows:

$$\tilde{C}_4 = \frac{100 N_{poly} M_{poly}}{N_{water} M_{water}} \qquad \text{Eq.6.69}$$

$$\frac{\partial \tilde{C}_4}{\partial V} = \begin{cases} \dfrac{100 N_{poly} M_{poly}}{N^2_{water} M_{water}} & if \quad V = N_{water} \\ \dfrac{100 M_{poly}}{N_{water} M_{water}} & if \quad V = N_{poly} \\ 0 & for \quad other \quad parameters \end{cases} \qquad \text{Eq.6.70}$$

$$\frac{\partial \tilde{C}_4}{\partial V} = \begin{cases} \dfrac{100 N_{poly} M_{poly}}{N^2_{water} M_{water}} & if \quad V = N_{water} \\ \dfrac{100 M_{poly}}{N_{water} M_{water}} & if \quad V = N_{poly} \\ 0 & for \quad other \quad parameters \end{cases} \qquad \text{Eq.6.70}$$

Since the effect of divalent cations and temperature on the effective salinity are neglected in this development, the effective salinity, C_{SE} is calculated as follows:

$$C_{SE} = C_{51} = 16.037 \xi_{water} \frac{N_{salt}}{N_{water}} \qquad \text{Eq.6.71}$$

where the constant 16.037 is the unit conversion for lb/ft^3 to eq/L of NaCl to be consistent with UTCHEM. The derivatives of effective salinity are calculated as follows:

$$\frac{\partial C_{SE}}{\partial N_i} = \begin{cases} 16.037 \dfrac{\xi_{water}}{N_{water}} \; if \; i = salt \\ -16.037 \dfrac{\xi_{water} N_{salt}}{N_{water}^2} \; if \; i = water \\ 0 \; for \; other \; components \end{cases} \qquad \text{Eq.6.72}$$

$$\frac{\partial C_{SE}}{\partial P} = 16.037 \xi_{water}^{o} c_{surf}^{o} \frac{N_{salt}}{N_{water}} \qquad \text{Eq.6.73}$$

Polymer and Surfactant Fluid Concentrations

Similar to UTCHEM, Langmuir type isotherms (Eq.6.74) are used to model both surfactant and polymer adsorption. The minimum in Eq.6.74 ensures that the overall adsorbed concentration of component κ does not exceed its overall concentration in a gridblock.

$$\hat{C}_\kappa = \min\left(\tilde{C}_\kappa, \frac{a_\kappa \left(\tilde{C}_\kappa - \hat{C}_\kappa \right)}{1 + b_\kappa \left(\tilde{C}_\kappa - \hat{C}_\kappa \right)} \right) \quad \kappa = 3 \;\; or \;\; 4 \qquad \text{Eq.6.74}$$

where

$$a_\kappa = a_{\kappa 1} + a_{\kappa 2} C_{SE} \qquad \text{Eq.6.75}$$

Total fluid concentration of component κ, C_κ^f is calculated by subtracting the adsorbed concentration $\hat{C}_\kappa$ from overall concentration for each species. Eq.6.74 is rearranged and solved. This results in a quadratic equation with two roots. The physically valid solution is the always positive root since the adsorbed concentration cannot be negative (for more details refer to Appendix B).

$$C_\kappa^f = \tilde{C}_\kappa - \hat{C}_\kappa = \frac{\tilde{C}_1}{2b_\kappa}\left(-a_\kappa - 1 + b_\kappa\frac{\tilde{C}_\kappa}{\tilde{C}_1} + \sqrt{\left(a_\kappa + 1 - b_\kappa\frac{\tilde{C}_\kappa}{\tilde{C}_1}\right)^2 + 4b_\kappa\frac{\tilde{C}_\kappa}{\tilde{C}_1}}\right) \quad \text{Eq.6.76}$$

The derivatives of the total fluid concentration of component κ is then calculated as follows:

$$\frac{\partial C_\kappa^f}{\partial N_i} = \frac{\partial C_\kappa^f}{\partial \tilde{C}_1}\frac{\partial \tilde{C}_1}{\partial N_i} + \frac{\partial C_\kappa^f}{\partial \tilde{C}_\kappa}\frac{\partial \tilde{C}_\kappa}{\partial N_i} + \frac{\partial C_\kappa^f}{\partial C_{SE}}\frac{\partial C_{SE}}{\partial N_i} \quad \text{Eq.6.77}$$

where

$$\frac{\partial C_\kappa^f}{\partial \tilde{C}_1} = \frac{1}{2b_\kappa}\left[A - \frac{b_\kappa\tilde{C}_\kappa}{\tilde{C}_1}\left(1 - \frac{1}{\sqrt{B}}\left(a_\kappa - \frac{b_\kappa\tilde{C}_\kappa}{\tilde{C}_1} - 1\right)\right)\right] \quad \text{Eq.6.78}$$

$$\frac{\partial C_\kappa^f}{\partial \tilde{C}_\kappa} = \frac{1}{2}\left[1 + \frac{1}{\sqrt{B}}\left(\frac{b_\kappa\tilde{C}_\kappa}{\tilde{C}_1} - a_\kappa + 1\right)\right] \quad \text{Eq.6.79}$$

$$\frac{\partial C_\kappa^f}{\partial \tilde{C}_\kappa} = \frac{1}{2}\left[1 + \frac{1}{\sqrt{B}}\left(\frac{b_\kappa\tilde{C}_\kappa}{\tilde{C}_1} - a_\kappa + 1\right)\right] \quad \text{Eq.6.80}$$

where

$$A = -a_\kappa - 1 + \frac{b_\kappa\tilde{C}_\kappa}{\tilde{C}_1} + \sqrt{\left(a_\kappa + 1 - \frac{b_\kappa\tilde{C}_\kappa}{\tilde{C}_1}\right)^2 + 4\frac{b_\kappa\tilde{C}_\kappa}{\tilde{C}_1}} \quad \text{Eq.6.81}$$

$$B = \left(a_\kappa + 1 - \frac{b_\kappa\tilde{C}_\kappa}{\tilde{C}_1}\right)^2 + 4\frac{b_\kappa\tilde{C}_\kappa}{\tilde{C}_1} \quad \text{Eq.6.82}$$

$$\frac{\partial C_\kappa^f}{\partial P} = \frac{\partial C_\kappa^f}{\partial C_1}\frac{\partial \tilde{C}_1}{\partial P} + \frac{\partial C_\kappa^f}{\partial C_\kappa}\frac{\partial \tilde{C}_\kappa}{\partial P} + \frac{\partial C_\kappa^f}{\partial C_{SE}}\frac{\partial \tilde{C}_{SE}}{\partial P} \quad \text{Eq.6.83}$$

The derivatives of overall surfactant concentration ($\kappa = 3$) used in the above equations are presented in Eq.6.67 and Eq.6.68 and the derivatives of overall polymer concentration ($\kappa = 4$) are presented in Eq.6.70.

Number of Moles of Polymer and Surfactant

Since GPAS is an EOS simulator, it is important to calculate the number of moles of each component per pore volume at each timestep. The total fluid concentrations of surfactant and polymer can be converted into number of moles as follows:

$$N_\kappa^f = \xi_\kappa C_\kappa^f \quad \kappa = 3 \; or \; 4 \qquad \text{Eq.6.84}$$

$$\frac{\partial N_\kappa^f}{\partial N_i} = \xi_\kappa \frac{\partial C_\kappa^f}{\partial N_i} \quad \kappa = 3 \; or \; 4 \qquad \text{Eq.6.85}$$

$$\frac{\partial N_\kappa^f}{\partial P} = \left(\xi_\kappa^o c_\kappa^o\right) C_\kappa^f + \xi_\kappa \frac{\partial C_\kappa^f}{\partial P} \quad \kappa = 3 \; or \; 4 \qquad \text{Eq.6.86}$$

Phase Compositions

The fluid concentration of surfactant is calculated as follows:

$$C_3 = \frac{N_{surf}^f}{\xi_{surf}} \left(\frac{1}{1 - \hat{C}_3} \right) \approx \frac{N_{surf}^f}{\xi_{surf}} = C_3^f \qquad \text{Eq.6.87}$$

The same assumption used for calculation of total water or oil fluid concentrations is used for the surfactant, i.e. the adsorbed surfactant concentration is assumed to be small and the derivatives of total fluid concentration of surfactant, C_3, are assumed to be the same as those of the overall concentration, C_3^f.

C_3 from Eq.6.87 should be above CMC for the surfactant to be active and to reduce the interfacial tension. If C_3 is less than CMC, only oleic and aqueous phases exist and all aqueous species reside in the water phase. If C_3 is above CMC, then the surfactant becomes active and three distinct phase environments may exist based on the salinity. At salinities lower than C_{SEL}, it is assumed that surfactant does not partition into the oleic phase, but some of the hydrocarbon components are dissolved in the aqueous phase creating a water-external ME phase (Type I). Figure 2.9 shows the idealized schematic of a ternary diagram in Type I environment. As shown in Fig. 2.9, the overall compositions falling in the area below the binodal curve would result in two phases with their

compositions given by the tie lines. Any overall composition falling in the area above the binodal curve would result in a single phase ME. At salinities above C_{SEU}, an oil-external ME phase containing all of the surfactant and some aqueous components is in equilibrium with an aqueous phase. This phase environment is called Winsor Type II (Fig. 2.10). For salinities between the C_{SEL} and C_{SEU} the phase behavior is shown in Fig. 2.11. The binodal curve has two two-phase regions that are connected through the invariant point. The invariant point and the pure water and oil pseudo-components are vertices of an inner triangle. Overall compositions falling in this area would result in three phases (aqueous, oleic and ME) in equilibrium. Overall phase compositions falling in the left and right lobes of the ternary diagram result in a Type II and Type I phase behavior, respectively. Overall compositions falling in the area above the binodal curve would result in a single ME phase.

The binodal curve is obtained from Eq.6.88:

$$\frac{C_{3j}}{C_{2j}} = A\left(\frac{C_{3j}}{C_{1j}}\right)^{-1} \quad j = 1,2,3 \qquad \text{Eq.6.88}$$

For each phase, the sum of the C_{ij} should be unity. This constraint in conjunction with Eq.6.88 results in the calculation of phase concentrations, provided parameter A is known.

Parameter A is a function of a normalized effective salinity which is the effective salinity divided by the optimal salinity. Since we do not currently consider the effect of divalent cations, co-solvent, and temperature on the phase behavior, the effective salinity is simply the total anion concentration (Eq.6.71). The optimal salinity however is calculated as follows:

$$C_{SEOP} = \frac{C_{SEL} + C_{SEU}}{2} \qquad \text{Eq.6.89}$$

Parameter A is related to the height of binodal curve:

$$A_s = \left(\frac{2C_{3\max,s}}{1 - C_{3\max,s}}\right)^2 \quad s = 0,1,2 \qquad \text{Eq.6.90}$$

The heights of binodal curve at 0, 1 and twice the optimal salinity are estimated based on the solubilization ratios measured in the lab and are input parameters. The *A* parameter is linearly interpolated based on salinity as follows:

$$A=\begin{cases}\left(A_0-A_1\right)\left(1-\dfrac{C_{SE}}{C_{SEOP}}\right)+A_1 & C_{SE}\le C_{SEOP}\\ \left(A_2-A_1\right)\left(\dfrac{C_{SE}}{C_{SEOP}}-1\right)+A_1 & C_{SE}>C_{SEOP}\end{cases} \qquad \text{Eq.6.91}$$

Derivatives of the A parameter would then be calculated as follows:

$$\frac{\partial A}{\partial V}=\begin{cases}\dfrac{\left(A_1-A_0\right)}{C_{SEOP}}\dfrac{\partial C_{SE}}{\partial V} & if \quad C_{SE}\le C_{SEOP}\\ \dfrac{\left(A_2-A_1\right)}{C_{SEOP}}\dfrac{\partial C_{SE}}{\partial V} & if \quad C_{SE}>C_{SEOP}\end{cases} \qquad \text{Eq.6.92}$$

The phase compositions are computed from Eq.6.88 and the constraint that for each phase the sum of C_{ij} should be unity for the volume occupying components, i.e., water, oil and surfactant.

Oleic and Aqueous

If $C_3^f \le CMC$ then surfactant does not reduce the IFT and there is no ME phase. All of the surfactant if present is in the aqueous phase. Based on the above we have

$$C_{11}=\frac{C_1}{C_1+C_3} \qquad \text{Eq.6.93}$$

$$\frac{\partial C_{11}}{\partial V}=\frac{\dfrac{\partial C_1}{\partial V}}{C_1+C_3}-\frac{C_1\left(\dfrac{\partial C_1}{\partial V}+\dfrac{\partial C_3}{\partial V}\right)}{\left(C_1+C_3\right)^2} \qquad \text{Eq.6.94}$$

$$C_{31}=\frac{C_3}{C_1+C_3} \qquad \text{Eq.6.95}$$

$$\frac{\partial C_{31}}{\partial V}=\frac{\dfrac{\partial C_3}{\partial V}}{C_1+C_3}-\frac{C_3\left(\dfrac{\partial C_1}{\partial V}+\dfrac{\partial C_3}{\partial V}\right)}{\left(C_1+C_3\right)^2} \qquad \text{Eq.6.96}$$

$$C_{21}=C_{13}=C_{23}=C_{33}=C_{12}=C_{32}=0 \qquad \text{Eq.6.97}$$

$$\frac{\partial C_{21}}{\partial V}=\frac{\partial C_{13}}{\partial V}=\frac{\partial C_{23}}{\partial V}=\frac{\partial C_{33}}{\partial V}=\frac{\partial C_{12}}{\partial V}=\frac{\partial C_{32}}{\partial V}=0 \quad \text{Eq.6.98}$$

$$C_{22}=1 \quad \text{Eq.6.99}$$

$$\frac{\partial C_{22}}{\partial V}=0 \quad \text{Eq.6.100}$$

ME and Aqueous

If $C_3^f > CMC$ and $C_{SE} \geq C_{SEU}$ then phase environment is Winsor Type II (Fig. 2.10) where there are ME and aqueous phases in equilibrium. Electrolytes, surfactant, and oil pseudo-components concentrations in the ME phase are calculated using two parameters *WS1* and *WS2* as follows:

$$WS1=\frac{C_3}{C_2} \quad \text{Eq.6.101}$$

C_3 and C_2 indicate the total fluid concentrations of the surfactant and aqueous components respectively. The derivatives of *WS1* are

$$\frac{\partial(WS1)}{\partial V}=\frac{1}{C_2}\left(\frac{\partial C_3}{\partial V}-\frac{C_3}{C_2}\frac{\partial C_2}{\partial V}\right) \quad \text{Eq.6.102}$$

$$WS2=\frac{A}{WS1} \quad \text{Eq.6.103}$$

$$\frac{\partial(WS2)}{\partial V}=\frac{1}{WS1}\left(\frac{\partial A}{\partial V}-\frac{A}{WS1}\frac{\partial WS1}{\partial V}\right) \quad \text{Eq.6.104}$$

$$C_{13}=\frac{WS1}{WS1+WS1\times WS2+WS2} \quad \text{Eq.6.105}$$

$$\frac{\partial C_{13}}{\partial V}=-\frac{1}{\alpha^2}\left(WS1(1+WS1)\frac{\partial WS2}{\partial V}-WS2\frac{\partial WS1}{\partial V}\right) \quad \text{Eq.6.106}$$

where

$$\alpha=WS1+WS1*WS2+WS2$$

$$C_{23}=1-(WS2+1)\,C_{13} \quad \text{Eq.6.107}$$

$$\frac{\partial C_{23}}{\partial V}=-\left[C_{13}\frac{\partial WS2}{\partial V}+\frac{\partial C_{13}}{\partial V}(WS2+1)\right] \quad \text{Eq.6.108}$$

$$C_{33} = 1 - C_{13} - C_{23} \quad \text{Eq.6.109}$$

$$\frac{\partial C_{33}}{\partial V} = -\left(\frac{\partial C_{13}}{\partial V} + \frac{\partial C_{23}}{\partial V}\right) \quad \text{Eq.6.110}$$

The corner plait point assumption helps calculating other phase compositions:

$$C_{11} = 1, \;\; C_{21} = C_{31} = 0 \quad \text{Eq.6.111}$$

$$\frac{\partial C_{11}}{\partial V} = \frac{\partial C_{21}}{\partial V} = \frac{\partial C_{31}}{\partial V} = 0 \quad \text{Eq.6.112}$$

If the concentration of the surfactant in the ME phase is smaller or equal to the total fluid concentration of surfactant ($C_{33} \leq C_3$), then the surfactant solubilizes aqueous and oleic components and forms a single ME phase. The phase compositions and their derivatives are

$$C_{13} = C_1; C_{23} = C_2; C_{33} = C_3 \quad \text{Eq.6.113}$$

$$\frac{\partial C_{13}}{\partial V} = \frac{\partial C_1}{\partial V}; \;\; \frac{\partial C_{23}}{\partial V} = \frac{\partial C_2}{\partial V}; \;\; \frac{\partial C_{33}}{\partial V} = \frac{\partial C_3}{\partial V} \quad \text{Eq.6.114}$$

$$C_{11} = C_{21} = C_{31} = 0 \quad \text{Eq.6.115}$$

$$\frac{\partial C_{11}}{\partial V} = \frac{\partial C_{21}}{\partial V} = \frac{\partial C_{31}}{\partial V} = 0 \quad \text{Eq.6.116}$$

Oleic and ME

If $C_3^f > CMC$ and $C_{SE} \leq C_{SEL}$ then phase environment is Winsor Type I or where ME and oleic phases are in equilibrium. Composition of the ME phase is calculated as follows:

$$WS1 = \frac{C_3}{C_1} \quad \text{Eq.6.117}$$

$$\frac{\partial (WS1)}{\partial V} = \frac{1}{C_1}\left(\frac{\partial C_3}{\partial V} - \frac{C_3}{C_1}\frac{\partial C_1}{\partial V}\right) \quad \text{Eq.6.118}$$

$$WS2 = \frac{A}{WS1} \quad \text{Eq.6.119}$$

$$\frac{\partial (WS2)}{\partial V} = \frac{1}{WS1}\left(\frac{\partial A}{\partial V} - \frac{A}{WS1}\frac{\partial WS1}{\partial V}\right) \quad \text{Eq.6.120}$$

$$C_{13} = \frac{WS2}{WS1 + WS1 \times WS2 + WS2} \qquad \text{Eq.6.121}$$

$$\frac{\partial C_{13}}{\partial V} = -\frac{1}{\alpha^2}\left(WS2(1+WS2)\frac{\partial WS1}{\partial V} - WS1\frac{\partial WS2}{\partial V} \right) \qquad \text{Eq.6.122}$$

where

$$\alpha = WS1 + WS1 \times WS2 + WS2$$

$$C_{23} = 1 - (WS1 + 1)\, C_{13} \qquad \text{Eq.6.123}$$

$$\frac{\partial C_{23}}{\partial V} = -\left[C_{13}\frac{\partial WS1}{\partial V} + \frac{\partial C_{13}}{\partial V}(WS1 + 1) \right] \qquad \text{Eq.6.124}$$

Corner plait point assumption is used again to obtain the composition of other phase:

$$C_{22} = 1, \;\; C_{12} = C_{32} = 0 \qquad \text{Eq.6.125}$$

$$\frac{\partial C_{12}}{\partial V} = \frac{\partial C_{22}}{\partial V} = \frac{\partial C_{32}}{\partial V} = 0 \qquad \text{Eq.6.126}$$

The surfactant concentration in the ME phase and its derivatives are calculated using Eq.6.109 and Eq.6.110 respectively. Same as Type II phase environment, there may be a single ME phase if $C_{33} \leq C_3$ in which case Eq.6.113 through Eq.6.116 describe the phase compositions and their derivatives.

Oleic, ME, Aqueous

For the conditions of $C_3^f > CMC$ and $C_{SEL} < C_{SE} < C_{SEU}$ there are three possibilities for the phase environment. Based on Fig. 2.11, if the overall composition falls within the triangular region enclosed by the invariant point and the oil and brine pseudo-components then three phases (ME, oleic and aqueous) coexist. In this case the composition of the ME phase is calculated as follows:

$$WS1 = \frac{C_{SE} - C_{SEL}}{C_{SEU} - C_{SEL}} \qquad \text{Eq.6.127}$$

$$\frac{\partial WS1}{\partial V} = \frac{1}{C_{SEU} - C_{SEL}}\frac{\partial C_{SE}}{\partial V} \qquad \text{Eq.6.128}$$

$$WS2 = 2(4 - A) \qquad \text{Eq.6.129}$$

$$\frac{\partial WS2}{\partial V} = -2\frac{\partial A}{\partial V} \quad \text{Eq.6.130}$$

$$WS3 = WS2 \times WS1 + A \quad \text{Eq.6.131}$$

$$\frac{\partial WS3}{\partial V} = WS2\frac{\partial WS1}{\partial V} + WS1\frac{\partial WS2}{\partial V} + \frac{\partial A}{\partial V} \quad \text{Eq.6.132}$$

$$WS4 = 8WS2 \times WS1^2 \quad \text{Eq.6.133}$$

$$\frac{\partial WS4}{\partial V} = 8WS1\left(2WS2\frac{\partial WS1}{\partial V} + WS1\frac{\partial WS2}{\partial V}\right) \quad \text{Eq.6.134}$$

$$WS7 = \frac{\left(WS3 - \sqrt{WS3^2 - WS4}\right)}{WS2} \quad \text{Eq.6.135}$$

$$\frac{\partial WS7}{\partial V} = \frac{1}{WS2^2}\left(WS2\frac{\partial \alpha}{\partial V} - \alpha\frac{\partial WS2}{\partial V}\right) \quad \text{Eq.6.136}$$

where

$$\alpha = WS3 - \sqrt{WS3^2 - WS4}$$

$$\frac{\partial \alpha}{\partial V} = \frac{\partial WS3}{\partial V} - \frac{1}{2\sqrt{WS3^2 - WS4}}\left(2WS3\frac{\partial WS3}{\partial V} - \frac{\partial WS4}{\partial V}\right)$$

$$WS8 = 2\left(WS1 - WS7\right) \quad \text{Eq.6.137}$$

$$\frac{\partial WS8}{\partial V} = 2\left(\frac{\partial WS1}{\partial V} - \frac{\partial WS7}{\partial V}\right) \quad \text{Eq.6.138}$$

$$WS6 = 1 - WS7 - WS8 \quad \text{Eq.6.139}$$

$$\frac{\partial WS6}{\partial V} = -\frac{\partial WS7}{\partial V} - \frac{\partial WS8}{\partial V} \quad \text{Eq.6.140}$$

The following conditions give the location of overall composition in the ternary diagram of Fig. 2.11 and whether three phases are present:

$$A : C_2 > WS7 \quad \text{Eq.6.141}$$

$$B : C_1 > WS6 \quad \text{Eq.6.142}$$

$$C : C_3 < \frac{C_1 WS8}{WS6} \quad \text{Eq.6.143}$$

$$D : C_2 \le WS7 \quad \text{Eq.6.144}$$

$$E: C_3 < \frac{C_2 WS8}{WS7} \qquad \text{Eq.6.145}$$

If condition *A* (Eq.6.141) was valid and either of conditions *B* (Eq.6.142) or *C* (Eq.6.143) were correct as well, or if conditions *D* and *E* were correct, then overall composition falls within the three phase triangle of Fig. 2.11 and the three phases coexist. Eq.6.146 specifies the condition for existence of three phases. This condition checks if overall composition is falling within the three phase region (Fig. 2.11), using geometric conditions of Eq.6.141 through Eq.6.145. If the outcome of Eq.6.146 is true, then three phases are present and ME phase composition is calculated as follows:

(*A*&(*B* or *C*)) or (*E*&*D*) Eq.6.146

$$C_{13} = WS6 \qquad \text{Eq.6.147}$$

$$\frac{\partial C_{13}}{\partial V} = \frac{\partial WS6}{\partial V} \qquad \text{Eq.6.148}$$

$$C_{23} = WS7 \qquad \text{Eq.6.149}$$

$$\frac{\partial C_{23}}{\partial V} = \frac{\partial WS7}{\partial V} \qquad \text{Eq.6.150}$$

$$C_{33} = WS8 \qquad \text{Eq.6.151}$$

$$\frac{\partial C_{33}}{\partial V} = \frac{\partial WS8}{\partial V} \qquad \text{Eq.6.152}$$

The assumption of corner plait point is used to compute the composition of the excess aqueous and oleic phases:

$$C_{11} = 1, \;\; C_{21} = C_{31} = 0 \qquad \text{Eq.6.153}$$

$$\frac{\partial C_{11}}{\partial V} = \frac{\partial C_{21}}{\partial V} = \frac{\partial C_{31}}{\partial V} = 0 \qquad \text{Eq.6.154}$$

$$C_{22} = 1, \;\; C_{12} = C_{32} = 0 \qquad \text{Eq.6.155}$$

$$\frac{\partial C_{12}}{\partial V} = \frac{\partial C_{22}}{\partial V} = \frac{\partial C_{32}}{\partial V} = 0 \qquad \text{Eq.6.156}$$

If the outcome of Eq.6.146 was not true then the conditions of Eq.6.157 determine whether the overall composition is in Type II lobe of Fig. 2.11.

($C_2 \leq WS7$) & ($C_3 \geq C2\ WS8/WS7$) Eq.6.157

If the conditions of Eq.6.157 are met, then the phase environment is Type II and the phase compositions and their derivatives are obtained using Eq.6.101 through Eq.6.116.

If neither conditions of Eq.6.146, nor those of Eq.6.157 are met then the overall composition is in the Type I lobe of Fig. 2.11 and phase compositions and their derivatives follow Eq.6.117 through Eq.6.126.

Concentration of Other Aqueous Components in Aqueous and ME Phases

After calculation of the concentration of three volume occupying pseudo-components in each phase, we can now calculate the concentration of other components in the ME and aqueous phases. It is assumed that the composition of the oil in the ME is the same as that of the excess oleic phase, therefore oil composition does not vary during the simulation.

Since the aqueous phase is assumed to be free of surfactant and oleic components, one can calculate the concentration of polymer in the aqueous phase as follows if this phase exists.

$$C_{41} = 100 \frac{M_{poly} N_{poly}^{f}}{M_{water} N_{water}} \qquad \text{Eq.6.158}$$

Eq.6.158 gives the polymer concentration in aqueous phase in wt% to be consistent with UTCHEM. The derivatives of C_{41} are as follows:

$$\frac{\partial C_{41}}{\partial N_i} = \begin{cases} 100 \dfrac{M_{poly}}{M_{water} N_{water}} \left(\dfrac{\partial N_{poly}^{f}}{\partial N_{water}} - \dfrac{N_{poly}^{f}}{N_{water}} \right) if\ i = water \\ 100 \dfrac{M_{poly}}{M_{water} N_{water}} \dfrac{\partial N_{poly}^{f}}{\partial N_{poly}} if\ i = poly \\ 100 \dfrac{M_{poly}}{M_{water} N_{water}} \dfrac{\partial N_{poly}^{f}}{\partial N_{salt}} if\ i = salt \\ 0\ for\ other\ components \end{cases} \qquad \text{Eq.6.159}$$

$$\frac{\partial C_{41}}{\partial P} = 100 \frac{M_{poly}}{M_{water} N_{water}} \frac{\partial N_{poly}^{f}}{\partial P} \qquad \text{Eq.6.160}$$

The concentration of polymer in the ME phase is given by

$$C_{43} = 100 \frac{M_{poly} N_{poly}^{f} C_{13}}{M_{water} N_{water}} \quad \text{Eq.6.161}$$

Polymer concentration is normalized by water concentration since polymer is assumed to be only soluble in water. The derivatives of C_{43} are obtained as follows:

$$\frac{\partial C_{43}}{\partial V} = 100 \frac{M_{poly}}{M_{water}} \left(\frac{C_{13}}{N_{water}} \frac{\partial N_{poly}^{f}}{\partial V} + \frac{N_{poly}^{f}}{N_{water}} \frac{\partial C_{13}}{\partial V} - \frac{C_{13} N_{poly}^{f}}{N_{water}^{2}} \frac{\partial N_{water}}{\partial V} \right) \quad \text{Eq.6.162}$$

Since the effects of divalent cations, cosolvent and temperature on phase behavior are neglected, the effective salinity is the same as the salt concentration in the aqueous phase and C_{51} is obtained from Eq.6.71 and its derivatives are given in Eq.6.72 and Eq.6.73. The concentration of salt in the ME is

$$C_{53} = C_{13} C_{SE} \quad \text{Eq.6.163}$$

The salinity in the ME phase is normalized by the volume of water in ME phase. The derivatives of C_{53} are defined as follows:

$$\frac{\partial C_{53}}{\partial V} = C_{13} \frac{\partial C_{SE}}{\partial V} + C_{SE} \frac{\partial C_{13}}{\partial V} \quad \text{Eq.6.164}$$

Solubilization Ratios

Solubilization ratios are key parameters used for IFT calculation. Solubilization ratio of water, R_{13}, is defined as the volume of water solubilized in the microemulsion phase divided by the volume of surfactant in that phase:

$$R_{13} = \frac{C_{13}}{C_{33}} \quad \text{Eq.6.165}$$

$$\frac{\partial R_{13}}{\partial V} = \frac{1}{C_{33}} \frac{\partial C_{13}}{\partial V} - \frac{C_{13}}{{C_{33}}^{2}} \frac{\partial C_{33}}{\partial V} \quad \text{Eq.6.166}$$

The oil solubilization ratio is calculated as follows:

$$R_{23} = \frac{C_{23}}{C_{33}} \quad \text{Eq.6.167}$$

$$\frac{\partial R_{23}}{\partial V} = \frac{1}{C_{33}} \frac{\partial C_{23}}{\partial V} - \frac{C_{23}}{{C_{33}}^{2}} \frac{\partial C_{33}}{\partial V} \quad \text{Eq.6.168}$$

Figure 2.12 illustrates the relationship between the oil and water solubilization ratios and salinity. At low salinities anionic surfactants tends to prefer the water more than oil and thus the solubilization ratio of water is much larger than that of oil. By increasing the salinity, one can make anionic surfactants more oil soluble. Solubilization ratios of water and oil become equal at the point where the water solubility of the surfactant becomes equal to its oil solubility. This is referred to as optimum conditions as mentioned in Chapter 2. Figure 2.12 also illustrates the correlation between IFTs and solubilization ratios. The calculation of IFTs for oil/ME and brine/ME is discussed later.

Molar Density

Aqueous phase molar density, ξ_{water}, is discussed in Eq.6.57. Aqueous phase molar density is a function of pressure only and its derivative is as follows:

$$\frac{\partial \xi_{water}}{\partial V} = \begin{cases} \xi^{o}_{water} c^{o}_{water} \ if \ V = P \\ 0 \ otherwise \end{cases} \qquad \text{Eq.6.169}$$

Molar density of the oleic phase is obtained from the EOS as a function of pressure, temperature, and oil phase composition:

$$\xi_2 = f\left(P, T, x_{i2}\right) \qquad \text{Eq.6.170}$$

where

$$x_{i2} = \frac{N_{i,2}}{N_{oil,2}} = \frac{N_i}{\sum_{i=1}^{n_c} N_i} \qquad \text{Eq.6.171}$$

Since composition of the oil in microemulsion phase is the same as that of the excess oleic phase, There is no need to modify the existing derivatives of ξ_2.

Molar density of the ME phase is obtained using its composition as follows:

$$\xi_3 = C_{13}\xi_{water} + C_{23}\xi_{oil} + C_{33}\xi_{surf} \qquad \text{Eq.6.172}$$

$$\frac{\partial \xi_3}{\partial V} = \xi_{water}\frac{\partial C_{13}}{\partial V} + C_{13}\frac{\partial \xi_{water}}{\partial V} + \xi_{oil}\frac{\partial C_{23}}{\partial V} + C_{23}\frac{\partial \xi_{oil}}{\partial V} + \xi_{surf}\frac{\partial C_{33}}{\partial V} + C_{33}\frac{\partial \xi_{surf}}{\partial V} \qquad \text{Eq.6.173}$$

Molar Phase Compositions

Molar phase compositions are calculated for the current phase environment in each gridblock at each timestep. The number of moles of each component in each phase is calculated first and then, the sum of the number of moles of all of the components present in a phase gives the total number of moles of that phase. The mole fraction of each component in a phase is obtained by dividing the number of moles of that component by total number of moles of all components of that phase.

Oleic and Aqueous

If fluid surfactant concentration is less than the CMC, only aqueous and oleic phases are present. Surfactant is assumed to be in the aqueous phase. The number of moles of each component in the aqueous phase can be written as follows considering the assumptions mentioned in Section 6.2.1.

$$N_{i,1} = \begin{cases} 0 \; if \; i = hydrocarbon \; comp \\ N_{water} \; if \; i = water \\ N^{f}_{surf} \; if \; i = surf \\ N^{f}_{poly} \; if \; i = poly \\ N_{salt} \; if \; i = salt \\ N_{trac} \; if \; i = trac \end{cases} \qquad \text{Eq.6.174}$$

$$\frac{\partial N_{water,1}}{\partial V} = \begin{cases} 1 \; if \; V = N_{water} \\ 0 \; for \; all \; other \; parameters \end{cases} \qquad \text{Eq.6.175}$$

$$\frac{\partial N_{surf,1}}{\partial V} = \begin{cases} \dfrac{\partial N^{f}_{surf}}{\partial V} \; for \; aqueous \; components \; and \; P \\ 0 \; for \; hydrocarbon \; components \end{cases} \qquad \text{Eq.6.176}$$

$$\frac{\partial N_{poly,1}}{\partial V} = \begin{cases} \dfrac{\partial N^{f}_{poly}}{\partial V} \; for \; aqueous \; components \; and \; P \\ 0 \; for \; hydrocarbon \; components \end{cases} \qquad \text{Eq.6.177}$$

$$\frac{\partial N_{salt,1}}{\partial V} = \begin{cases} 1 \; if \; V = N_{salt} \\ 0 \; for \; all \; other \; parameters \end{cases} \qquad \text{Eq.6.178}$$

$$\frac{\partial N_{trac,1}}{\partial V} = \begin{cases} 1 \; if \; V = N_{trac} \\ 0 \; for \; all \; other \; parameters \end{cases} \qquad \text{Eq.6.179}$$

$$\frac{\partial N_{i,1}}{\partial V} = 0 \; for \; hydrocarbon \; component \; i \qquad \text{Eq.6.180}$$

Total number of moles in the aqueous phase, $N_{T,1}$, is obtained as follows:

$$N_{T,1} = N_{water,1} + N_{poly,1} + N_{surf,1} + N_{salt,1} + N_{trac,1} \qquad \text{Eq.6.181}$$

$$\frac{\partial N_{T,1}}{\partial V} = \frac{\partial N_{water,1}}{\partial V} + \frac{\partial N^{f}_{surf}}{\partial V} + \frac{\partial N^{f}_{poly}}{\partial V} + \frac{\partial N_{salt,1}}{\partial V} + \frac{\partial N_{trac,1}}{\partial V} \qquad \text{Eq.6.182}$$

The mole fraction of component *i* in the aqueous phase, x_{i1}, is calculated from:

$$x_{i1} = \begin{cases} \dfrac{N_{i,1}}{N_{T,1}} \; for \; aqueous \; components \\ 0 \; for \; hydrocarbon \; component \; i \end{cases} \qquad \text{Eq.6.183}$$

$$\frac{\partial x_{i1}}{\partial V} = \begin{cases} \dfrac{1}{N_{T,1}} \left(\dfrac{\partial N_{i,1}}{\partial V} - \dfrac{N_{i,1}}{N_{T,1}} \dfrac{\partial N_{T,1}}{\partial V} \right) if \; V = aqueous \; comp \; or \; P \\ 0 \; for \; hydrocarbon \; component \; i \end{cases} \qquad \text{Eq.6.184}$$

The mole fractions of the oleic phase and their derivatives are obtained as follows since the oleic phase is assumed to consist of hydrocarbon components only.

$$x_{i2} = \begin{cases} \dfrac{N_{i,2}}{N_{T,2}} = \dfrac{N_i}{\sum_{i=1}^{n_c} N_i} \; for \; hydrocarbon \; components \\ 0 \; for \; aqueous \; components \end{cases} \qquad \text{Eq.6.185}$$

The derivatives of oleic phase mole fractions with respect to number of moles of a hydrocarbon component per pore volume are as follows:

$$\frac{\partial x_{i2}}{\partial N_k} = \begin{cases} \dfrac{1}{\sum_{i=1}^{n_c} N_i} \left(1 - \dfrac{N_i}{\sum_{i=1}^{n_c} N_i} \right) if \; k = i \\ -\dfrac{N_i}{\left(\sum_{i=1}^{n_c} N_i \right)^2} if \; k \neq i \end{cases} \qquad \text{Eq.6.186}$$

The derivatives of oleic phase mole fractions with respect to the number of moles of aqueous components and pressure are zero:

$$\frac{\partial x_{i2}}{\partial V} = 0 \; for \; pressure \; and \; aqueous \; components \qquad \text{Eq.6.187}$$

As mentioned before, there is no microemulsion phase in this case, hence,

$$x_{i3} = \frac{\partial x_{i3}}{\partial V} = 0 \qquad \text{Eq.6.188}$$

Aqueous and ME

It is assumed that surfactant and oleic components are in the microemulsion phase. Aqueous components are partitioned into the microemulsion and aqueous phases based on the volume of water in each phase. The moles of water partitioned into the microemulsion phase, $N_{water,3}$, is calculated based on the volume of the water in ME phase.

$$N_{water,3} = \frac{\xi_{water} C_{13}}{1 - C_{13}} \left(\frac{\sum_{i=1}^{n_c} N_i}{\xi_2} + \frac{N_{surf}^f}{\xi_{surf}} \right) \qquad \text{Eq.6.189}$$

$$\frac{\partial N_{water,3}}{\partial N_k} = \frac{1}{1 - C_{13}} \left(C_{13} F \frac{\partial \xi_{water}}{\partial N_k} + \frac{\xi_{water} F}{1 - C_{13}} \frac{\partial C_{13}}{\partial N_k} + \xi_{water} C_{13} \frac{\partial F}{\partial N_k} \right) \qquad \text{Eq.6.190}$$

where

$$F = \frac{\sum_{i=1}^{n_c} N_i}{\xi_2} + \frac{N_{surf}^f}{\xi_{surf}} \qquad \text{Eq.6.191}$$

$$\frac{\partial F}{\partial V}=\begin{cases}\dfrac{1}{\xi_2}-\dfrac{\sum_{i=1}^{n_c}N_i}{\xi_2^2}\dfrac{\partial\xi_2}{\partial V}+\dfrac{1}{\xi_{surf}}\dfrac{\partial N_{surf}^f}{\partial V}\ for\ hydrocarbons\\ \dfrac{1}{\xi_{surf}}\dfrac{\partial N_{surf}^f}{\partial V}\ for\ water\ or\ surf\ or\ salt\\ -\dfrac{\sum_{i=1}^{n_c}N_i}{\xi_2^2}\dfrac{\partial\xi_2}{\partial V}+\dfrac{1}{\xi_{surf}}\dfrac{\partial N_{surf}^f}{\partial V}-\xi_{surf}^o c_{surf}\dfrac{1}{\xi_{surf}^2}\dfrac{\partial\xi_{surf}}{\partial V}\ for\ P\\ 0\ for\ polymer\ or\ tracer\end{cases} \quad \text{Eq.6.192}$$

The number of moles of polymer in the ME phase and its derivatives are

$$N_{poly,3}=N_{poly}^f C_{13}S_3/C_1 \quad \text{Eq.6.193}$$

$$\frac{\partial N_{poly,3}}{\partial V}=\frac{\partial N_{poly}^f}{\partial V}\frac{C_{13}S_3}{C_1}+\frac{\partial S_3}{\partial V}\frac{N_{poly}^f C_{13}}{C_1}+\frac{\partial C_{13}}{\partial V}\frac{N_{poly}^f S_3}{C_1}-\frac{\partial C_1}{\partial V}\frac{N_{poly}^f C_{13}S_3}{C_1^2} \quad \text{Eq.6.194}$$

A similar approach is taken for the number of moles of salt in the ME.

$$N_{salt,3}=N_{salt}C_{13}S_3/C_1 \quad \text{Eq.6.195}$$

$$\frac{\partial N_{salt,3}}{\partial V}=\frac{\partial N_{salt}}{\partial V}\frac{C_{13}S_3}{C_1}+\frac{\partial S_3}{\partial V}\frac{N_{salt}C_{13}}{C_1}+\frac{\partial C_{13}}{\partial V}\frac{N_{salt}S_3}{C_1}-\frac{\partial C_1}{\partial V}\frac{N_{salt}C_{13}S_3}{C_1^2} \quad \text{Eq.6.196}$$

Number of moles of tracer in the ME phase is calculated similar to salt.

$$N_{trac,3}=N_{trac}C_{13}S_3/C_1 \quad \text{Eq.6.197}$$

$$\frac{\partial N_{trac,3}}{\partial V}=\frac{\partial N_{trac}}{\partial V}\frac{C_{13}S_3}{C_1}+\frac{\partial S_3}{\partial V}\frac{N_{trac}C_{13}}{C_1}+\frac{\partial C_{13}}{\partial V}\frac{N_{trac}S_3}{C_1}-\frac{\partial C_1}{\partial V}\frac{N_{trac}C_{13}S_3}{C_1^2} \quad \text{Eq.6.198}$$

The number of moles of the surfactant in the ME is easy to figure out since we assume that surfactant is only in the ME phase.

$$N_{surf,3}=N_{surf}^f \quad \text{Eq.6.199}$$

$$\frac{\partial N_{surf,3}}{\partial V}=\frac{\partial N_{surf}^f}{\partial V} \quad \text{Eq.6.200}$$

In this case, oleic components are only in the ME phase so we have

$$N_{oil,3}=\sum_{i=1}^{n_c}N_i \quad \text{Eq.6.201}$$

$$\frac{\partial N_{oil,3}}{\partial V} = \frac{\partial}{\partial V}\left(\sum_{i=1}^{n_c} N_i\right) = \begin{cases} 1 \; if \; V = N_i \\ 0 \; for \; other \; parameters \end{cases} \quad \text{Eq.6.202}$$

The total number of moles in ME phase and its derivative is as follows:

$$N_{T,3} = N_{water,3} + N_{poly,3} + N^f_{surf} + N_{salt,3} + N_{trac,3} + N_{oil,3} \quad \text{Eq.6.203}$$

$$\frac{\partial N_{T,3}}{\partial V} = \frac{\partial N_{water,3}}{\partial V} + \frac{\partial N_{poly,3}}{\partial V} + \frac{\partial N^f_{surf}}{\partial V} + \frac{\partial N_{salt,3}}{\partial V} + \frac{\partial N_{trac,3}}{\partial V} + \frac{\partial N_{oil,3}}{\partial V} \quad \text{Eq.6.204}$$

The mole fraction of all components except the hydrocarbons is as follows:

$$x_{i3} = \frac{N_{i,3}}{N_{T,3}} \quad \text{Eq.6.205}$$

$$\frac{\partial x_{i3}}{\partial V} = \frac{1}{N_{T,3}}\left(\frac{\partial N_{i,3}}{\partial V} - \frac{N_{i,3}}{N_{T,3}}\frac{\partial N_{T,3}}{\partial V}\right) \quad \text{Eq.6.206}$$

For any hydrocarbon component we have

$$x_{i3} = \frac{N_i}{N_{T,3}} \quad \text{Eq.6.207}$$

$$\frac{\partial x_{i3}}{\partial N_k} = \begin{cases} \frac{1}{N_{T,3}}\left(1 - \frac{N_i}{N_{T,3}}\frac{\partial N_{T,3}}{\partial N_k}\right) if \; i = k \\ -\frac{N_i}{\left(N_{T,3}\right)^2}\frac{\partial N_{T,3}}{\partial N_k} if \; i \neq k \end{cases} \quad \text{Eq.6.208}$$

$$\frac{\partial x_{i3}}{\partial P} = \frac{1}{N_{T,3}}\left(-\frac{N_i}{N_{T,3}}\frac{\partial N_{T,3}}{\partial P}\right) \quad \text{Eq.6.209}$$

Number of moles of water in the aqueous phase is as follows:

$$N_{water,1} = N_{water} - N_{water,3} \quad \text{Eq.6.210}$$

$$\frac{\partial N_{water,1}}{\partial V} = \frac{\partial N_{water}}{\partial V} - \frac{\partial N_{water,3}}{\partial V} \quad \text{Eq.6.211}$$

As mentioned before, the aqueous components partition into different phases based on the volume of water in each phase.

$$N_{poly,1} = N^f_{poly} C_{11} S_1 / C_1 = N^f_{poly} S_1 / C_1 \quad \text{Eq.6.212}$$

$$\frac{\partial N_{poly,1}}{\partial V} = \frac{\partial N_{poly}^{f}}{\partial V}\frac{S_1}{C_1} + \frac{\partial S_1}{\partial V}\frac{N_{poly}^{f}}{C_1} - \frac{\partial C_1}{\partial V}\frac{N_{poly}^{f} S_1}{C_1^2} \quad \text{Eq.6.213}$$

$$N_{salt,1} = N_{salt} C_{11} S_1 / C_1 = N_{salt} S_1 / C_1 \quad \text{Eq.6.214}$$

$$\frac{\partial N_{salt,1}}{\partial V} = \frac{\partial N_{salt}}{\partial V}\frac{S_1}{C_1} + \frac{\partial S_1}{\partial V}\frac{N_{salt}}{C_1} - \frac{\partial C_1}{\partial V}\frac{N_{salt} S_1}{C_1^2} \quad \text{Eq.6.215}$$

$$N_{trac,1} = N_{trac} C_{11} S_1 / C_1 = N_{trac} S_1 / C_1 \quad \text{Eq.6.216}$$

$$\frac{\partial N_{trac,1}}{\partial V} = \frac{\partial N_{trac}}{\partial V}\frac{S_1}{C_1} + \frac{\partial S_1}{\partial V}\frac{N_{trac}}{C_1} - \frac{\partial C_1}{\partial V}\frac{N_{trac} S_1}{C_1^2} \quad \text{Eq.6.217}$$

There are no surfactant or hydrocarbon components in the excess aqueous phase based on corner plait point assumption.

$$N_{i,1} = \frac{\partial N_{i,1}}{\partial V} = 0 \quad \text{Eq.6.218}$$

We can calculate the total number of moles of the aqueous phase as

$$N_{T,1} = N_{water,1} + N_{poly,1} + N_{salt,1} + N_{trac,1} \quad \text{Eq.6.219}$$

$$\frac{\partial N_{T,1}}{\partial V} = \frac{\partial N_{water,1}}{\partial V} + \frac{\partial N_{poly,1}}{\partial V} + \frac{\partial N_{salt,1}}{\partial V} + \frac{\partial N_{trac,1}}{\partial V} \quad \text{Eq.6.220}$$

The mole fractions of each component in the aqueous phase and their derivatives are then calculated as follows:

$$x_{i1} = \frac{N_{i,1}}{N_{T,1}} \quad \text{Eq.6.221}$$

$$\frac{\partial x_{i1}}{\partial V} = \frac{1}{N_{T,1}}\left(\frac{\partial N_{i,1}}{\partial V} - \frac{N_{i,1}}{N_{T,1}}\frac{\partial N_{T,1}}{\partial V}\right) \quad \text{Eq.6.222}$$

Since there is no oleic phase present, we have

$$x_{i2} = \frac{\partial x_{i2}}{\partial V} = 0 \quad \text{Eq.6.223}$$

Oleic and ME

In this case the aqueous components are assumed to be in the microemulsion phase only. The oleic phase consists of only hydrocarbon components and since the composition of

solubilized oil in the microemulsion is assumed to be the same as the oleic phase, the composition of remaining oleic phase does not change. The mole fraction of the oleic phase can be written as follows:

$$x_{i2} = \begin{cases} \dfrac{N_{i,2}}{N_{T,2}} = \dfrac{N_i}{\sum_{i=1}^{n_c} N_i} \; for\ hydrocarbon\ components \\ 0 \; for\ aqueous\ components \end{cases} \qquad \text{Eq.6.224}$$

The derivation of Eq.6.224 can be found in Appendix B. For a hydrocarbon component *i* the derivatives of x_{i2} are:

$$\frac{\partial x_{i2}}{\partial N_k} = \begin{cases} \dfrac{1}{\sum_{i=1}^{n_c} N_i}\left(1 - \dfrac{N_i}{\sum_{i=1}^{n_c} N_i}\right) if\ k = i \\ -\dfrac{N_i}{\left(\sum_{i=1}^{n_c} N_i\right)^2} if\ k \neq i\ k\ is\ hydrocarbon\ component \\ 0\ if\ k \neq i\ k\ is\ not\ hydrocarbon\ component \end{cases} \qquad \text{Eq.6. 225}$$

Eq.6. 225

For aqueous component *i* the derivatives of x_{i2} are zero.

$$\frac{\partial x_{i2}}{\partial N_k} = 0 \qquad \text{Eq.6.226}$$

The derivatives of mole fractions of all components in the oleic phase with respect to pressure are zero.

$$\frac{\partial x_{i2}}{\partial P} = 0 \qquad \text{Eq.6.227}$$

The number of moles of the oleic components dissolved in the ME phase is

$$N_{oil,3} = \frac{\xi_2 C_{23}}{1 - C_{23}}\left(\frac{N_{water}}{\xi_{water}} + \frac{N_{surf}^f}{\xi_{surf}}\right) \qquad \text{Eq.6.228}$$

$$\frac{\partial N_{oil,3}}{\partial N_k} = \frac{1}{1 - C_{23}}\left(C_{23} F \frac{\partial \xi_2}{\partial N_k} + \frac{\xi_2 F}{1 - C_{23}} \frac{\partial C_{23}}{\partial N_k} + \xi_2 C_{23} \frac{\partial F}{\partial N_k}\right) \qquad \text{Eq.6.229}$$

where

$$F = \left(\frac{N_{water}}{\xi_{water}} + \frac{N_{surf}^{f}}{\xi_{surf}} \right) \qquad \text{Eq.6.230}$$

$$\frac{\partial F}{\partial N_k} = \begin{cases} 0 \; if \; k = hydrocarbon, polymer \; or \; tracer \\ \dfrac{1}{\xi_{water}} + \dfrac{1}{\xi_{surf}} \dfrac{\partial N_{surf}^{f}}{\partial N_k} \; if \; k = water \\ \dfrac{1}{\xi_{surf}} \dfrac{\partial N_{surf}^{f}}{\partial N_k} \; if \; k = surf \; or \; salt \end{cases} \qquad \text{Eq.6.231}$$

$$\frac{\partial N_{oil,3}}{\partial P} = \frac{1}{1 - C_{23}} \left(C_{23} F \frac{\partial \xi_2}{\partial P} + \frac{\xi_2 F}{1 - C_{23}} \frac{\partial C_{23}}{\partial P} + \xi_2 C_{23} \frac{\partial F}{\partial P} \right) \qquad \text{Eq.6.232}$$

where F is defined in Eq.6.230 and its derivative WRT pressure is as follows:

$$\frac{\partial F}{\partial P} = -\frac{N_{water}}{{\xi_{water}}^2} \xi_{water}^{o} c_{water} + \frac{1}{\xi_{surf}} \left(\frac{\partial N_{surf}^{f}}{\partial P} - \frac{N_{surf}^{f}}{\xi_{surf}} \xi_{surf}^{o} c_{surf} \right) \qquad \text{Eq.6.233}$$

The number of moles of each hydrocarbon component in the ME phase is computed as follows:

$$N_{i,3} = \frac{N_i N_{oil,3}}{\sum_{i=1}^{n_c} N_i} \qquad \text{Eq.6.234}$$

$$\frac{\partial N_{i,3}}{\partial N_k} = \begin{cases} \dfrac{N_{oil,3} + N_i \dfrac{\partial N_{oil,3}}{\partial N_k} - \dfrac{N_i N_{oil,3}}{\sum_{i=1}^{n_c} N_i}}{\sum_{i=1}^{n_c} N_i} \quad if \quad i = k \\ \dfrac{N_i \dfrac{\partial N_{oil,3}}{\partial N_k} - \dfrac{N_i N_{oil,3}}{\sum_{i=1}^{n_c} N_i}}{\sum_{i=1}^{n_c} N_i} \quad if \quad i \neq k \end{cases} \qquad \text{Eq.6.235}$$

$$\frac{\partial N_{i,3}}{\partial P} = \frac{N_i \dfrac{\partial N_{oil,3}}{\partial P}}{\sum_{i=1}^{n_c} N_i} \qquad \text{Eq.6.236}$$

The number of moles of aqueous components per pore volume in the ME phase are obtained keeping in mind that aqueous components are only in the ME phase.

$$N_{i,3} = \begin{cases} N_{water} \ if \ i = water \\ N^f_{surf} \ if \ i = surf \\ N^f_{poly} \ if \ i = poly \\ N_{salt} \ if \ i = salt \\ N_{trac} \ if \ i = trac \end{cases} \qquad \text{Eq.6.237}$$

The derivatives of these components are as follows:

$$\frac{\partial N_{i,3}}{\partial V} = \begin{cases} \dfrac{\partial N_{water}}{\partial V} \ if \ i = water \\ \dfrac{\partial N^f_{surf}}{\partial V} \ if \ i = surf \\ \dfrac{\partial N^f_{poly}}{\partial V} \ if \ i = poly \\ \dfrac{\partial N_{salt}}{\partial V} \ if \ i = salt \\ \dfrac{\partial N_{trac}}{\partial V} \ if \ i = trac \end{cases} \qquad \text{Eq.6.238}$$

The total number of moles per pore volume in the ME phase is then obtained as

$$N_{T,3} = N_{water} + N_{oil,3} + N^f_{surf} + N^f_{poly} + N_{salt} + N_{trac} \qquad \text{Eq.6.239}$$

$$\frac{\partial N_{T,3}}{\partial V} = \frac{\partial N_{water}}{\partial V} + \frac{\partial N_{oil,3}}{\partial V} + \frac{\partial N^f_{surf}}{\partial V} + \frac{\partial N^f_{poly}}{\partial V} + \frac{\partial N_{salt}}{\partial V} + \frac{\partial N_{trac}}{\partial V} \qquad \text{Eq.6.240}$$

Eq.6.205 and Eq.6.206 give the mole fraction of each component in the ME phase and the derivatives respectively. Since there is no aqueous phase present, we have

$$x_{i1} = \frac{\partial x_{i,1}}{\partial V} = 0 \qquad \text{Eq.6.241}$$

Oleic, Aqueous, ME

If all three phases coexist then the mole fractions of the ME phase are obtained as follows. Based on our assumption, the surfactant component is entirely in the ME phase as specified by Eq.6.199. First we need to calculate the number of moles of water and hydrocarbons in the ME phase. Number of moles of water per pore volume in the ME phase and its derivatives is obtained as follows:

$$N_{water,3} = \xi_{water} C_{13} \tilde{C}_3 / C_{33} \qquad \text{Eq.6.242}$$

$$\frac{\partial N_{water,3}}{\partial V} = \frac{\partial \xi_1}{\partial V} C_{13} \tilde{C}_3 / C_{33} + \frac{\partial C_{13}}{\partial V} \xi_1 \tilde{C}_3 / C_{33} + \frac{\partial \tilde{C}_3}{\partial V} \xi_1 C_{13} / C_{33} - \frac{\partial C_{33}}{\partial V} \xi_1 C_{13} \tilde{C}_3 / C_{33}^{\ 2} \qquad \text{Eq.6.243}$$

The number of moles of hydrocarbons per pore volume in the ME phase is obtained as follows:

$$N_{oil,3} = \xi_2 C_{23} \tilde{C}_3 / C_{33} \qquad \text{Eq.6.244}$$

The derivatives of Eq.6.244 are

$$\frac{\partial N_{oil,3}}{\partial V} = \frac{\partial \xi_2}{\partial V} C_{23} \tilde{C}_3 / C_{33} + \frac{\partial C_{23}}{\partial V} \xi_2 \tilde{C}_3 / C_{33} + \frac{\partial \tilde{C}_3}{\partial V} \xi_2 C_{23} / C_{33} - \frac{\partial C_{33}}{\partial V} \xi_2 C_{23} \tilde{C}_3 / C_{33}^2 \qquad \text{Eq.6.245}$$

Number of moles of each hydrocarbon component in ME phase is calculated as follows:

$$N_{i,3} = \frac{N_i N_{oil,3}}{\sum_{i=1}^{n_c} N_i} \qquad \text{Eq.6.246}$$

The derivative of Eq.6.246 for hydrocarbon component *i* WRT hydrocarbon component *k*, is

$$\frac{\partial N_{i,3}}{\partial N_k} = \begin{cases} \dfrac{N_{oil,3} + N_i \dfrac{\partial N_{oil,3}}{\partial N_k}}{\sum_{i=1}^{n_c} N_i} - \dfrac{N_i N_{oil,3}}{\left(\sum_{i=1}^{n_c} N_i\right)^2} & if \quad i = k \\ \dfrac{N_i}{\sum_{i=1}^{n_c} N_i} \dfrac{\partial N_{oil,3}}{\partial N_k} - \dfrac{N_i N_{oil,3}}{\left(\sum_{i=1}^{n_c} N_i\right)^2} & if \quad i \neq k \end{cases} \qquad \text{Eq.6.247}$$

Derivative of Eq.6.246 for hydrocarbon component *i* WRT aqueous component *k*, is

$$\frac{\partial N_{i,3}}{\partial N_k} = \frac{N_i}{\sum_{i=1}^{n_c} N_i} \frac{\partial N_{oil,3}}{\partial N_k} \qquad \text{Eq.6.248}$$

The derivative WRT pressure is

$$\frac{\partial N_{i,3}}{\partial P} = \frac{N_i}{\sum_{i=1}^{n_c} N_i} \frac{\partial N_{oil,3}}{\partial P} \qquad \text{Eq.6.249}$$

The aqueous components are partitioned into the aqueous and ME phases according to the volume of water in each phase (Eq.6.193 through Eq.6.200). Total number of moles in the ME phase is computed as follows:

$$N_{T,3} = N_{water,3} + N_{oil,3} + N^f_{surf} + N_{poly,3} + N_{salt,3} + N_{trac,3} \qquad \text{Eq.6.250}$$

$$\frac{\partial N_{T,3}}{\partial V} = \frac{\partial N_{water,3}}{\partial V} + \frac{\partial N_{oil,3}}{\partial V} + \frac{\partial N^f_{surf}}{\partial V} + \frac{\partial N_{npoly,3}}{\partial V} + \frac{\partial N_{salt,3}}{\partial V} + \frac{\partial N_{trac,3}}{\partial V} \qquad \text{Eq.6.251}$$

The mole fractions of components in the ME phase and the derivatives follow Eq.6.205 and Eq.6.206, respectively. Calculation of the aqueous phase mole fractions is similar to what was explained in Eq.6.210 through Eq.6.222. Since we assume that the composition of the solubilized oil in the ME is the same as that of the free excess oil, the mole fraction of each hydrocarbon component in the oleic phase does not change and is computed from Eq.6.224 with derivatives given in Eq.6. 225 through Eq.6.227.

Relative Permeabilities as a Function of Trapping Number

The calculation of the IFTs and relative permeabilities is function of the phase behavior. Corey type relative permeability functions are used. The residual saturations and relative permeability curves are functions of the trapping number (Delshad, 1990). Here we describe the relative permeability calculation for each phase environment.

Two Phases Aqueous and Oleic

The relative permeabilities are obtained as follows:

$$k_{rj} = k_{rj}^{\,o}\,\overline{S}_j^{\,n_j} \qquad \text{Eq.6.252}$$

where

$$k_{rj}^{o} = k_{rj}^{o^{Low}} + \frac{S_{j'r}^{Low} - S_{j'r}}{S_{j'r}^{Low} - S_{j'r}^{High}}\left(k_{rj}^{o^{High}} - k_{rj}^{o^{Low}}\right) \qquad \text{Eq.6.253}$$

$$\overline{S}_j = \frac{S_j - S_{jr}}{1 - S_{jr} - S_{j'r}} \qquad \text{Eq.6.254}$$

where

$$S_j = \begin{cases} \left(\dfrac{N_{water}}{\xi_{water}} + \dfrac{N_{surf}^{f}}{\xi_{surf}}\right)\dfrac{1}{\left(1-\hat{C}_3\right)} & if \quad j=1 \\ \dfrac{\sum_{i=1}^{n_c} N_i}{\xi_2\left(1-\hat{C}_3\right)} & if \quad j=2 \\ 0 \quad if \quad j=3 \end{cases} \qquad \text{Eq.6.255}$$

$$\frac{\partial S_1}{\partial V} = \begin{cases} \left(\dfrac{1}{\xi_{water}} + \dfrac{1}{\xi_{surf}} \dfrac{\partial N_{surf}^f}{\partial V} \right) & for \quad water \\ \dfrac{1}{\xi_{surf}} \dfrac{\partial N_{surf}^f}{\partial V} & for \quad surf \\ -\xi_{water}^o c_{water} \dfrac{N_{water}}{\xi_{water}^2} + \dfrac{1}{\xi_{surf}} \dfrac{\partial N_{surf}}{\partial V} - & \\ \xi_{surf}^o c_{surf} \dfrac{N_{surf}}{\xi_{surf}^2} & for \quad P \\ 0 & for \quad other \quad parameters \end{cases} \qquad \text{Eq.6.256}$$

$$\frac{\partial S_2}{\partial V} = \begin{cases} \dfrac{1}{\xi_2} - \dfrac{\sum_{i=1}^{n_c} N_i}{\xi_2^2} \dfrac{\partial \xi_2}{\partial V} & for \quad hydrocarbons \\ -\dfrac{\sum_{i=1}^{n_c} N_i}{\xi_2^2} \dfrac{\partial \xi_2}{\partial V} & for \quad P \\ 0 & for \quad other \quad parameters \end{cases} \qquad \text{Eq.6.257}$$

$$S_{jr} = \min \left\{ S_j, S_{jr}^{High} + \frac{S_{jr}^{Low} - S_{jr}^{High}}{1 + T_j N_{T_j}^{\tau_j}} \right\} \qquad \text{Eq.6.258}$$

End point and exponent of the relative permeability of phase j is scaled based on the saturation of its conjugate phase, j'. Trapping number is given in Eq.3.15. For a special case when the principal direction of permeability tensor is on the x, y, and z axes of the simulation and the reservoir is horizontal (not dipped), one can write Eq.3.15 as follows (Jin, 1994):

$$N_{T_j} = 2.23\times10^{-8}\frac{1}{\sigma_{jj'}}\left\{\begin{array}{l}\left(k_x\left(-\frac{\partial\Phi_{j'}}{\partial x}\right)\right)^2+\left(k_y\left(-\frac{\partial\Phi_{j'}}{\partial y}\right)\right)^2+\\ \left(k_z\left(-\frac{\partial\Phi_{j'}}{\partial z}\right)\right)^2+2\frac{\partial\Phi_{j'}}{\partial z}k_z^2\rho_j g+\left(k_z\rho_j g\right)^2\end{array}\right\}^{1/2} \quad \text{Eq.6.259}$$

where

$$\sigma_{jj'} = \sigma_{ow} \quad \text{Eq.6.260}$$

$\Phi_{j'}$ in Eq.6.259 is the flow potential of the conjugate phase that is pushing the displaced phase. It should be noted that in this case the surfactant concentration is below the CMC and it is assumed that surfactant does not form a ME phase or change the IFT between the oleic and aqueous phases. The definition of trapping number given in Eq.6.259 is taken from Jin (1994) for a special case when the principal direction of permeability tensor is in the directions of x, y, and z axes of the simulation.

The endpoint and exponent of the relative permeability curves, k_{rj}^o and n_j, are linearly interpolated between their values at high and low trapping number based on the residual saturation of the conjugate phase. In this case, it is obvious that the conjugate of the oleic phase is the aqueous phase and visa versa. This relationship for the relative permeability endpoints is stated in Eq.6.253. For relative permeability exponents we have

$$n_j = n_j^{Low} + \frac{S_{j'r}^{Low} - S_{j'r}}{S_{j'r}^{Low} - S_{j'r}^{High}}\left(n_j^{High} - n_j^{Low}\right) \quad \text{Eq.6.261}$$

The derivatives of the relative permeability curves are written as follows:

$$\frac{\partial k_{rj}}{\partial V} = \frac{\partial k_{rj}^o}{\partial V}\overline{S}_j^{n_j} + k_{rj}^o\left(n_j\overline{S}_j^{n_j-1}\frac{\partial\overline{S}_j}{\partial V} + \overline{S}_j^{n_j}\ln\left(\overline{S}_j\right)\frac{\partial n_j}{\partial V}\right) \quad \text{Eq.6.262}$$

where

$$\frac{\partial k_{rj}^o}{\partial V} = -\frac{k_{rj}^{o^{High}} - k_{rj}^{o^{Low}}}{S_{j'r}^{Low} - S_{j'r}^{High}}\frac{\partial S_{j'r}}{\partial V} \quad \text{Eq.6.263}$$

where

$$\frac{\partial S_{jr}}{\partial V} = -\frac{\tau_j T_j N_{T_j}^{\tau_j - 1}\left(S_{jr}^{Low} - S_{jr}^{High}\right)}{\left(1 + T_j N_{T_j}^{\tau_j}\right)^2}\frac{\partial N_{T_j}}{\partial V} \qquad \text{Eq.6.264}$$

where

$$\frac{\partial N_{T_j}}{\partial V} = 4.9729\times 10^{-16}\frac{g k_z^2}{\sigma_{jj'}{}^2 N_{T_j}}\left(\rho_j g \frac{\partial \Phi_{j'}}{\partial z}\right)\frac{\partial \rho_j}{\partial V} \qquad \text{Eq.6.265}$$

where

$$\frac{\partial \rho_j}{\partial V} = \frac{\partial\left(\xi_j \overline{M}_j\right)}{\partial V} = \frac{\partial \xi_j}{\partial V}\overline{M}_j + \xi_j \frac{\partial \overline{M}_j}{\partial V} \qquad \text{Eq.6.266}$$

where

$$\frac{\partial \overline{M}_j}{\partial V} = \begin{cases} 0 \quad if \quad j = 1 \\ \sum_{i=1}^{n_c} \frac{\partial x_{ij}}{\partial V} M_j \quad if \quad j = 2 \end{cases} \qquad \text{Eq.6.267}$$

$$\frac{\partial \overline{S}_j}{\partial V} = \frac{\left(\frac{\partial S_j}{\partial V} - \frac{\partial S_{jr}}{\partial V}\right)}{\left(1 - S_{jr} - S_{j'r}\right)} + \frac{\left(S_j - S_{jr}\right)\left(\frac{\partial S_{j'r}}{\partial V} + \frac{\partial S_{jr}}{\partial V}\right)}{\left(1 - S_{jr} - S_{j'r}\right)^2} \qquad \text{Eq.6.268}$$

$$\frac{\partial n_j}{\partial V} = -\frac{n_j^{High} - n_j^{Low}}{S_{j'r}^{Low} - S_{j'r}^{High}}\frac{\partial S_{j'r}}{\partial V} \qquad \text{Eq.6.269}$$

Aqueous and ME

The formulation is the same as the one specified above except that surfactant concentration is above CMC, the ME phase is formed, and IFT is reduced. Based on the above, Eq.6.252 through Eq.6.254 are relevant to the Type II system except that in this case the conjugate of the aqueous phase is the ME phase and visa versa. Hydrocarbon components are present in the ME phase only. Phase saturations and their derivatives are obtained as follows:

$$S_j = \begin{cases} \dfrac{N_{water} - N_{water,3}}{\xi_{water}\left(1-\hat{C}_3\right)} & if \quad j=1 \\ 0 \quad if \quad j=2 \\ \left(\dfrac{N_{water,3}}{\xi_{water}} + \dfrac{\sum_{i=1}^{n_c} N_i}{\xi_2} + \dfrac{N_{surf}^f}{\xi_{surf}} \right) \dfrac{1}{\left(1-\hat{C}_3\right)} & if \quad j=3 \end{cases} \qquad \text{Eq.6.270}$$

$$\frac{\partial S_1}{\partial V} = \begin{cases} \left(1 - \dfrac{\partial N_{water,3}}{\partial V}\right)\dfrac{1}{\xi_{water}} \; for\ water \\ -\dfrac{\partial N_{water,3}}{\partial V}\dfrac{1}{\xi_{water}} \; for\ surf\ and\ salt \\ -\dfrac{\partial N_{water,3}}{\partial V}\dfrac{1}{\xi_{water}} - \xi_{water}^o c_{water} \dfrac{N_{water} - N_{water,3}}{\xi_{water}^2} \; for\ P \\ 0 \; for\ other\ parameters \end{cases} \qquad \text{Eq.6.271}$$

$$\frac{\partial S_3}{\partial V} = \begin{cases} \dfrac{1}{\xi_2} - \sum_{i=1}^{n_c} N_i \dfrac{1}{\xi_2^2}\dfrac{\partial \xi_2}{\partial V} \; for\ hydrocarbons \\ \dfrac{1}{\xi_{water}}\dfrac{\partial N_{water,3}}{\partial V} + \dfrac{1}{\xi_{surf}}\dfrac{\partial N_{surf}^f}{\partial V} \; for\ water, salt, surf \\ \dfrac{1}{\xi_{water}}\dfrac{\partial N_{water,3}}{\partial V} - \xi_{water}^o c_{water}\dfrac{N_{water,3}}{\xi_{water}^2} - \sum_{i=1}^{n_c} N_i \dfrac{1}{\xi_2^2}\dfrac{\partial \xi_2}{\partial V} \\ + \dfrac{1}{\xi_{surf}}\dfrac{\partial N_{surf}^f}{\partial V} - \xi_{surf}^o c_{surf}\dfrac{N_{surf}^f}{\xi_{surf}^2} \; for\ P \\ 0 \; for\ other\ parameters \end{cases} \qquad \text{Eq.6.272}$$

The derivatives of oil saturation are zero. Eq.6.258 is used for calculation of the residual saturations and Eq.6.259 gives the trapping number. The IFT between the aqueous/ME interface is calculated based on Chun Huh equation (1979) modified by Hirasaki (1981) and Delshad et al. (1996), as follows:

$$\sigma_{jj'} = \sigma_{ow} e^{-aR_{13}} + \frac{cF_2}{R_{13}^2}\left(1 - e^{-aR_{13}^3}\right) \qquad \text{Eq.6.273}$$

where

$$F_2 = \frac{1-\exp\left(-\sqrt{\sum_{k=1}^{3}\left(C_{k1}-C_{k3}\right)^2}\right)}{1-e^{-\sqrt{2}}} \qquad \text{Eq.6.274}$$

Eqs.6.258 through 6.264 are relevant for this case except Eq.6.260 which is replaced with Eq.6.274. The derivatives of the trapping number are as follows:

$$\frac{\partial N_{T_j}}{\partial V} = 4.9729\times10^{-16}\frac{gk_z^2}{{\sigma_{jj'}}^2 N_{T_j}}\left(\rho_j g - \frac{\partial P_{j'}}{\partial z}\right)\frac{\partial \rho_j}{\partial V} - \frac{N_{Tj}}{\sigma_{jj'}}\frac{\partial \sigma_{jj'}}{\partial V} \qquad \text{Eq.6.275}$$

The mass density of the ME phase is calculated as follows:

$$\rho_3 = \left(C_{13}+C_{33}\right)\rho_1 + C_{23}\rho_2 \qquad \text{Eq.6.276}$$

It should be noted that although an oleic phase does not exist in this case, we would still need to calculate the oil density and its derivatives to be used for calculation of the ME density. Equations 6.266 and 6.267 are used for the oleic and aqueous phases and the derivative of the ME mass density is calculated as follows:

$$\frac{\partial \rho_3}{\partial V} = \left(\frac{\partial C_{13}}{\partial V}+\frac{\partial C_{33}}{\partial V}\right)\rho_1 + \left(C_{13}+C_{33}\right)\frac{\partial \rho_1}{\partial V} + \frac{\partial C_{23}}{\partial V}\rho_2 + C_{23}\frac{\partial \rho_2}{\partial V} \qquad \text{Eq.6.277}$$

The derivative of the IFT in Eq.6.275 is calculated as follows:

$$\frac{\partial \sigma_{jj'}}{\partial V} = \frac{c}{R_{13}^2}\left(1-e^{-aR_{13}^3}\right)\frac{\partial F_2}{\partial V} + \left[-a\sigma_{ow}e^{-aR_{13}} + cF_2\left(3ae^{-aR_{13}^3} - \frac{2\left(1-e^{-aR_{13}^3}\right)}{R_{13}^3}\right)\right]\frac{\partial R_{13}}{\partial V} \qquad \text{Eq.6.278}$$

where

$$\frac{\partial F_2}{\partial V} = \frac{e^{-f}}{1-e^{-\sqrt{2}}}\frac{\partial f}{\partial V} \qquad \text{Eq.6.279}$$

where

$$f = \sqrt{\sum_{k=1}^{k=3}\left(C_{k1}-C_{k3}\right)^2} \qquad \text{Eq.6.280}$$

$$\frac{\partial f}{\partial V} = \frac{\partial \sqrt{g}}{\partial V} = \frac{1}{2\sqrt{g}}\frac{\partial g}{\partial V} \qquad \text{Eq.6.281}$$

where

$$g = \sum_{k=1}^{k=3} \left(C_{k1} - C_{k3} \right)^2 \; and \; \left(C_{11} = 1, C_{21} = C_{31} = 0 \right) \qquad \text{Eq.6.282}$$

$$\frac{\partial g}{\partial V} = -2\left(1 - C_{13}\right)\frac{\partial C_{13}}{\partial V} + 2\left(C_{23}\frac{\partial C_{23}}{\partial V} + C_{33}\frac{\partial C_{33}}{\partial V} \right) \qquad \text{Eq.6.283}$$

The derivatives of the normalized saturation and the relative permeability exponent are the same as specified in Eqs.6.268 and 6.269.

Oleic and ME

The calculation of relative permeability curves is very similar to what was specified above for aqueous and ME phases except that in this case we need to calculate the IFT between the ME/oleic interface. Equations 6.252 through 6.254 are used. Aqueous components are in the ME phase only and phase saturations and the derivatives are as follows:

$$S_j = \begin{cases} 0 \quad if \quad j = 1 \\ \dfrac{1}{\left(1 - \hat{C}_3\right)\xi_2}\left(\sum_{i=1}^{n_c} N_i - N_{oil,3} \right) \quad if \quad j = 2 \\ \left(\dfrac{N_{water}}{\xi_{water}} + \dfrac{N_{surf}^f}{\xi_{surf}} + \dfrac{N_{oil,3}}{\xi_2} \right)\dfrac{1}{\left(1 - \hat{C}_3\right)} \quad if \quad j = 3 \end{cases} \qquad \text{Eq.6.284}$$

$$\frac{\partial S_2}{\partial V} = \begin{cases} \left(1 - \dfrac{\partial N_{oil,3}}{\partial V}\right)\dfrac{1}{\xi_2} - \left(\sum_{i=1}^{n_c} N_i - N_{oil,3} \right)\dfrac{1}{\xi_2^2}\dfrac{\partial \xi_2}{\partial V} \quad for \quad hydrocarbons \\ -\dfrac{\partial N_{oil,3}}{\partial V}\dfrac{1}{\xi_2} \quad for \quad salt, surf \\ -\dfrac{\partial N_{oil,3}}{\partial V}\dfrac{1}{\xi_2} - \left(\sum_{i=1}^{n_c} N_i - N_{oil,3} \right)\dfrac{1}{\xi_2^2}\dfrac{\partial \xi_2}{\partial V} \quad for \quad P \\ 0 \quad for \quad other \quad parameters \end{cases} \qquad \text{Eq.6.285}$$

$$\frac{\partial S_3}{\partial V}=\begin{cases}\dfrac{1}{\xi_2}\dfrac{\partial N_{oil,3}}{\partial V}-\dfrac{N_{oil,3}}{\xi_2^2}\dfrac{\partial \xi_2}{\partial V} & for\quad hydrocarbons\\ \dfrac{1}{\xi_{water}}+\dfrac{1}{\xi_{surf}}\dfrac{\partial N_{surf}^f}{\partial V} & for\quad water\\ \dfrac{1}{\xi_{surf}}\dfrac{\partial N_{surf}^f}{\partial V}+\dfrac{1}{\xi_2}\dfrac{\partial N_{oil,3}}{\partial V} & for\quad salt,surf\\ -\xi_{water}^o c_{water}\dfrac{N_{water}}{\xi_{water}^2}+\dfrac{1}{\xi_2}\dfrac{\partial N_{oil,3}}{\partial V}-\dfrac{N_{oil,3}}{\xi_2^2}\dfrac{\partial \xi_2}{\partial V} & \\ +\dfrac{1}{\xi_{surf}}\dfrac{\partial N_{surf}^f}{\partial V}-\xi_{surf}^o c_{surf}\dfrac{N_{surf}^f}{\xi_{surf}^2} & for\quad P\\ 0 & for\quad other\quad parameters\end{cases} \qquad \text{Eq.6.286}$$

The derivatives of the aqueous phase saturation are zero. Equation 6.258 is used for residual phase saturations and Eq.6.259 gives the trapping number. The IFT of ME/oleic phases is calculated as follows:

$$\sigma_{jj'}=\sigma_{ow}e^{-aR_{23}}+\frac{cF_2}{R_{23}^2}\left(1-e^{-aR_{23}^3}\right) \qquad \text{Eq.6.287}$$

where

$$F_2=\frac{1-\exp\left(-\sqrt{\sum_{k=1}^{3}\left(C_{k2}-C_{k3}\right)^2}\right)}{1-e^{-\sqrt{2}}} \qquad \text{Eq.6.288}$$

We can use Eqs.6.261 through 6.264 for calculation of relative permeability exponents, the derivative of the relative permeability, the derivative of the endpoint relative permeability and derivative of residual saturation, respectively. The derivative of the trapping number is obtained using Eq.6.275. ME mass density is calculated using Eq.6.276 and the derivative of the ME mass density is obtained from Eq.6.277. Equations 6.266 and 6.267 are used to calculate the mass density of the oleic and aqueous phases and the derivatives. The derivative of the IFT is calculated as follows:

$$\frac{\partial \sigma_{jj'}}{\partial V} = \frac{c}{R_{23}^2}\left(1 - e^{-aR_{23}^3}\right)\frac{\partial F_2}{\partial V} + \left[-a\sigma_{ow}e^{-aR_{23}} + cF_2\left(3ae^{-aR_{23}^3} - \frac{2\left(1 - e^{-aR_{23}^3}\right)}{R_{23}^3}\right)\right]\frac{\partial R_{23}}{\partial V} \quad \text{Eq.6.289}$$

where

$$\frac{\partial F_2}{\partial V} = \frac{e^{-f}}{1 - e^{-\sqrt{2}}}\frac{\partial f}{\partial V} \quad \text{Eq.6.290}$$

where

$$f = \sqrt{\sum_{k=1}^{k=3}\left(C_{k2} - C_{k3}\right)^2} \quad \text{Eq.6.291}$$

$$\frac{\partial f}{\partial V} = \frac{\partial \sqrt{g}}{\partial V} = \frac{1}{2\sqrt{g}}\frac{\partial g}{\partial V} \quad \text{Eq.6.292}$$

where

$$g = \sum_{k=1}^{k=3}\left(C_{k2} - C_{k3}\right)^2 \; and \; \left(C_{22} = 1, C_{12} = C_{32} = 0\right) \quad \text{Eq.6.293}$$

$$\frac{\partial g}{\partial V} = -2\left(1 - C_{23}\right)\frac{\partial C_{23}}{\partial V} + 2\left(C_{13}\frac{\partial C_{13}}{\partial V} + C_{33}\frac{\partial C_{33}}{\partial V}\right) \quad \text{Eq.6.294}$$

The derivatives of the normalized saturation and the relative permeability exponent are the same as what is specified in Eq.6.268 and Eq.6.269.

Aqueous, Oleic and ME

We assume that the conjugate of the oleic phase is the aqueous phase and visa versa. For the ME phase, the conjugate is determined based on the saturation of the oleic and aqueous phases. If the aqueous phase is at residual saturation and the saturation of the oleic phase is above residual, then the oleic phase is assumed to be the conjugate of the ME phase. Otherwise the aqueous phase is assumed to be the conjugate of the ME phase. The relative permeability of each phase is calculated from Eq.6.252 and the relative permeability endpoint is calculated from Eq.6.253. Normalized saturations are obtained from Eq.6.295.

$$\bar{S}_\ell = \frac{S_\ell - S_{\ell r}}{1 - \sum_{\ell=1}^{3} S_{\ell r}} \qquad \text{Eq.6.295}$$

The phase saturations and the derivatives are calculated below:

$$S_j = \begin{cases} \dfrac{N_w - N_{water,3}}{\left(1-\hat{C}_3\right)\xi_w} & if \quad j=1 \\ \dfrac{\sum_{i=1}^{n_c} N_i - N_{oil,3}}{\left(1-\hat{C}_3\right)\xi_2} & if \quad j=2 \\ \dfrac{1}{\left(1-\hat{C}_3\right)}\left(\dfrac{N_{surf}^f}{\xi_{surf}} + \dfrac{N_{water,3}}{\xi_w} + \dfrac{N_{oil,3}}{\xi_2}\right) & if \quad j=3 \end{cases} \qquad \text{Eq.6.296}$$

Derivatives of the aqueous, oleic and ME phases are obtained from Eq.6.271, Eq.6.285 and Eq.6.286, respectively. Residual saturations and trapping number are the same as Eqs.6.258 and 6.259. Equation 6.273 gives the IFT for the aqueous/ME and the IFT of the oleic/ME is obtained from Eq.6.287. The derivatives of the trapping number are calculated from Eq.6.275. Equations 6.266 and 6.267 are used to calculate the mass density of the aqueous and oleic phases and the derivatives. Mass density of the ME phase and its derivatives are specified in Eq.6.276 and Eq.6.277 respectively. Equations 6.278 through 6.283 are used to calculate the derivatives of the aqueous/ME IFT. Equations 6.289 through Eq.6.294 give the derivatives of the oleic/ME IFT. Derivatives of normalized saturations and the relative permeability exponents are obtained from Eq.6.268 and Eq.6.269 respectively.

Phase Viscosities

There are two options in GPAS for oleic viscosity calculation. It could be obtained from the equation of state as a function of pressure, temperature and composition, or it could be specified by the user as an input. If oil viscosity is specified by the user, then it is assumed to remain constant during the simulation for the following reasons:

1. The simulation is assumed to be isothermal and thus the oil viscosity does not change due a change in temperature.

2. Oil composition is constant and thus oil viscosity cannot change due to a change in the composition.
3. Polymer is water soluble and since no water is assumed in the oleic phase, then there is no polymer in the oleic phase to change its viscosity.
4. Neglect the effect of pressure on oil viscosity.

The aqueous and ME viscosity in the absence of polymer is calculated as follows:

$$\mu_\ell = C_{1\ell}\mu_w e^{\alpha_1(C_{2\ell}+C_{3\ell})} + C_{2\ell}\mu_o e^{\alpha_2(C_{1\ell}+C_{3\ell})} + C_{3\ell}\alpha_3 e^{(\alpha_4 C_{1\ell}+\alpha_5 C_{2\ell})} \quad for \quad \ell = 1 or 3 \qquad \text{Eq.6.297}$$

Eq.6.297

$$\begin{aligned}\frac{\partial \mu_\ell}{\partial V} = {} & \frac{\partial C_{1\ell}}{\partial V}\left(\mu_w e^{\alpha_1(C_{2\ell}+C_{3\ell})} + C_{2\ell}\mu_o\alpha_2 e^{\alpha_2(C_{1\ell}+C_{3\ell})} + C_{3\ell}\alpha_3\alpha_4 e^{(\alpha_4 C_{1\ell}+\alpha_5 C_{2\ell})}\right) \\ & + \frac{\partial C_{2\ell}}{\partial V}\left(\mu_o e^{\alpha_2(C_{1\ell}+C_{3\ell})} + C_{1\ell}\mu_w\alpha_1 e^{\alpha_1(C_{2\ell}+C_{3\ell})} + C_{3\ell}\alpha_3\alpha_5 e^{(\alpha_4 C_{1\ell}+\alpha_5 C_{2\ell})}\right) \\ & + \frac{\partial C_{3\ell}}{\partial V}\left(\alpha_3 e^{(\alpha_4 C_{1\ell}+\alpha_5 C_{2\ell})} + C_{1\ell}\mu_w\alpha_1 e^{\alpha_1(C_{2\ell}+C_{3\ell})} + C_{2\ell}\mu_o\alpha_2 e^{\alpha_2(C_{1\ell}+C_{3\ell})}\right)\end{aligned} \qquad \text{Eq.6.298}$$

where α_1 through α_5 are input parameters obtained by matching the measured ME phase viscosities in the lab.

If polymer is added to the surfactant solution, the aqueous and ME phase viscosities are calculated as follows:

$$\mu_\ell = C_{1\ell}\mu_p e^{\alpha_1(C_{2\ell}+C_{3\ell})} + C_{2\ell}\mu_o e^{\alpha_2(C_{1\ell}+C_{3\ell})} + C_{3\ell}\alpha_3 e^{(\alpha_4 C_{1\ell}+\alpha_5 C_{2\ell})} \quad for \quad \ell = 1,3 \qquad \text{Eq.6.299}$$

where

$$\mu_p^o = \mu_w\left(1+\left(A_{p1}C_{4\ell} + A_{p2}C_{4\ell}^2 + A_{p3}C_{4\ell}^3\right)C_{SE}^{S_p}\right) \qquad \text{Eq.6.300}$$

Eq.6.300 specifies the dependency of polymer viscosity on polymer concentration and salinity. Polymer viscosity is also a strong function of shear rate and is modeled as follows (Meter and Bird, 1964).

$$\mu_p = \frac{\mu_p^o - \mu_w}{1+\left(\frac{\dot{\gamma}}{\dot{\gamma}_{1/2}}\right)^{P_\alpha - 1}} \qquad \text{Eq.6.301}$$

where $\dot{\gamma}_{1/2}$ is the shear rate at which viscosity is the average of μ_p^o and μ_w and P_α is an empirical coefficient. Meter and Bird (1964) have developed Eq.6.301 for flow of polymer in tubes. In a permeable medium, μ_p is the apparent viscosity and the shear rate is an equivalent shear rate, $\dot{\gamma}_{eq}$. The in-situ shear rate for phase ℓ is obtained from modified Blake-Kozeney capillary bundle equation for multiphase flow (Lin, 1981, Sorbie, 1991).

$$\dot{\gamma}_{eq} = \frac{\dot{\gamma}_c |u_\ell|}{\sqrt{\bar{k} k_{r\ell} \phi S_\ell}} \qquad \text{Eq.6.302}$$

$$\frac{\partial \dot{\gamma}_{eq}}{\partial V} = \begin{cases} -\dot{\gamma}_c |u_\ell| \dfrac{(k_{r\ell}\phi S_\ell)^{-1.5}}{2(\bar{k})^{0.5}} \left(\begin{array}{l} \phi S_\ell \dfrac{\partial k_{r\ell}}{\partial V} + \\ k_{r\ell}\phi \dfrac{\partial S_\ell}{\partial V} + k_{r\ell} S_\ell \phi_r c_f \end{array} \right) & for \quad P \\ -\dot{\gamma}_c |u_\ell| \dfrac{(k_{r\ell}\phi S_\ell)^{-1.5}}{2(\bar{k})^{0.5}} \left(\begin{array}{l} \phi S_\ell \dfrac{\partial k_{r\ell}}{\partial V} + \\ k_{r\ell}\phi \dfrac{\partial S_\ell}{\partial V} \end{array} \right) & for \quad other \quad parameters \end{cases} \qquad \text{Eq.6.303}$$

where $\dot{\gamma}_c$ is equal to $3.97C$ sec^{-1} and C is the shear rate coefficient used for taking non-ideal effects such as slip at the pore wall into account (Wreath *et al*., 1990; Sorbie, 1991). The average permeability used in Eq.6.302 is calculated as follows:

$$\bar{k} = \left[\frac{1}{k_x} \left(\frac{u_{x\ell}}{u_\ell} \right)^2 + \frac{1}{k_y} \left(\frac{u_{y\ell}}{u_\ell} \right)^2 + \frac{1}{k_z} \left(\frac{u_{z\ell}}{u_\ell} \right)^2 \right]^{-1} \qquad \text{Eq.6.304}$$

The derivatives of Eq.6.299 are obtained as follows:

$$\begin{aligned} \frac{\partial \mu_\ell}{\partial V} &= C_{1\ell} e^{\alpha_1 (C_{2\ell} + C_{3\ell})} \frac{\partial \mu_p}{\partial V} \\ &+ \frac{\partial C_{1\ell}}{\partial V} \left(\mu_w e^{\alpha_1 (C_{2\ell} + C_{3\ell})} + C_{2\ell} \mu_o \alpha_2 e^{\alpha_2 (C_{1\ell} + C_{3\ell})} + C_{3\ell} \alpha_3 \alpha_4 e^{(\alpha_4 C_{1\ell} + \alpha_5 C_{2\ell})} \right) \\ &+ \frac{\partial C_{2\ell}}{\partial V} \left(\mu_o e^{\alpha_2 (C_{1\ell} + C_{3\ell})} + C_{1\ell} \mu_w \alpha_1 e^{\alpha_1 (C_{2\ell} + C_{3\ell})} + C_{3\ell} \alpha_3 \alpha_5 e^{(\alpha_4 C_{1\ell} + \alpha_5 C_{2\ell})} \right) \\ &+ \frac{\partial C_{3\ell}}{\partial V} \left(\alpha_3 e^{(\alpha_4 C_{1\ell} + \alpha_5 C_{2\ell})} + C_{1\ell} \mu_w \alpha_1 e^{\alpha_1 (C_{2\ell} + C_{3\ell})} + C_{2\ell} \mu_o \alpha_2 e^{\alpha_2 (C_{1\ell} + C_{3\ell})} \right) \end{aligned} \qquad \text{Eq.6.305}$$

where

$$\frac{\partial \mu_p}{\partial V} = \mu_w C_{SE}^{S_p - 1} \begin{bmatrix} C_{SE}\left(A_{p1} + 2A_{p2}C_{4\ell} + 3A_{p3}C_{4\ell}^2\right)\dfrac{\partial C_{4\ell}}{\partial V} \\ +S_p\left(A_{p1}C_{4\ell} + A_{p2}C_{4\ell}^2 + A_{p3}C_{4\ell}^3\right)\dfrac{\partial C_{SE}}{\partial V} \end{bmatrix} \qquad \text{Eq.6.306}$$

If shear rate dependency of polymer viscosity is modeled, then the derivatives of Eq.6.306 are used in the RHS of Eq.6.307 to obtain the final derivatives of polymer viscosity as follows:

$$\frac{\partial \mu_p}{\partial V} = \beta \frac{\partial \mu_p}{\partial V} - \frac{1 - P_\alpha}{\beta^2}\left(\mu_p^o - \mu_w\right)\dot{\gamma}_{1/2}^{1-P_\alpha}\dot{\gamma}_{eq}^{P_\alpha - 2}\frac{\partial \dot{\gamma}_{eq}}{\partial V} \qquad \text{Eq.6.307}$$

where

$$\beta = 1 + \left(\frac{\dot{\gamma}_{eq}}{\dot{\gamma}_{1/2}}\right)^{P_\alpha - 1} \qquad \text{Eq.6.308}$$

This concludes the formulation of the chemical flooding module.

6.2.4 Solution Procedure

Finite difference scheme is applied to Eq.6.3 and Eq.6.4 and the resulting $n_b(n_c+n_a+2)$ equations for n_b number of gridblocks are solved simultaneously using the fully implicit algorithm. Each gridblock has n_c+n_a+2 unknowns denoted as follows:

$$\vec{x}_I = \left(N_1, ..., N_{n_c}, N_{n_c+1}, ..., N_{n_c+n_a}, P_1, N_{H2O}\right) \qquad \text{Eq.6.309}$$

where subscript I denotes I^{th} gridblock. The vector of total unknowns consists of n_b vectors of Eq.6.309 such as the one shown in Eq.6.310:

$$\vec{x} = \left(\vec{x}_1, \vec{x}_2, ..., \vec{x}_{n_b}\right) \qquad \text{Eq.6.310}$$

Newton's method is used to solve the non-linear system of equations. The residual vector (Eq.6.1) and the finite difference formulation of Eqs.6.3 and 6.4 (as a function of $\vec{x}$) is then evaluated. $\vec{x}$ is considered as the solution vector in the new time level if the constraint of $\vec{R}(\vec{x}) \approx \vec{0}$ is satisfied. Other convergence criteria such as "sufficiently small" pressure and saturation changes for a given change in $\vec{x}$ can also be used. This criterion becomes very useful when a small change in composition causes a large saturation change.

Newton's method is applied in three steps to solve the system of equations described above.

1. Guess a solution vector. Usually the solution vector at the old timestep is used as the initial guess for the next step. At the beginning of the simulation, the initial conditions are used as the guessed solution vector.
2. The guessed solution vector is used to calculate the residual vector. The convergence is checked to see if the solution is good enough. In order to calculate the residual vector, one needs to calculate the variables depending on $\vec{x}$ such as molar density, molar composition, relative permeability, phase viscosities and sink and source terms. Section 6.2.3 describes this procedure in detail.
3. If the residual vector is converged, then the guessed solution is accepted as the true solution of the system for the new timestep. If the residual vector has not converged then a new solution vector is guessed using the Jacobian (*J*) of the system evaluated at the current guessed solution. Steps 2 and 3 are then repeated until convergence is reached. The new solution vector is guessed by updating $\vec{X}$ as follows:

$$\vec{X}^{new} = \vec{X}^{old} + \Delta\vec{X} \qquad \text{Eq.6.311}$$

where $\Delta\vec{X}$ is obtained from Eq.6.312:

$$J\left(\vec{X}^{old}\right)\Delta\vec{X} = -\vec{R}\left(\vec{X}^{old}\right) \qquad \text{Eq.6.312}$$

Equation 6.312 is written as follows:

$$\begin{pmatrix} J_{1,1} & J_{1,2} & \dots & J_{1,n_b} \\ J_{2,1} & J_{2,2} & \dots & J_{2,n_b} \\ . & & & . \\ . & & & . \\ . & & & . \\ J_{n_b,1} & J_{n_b,2} & \dots & J_{n_b,n_b} \end{pmatrix} \begin{pmatrix} \Delta\vec{X}_1 \\ \Delta\vec{X}_2 \\ . \\ . \\ . \\ \Delta\vec{X}_{n_b} \end{pmatrix} = - \begin{pmatrix} \vec{R}_1 \\ \vec{R}_2 \\ . \\ . \\ . \\ \vec{R}_{n_b} \end{pmatrix} \qquad \text{Eq.6.313}$$

where

$$J_{I,J}=\begin{pmatrix}
\frac{\partial R_v|_I}{\partial N_1|_J} & \cdots & \frac{\partial R_v|_I}{\partial N_{n_c}|_J} & \frac{\partial R_v|_I}{\partial N_{n_c+1}|_J} & \cdots & \frac{\partial R_v|_I}{\partial N_{n_c+n_a+1}|_J} & \frac{\partial R_v|_I}{\partial P_1|_J} & \frac{\partial R_v|_I}{\partial N_{H_2O}|_J} \\
\frac{\partial R_{m_1}|_I}{\partial N_1|_J} & \cdots & \frac{\partial R_{m_1}|_I}{\partial N_{n_c}|_J} & \frac{\partial R_{m_1}|_I}{\partial N_{n_c+1}|_J} & \cdots & \frac{\partial R_{m_1}|_I}{\partial N_{n_c+n_a+1}|_J} & \frac{\partial R_{m_1}|_I}{\partial P_1|_J} & \frac{\partial R_{m_1}|_I}{\partial N_{H_2O}|_J} \\
. & & . & . & & . & . & . \\
. & & . & . & & . & . & . \\
. & & . & . & & . & . & . \\
\frac{\partial R_{m_{n_c}}|_I}{\partial N_1|_J} & \cdots & \frac{\partial R_{m_{n_c}}|_I}{\partial N_{n_c}|_J} & \frac{\partial R_{m_{n_c}}|_I}{\partial N_{n_c+1}|_J} & \cdots & \frac{\partial R_{m_{n_c}}|_I}{\partial N_{n_c+n_a+1}|_J} & \frac{\partial R_{m_{n_c}}|_I}{\partial P_1|_J} & \frac{\partial R_{m_{n_c}}|_I}{\partial N_{H_2O}|_J} \\
\frac{\partial R_{m_{n_c+1}}|_I}{\partial N_1|_J} & \cdots & \frac{\partial R_{m_{n_c+1}}|_I}{\partial N_{n_c}|_J} & \frac{\partial R_{m_{n_c+1}}|_I}{\partial N_{n_c+1}|_J} & \cdots & \frac{\partial R_{m_{n_c+1}}|_I}{\partial N_{n_c+n_a+1}|_J} & \frac{\partial R_{m_{n_c+1}}|_I}{\partial P_1|_J} & \frac{\partial R_{m_{n_c+1}}|_I}{\partial N_{H_2O}|_J} \\
. & & . & . & & . & . & . \\
. & & . & . & & . & . & . \\
. & & . & . & & . & . & . \\
\frac{\partial R_{m_{n_c+n_a}}|_I}{\partial N_1|_J} & \cdots & \frac{\partial R_{m_{n_c+n_a}}|_I}{\partial N_{n_c}|_J} & \frac{\partial R_{m_{n_c+n_a}}|_I}{\partial N_{n_c+1}|_J} & \cdots & \frac{\partial R_{m_{n_c+n_a}}|_I}{\partial N_{n_c+n_a+1}|_J} & \frac{\partial R_{m_{n_c+n_a}}|_I}{\partial P_1|_J} & \frac{\partial R_{m_{n_c+n_a}}|_I}{\partial N_{H_2O}|_J} \\
\frac{\partial R_{m_{H_2O}}|_I}{\partial N_1|_J} & \cdots & \frac{\partial R_{m_{H_2O}}|_I}{\partial N_{n_c}|_J} & \frac{\partial R_{m_{H_2O}}|_I}{\partial N_{n_c+1}|_J} & \cdots & \frac{\partial R_{m_{H_2O}}|_I}{\partial N_{n_c+n_a+1}|_J} & \frac{\partial R_{m_{H_2O}}|_I}{\partial P_1|_J} & \frac{\partial R_{m_{H_2O}}|_I}{\partial N_{H_2O}|_J}
\end{pmatrix}$$

$$\Delta\vec{X}_I=\left(\Delta N_1,...,\Delta N_{n_c},\Delta N_{n_c+1},...,\Delta N_{n_c+n_a},\Delta P_1,\Delta N_{H2O}\right)$$

$$\vec{R}_I=\left(R_v,R_{m_1},...,R_{m_{n_c}},R_{m_{n_c+1}},...,R_{m_{n_c+n_a}},R_{m_{H_2O}}\right)$$

6.2.5 Framework and the Linear Solver for Parallel Processing

As shown in Eq.6.313, number of linear equations to be solved for Newton iteration is a function of both number of components and number of gridblocks. This means that as these numbers increase, so does the computational overhead. When running large cases, this can cause the simulation to be very slow or the memory to be insufficient for running on a single processor. To overcome this problem, one can run large problems in parallel. The parallelization method used in GPAS is relatively simple. The total number of

gridblocks is divided by the number of processors. This allows each processor to calculate the Jacobian and residual vector of the gridblocks associated to it simultaneously. This makes the simulation much faster and the required memory for each processor is reduced. In order to calculate the Jacobian and residual vector of a gridblock adjacent to a neighboring gridblock that belongs to another processor, some information from that gridblock (such as its mobility) is required. Therefore the two processors need to communicate this information during the simulation. GPAS uses a framework called Integrated Parallel Accurate Reservoir Simulator (IPARS) (Parashar *et al*., 1997) for the allocation of memory, decomposition of the simulation domain and communication between the processors. IPARS uses Message Passing Interface (MPI) (Gropp *et al*., 1994) functions for communication between processors.

After construction of the Jacobian matrix and the residual vector by each processor, a solver should gather all the information from each processor and solve the linear system of equations shown in Eq.6.313. So the solver should support parallel processing. The Portable Extensible Toolkit for Scientific Computation (PETSc) (Balay *et al*., 1997) from Argonne National Laboratory is a linear solver that supports parallel computation and is used in GPAS.

6.3 Summary

In this chapter we first introduced GPAS in Section 6.1. Then we took a close look at the chemical flooding module of GPAS in Section 6.2. The main assumptions in the development were stated in Section 6.2.1. An overview of the chemical flooding module was presented in Section 6.2.2. In Section 6.2.3 we specified the governing equations and physical properties and their derivatives. The solution procedure was described in Section 6.2.4 and the parallel computing procedure was given in Section 6.2.5.

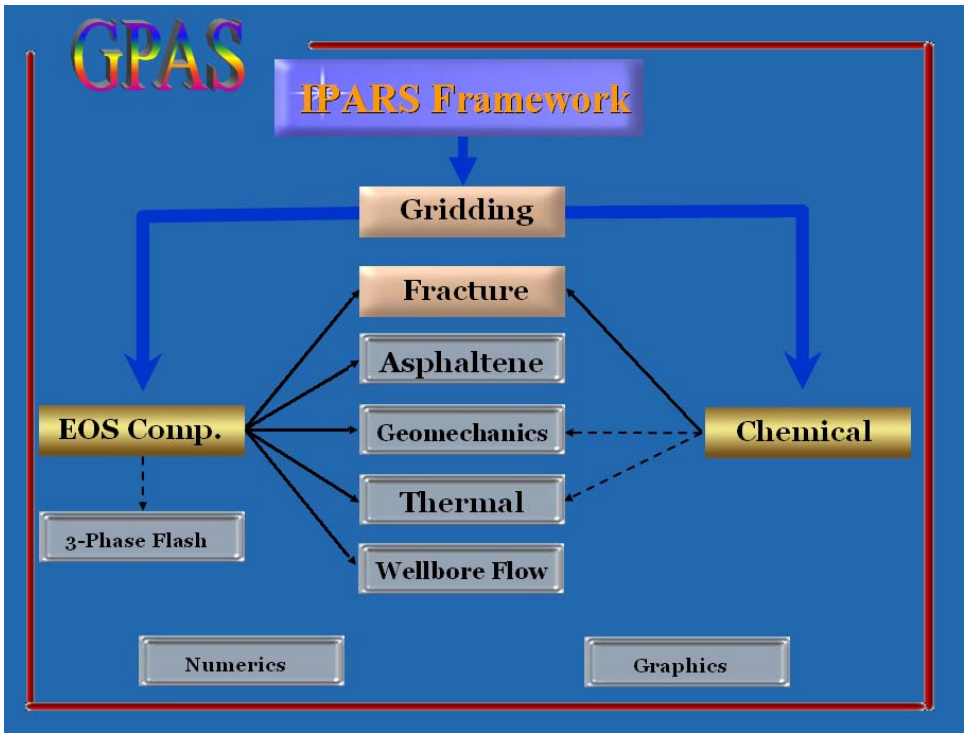

Figure 6.1: Structure of GPAS (Solid lines: completed modules; dashed lines: projects under development).

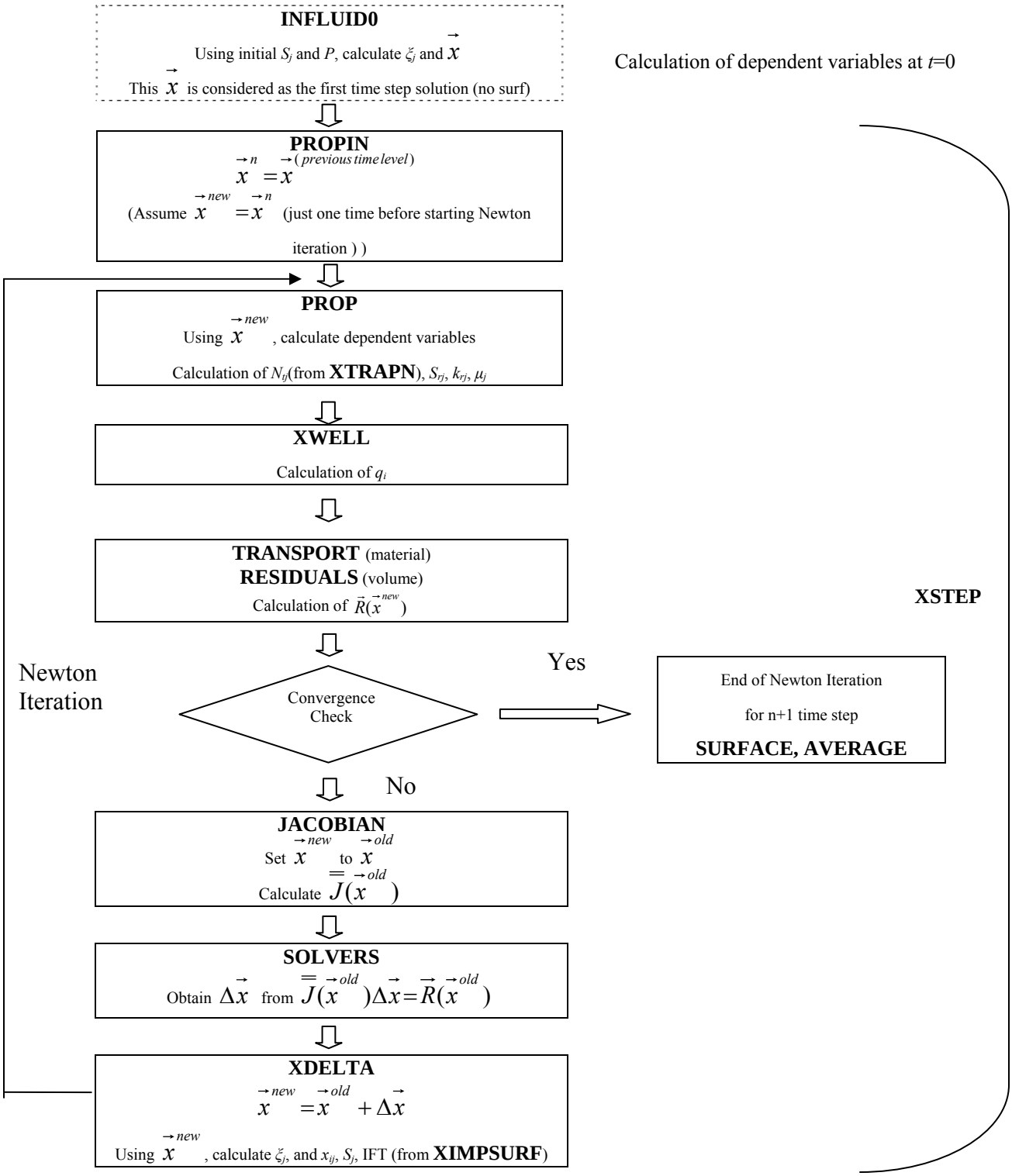

Fig.6.2: Flow chart of the chemical flooding module of GPAS.

Chapter 7: Validation of GPAS Chemical Flooding Module

7.1 Introduction

In Chapter 6 we discussed the new chemical flooding module of GPAS with comprehensive oil/brine/surfactant phase behavior. This new development is validated against the results of UTCHEM. It should be noted that UTCHEM and GPAS have different assumptions and formulations. The most important differences between UTCHEM and GPAS are as follows:

1. In UTCHEM, the rock/fluid system is assumed to be slightly compressible whereas in GPAS the oil density is obtained from the Peng-Robinson EOS. The difference in phase behavior and resulting oil phase properties may lead to differences between the results of the two simulators.
2. UTCHEM uses an IMPEC approach and GPAS is a fully implicit simulator. This means that in general, results of GPAS are more diffusive compared to UTCHEM (Anthony *et al*., 1980).
3. GPAS uses a single point upstream method whereas UTCHEM has the option of higher order numerical scheme and a flux limiter in addition to single point upstream. Therefore, for the purpose of comparison and validation, we used single point upstream option in UTCHEM.
4. Automatic timestep controls of UTCHEM and GPAS are different. In UTCHEM, there are 3 automatic timestep controls: 1- based on dimensional changes in concentration (ΔC_{max}) of the first three components (water, oil and surfactant). 2- based on dimensional changes in concentration of all components and 3- based on dimensionless change in concentration (ΔC_{Dmax}) of all components. GPAS has one automatic timestep option which is based on dimensionless changes in concentration (ΔC_{Dmax}) of oil and water components and pressure. One should be careful about these options when comparing the two simulators.

Several validation test cases were set up. First few 1D cases are presented and the results obtained from GPAS are compared to UTCHEM results. Then 2D vertical cases are presented. Next the results of UTCHEM and GPAS for 3D cases are compared. A heterogeneous example is presented afterwards. A case study is then presented that benchmarks UTCHEM versus GPAS for cases with different number of gridblocks. Validation of parallel processing option of GPAS is presented next.

7.2 Validation 1D Cases

Validation tests are performed for waterflood, polymer flood, and surfactant/polymer floods. The model geometry and physical properties are based on a 1D coreflood simulation documented as Example 6 in the benchmark input files of UTCHEM (UTCHEM 9.82).

The core dimension is 0.8785' x 0.1104' x 0.1104' with 80 gridblocks in the x direction. The gridblock sizes are 0.01098' x 0.1104' x 0.1104'. Permeability and porosity are 236 md and 0.1988 respectively. The core is placed horizontally and is subjected to constant rate injection and constant pressure production. The outlet is open to atmospheric pressure. Oil and water viscosities are 0.995 cp and 24.3 cp respectively. Initial water saturation in the core is assumed to be different for different recovery processes (0.3829 for water and polymer floods and 0.6 for the surfactant polymer flood). Table 7.1 summarizes input parameters used in the coreflood simulations.

Relative permeability curves of aqueous and oleic phases at low and high trapping numbers are presented in Fig. 7.1 and Fig. 7.2 respectively. Figure 7.3 shows the capillary desaturation curves used in these simulations. Table 7.2 summarizes the relative permeability and capillary desaturation input parameters.

Polymer properties are given in Table 7.3. Figure 7.4 presents polymer viscosity as a function of polymer concentration at effective salinity of 0.3 eq/L and shear rate of 10 sec^{-1}. Figure 7.5 shows the effect of salinity on polymer viscosity at a polymer

concentration of 0.12 wt% and shear rate of 10 sec^{-1}. In Fig. 7.7 the shear thinning behavior of polymer viscosity is shown as a function of shear rate for polymer concentration of 0.12 wt% and effective salinity of 0.3 eq/L.

Table 7.4 gives the surfactant phase behavior and IFT input parameters used in surfactant/ polymer simulation.

7.2.1 Simulation of 1-D Waterflood

The injection rate is 0.001 ft^3/day and water is injected for 1 PVs (2.12 days). Automatic time step is used with UTCHEM and GPAS. UTCHEM time step is based on maximum dimensional concentration change (ΔC_{max}) of 1% for each component (IMES=3). GPAS uses a maximum dimensionless concentration change (ΔC_{Dmax}) of 1% for each component. Figure 7.7 compares the recovery factors of UTCHEM and GPAS where a good match is obtained. Figures 7.8 and 7.9 show the quality of the match for oil and water production rates respectively.

Figures 7.10 through 7.13 show saturation and pressure profiles at 0.2 PVs (0.4233 days) and 0.57 PVs (1.21 days) of water injection. A very good match is obtained between the two simulators.

GPAS has a fully implicit formulation which means that each timestep can be more CPU intensive compared to UTCHEM. On the other hand, with the fully implicit formulation much larger timesteps are possible. The CPU times are 19 sec for GPAS and 0.43 sec for UTCHEM. GPAS takes 732 timesteps with an average timestep of 0.0029 days. UTCHEM takes 1000 timesteps with an average timestep of 0.00212 days.

1D waterflood simulation was repeated with constant time steps of 0.001 and 0.01 days. The first value is smaller than that taken in the previous simulation and the second value is an order of magnitude larger. Figure 7.14 shows that GPAS solution is still accurate while UTCHEM results vary greatly when the time step is increased to a constant value of 0.01 days. There are warning messages in UTCHEM warning file about large material

balance errors. It takes 6 secs for GPAS with time steps of 0.01 days and 47 seconds with time steps of 0.001 days to simulate this waterflood. UTCHEM needs 0.7 secs with constant time step of 0.001 day. It is important to note that in practice, one never uses a constant time step for the entire simulation time.

Figures 7.15 through 7.17 compare oil production rate, oil saturation profile and aqueous phase pressure profiles for the constant timestep cases. It is clearly seen that as timestep gets larger, the smearing of the oil production rate and oil saturation profile estimated by GPAS increases due to increased truncation errors.

7.2.2 1D Polymer Flood Simulation

The injection rate is 0.001 ft^3/day and a continuous polymer slug at 0.12 wt% is injected for 1.5 PVs (3.2 days). Initial salinity is 0.4 eq/L and the injected salinity is 0.3 eq/L to test the salinity dependency of polymer viscosity. Tables 7.1 through 7.3 give the input parameters.

Automatic timestep control was used for both GPAS and UTCHEM. Maximum change in concentration of each component for UTCHEM is 1% (IMES = 3) and maximum dimensionless concentration change for GPAS is 1%.

Figure 7.18 shows almost identical results for oil recovery of UTCHEM and GPAS. Figures 7.19 and 7.20 favorably compare oil and water production rates.

Figures 7.21 and 7.22 compare GPAS and UTCHEM results of produced polymer and anion concentration respectively. It is noted that GPAS results show more smearing indicating its higher numerical dispersion. It is interesting to see that the smearing of anion concentration is very close to symmetric (Fig. 7.22) but the polymer production smearing is not symmetric (Fig. 7.21). The difference might be due to polymer adsorption that suppresses numerical dispersion at early time.

Profiles of polymer concentration are presented in Figs. 7.23 and 7.24 at 0.2 PVs (0.423 days) and 0.48 PVs (1.02 days) respectively. It is interesting to note that as time passes, the smearing in GPAS results increases. At 0.2 PVs the polymer concentration profiles predicted by two simulators almost overlap (Fig. 7.23) but at 0.48 PVs the profile predicted by GPAS shows small smearing compared to UTCHEM results (Fig. 7.24).

Figures 7.25 and 7.26 show anion concentration profiles at different times. Once again there is smearing evident in GPAS results. Figures 7.27 and 7.28 show the saturation profiles at 0.2 and 0.48 PVs respectively. The saturation profiles match to a great extent and so do the pressure profiles presented in Figs. 7.29 and 7.30 at 0.2 and 0.48 PVs respectively. The close agreement in pressure profiles and breakthrough times validates the correct implementation of polymer properties in GPAS.

GPAS takes 49 seconds and UTCHEM takes 6.5 seconds to run this case on the same computer. It takes 12000 timesteps with an average timestep of 0.000267 days running UTCHEM. GPAS takes 989 steps with an average timestep size of 0.00323 days. This may be a reason for smearing in GPAS results since GPAS takes timesteps that are an order of magnitude larger than UTCHEM.

The same case was repeated with constant time steps of 0.0005 and 0.005 days. Figure 7.31 compares cumulative oil recovery for constant timesteps. Figure 7. 32 compares oil production rates where UTCHEM results greatly deteriorate as timestep increases. For timesteps of 0.005 days UTCHEM predicts a higher oil production rate at initial times and a lower rate at later times compared to the smaller timestep simulation. GPAS results show a smaller oil production rate at early times and larger rate at later times. This behavior can be explained by polymer concentration shown in Fig. 7.33. Figure 7.34 compares the produced anion concentration where GPAS shows significant smearing at larger timestep of 0.005 days. Figures 7.35 and 7.36 compare polymer and anion concentration profiles at 0.5 PVs (1.06 days) of polymer flood.

The CPU times with constant timesteps for UTCHEM are 1 and 3.8 seconds for 0.005 and 0.0005 day timesteps respectively. GPAS CPU times are 35 and 253 seconds for 0.005 and 0.0005 day timesteps respectively.

7.2.3 1D Surfactant/Polymer Flood Simulation

Surfactant phase behavior parameters are given in Table 7.4. The initial water saturation is 0.6 and polymer properties are in Table 7.3.

Two slugs are injected: first the chemical slug containing 1 vol.% surfactant, 0.43 eq/L anion and 0.12 wt% polymer is injected at a rate of 0.001 ft^3/day for 0.3 PVs (0.64 days). The polymer flood chase containing 0.3 eq/L salt and 0.12 wt% polymer is then injected for 1.2 PVs (2.56 days). The initial salinity is 0.3 eq/L which is below the lower limit of three phase region (C_{SEL}=0.33 eq/L in Table 7.4). The injected slug is at optimum salinity of 0.43 eq/L and the chase polymer flood has the same salinity as the initial of 0.3 eq/L. Automatic time step option is used for both simulators. Maximum change in the concentration for UTCHEM is 0.001 (IMES = 3)) and maximum dimensionless change in concentration for GPAS is 0.001.

Figure 7.37 shows the good match obtained for oil recovery. Figures 7.38 and 7.39 compare oil and water productions rates respectively. Figures 7.40 and 7.41 show very close agreement for effluent polymer and anion concentrations in the aqueous phase present. Figure 7.42 compares the concentration of surfactant in ME phase.

Figures 7.43 through 7.47 show profiles of polymer concentration in aqueous and ME phases, anion concentration in aqueous and ME phases, surfactant concentration in ME phase, saturation, and pressure at 0.2 PVs (0.423 days). There is an excellent agreement between the results of the two simulators. Figures 7.48 through 7.52 show the profiles at 0.5 PVs (1.06 days).

7.3 2D Simulations

A 2D vertical cross section 660' in x, 66' in y and 100' in z direction is simulated. The cross section is divided into 10 horizontal and 5 vertical grids. An injector with a constant rate of 100 bbls/d is placed in the first grid in the x direction and is completed through five layers. The producer is at constant pressure and is placed at the 10^{th} horizontal grid and is completed through all layers. The porosity is 0.2 and horizontal and vertical permeabilities are 100 and 10 md respectively. The reservoir is assumed to be at the pressure of 200 psia initially and the production well operates at this pressure. Table 7.5 summarizes reservoir input parameters.

Water and oil viscosities are 0.995 and 2.43 cp respectively. Table 7.6 summarizes the relative permeability and capillary desaturation parameters. Polymer and surfactant properties are specified in Table 7.3 and Table 7.4 respectively. Water, polymer, and surfactant/polymer flood are simulated with both GPAS and UTCHEM.

7.3.1 Waterflood

Two components (oil and water) are considered and the reservoir is assumed to be at residual water saturation of 0.2. Water is injected at 100 bbls/day for 3000 days (1.93 PVs).

Figure 7.53 shows the excellent agreement in oil recovery factors between UTCHEM and GPAS results. Figures 7.54 and 7.55 show similar oil and water production rates.

Figures 7.56 and 7.57 compare water pressure and oil saturation profiles at 310 days (0.2 PVs) and 773 days (0.5 PVs). Figure 7.57 shows oil gravity override and both simulators capture this effect. This gravity override changes the pressure gradient in the z direction as evident in Fig. 7.56 A and 7.56 B.

These results validate the implementation of gravity in GPAS and show its capability for simulation of 2D waterflood problems.

The results explained above are obtained using variable timesteps. For UTCHEM the maximum concentration change of water and oil is 0.01 (IMES = 3) and for GPAS maximum dimensionless concentration change of water and oil is 0.01. The CPU times are 17 secs for GPAS and 0.7 secs for UTCHEM.

7.3.2 Polymer Flood

Four components of water, oil, salt and polymer are simulated. The reservoir is assumed to be at residual water saturation of 0.2. A polymer solution containing 0.1 wt% polymer is injected at 100 bbls/day for 3000 days (1.93 PVs). Initial salinity is 0.4 eq/L NaCl and that in the injected polymer solution is 0.3 eq/L salt.

Figures 7.58 through 7.62 compare recovery factors, oil and water production rates and polymer and salt effluent concentrations respectively. A very good match is obtained between the results of the two simulators. Figures 7.63 through 7.66 compare pressure, oil saturation, polymer, and salt concentration profiles at 310 days (0.2 PVs) and 773 days (0.5 PVs). Figure 7.65 shows polymer concentration profiles. The salinity profile (Fig. 7.66) shows that salinity front is more dispersed and travels faster compared to polymer front since salt is not adsorbed on the rock as opposed to polymer.

The results are obtained by using automatic timestep selection in both simulators. For UTCHEM the maximum concentration change of the first three components is set to be 0.01 and for GPAS maximum dimensionless concentration change is set at 0.01. GPAS simulates this problem in 47 secs and UTCHEM in 1.2 secs.

7.3.3 Surfactant/Polymer Flood

The reservoir is assumed to be at residual oil saturation of 0.3. Initial reservoir salinity is assumed to be 0.3 eq/L. A chemical slug containing 1 Vol. % surfactant, 0.1 wt. % polymer and 0.43 eq/L salt is injected at 100 bbl/day for 465 days (0.3 PVs). Then a polymer chase is injected for 2035 days (1.31 PVs). The polymer chase contains 0.1 wt. % polymer and 0.3 eq/L of salt.

Maximum change in concentration of the first three components is 0.001 (IMES=2) and GPAS uses 0.01 or 0.001 as the maximum dimensionless concentration change of each component.

Figure 7.67 shows the comparison of oil recovery factors where the blue solid line is UTCHEM result and the two dotted lines are GPAS results. The red dotted curve from GPAS gives better agreement to UTCHEM results when a stiffer concentration tolerance of ΔC_{Dmax}=0.001 is used. Figure 7.67 shows that increasing the maximum concentration tolerance in GPAS by an order of magnitude has a small effect and reduces the oil recovery from 21.7 % OOIP to 21.5 % OOIP. However, the increase in the concentration tolerance has a great effect on the CPU time required and reduces CPU time from 166 secs to 44 secs. It takes 7 secs to run with UTCHEM.

Figure 7.68 compares oil production rates. Figure 7.69 shows the effluent polymer concentration in aqueous phase. GPAS with larger concentration tolerance (the green curve) shows an earlier breakthrough and higher polymer concentration. Figure 7.70 shows the effluent aqueous phase salinity with close agreement. Figure 7.71 compares the effluent ME phase surfactant concentration where UTCHEM predicts a slightly earlier breakthrough and the two GPAS curves are very close.

Figure 7.72 compares pressure profiles at 310 days (0.2 PVs) and 773 days (0.5 PVs). There is a very good agreement between the pressure profiles from two simulators. Figure 7.73 gives the oil saturation profiles. Figure 7.74 compares the surfactant concentration in the ME phase with good agreement between GPAS and UTCHEM. Figures 7.75 and 7.76 give polymer and salinity profiles in the ME phase. High polymer adsorption causes the polymer front to be delayed compared to the surfactant front (Figs. 7.74 and 7.75).

7.4 3D Simulations

The reservoir model is 660'x660'x100' and is discretized in 10x10x5 gridblocks. Horizontal permeability is 100 md and vertical permeability is 10 md. Table 7.7 summarizes input parameters. Relative permeability and capillary desaturation parameters used are those from Section 4.3 (Table 7.6). Polymer and surfactant properties used in this case are described in Table 7.3 and Table 7.4 respectively.

7.4.1 Waterflood

Initial water saturation is 0.3. An injector with constant rate of 1000 bbls/day and a constant pressure producer with 200 psia are used. Only two components (water and oil) are simulated.

Automatic timestep option is used. Maximum concentration change is 0.001 for UTCHEM whereas GPAS is run twice, once with no concentration restriction (ΔC_{Dmax}=1) and once with maximum change in concentration of 0.1 (ΔC_{Dmax}=0.1).

Figure 7.77 compares recovery factors. GPAS with maximum concentration change of 0.1 runs in 11 secs and gives a very close recovery factor compared to UTCHEM which runs in 3.7 secs (Fig. 7.77). GPAS with no concentration restriction runs in 5.7 secs and gives a fairly close recovery compared to UTCHEM. Figures 7.78 and 7.79 compare oil and water production rates where the production rates are more smeared in GPAS as a result of larger numerical dispersion compared to UTCHEM.

Figures 7.80 and 7.81 compare the pressure and oil saturation profiles of UTCHEM and GPAS (ΔC_{Dmax}=1) at 358 days (0.226 PVs) and 854 days (0.55 PVs). Pressure profiles are reasonably close but oil saturation front is more dispersed in GPAS results compared to UTCHEM especially at 0.226 PVs.

Figures 7.82 and 7.83 compare the pressure and oil saturation profiles of UTCHEM and GPAS with (ΔC_{Dmax}= 0.1) at 318 days (0.2 PVs) and 854 days (0.55 PVs). The pressure

profiles of GPAS are now closer to UTCHEM and the reason is clearly due to smaller numerical dispersion. Figure 7.83 shows a great improvement in the oil saturation profiles of GPAS with 0.1 concentration restriction compared to the case with no concentration restriction (Fig. 7.81).

7.4.2 Polymer Flood

Initial water saturation is 0.3 with initial salinity of 0.5 eq/L. Two polymer slugs are injected. First a slug containing 1000 ppm (0.1 wt.%) and 0.3 eq/L salt is injected for 0.6 PVs (930 days). The first slug is followed by a second polymer slug containing 500 ppm (0.05 wt.%) and salinity of 0.1 eq/L.

UTCHEM with automatic timestep is used and maximum concentration change of all components is 0.1% (IMES = 3). Three simulations are performed with GPAS with automatic timestep selection but different tolerance for maximum change in dimensionless concentration. The concentration tolerances are 100% (ΔC_{Dmax}=1), 10% (ΔC_{Dmax}=0.1) and 0.01% (ΔC_{Dmax}=0.01). Maximum courant number for UTCHEM is 0.1 which results in a maximum timestep of 1.55 days. The maximum timestep for GPAS is set to 30 days for the first slug and 50 days for the second slug. UTCHEM simulates this case in 16 secs and GPAS in 21.8, 29.1 and 148 secs as the concentration constraint is tightened.

Figure 7.84 compares the recovery factors. It is interesting to note that although GPAS uses a much looser timestep control compared to UTCHEM, it is still able to predict the results of UTCHEM to a great extent. The GPAS recovery factor curve with ΔC_{Dmax}=0.01 virtually overlaps with UTCHEM result with ΔC_{Dmax}=0.001. Figures 7.85 and 7.86 compare the oil and water production rates respectively. As concentration constraint on GPAS is tightened, the oil and water production rates get closer and closer to that predicted by UTCHEM (Figs. 7.85 and 7.86). Similar observation is made for the effluent polymer and anion concentrations in Figs. 7.87 and 7.88 respectively.

Profiles from the least accurate case simulated by GPAS are compared to those obtained from UTCHEM at 310 days (0.2 PVs) and 930 days (0.6 PVs). Figure 7.89 shows the pressure profiles with good agreement between the results. Figure 7.90 shows the oil saturation profiles where GPAS results are slightly more smeared as evident in Fig. 7.90-A. Figure 7.91 shows very similar polymer concentration profiles for both simulators As a result of that, both simulators predict the distance travelled by polymer almost identically (Fig. 7.91). But the smearing takes place behind the polymer front due to numerical dispersion. Figure 7.92 compares the anion concentration profiles (eq/L) and it is evident the anion front is dispersed ahead and behind the front. As a result of this, the distance traveled by the anion fronts in UTCHEM and GPAS is not the same at any given time. The dispersion in the salinity front can explain discrepancies in oil recoveries since polymer viscosity is a strong function of salinity (Eq.6.300 and Table 7.3).

In general, it can be concluded that looser concentration constraints may produce reasonably good results in polymer flood compared to waterfloods. The main reason is the polymer adsorption that limits the smearing of the polymer front and results in more accurate recovery predictions with looser concentration constraints compared to waterfloods.

7.4.3 Surfactant/Polymer Flood

The reservoir described in Section 7.4 is assumed to have an initial residual oil saturation of 0.3 (Table 7.6). Initial reservoir salinity is 0.3 eq/L. A chemical slug containing 1 vol. % surfactant, 1000 ppm polymer, and 0.43 eq/L salt is injected for 465 days (0.3 PVs). This slug is chased with a polymer drive containing 1000 ppm polymer at 0.3 eq/L salinity for 2035 days (1.31 PVs).

Both UTCHEM and GPAS use the automatic timestep control and maximum concentration change of UTCHEM is 0.01% (IMES = 3). Three different simulations with GPAS are presented where ΔC_{Dmax} is varied from 1 to 0.1 to 0.01. Maximum courant number of 0.1 is used for UTCHEM and maximum timesteps of 5 and 30 days are used for GPAS in the first and second slug.

Figure 7.93 compares the oil recovery indicating that GPAS result with ΔC_{Dmax} =1 is not very far from UTCHEM result using concentration tolerance of 0.001. As the concentration constraint is tightened in GPAS, the recovery factor converges to UTCHEM results. There is a significant improvement in GPAS oil recovery results when the concentration tolerance is reduced from 1 to 0.1 but the CPU time moderately increases from 199 to 582 sec (Fig. 7.93). The tighter concentration constraint of 0.01 requires a significantly higher CPU of 2980.3 secs. Figures 7.94 and 7.95 compare the oil and water production rates respectively. GPAS with ΔC_{Dmax} =1 predicts the oil and water rates to a great extent and as the concentration tolerance is reduced, GPAS and UTCHEM results become closer (Figs. 7.94 and 7.95). Figures 7.96 through 7.98 show polymer, anion and surfactant concentration histories respectively. As the concentration tolerance is reduced , the difference between the breakthrough times of surfactant and polymer is also reduced and the results are in better agreement because of reduced numerical dispersion in GPAS. Despite the loose concentration constraint of GPAS the effluent surfactant concentrations are still very close to those from UTCHEM (Fig. 7.98). The main reason is that surfactant adsorption nearly eliminates the smearing of surfactant front.

The results discussed in this section are for GPAS with the largest concentration constraint of ΔC_{Dmax} =1. The results of GPAS runs with smaller concentration tolerance are expected to be closer to UTCHEM results. Figure 7.99 compares the pressure profiles after 310 days (0.2 PVs) and 773 days (0.5 PVs). The pressure profiles are very close but GPAS gives the pressures slightly higher than UTCHEM. Figure 7.100 compares the oil saturation profiles and it is interesting to note that the results are very close. The main reasons for this similarity are surfactant and polymer adsorptions that help reducing the smearing of polymer and surfactant fronts. The most important parameters in surfactant/polymer flood are surfactant and electrolytes concentration and the phase behavior. Figure 7.101 favorably compares the profiles of surfactant concentration in the ME phase at 0.2 and 0.5 PVs. A small smearing behind the surfactant bank can be

observed after 0.5 PVs (Fig. 7.101 C and D). Figure 7.102 shows the profiles of polymer concentration in the ME phase at 0.2 and 0.5 PVs. Figure 7.103 compares anion concentration profiles in the ME phase at 0.2 and 0.5 PVs. It is interesting to see that the profiles are almost identical. Aqueous phase anion concentration was pretty smeared during the polymer flood (Fig. 7.92). The reason is that ME phase anion concentration is directly dependant on the concentration of water in the ME phase (Eq.6.163). The concentration of water in the ME phase is a function of solubilization ratio of water and in turn a function of surfactant concentration in the ME phase (Eq.6.88). Since surfactant adsorption results in an accurate modeling of surfactant concentration at each time, the anion concentration in the ME phase is also modeled more accurately compared to aqueous phase anion concentration and shows less smearing (Figs. 7.92 and 7.103).

7.4.4 3D Surfactant/Polymer Flood in a Heterogeneous Reservoir

As final validation is a 3D model with heterogeneous permeability. The reservoir model has dimensions of 660'x660'x50' with a quarter of five spot well pattern. It is discretized to 11x11x5 gridblocks with gridblock dimensions of 60'x60'x10'.

Figure 7.104 gives the x (or y) direction permeability. The vertical to horizontal permeability ratio (k_v / k_h) is 0.01. Porosity is assumed to be 0.136. Initial reservoir pressure is 2000 psia and initial water saturation is 0.65. Initial salinity is 0.4 eq/L. Table 7.8 summarizes simulation input parameters.

Relative permeability and polymer properties are based on those presented by Saad (1989) for history matching of a real surfactant/polymer flood pilot. Table 7.9 summarizes the relative permeability and CDC parameters. Polymer properties are given in Table 7.10. The oil/brine/surfactant phase behavior, IFT, and ME viscosity parameters are given in Table 7.11.

A 0.3 PV (1560 days) of chemical slug composed of water with 2 vol.% surfactant, 200 ppm polymer, and 0.3 eq/L salt is injected. The injection rate is 100 bbls/day. Then the

chase polymer drive with 300 ppm polymer and salinity of 0.15 eq/L is injected for 0.11 PVs (640 days). A post water injection at 0.15 eq/L salinity is continued for 0.51 PVs (2700 days). The producer operates at 200 psia pressure. This is a salinity gradient starting in the Type II(+) region and ending in Type I region.

Maximum concentration change used for the first three components of UTCHEM is 0.001 (IMES = 2). GPAS uses a dimensionless concentration change of 1 (ΔC_{Dmax}=0.01). Maximum timesteps for GPAS is set on 10 days and for UTCHEM, maximum courant number is set on 0.01. Figure 7.105 compares the recovery factors predicted by UTCHEM and GPAS. Although GPAS uses relatively large concentration tolerance, it still gives a recovery factor very close to UTCHEM. GPAS simulates this case in 1560 secs and UTCHEM takes 363 secs.

Figure 7.106 shows a good agreement for oil production rate between the two codes. GPAS computes the breakthrough of oil to a great extent and maximum oil production rate of UTCHEM and GPAS are very close. The water production rates are also in agreement (Fig. 7.107). Figure 7.108 shows the effluent polymer concentration in the aqueous phase. There is a very good agreement between UTCHEM and GPAS in this case. Figures 7.109 and 7.110 compare aqueous phase anion concentration and ME phase surfactant concentration.

Figure 7.111 gives the comparison of pressure profiles (psia) at 0.2 PVs (1055 days) and 0.5 PVs (2622 days) with very close agreement. The oil saturation profiles (Fig. 7.112) at 0.2 PVs are very close, but there is a slight difference at 0.5 PVs and this difference leads to slightly different oil and water production rates (Figs. 7.106 and 7.107). The main cause of this difference is the difference in density and fluid compressibility calculations. UTCHEM assumes slightly compressible fluids and fluid densities are calculated as a function of composition and pressure. GPAS uses Peng-Robinson EOS for calculation of the oleic phase density. This leads to slight differences in oil density and compressibility especially when pressure gradients are large (Fig. 7.111). A close agreement in surfactant

concentration profiles in the ME phase is given in Fig. 7.113 due to surfactant adsorption and small grid sizes that limit the numerical dispersion. Figure 7.114 shows the polymer concentration profiles in the ME phase at 0.2 and 0.5 PVs injected. There is a good agreement between the profiles predicted by UTCHEM and GPAS. Similar to the case for surfactant concentration profiles, the reason is polymer adsorption and small grid sizes. Figure 7.115 compares the anion concentration profiles in the ME phase and one can see a reasonably good agreement between the results of the two simulators.

7.5 Single Processor Efficiency of GPAS

The objective is to test the CPU times and efficiency of GPAS for larger problem sizes. The simulations of this section are all in homogeneous reservoirs. First waterflood simulations with two components of oil and water are presented. Then polymer floods with four components of oil, water, salt and polymer are discussed and at last surfactant/polymer floods with 5 components (water, oil, surfactant, polymer and salt) are evaluated. A base case for each process is presented and the results of GPAS are compared with UTCHEM. Base case model is 250'x250'x10' with a quarter of five spot well pattern. This domain is discretized to 11x11x2 with gridblock size of 22.727'x22.727'x5'.

To create larger reservoirs, the base case pattern is repeated keeping the size of the grids the same as the base case. The base case has 242 gridblocks. To generate a reservoir with 484 gridblocks, number of layers of the base case is doubled. The quarter five spot pattern of the base case is repeated to create a five spot pattern of 21x21x2 gridblocks which is a reservoir with 882 gridblocks. Doubling the number of layers of this five spot pattern gives reservoirs with 1764 and 3528 gridblocks.

Reservoir permeability in the x and y directions is 500 md with vertical permeability of 50 md. Porosity is 0.2 and initial reservoir pressure is 2000 psia. Initial water saturation varies for different processes. Producers are on 2000 psia bottomhole pressure and injectors inject at a constant rate of 2 STB/(day.ft). Oil and water viscosities are 4.0 and 0.86 cp respectively. Table 7.12 gives key input parameters.

Relative permeability and capillary desaturation curves used in this section are presented in Table 7.9. Polymer properties used in this section are given in Table 7.10. The oil/brine/surfactant phase behavior, IFT and ME viscosity parameters are given in Table 7.13.

7.5.1 Waterflood

The model with an initial water saturation of 0.37 is waterflooded for 3337.5 days (3.0 PVs). An important observation is that UTCHEM results become unstable if courant number of larger than 0.4 are used. Therefore the automatic timestep control in UTCHEM with maximum courant number of 0.4 and maximum concentration change of 0.001 (IMES = 2) for water and oil components is used. This allows UTCHEM to take large timesteps without compromising the numerical stability.

The results obtained by GPAS are very sensitive to timestep size. As larger and larger timesteps are taken, truncation errors increase and the results are more diffuse and dispersed. Two simulations for GPAS are presented. In one simulation, maximum dimensionless concentration change in each timestep is 0.1 (ΔC_{Dmax}=0.1) and in the second run, this tolerance is increased to 20% (ΔC_{Dmax}=0.2). The maximum timestep is 500 days.

Figures 7.116 and 7.117 show the comparison of recovery factors and oil production rate. As concentration tolerance increases, the difference increases due to increased truncation errors in GPAS. Figure 7.118 compares CPU times required as a function of number of gridblocks. If GPAS results with 20% concentration tolerance are considered adequate, then GPAS is unconditionally faster than UTCHEM. If GPAS results with 10% concentration tolerance are considered adequate, then GPAS is faster than UTCHEM in problems with more than about 700 gridblocks.

7.5.2 Polymer Flood Benchmarking

The model described in Section 7.5 with an initial water saturation of 0.5 is used for polymer flooding. Polymer solution containing 500 ppm polymer with 0.25 eq/L salinity is injected for 1.5 PVs (1668.75 days) and followed by water at 0.15 eq/L salinity for another 1.5 PVs (1668.75 days). Initial reservoir salinity is 0.4 eq/L. Automatic timestep control with maximum courant number of 0.2 and a maximum concentration tolerance of 0.001 (IMES = 2) for water and oil components is used in UTCHEM.

Two cases for GPAS are presented. In one simulation, maximum dimensionless concentration change in each timestep is 0.1 (ΔC_{Dmax}=0.1) and in the second run, this tolerance is increased to 20% (ΔC_{Dmax}=0.2) with a maximum timestep of 500 days.

Figures 7.119 and 7.120 compare the polymer flood recovery factors and oil production rates. As expected, the recovery factors and oil rates are fairly close and the higher concentration tolerance with GPAS exhibit more smearing in the results. Figures. 7.121 and 7.122 compare the aqueous phase polymer and anion concentrations where numerical dispersion is clearly observed in GPAS results due to large timesteps. Figure 7.123 compares the CPU times. If GPAS results with 20% concentration tolerance are considered satisfactory, then GPAS is faster than UTCHEM when the number of gridblocks is larger than 600. If the results with 10% concentration tolerance are considered adequate, then GPAS is faster than UTCHEM when more than about 900 gridblocks is used.

7.5.3 Surfactant/Polymer Flood

The reservoir described in Section 7.5 is assumed to have initial oil at residual saturation of 0.35. Reservoir and fluid properties are the same as the case in Section 7.5.2. Three slugs are injected; the surfactant slug contains 2 Vol. % surfactant, 500 ppm polymer and 0.25 eq/L anions. The surfactant slug is injected for 335 days (0.3 PVs). The polymer chase is injected next with 500 ppm polymer at a salinity of 0.15 eq/L. The polymer drive is injected for 465 days (0.4 PVs). The reservoir is then waterflooded at the same salinity

as that of the polymer chase (0.15 eq/L) for 700 days (0.65 PVs). Relative permeability, polymer, and surfactant properties are presented in Tables 7.9 to 7.11 respectively.

The results are obtained running both UTCHEM and GPAS with automatic timestep control options. For UTCHEM the maximum courant number is 0.2 with the constant concentration tolerance for water, oil and surfactant of 0.001 (IMES =2). GPAS is used with the default timestep control (CVGOPT = 1). This option works based on overall water and hydrocarbon component concentration. A maximum timestep of 10 days is chosen for GPAS. Two cases are presented for GPAS. In the first case, the timesteps are chosen based on the criteria that maximum dimensionless change in concentration of water and oil components does not exceed 0.01 (ΔC_{Dmax}=0.01). This tolerance is increased to 0.03 for the second simulation (ΔC_{Dmax}=0.03).

Figure 7.124 compares the recovery factors simulated by UTCHEM and GPAS for the base case where a good agreement is observed. Figures 7.125 and 7.126 show the oil and water production rates. It is interesting to see that although the production rates are not exactly the same, the trend in the oil recovery curve of GPAS is very close to UTCHEM (Fig. 7.125). It is noticed that as the tolerance in GPAS is increased, the oscillation in the oil and water production rates increases. Figures 7.127 and 7.128 show the concentration of polymer and anion in the effluent aqueous phase respectively. Figure 7.129 shows surfactant concentration in the effluent ME phase with a good agreement between the results. The slight differences in the results of UTCHEM and GPAS could be due to higher truncation errors of GPAS. These errors increase quickly as the timestep size increases (Anthoney, *et al.*, 1980).

Figure 7.130 compares the times step sizes where GPAS has relatively less oscillations in the timestep size compared to UTCHEM and takes timesteps that are orders of magnitude larger than those taken by UTCHEM. Even though GPAS takes much larger timesteps, it is still slower than UTCHEM in the base case with 242 gridblocks. UTCHEM takes only 11 seconds whereas GPAS with a concentration tolerance of 0.01 (ΔC_{Dmax}=0.01) takes

32.4 seconds and 24.5 seconds for the larger tolerance. Thus GPAS is slower than UTCHEM by a factor of 2.23 to run the base case. However, this ratio decreases as the number of gridblocks increases. Figure 7.131 compares the CPU times required by UTCHEM and GPAS to simulate a surfactant/polymer flood as the number of gridblocks increases. The figure shows that if number of gridblocks is larger than about 2300, then GPAS with concentration tolerance of 0.03 (ΔC_{Dmax}=0.03) runs faster than UTCHEM.

7.6 Parallel Processing

To test the parallel processing capability and performance of GPAS after the addition of comprehensive chemical module, a relatively large five spot surfactant/polymer flood model was set up and run on multiple processors. The reservoir model is 4422'x4422'x50' and it is discretized in 128x128x5 gridblocks. Table 7. 14 summarizes the input parameters. Table 7. 15 gives the polymer viscosity, adsorption, and permeability reduction parameters. Relative permeability and capillary desaturation data are the same as those in Table 7.6. Surfactant phase behavior, microemulsion viscosity, and IFT parameters are presented in Table 7.16.

The reservoir is assumed to be at residual oil saturation. Initial reservoir salinity is assumed to be 0.3 eq/l which is below the lower limit of Type III region (Table 7.16). The four injectors inject a chemical slug containing 1 vol. % surfactant and 1000 ppm polymer and 0.43 eq/l salt. The chemical slug is injected for 2380.8 days (0.3 PVs). After that a polymer chase containing 1000 ppm polymer and 0.3 eq/l salt is injected for 0.87 PVs (6926.2 days).

This case is simulated with 8, 16, 32 and 64 processors. The simulation results overlap and simulation time decreases as number of processors increases. Figure 7.132 shows the recovery factors and Figs. 7.133 and 7.134 compare the oil and water production rates obtained from the parallel simulations. Figures 7.135 and 7.136 give the effluent salt concentration and surfactant concentration in microemulsion phase respectively. Due to high polymer adsorption, polymer does not breakthrough even after 1.17 PVs of injection.

Figure 7.137 shows the simulation time as a function of number of processors and Fig. 7.138 compares the speedup obtained with the ideal speedup line (a line with slope of unity). It is interesting to see that the speedup from 8 processors to 16 processors is very close to ideal but the performance deteriorates as the number of processors increases beyond 32. This is due to the fact that as number of processors increases, so does the time required for communication between the processors and this increases the simulation time causing the speed up to be less than ideal. It can be seen in Fig. 7.138 that the speedup of GPAS is not far from ideal and this proves parallel processing to be a powerful tool for reduction of simulation time and feasible simulation of field scale chemical floods.

Table 7.1: 1D coreflood input parameters

Core dimension, ft	0.8785x0.1104x0.1104
Grid size, ft	0.01098x0.1104x0.1104
Number of gridblocks	80x1x1
Permeability, md	236
Porosity	0.1988
Water viscosity, cp	0.995
Oil viscosity, cp	24.3
Injection rate, ft^3/day	0.001

Table 7.2: Relative permeability and capillary desaturation input parameters for 1D coreflood simulations.

	Water		**Oil**	
	Low trapping No.	**High trapping No.**	**Low trapping No.**	**High trapping No.**
Relative permeability endpoint	0.0275	0.5	1	1
Relative permeability exponent	1.12	1	1.3	1
Residual saturation	0.382	0	0.3803	0
Trapping parameter	1865		8000	

Table 7.3: Polymer input parameters for 1D coreflood, 2D, and 3D homogeneous simulations.

Viscosity parameters, A_{p1}, A_{p2}, A_{p3}, S_p	10.21, 17.77, 626.14, -0.6
Shear rate parameters , γ_c, $\gamma_{1/2}$, P_α	4.0, 56.1, 1.643
Adsorption parameters, a_{41}, a_{42}, b_4	9.5, 0, 100
Permeability reduction parameters, C_{rk}, B_{rk}	0.0186, 100

Table 7.4: Surfactant phase behavior and IFT input parameters for 1D coreflood, 2D vertical and 3D homogeneous simulations.

Heights of binodal curve at 0, opt. and twice opt. salinity, *HBN*70, *HBN*71, *HBN*72	0.05, 0.03, 0.05
Lower salinity limit of three phase region(C_{SEL}), eq/L	0.33
Upper salinity limit of three phase region (C_{SEU}), eq/L	0.53
Surfactant adsorption parameters, a31, a32, b3	1.5, 0.5, 1000
ME viscosity parameters, α_1,α_2,α_3, α_4, α_5	1.5, 1.45, 0, 0.9, 1.7
Interfacial tension parameters, a, c	10, 0.35

Table 7.5: 2D simulation input parameters

Reservoir size, ft	660x66x0.100
Grid size, ft	66x0.66x0.20
Number of gridblocks	10x1x5
Horizontal and vertical permeability, md	100, 10
Porosity	0.2
Water viscosity, cp	0.995
Oil viscosity, cp	2.43
Injection rate, ft^3/day	100

Table 7.6: Relative permeability and capillary desaturation input parameters for 2D and 3D homogeneous cases

	Water		**Oil**	
	Low trapping No.	**High trapping No.**	**Low trapping No.**	**High trapping No.**
Relative permeability endpoint	0.2	1	1	1
Relative permeability exponent	1.5	1	1.3	1
Residual saturation	0.2	0	0.3	0
Trapping parameter	300		1000	

Table 7.7: Input parameters for 3D homogeneous simulations.

Reservoir size, ft	660x660x0.100
Grid size, ft	66x0.66x0.20
Number of gridblocks	10x10x5
Horizontal and vertical permeability, md	100, 10
Porosity	0.2
Water viscosity, cp	0.995
Oil viscosity, cp	2.43
Injection rate, ft^3/day	1000

Table 7.8: Input parameters for 3D heterogeneous simulations.

Reservoir size, ft	660x660x50
Grid size, ft	60x60x10
Number of gridblocks	11x11x5
Permeability, md	Heterogeneous (Fig. 7.104)
Porosity	0.136
Water viscosity, cp	0.86
Oil viscosity, cp	4.
Injection rate, ft^3/day	561.5

Table 7.9: Relative permeability and CDC curves used in the 3D heterogeneous.

	Water		**Oil**	
	Low trapping No.	**High trapping No.**	**Low trapping No.**	**High trapping No.**
Relative permeability endpoint	0.11	1	0.95	1
Relative permeability exponent	1	1	2.16	2.16
Residual saturation	0.37	0	0.35	0
Trapping parameter	1865		59074	

Table 7.10: Polymer input parameters used in 3D heterogeneous simulations.

Viscosity parameters, A_{p1}, A_{p2}, A_{p3}, S_p	81, 2700, 2500, 0.17
Shear rate parameters, γ_c, $\gamma_{1/2}$, P_α	20, 10, 1.8
Adsorption parameters, a_{41}, a_{42}, b_4	0.7, 0.0, 100
Permeability reduction parameters, C_{rk}, B_{rk}	0.0186, 1000

Table 7.11: Surfactant phase behavior and IFT parameters used in 3D heterogeneous simulations.

Heights of binodal curve at 0, opt. and twice opt. salinity, *HBN*70, *HBN*71, *HBN*72	0.06, 0.04, 0.06
Lower salinity limit of three phase region(C_{SEL}), eq/L	0.177
Upper salinity limit of three phase region (C_{SEU}), eq/L	0.344
Surfactant adsorption parameters, a31, a32, b3	1.5, 0.5, 1000
ME viscosity parameters, α_1,α_2,α_3, α_4, α_5	2.5, 2.3, 10, 1, 1.
Interfacial tension parameters, a, c	9, 0.2

Table 7.12: Input parameters for the case for CPU comparison of GPAS and UTCHEM.

Reservoir size, ft	250x250x10
Grid size, ft	22.727x22.727x2
Number of gridblocks	11x11x5
Permeability, md	500
Porosity	0.2
Water viscosity, cp	0.86
Oil viscosity, cp	4.
Injection rate, ft^3/(day.ft)	2

Table 7.13: Surfactant phase behavior and IFT parameters used in CPU comparison.

Heights of binodal curve at 0, opt. and twice opt. salinity, *HBN*70, *HBN*71, *HBN*72	0.06, 0.035, 0.06
Lower salinity limit of three phase region(C_{SEL}), eq/L	0.177
Upper salinity limit of three phase region (C_{SEU}), eq/L	0.344
Surfactant adsorption parameters, a31, a32, b3	1.5, 0.5, 1000
ME viscosity parameters, α_1,α_2,α_3, α_4, α_5	2.5, 2.3, 10, 1, 1.
Interfacial tension parameters, a, c	9, 0.2

Table 7. 14: Input parameters for parallel simulations.

Reservoir dimension, ft	4224x4224x50
Grid size, ft	33x33x10
Number of gridblocks	128x128x5
Horizontal permeability, md	100
Vertical Permeability, md	10
Water and oil viscosity, cp	0.995, 2.43
Porosity	0.2
Injection rate, ft^3/day	1000

Table 7. 15: Polymer input parameters used in parallel simulations.

Viscosity parameters, A_{p1}, A_{p2}, A_{p3}, S_p	10.21, 17.77, 626.14, -0.6
Shear rate parameters, γ_c, $\gamma_{1/2}$, P_α	4, 56.1, 1.643
Adsorption parameters, a_{41}, a_{42}, b_4	9.5, 0.0, 100
Permeability reduction parameters, C_{rk}, B_{rk}	0.0186, 1000

Table 7.16: Surfactant phase behavior and IFT parameters used in parallel simulations.

Heights of binodal curve at 0, opt. and twice opt. salinity, *HBN*70, *HBN*71, *HBN*72	0.05, 0.03, 0.05
Lower salinity limit of three phase region(C_{SEL}), eq/L	0.33
Upper salinity limit of three phase region (C_{SEU}), eq/L	0.53
Surfactant adsorption parameters, a31, a32, b3	1.5, 0.5, 1000
ME viscosity parameters, α_1,α_2,α_3, α_4, α_5	0, 0, 0, 0.0, 1.7
Interfacial tension parameters, a, c	10, 0.35

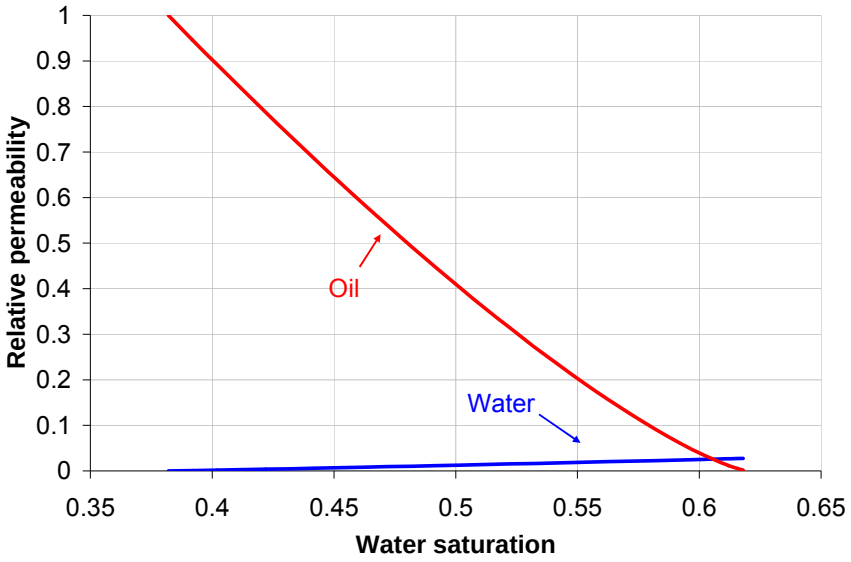

Figure 7.1: Relative permeability curves at low trapping numbers used in 1D coreflood simulations.

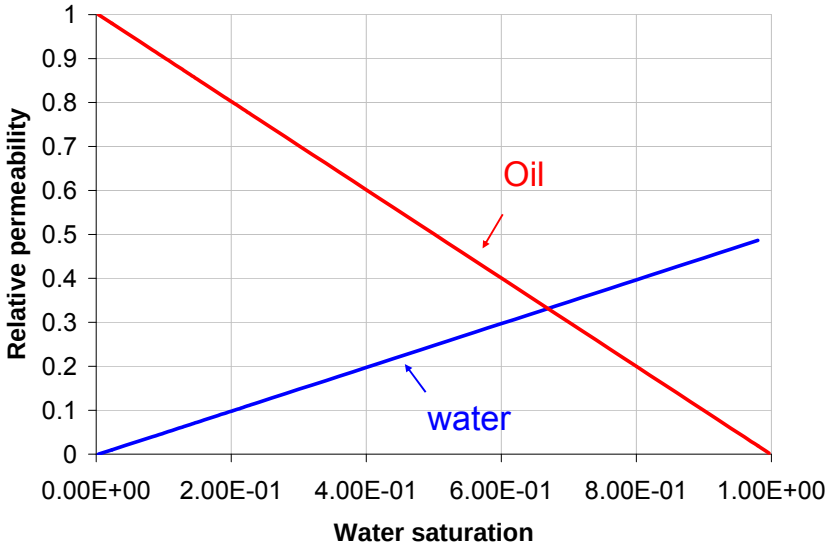

Figure 7.2: Relative permeability curves at high trapping numbers used in 1D coreflood simulations.

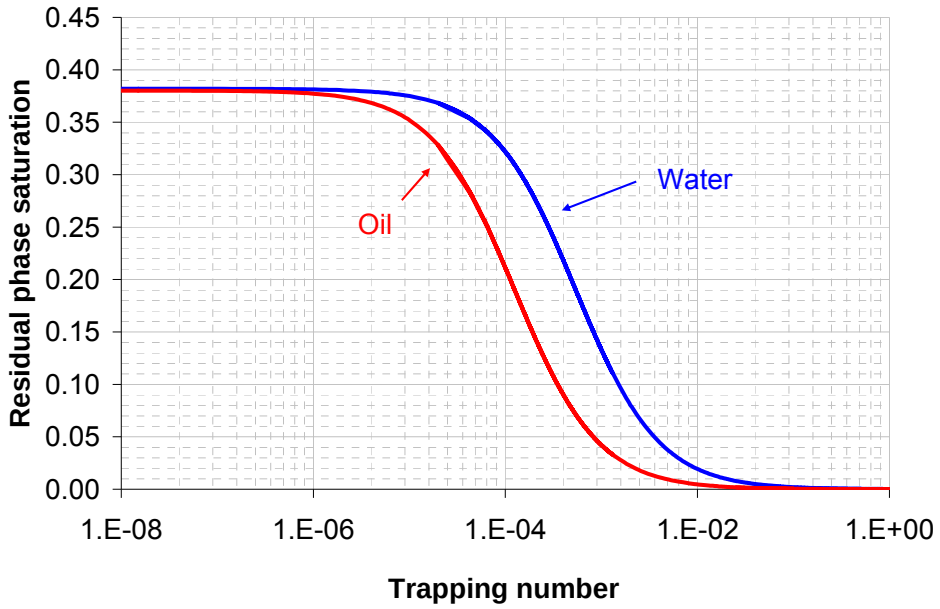

Figure7.3: Capillary desaturation curves used in 1D coreflood simulations.

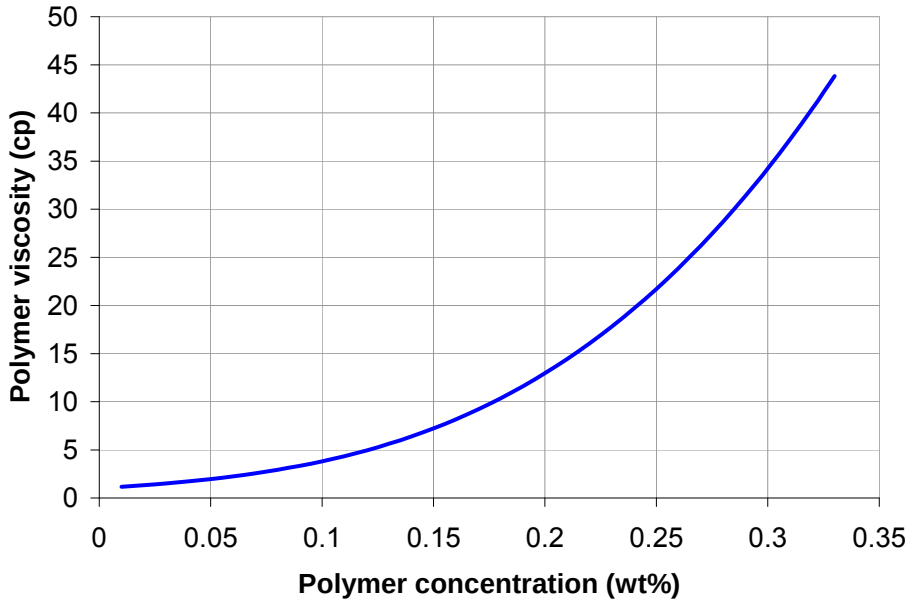

Figure 7.4: Polymer viscosity as a function of polymer concentration at an effective salinity of 0.3 eq/L and shear rate of 10 sec^{-1}.

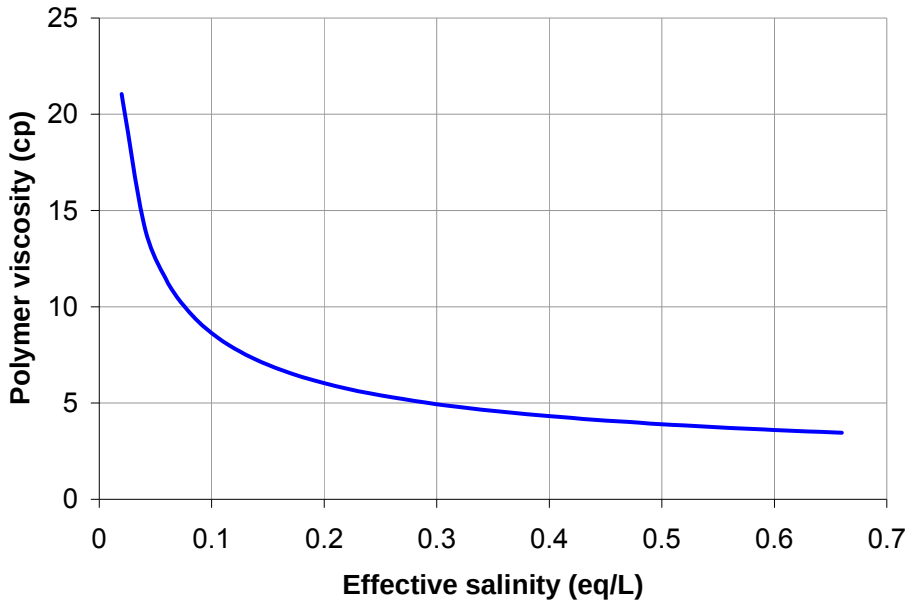

Figure 7.5: Polymer viscosity as a function of effective salinity at polymer concentration of 0.12 wt% and shear rate of 10 sec^{-1}.

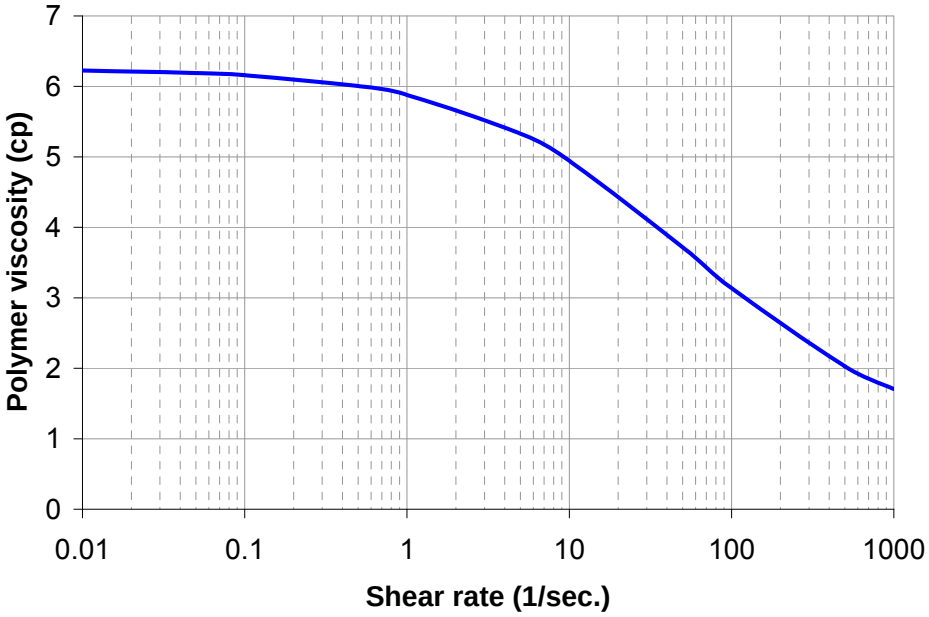

Figure 7.6: Polymer viscosity as a function of shear rate at effective salinity of 0.3 eq/L and polymer concentration of 0.12 wt%.

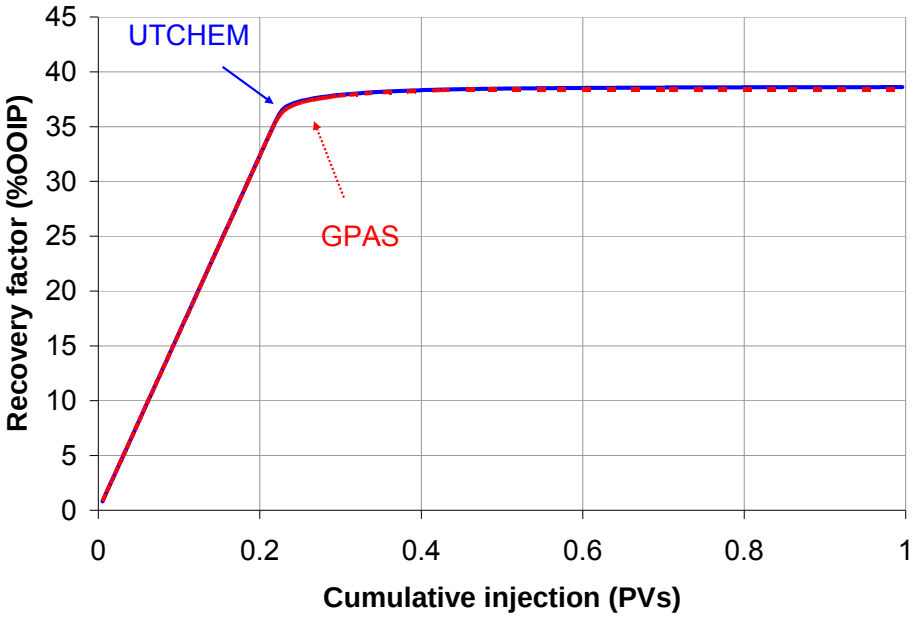

Figure 7.7: Comparison GPAS and UTCHEM waterflood oil recovery factors for 1D simulation.

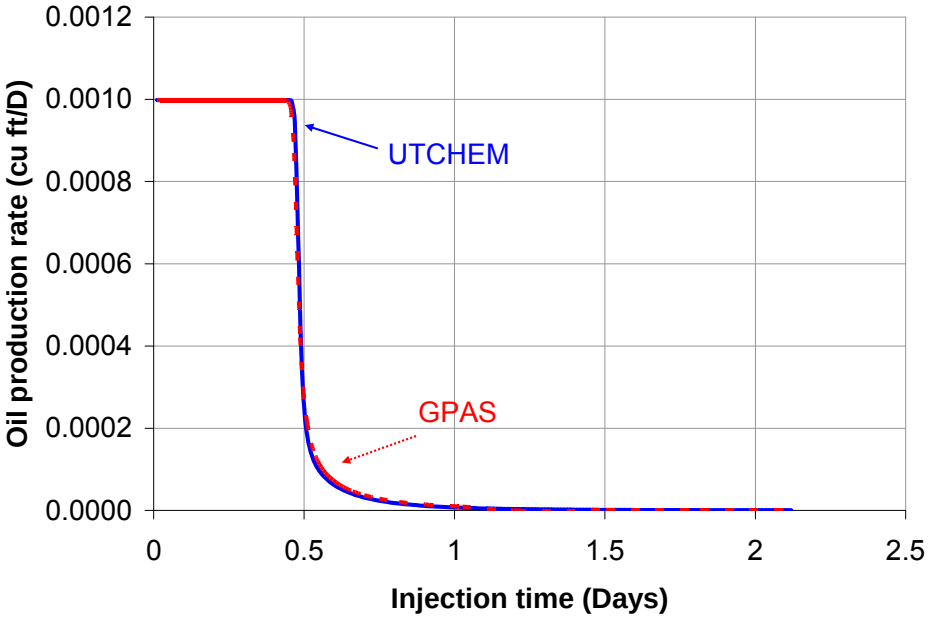

Figure 7.8: Comparison of oil production rates of UTCHEM and GPAS for a 1D waterflood simulation.

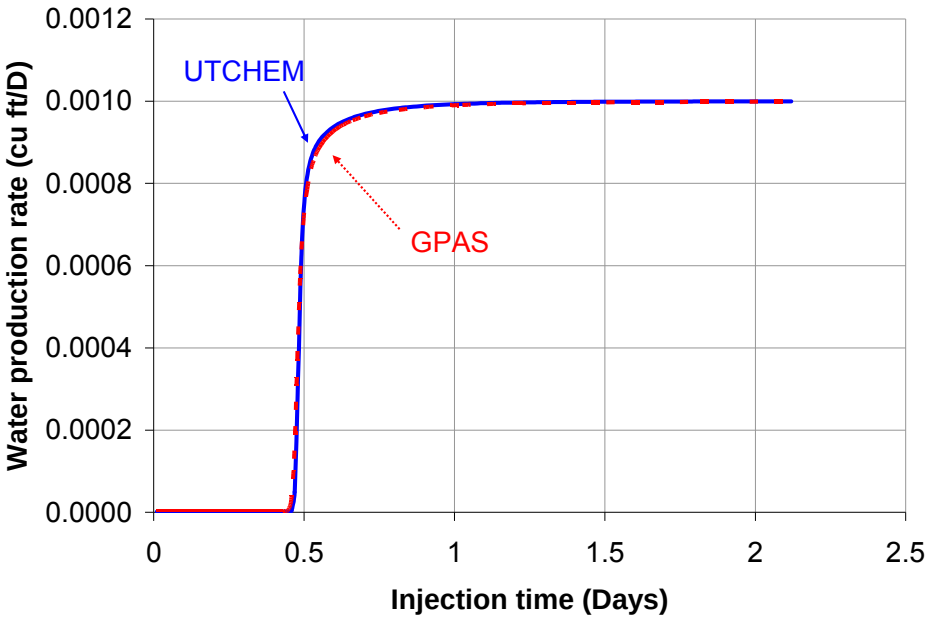

Figure 7.9: Comparison of water production rates of UTCHEM and GPAS for a 1D waterflood simulation.

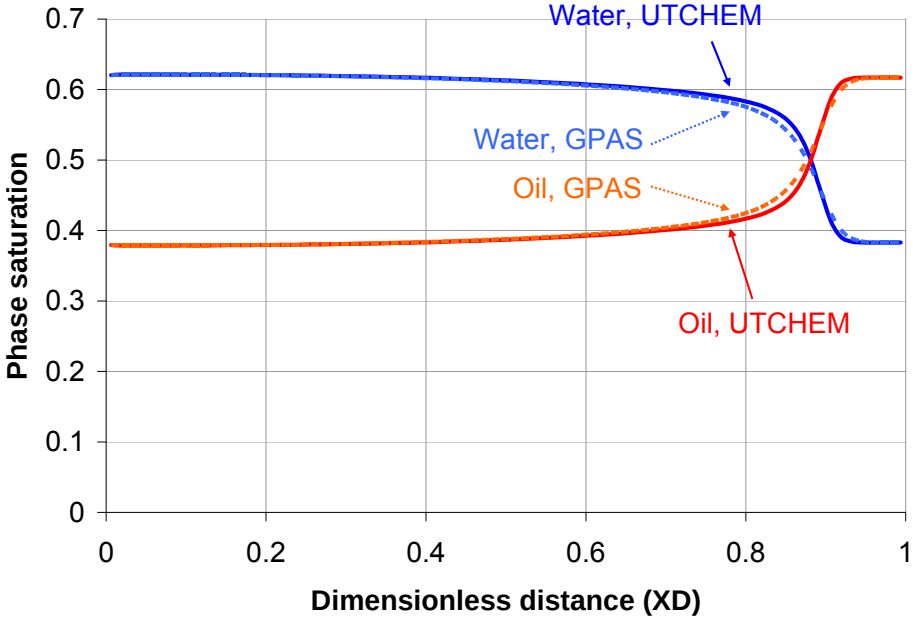

Figure 7.10: Oil and water saturation profiles at 0.2 PVs (0.4233 days) of water injection in a 1D simulation.

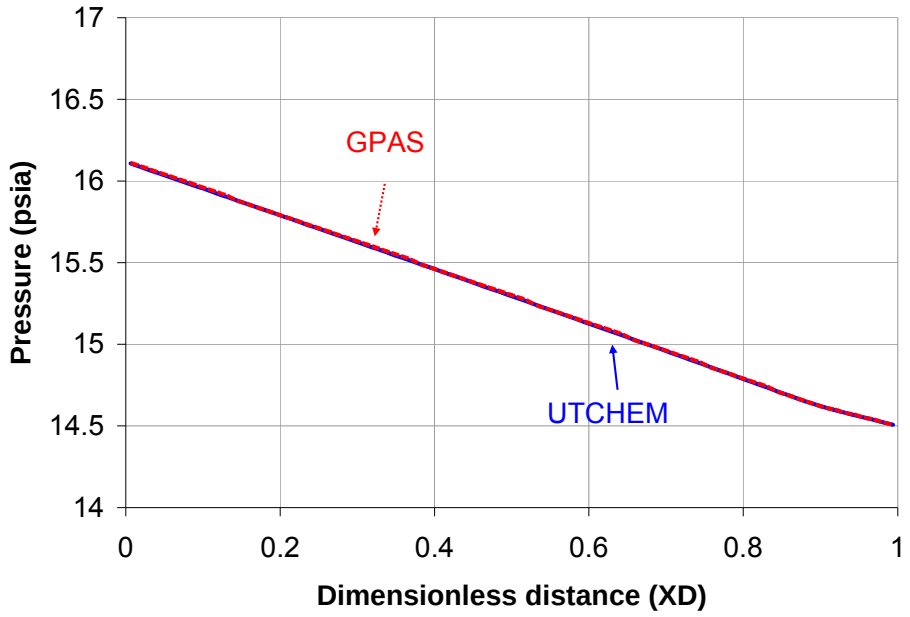

Figure 7.11: Comparison of pressure profiles at 0.2 PVs (0.4233 days) of water injection in a 1D coreflood simulation.

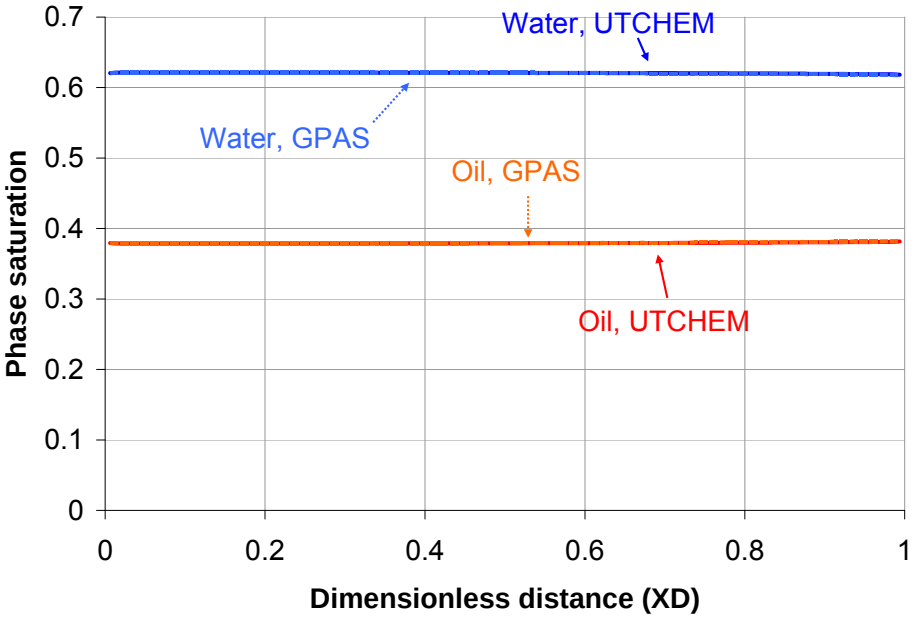

Figure 7.12: Comparison of saturation profiles at 0.57 PVs (1.21 days) of water injection in a 1D coreflood simulation.

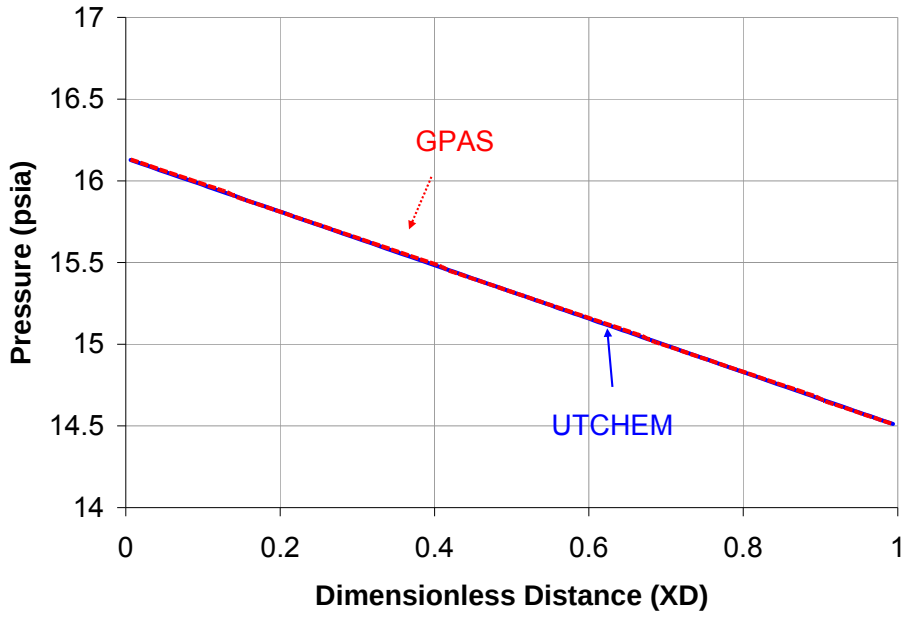

Figure 7.13: Comparison of pressure profile at 0.57 PVs (1.21 days) of water injection in 1D coreflood simulation.

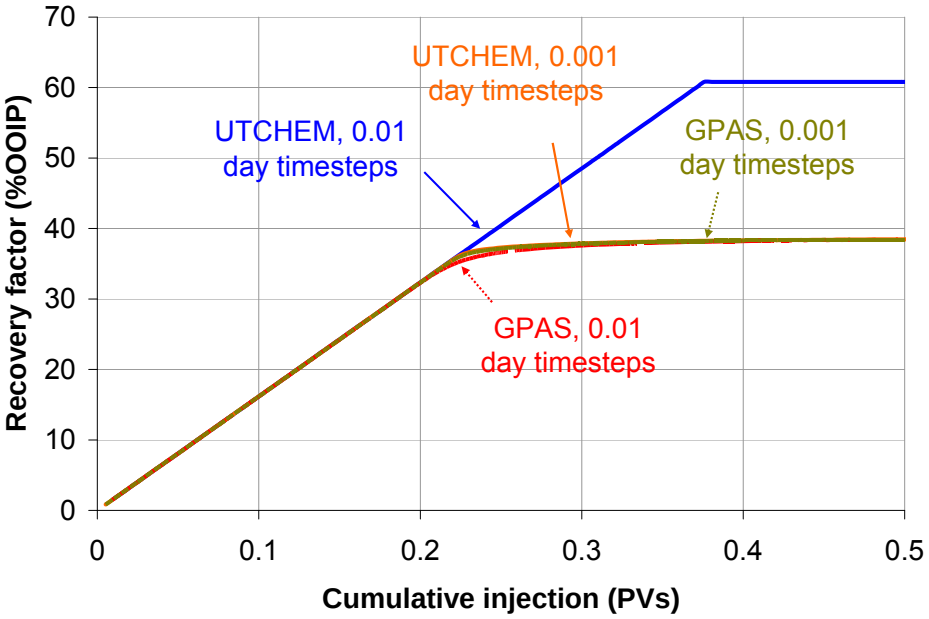

Figure 7.14: Comparison of waterflood cumulative oil recovery of UTCHEM and GPAS in a 1D core using constant timesteps.

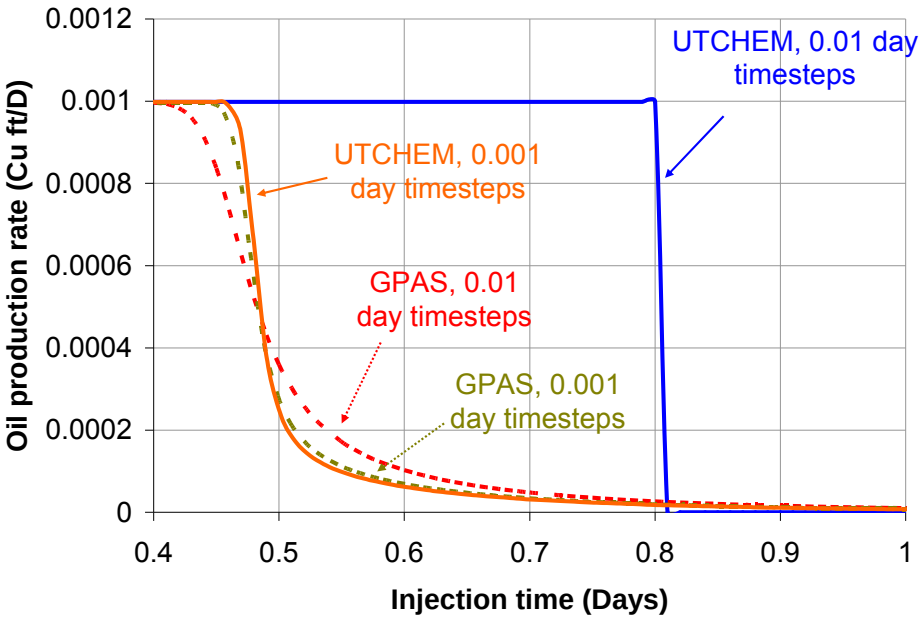

Figure 7.15: Comparison of waterflood oil production rates of UTCHEM and GPAS in a 1D core using constant timesteps.

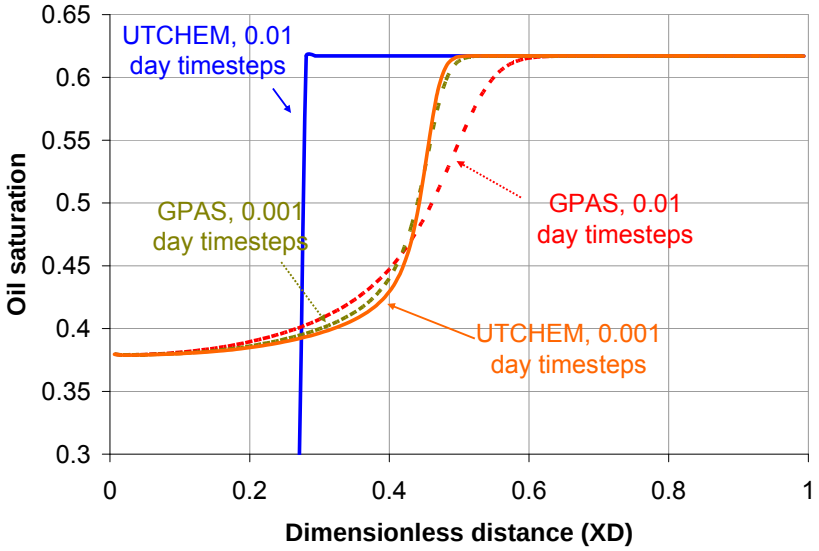

Figure 7.16: Comparison of oil saturation profiles of UTCHEM and GPAS in waterflood simulation of a 1D core using constant timesteps.

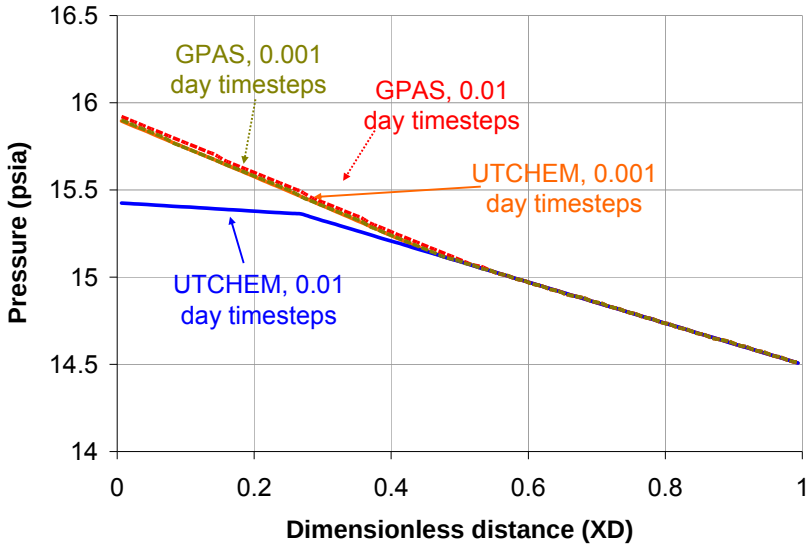

Figure 7.17: Comparison of aqueous phase pressure profiles of UTCHEM and GPAS in waterflood simulation of a 1D core using constant timesteps.

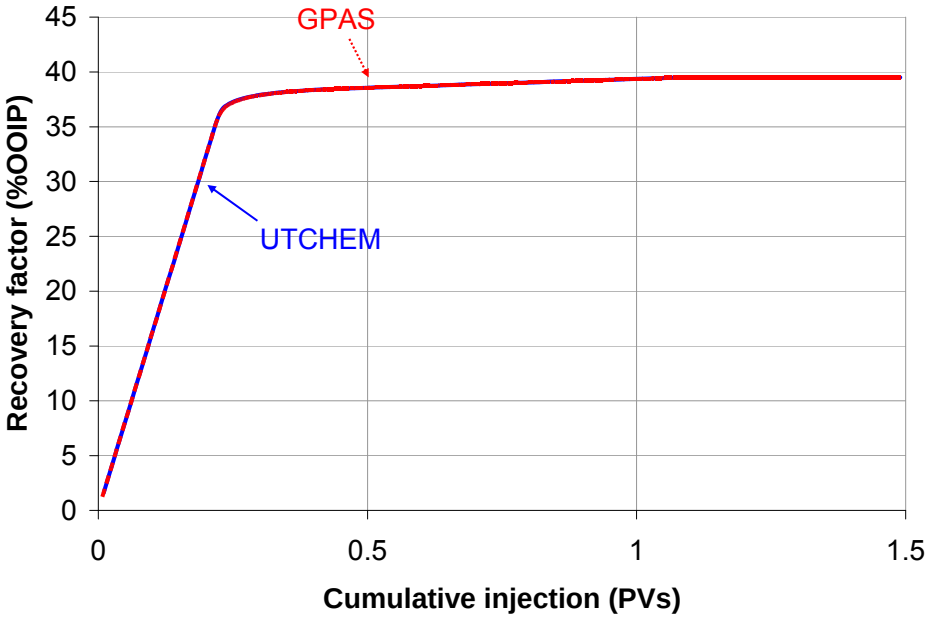

Figure 7.18: Comparison of 1D polymer flood cumulative oil recovery with automatic timestep control.

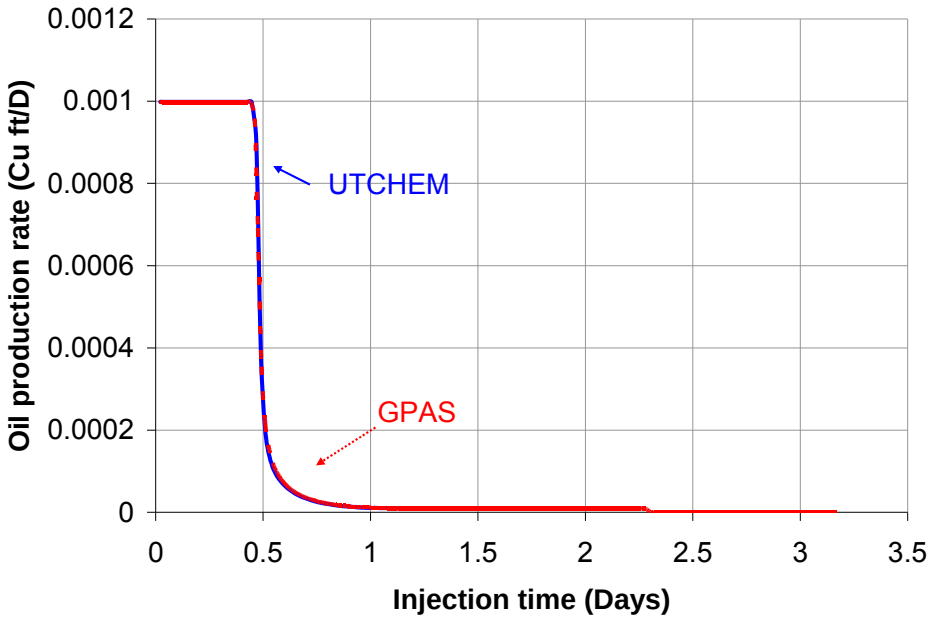

Figure 7.19: Comparison of 1D polymer flood oil production rate with automatic timestep control.

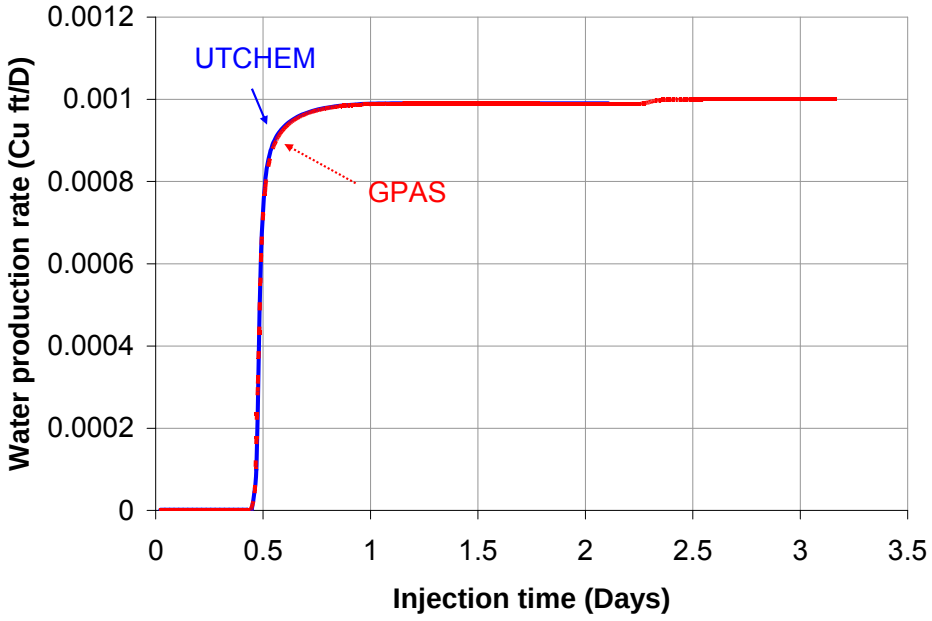

Figure 7.20: Comparison of 1D polymer flood water production rate with automatic timestep control.

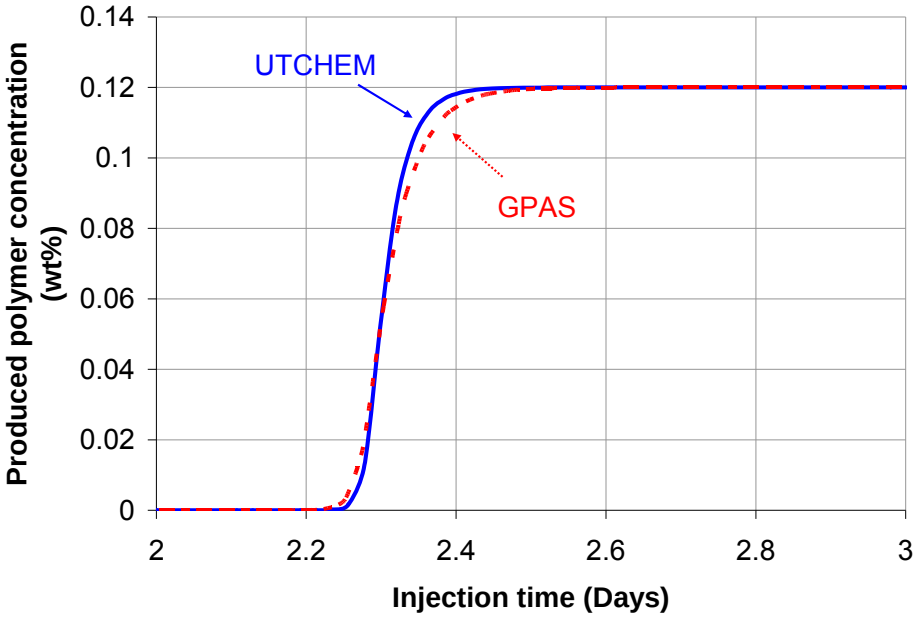

Figure 7.21: Comparison of produced polymer concentration (wt%) of GPAS and UTCHEM with automatic timestep control in 1D polymer flood.

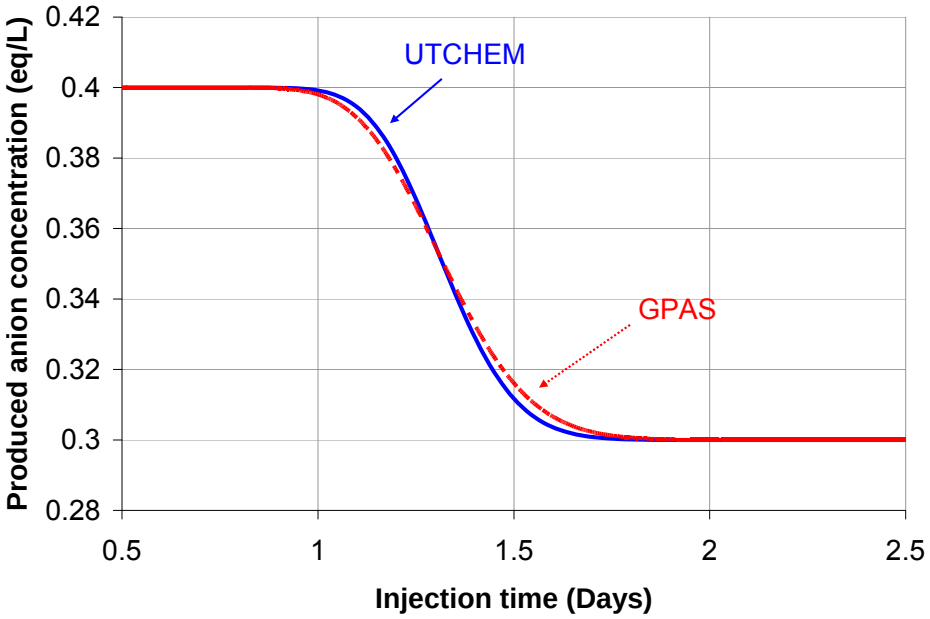

Figure 7.22: Comparison of produced anion concentration (eq/L) for 1D polymer flood with automatic timestep control.

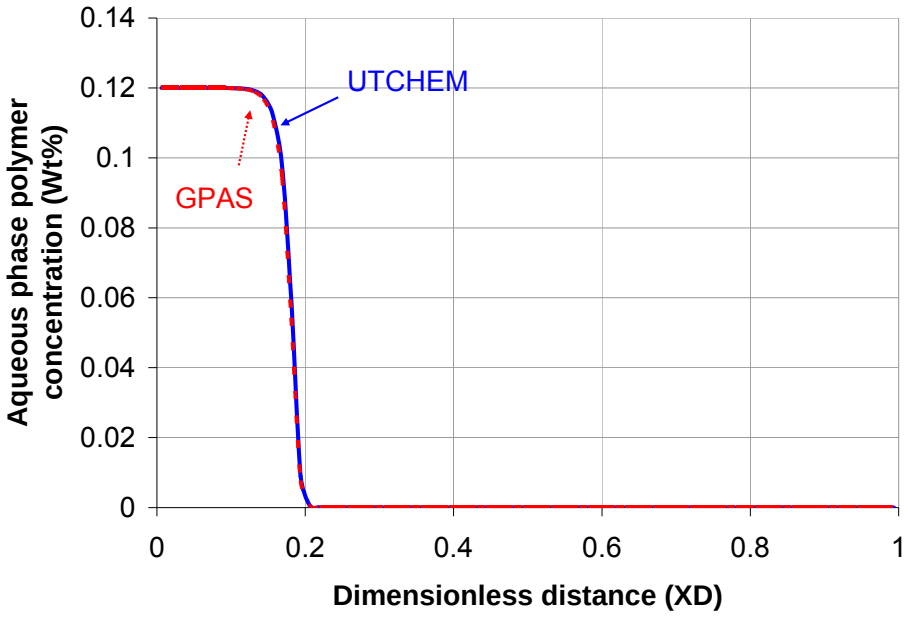

Figure 7.23: Comparison of polymer concentration profiles at 0.2 PVs (0.423 days) of polymer injection.

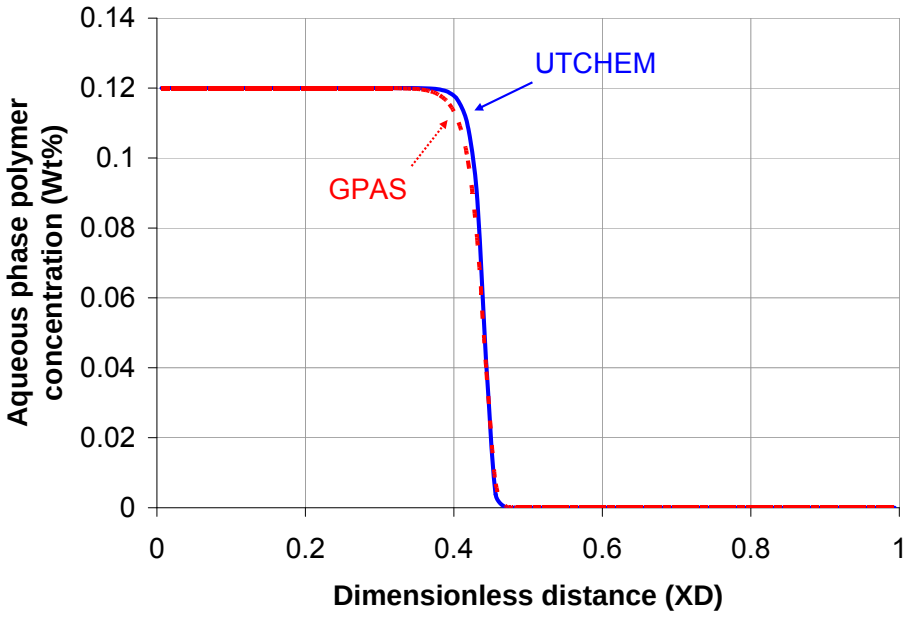

Figure 7.24: Comparison of polymer concentration profiles after 0.48 PVs (1.02 days) of polymer injection.

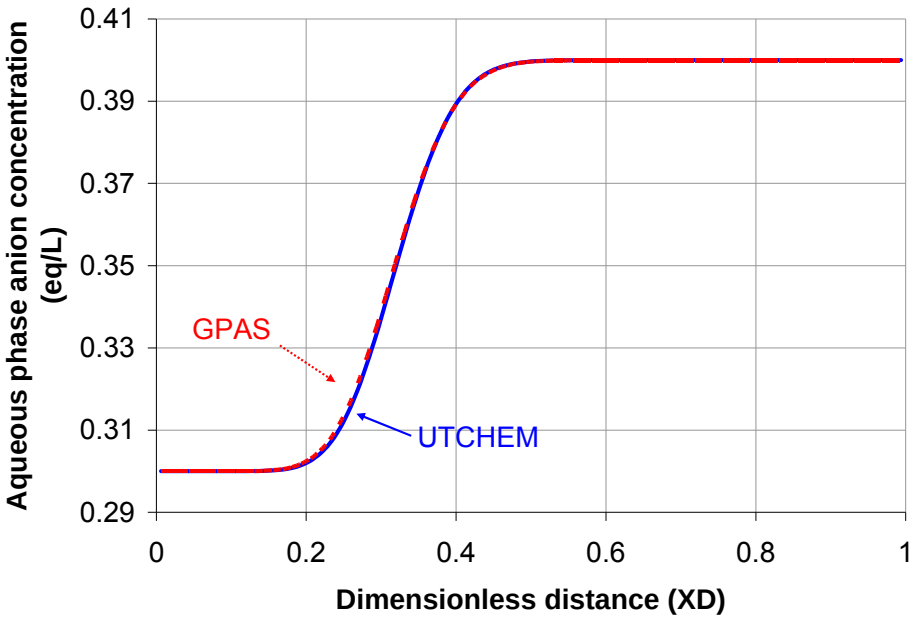

Figure 7.25: Comparison of anion concentration profiles after 0.2 PVs (0.423 days) of polymer injection.

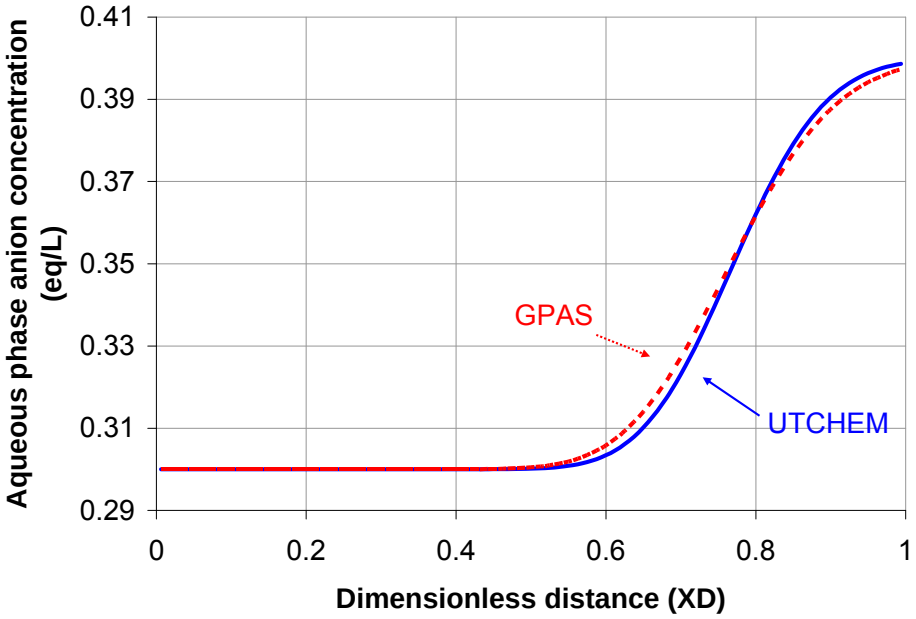

Figure 7.26: Comparison of anion concentration profiles after 0.48 PVs (1.02 days) of polymer injection.

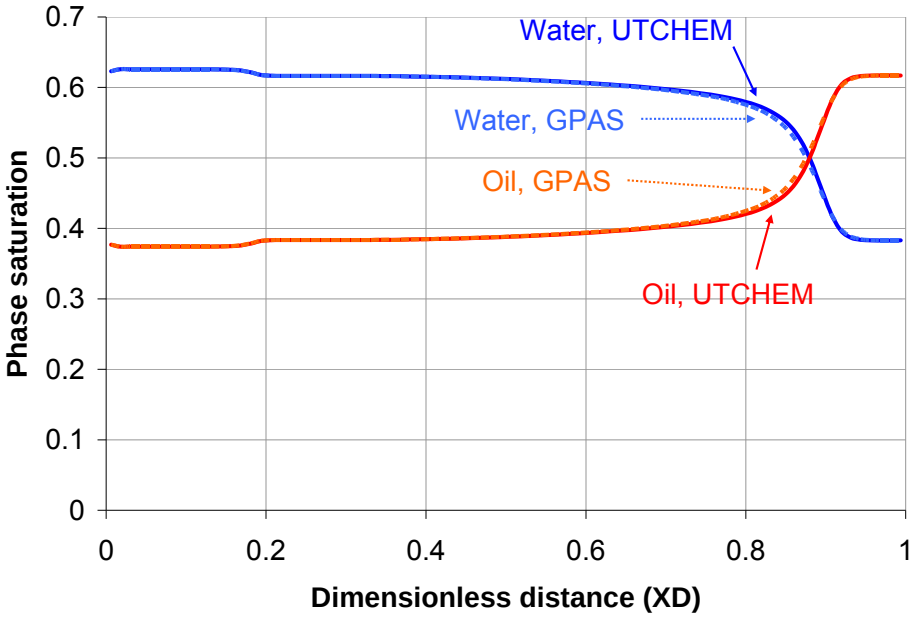

Figure 7.27: Comparison of saturation profiles at 0.2 PVs (0.423 days) of polymer injection.

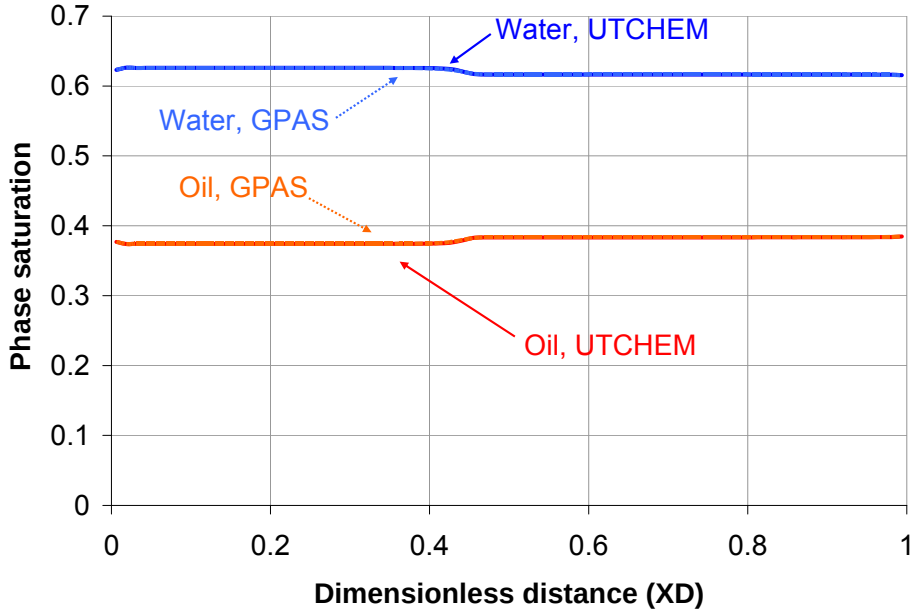

Figure 7.28: Comparison of saturation profiles at 0.48 PVs (1.02 days) of polymer injection.

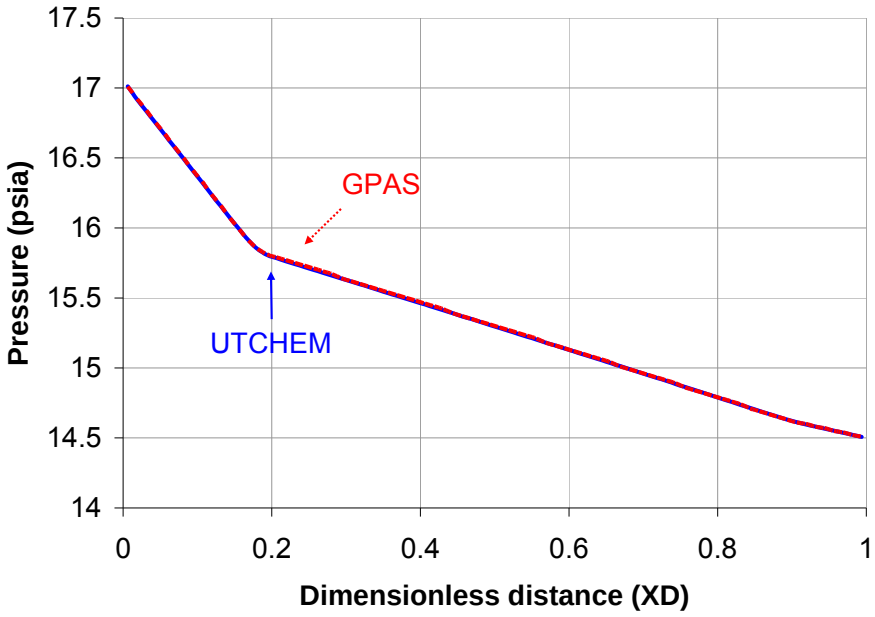

Figure 7.29: Comparison of pressure profiles at 0.2 PVs (0.423 days) of polymer injection.

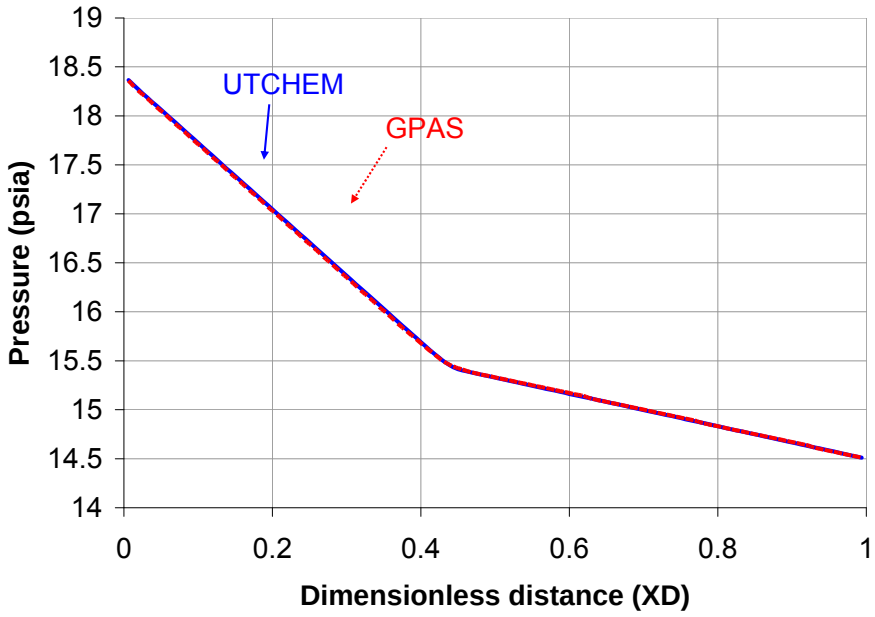

Figure 7.30: Comparison of pressure profiles at 0.48 PVs (1.02 days) of polymer injection.

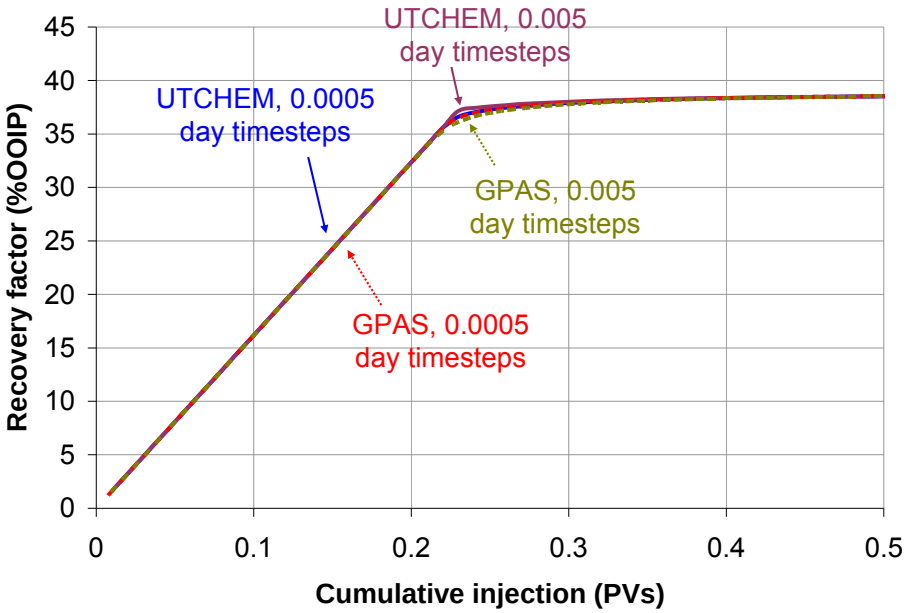

Figure 7.31: Comparison of polymer flood oil recovery with constant timesteps. 7.31

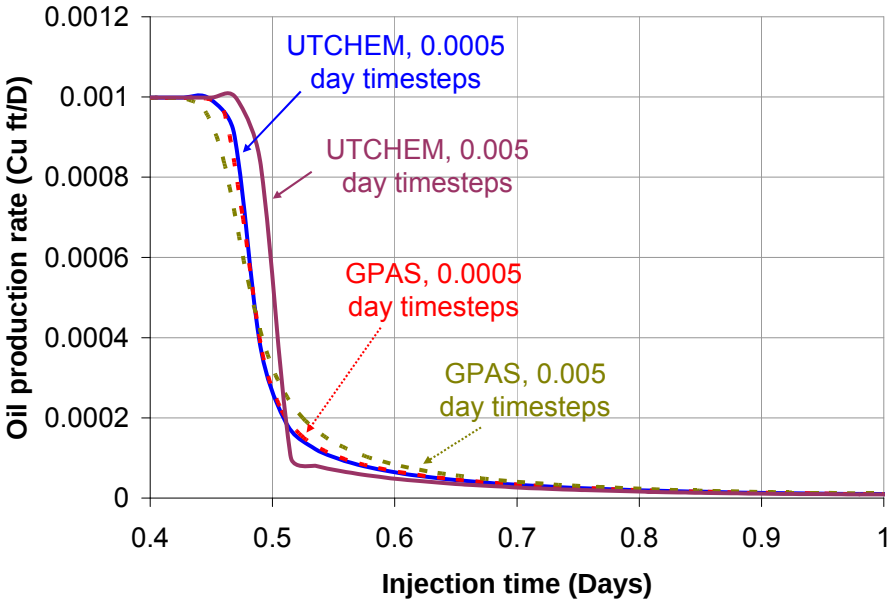

Figure 7. 32: Comparison of 1D polymer flood oil production rate with constant timesteps.

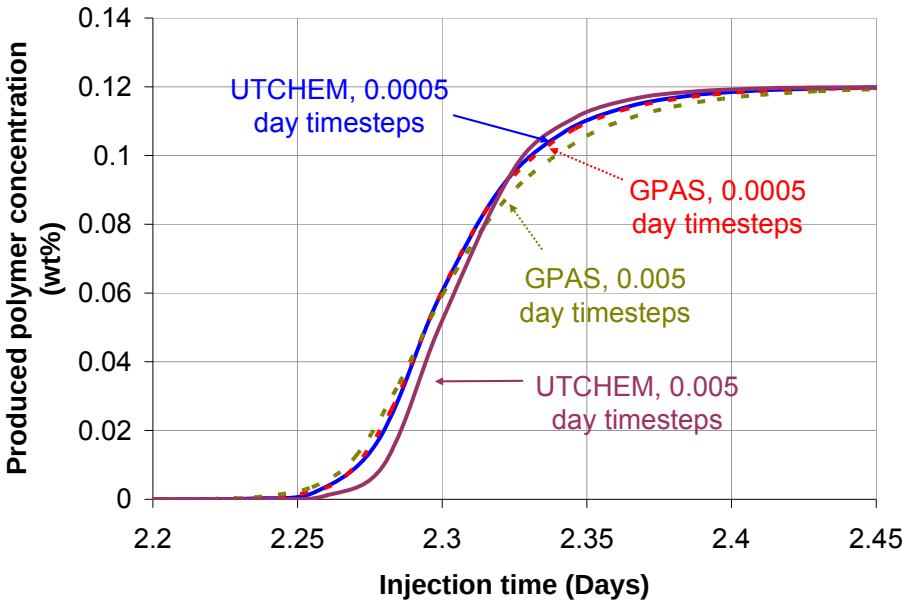

Figure 7.33: Comparison of polymer concentration with constant timesteps.

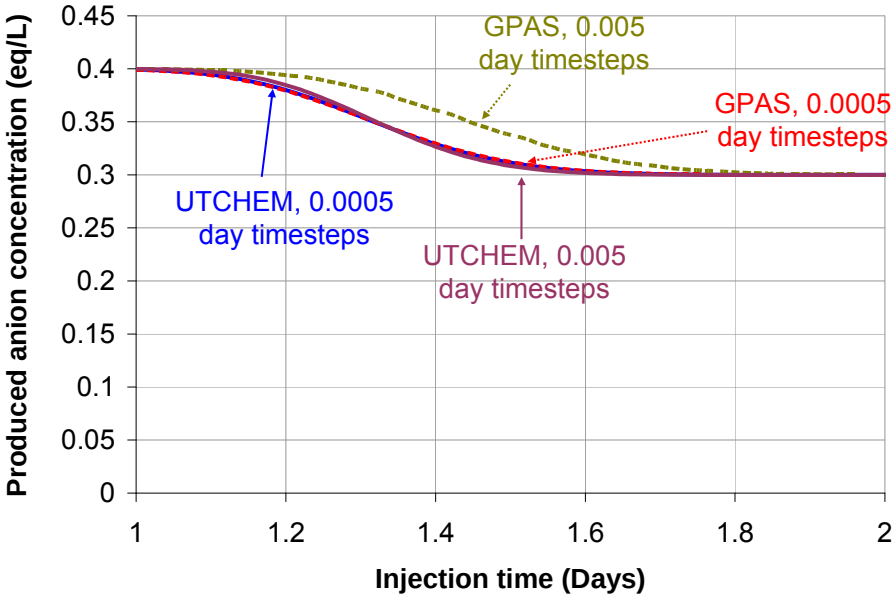

Figure 7.34: Comparison of anion concentration with constant timesteps.

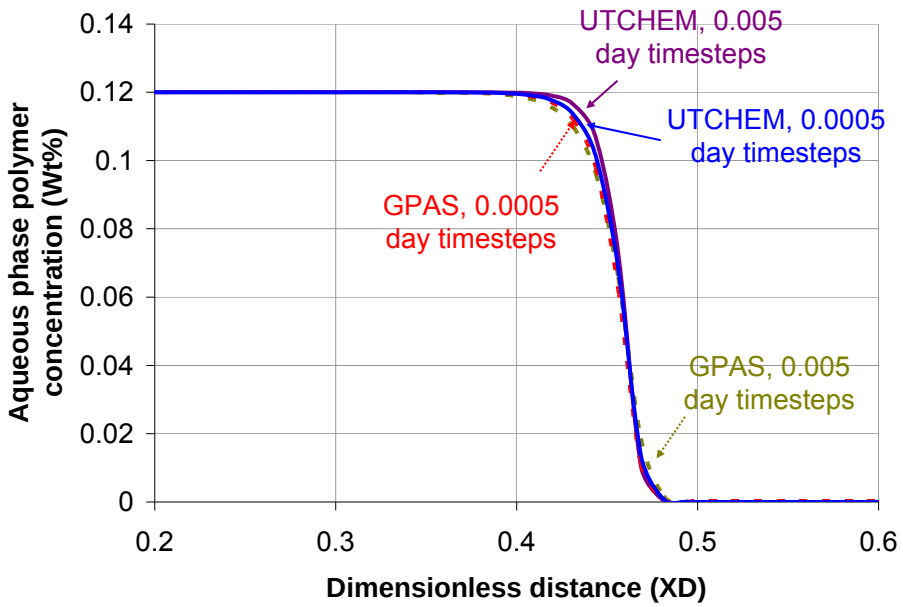

Figure 7.35: Polymer concentration profiles at 0.5 PV polymer injection with constant timesteps.

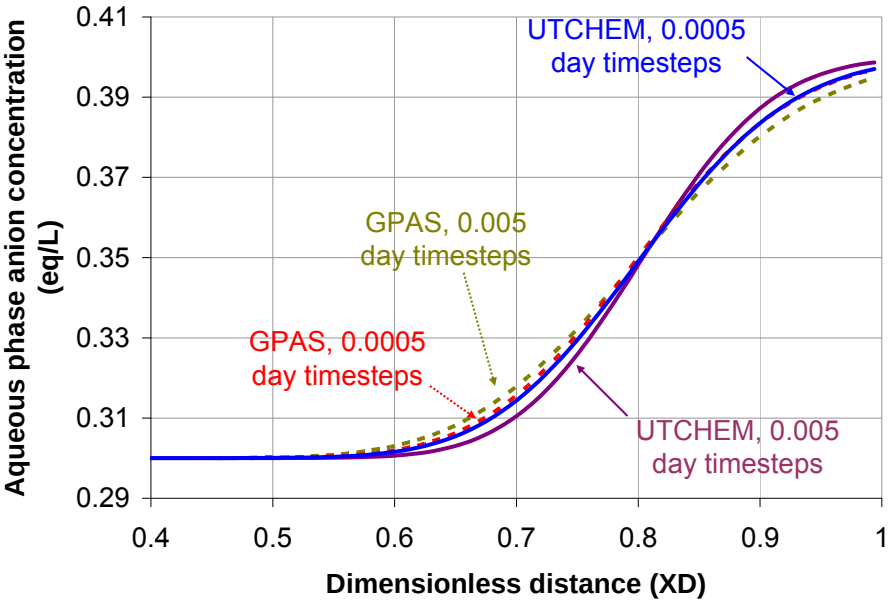

Figure 7.36: Anion concentration profiles at 0.5 PV polymer injection with constant timesteps.

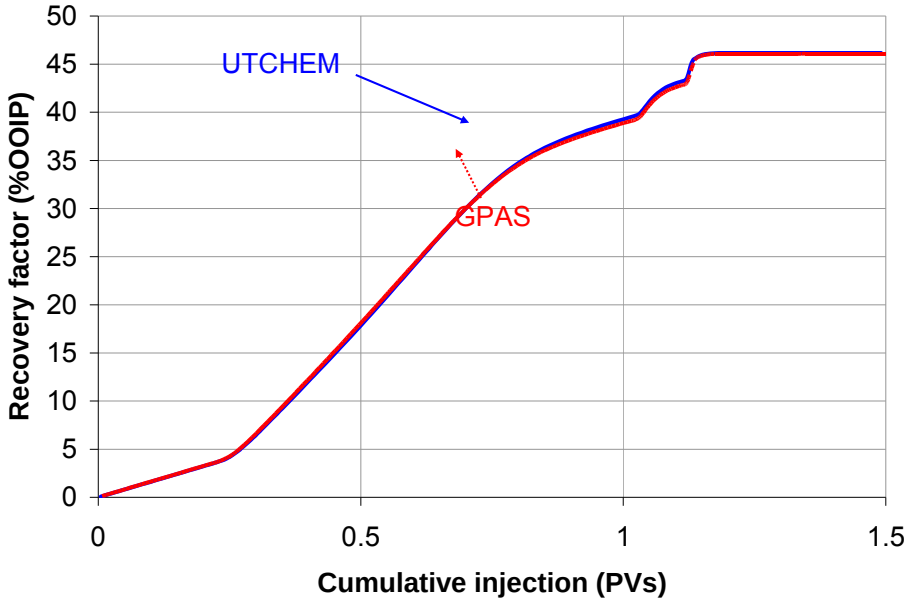

Figure 7.37: Comparison of 1D surfactant/polymer recovery factors.

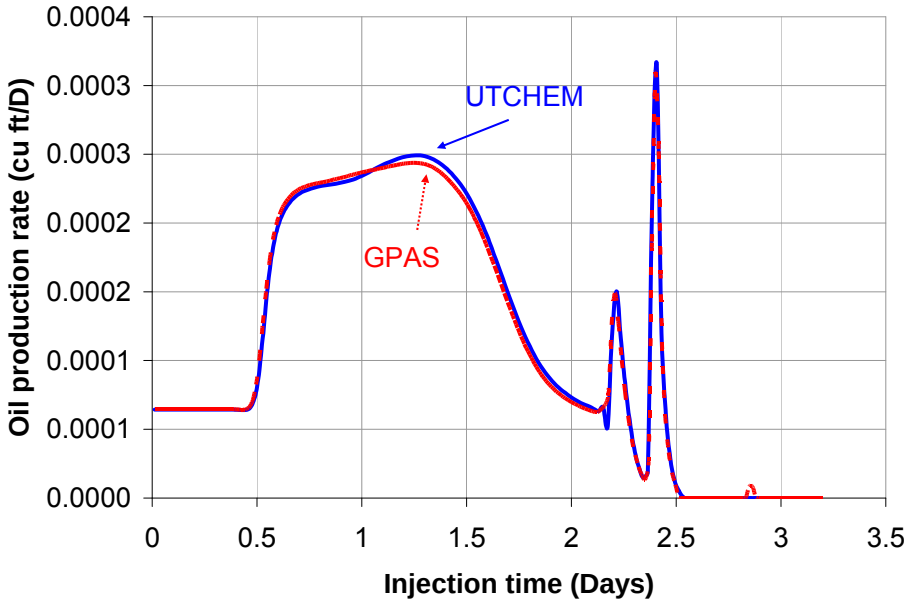

Figure 7.38: Comparison of 1D surfactant/polymer oil production rate.

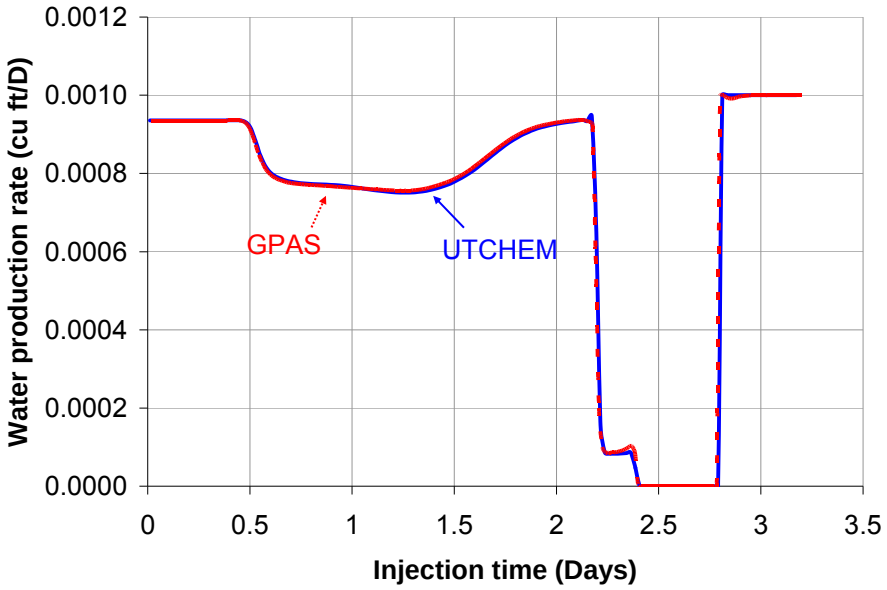

Figure7.39: Comparison of 1D surfactant/polymer water production rate.

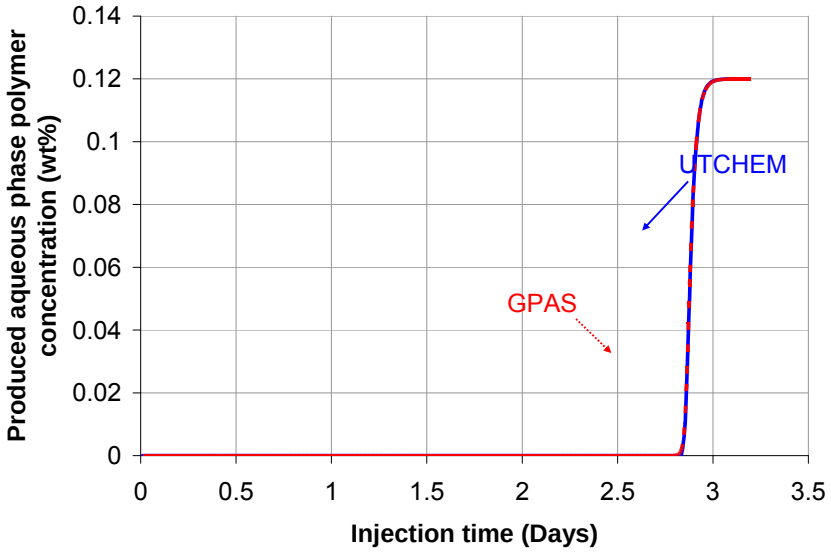

Figure 7.40: Comparison of 1D surfactant/polymer polymer concentration.

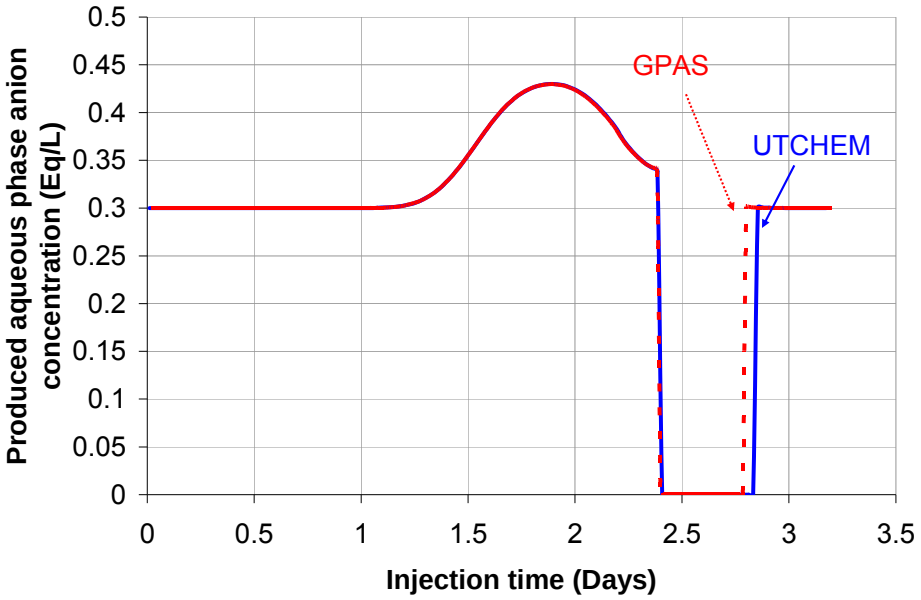

Figure 7.41: Comparison of 1D surfactant/polymer aqueous phase anion concentration.

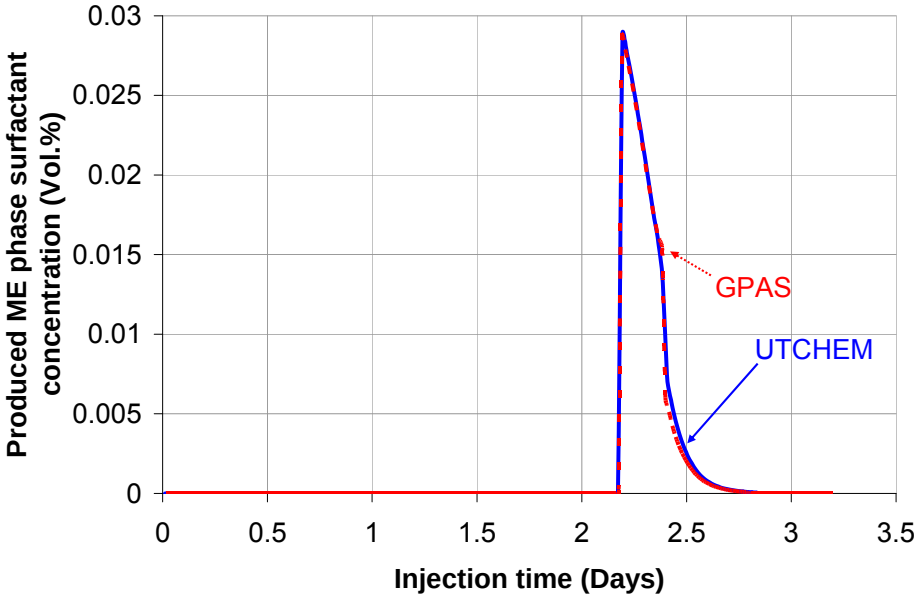

Figure 7.42: Comparison of 1D surfactant/polymer surfactant concentration in ME phase.

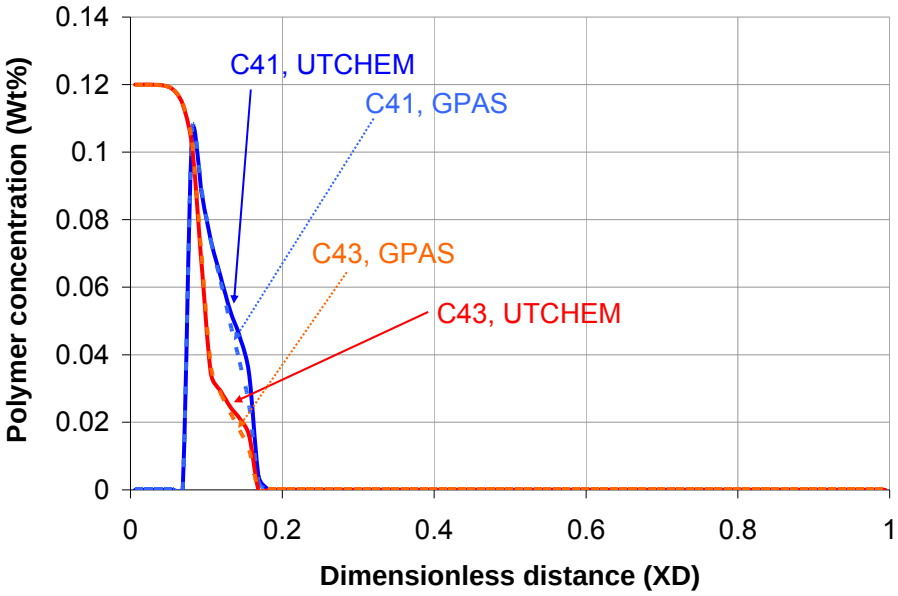

Figure 7.43: Comparison of polymer concentration in aqueous and ME phases at 0.2 PVs (0.423 days).

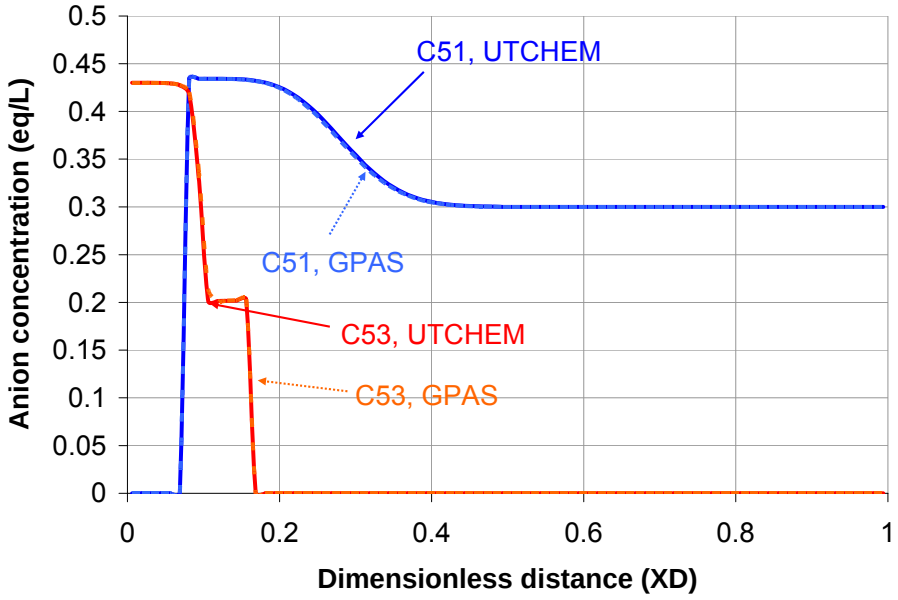

Figure 7.44: Comparison of anion concentration in aqueous and ME phases 0.2 PVs (0.423 days).

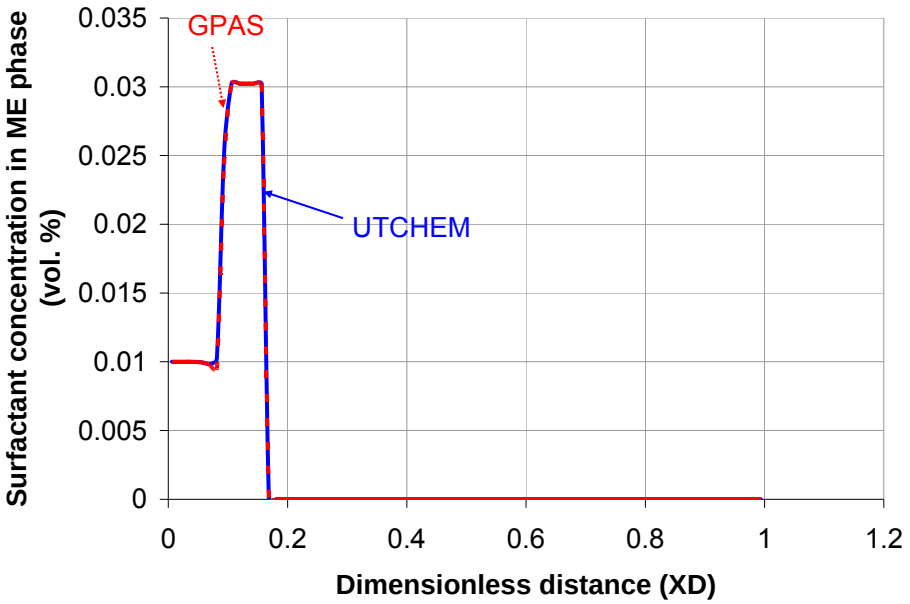

Figure 7.45: Comparison of surfactant concentration in ME phase at 0.2 PVs (0.423 days).

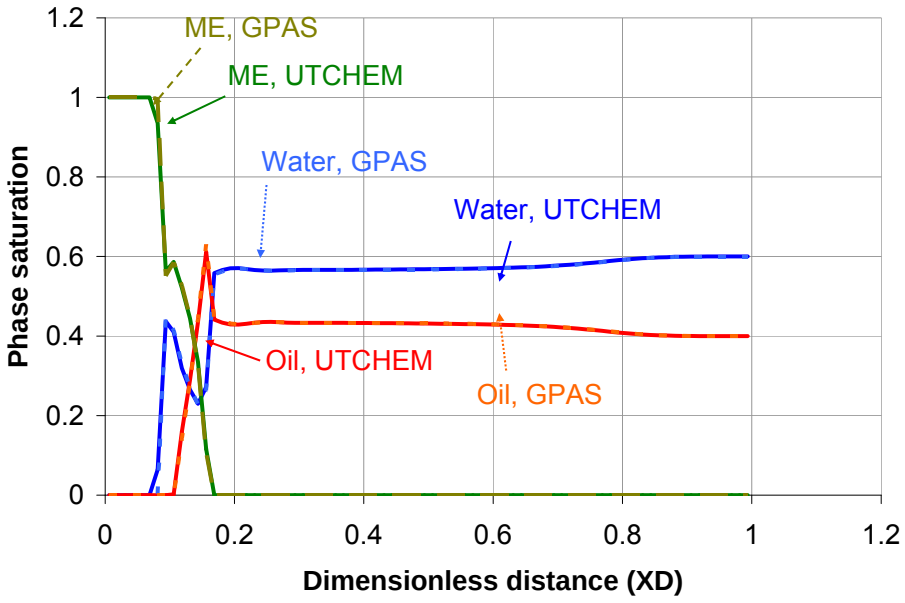

Figure 7.46: Comparison of saturations at 0.2 PVs (0.423 days).

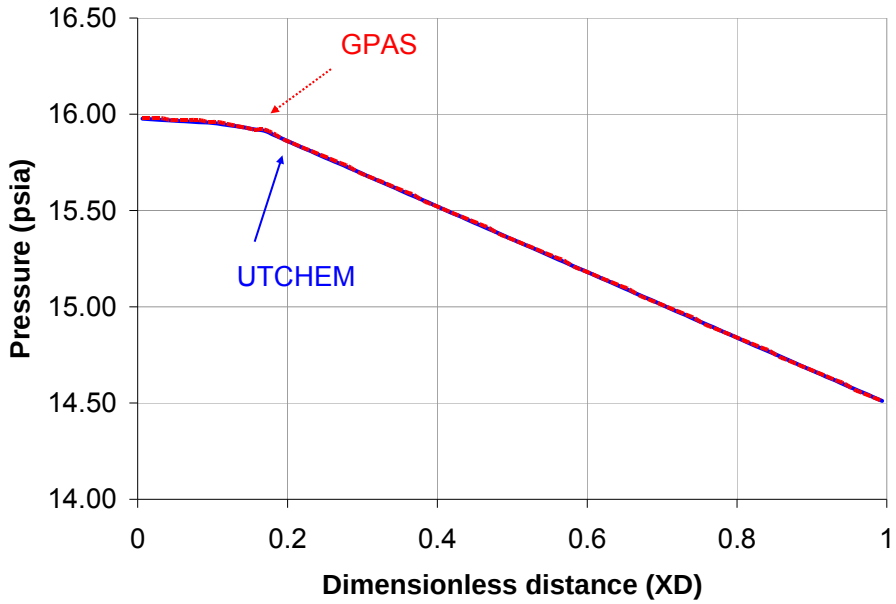

Figure 7.47: Comparison of pressure profile at 0.2 PVs (0.423 days).

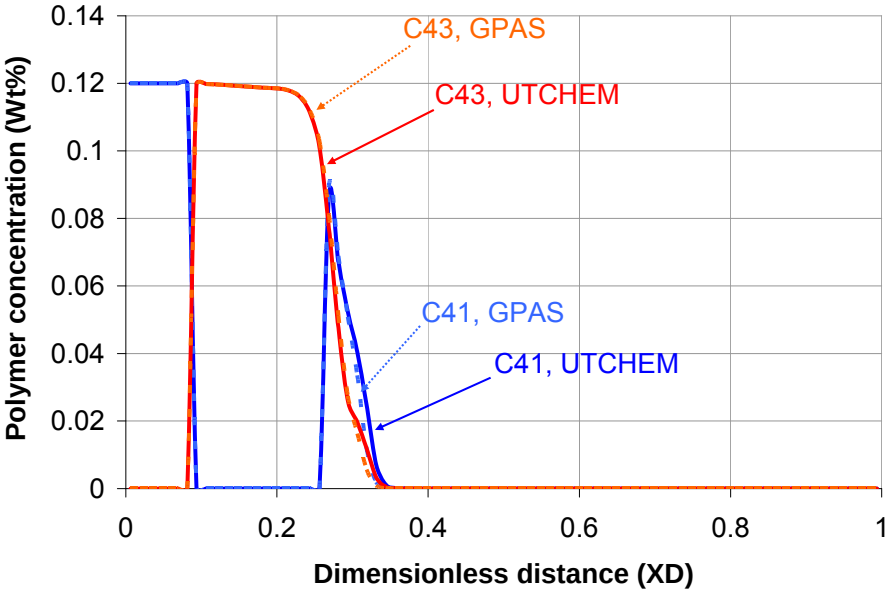

Figure 7.48: Comparison of polymer concentration in aqueous and ME phases at 0.5 PVs (1.06 days).

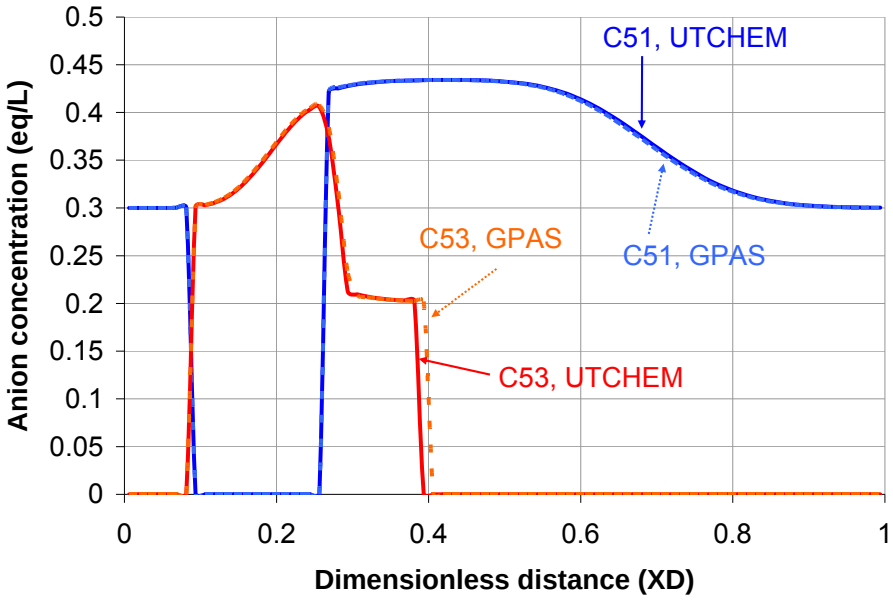

Figure 7.49: Comparison of anion concentration in aqueous and ME phases (at 0.5 PVs (1.06 days).

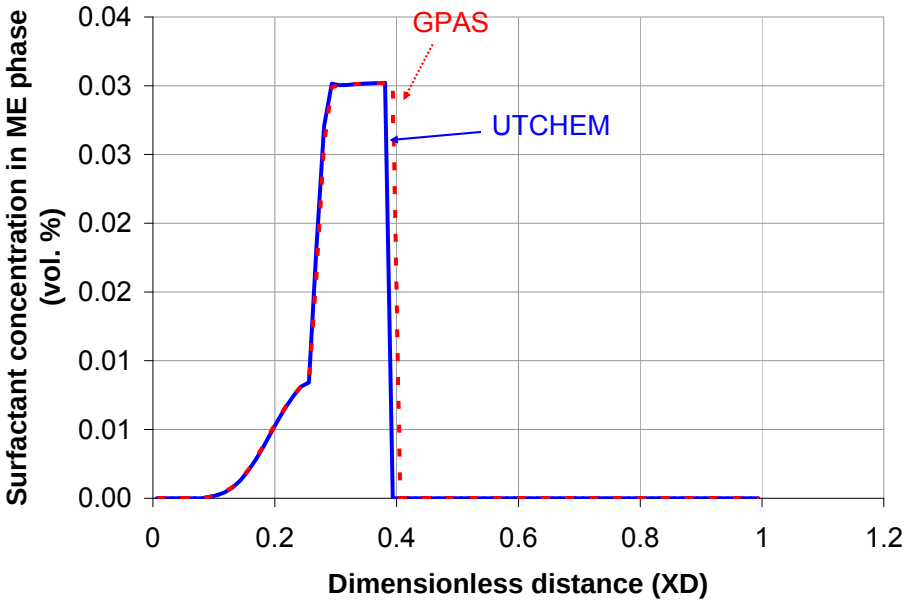

Figure 7.50: Comparison of surfactant concentration in ME phase 0.5 PVs (1.06 days).

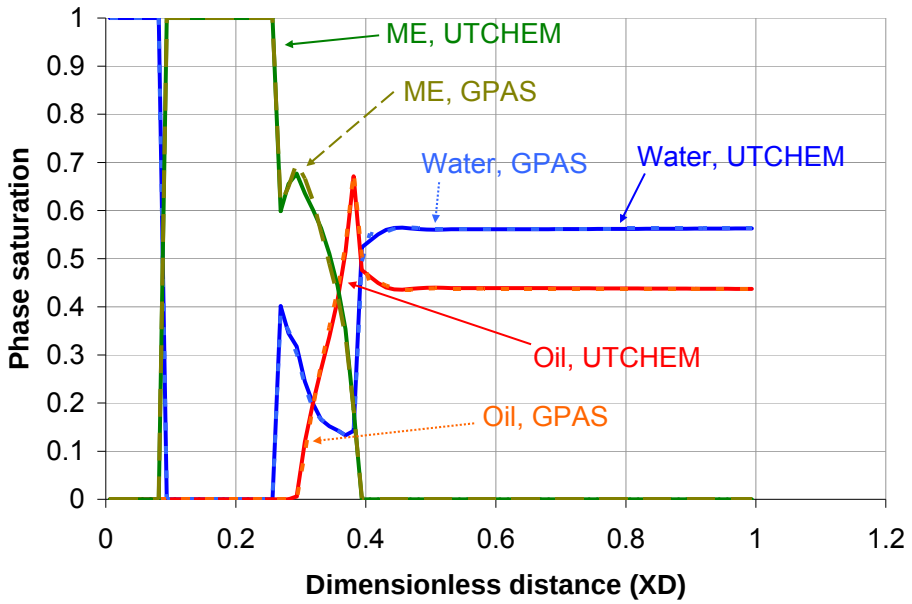

Figure 7.51: Comparison of phase saturations after 0.5 PVs (1.06 days).

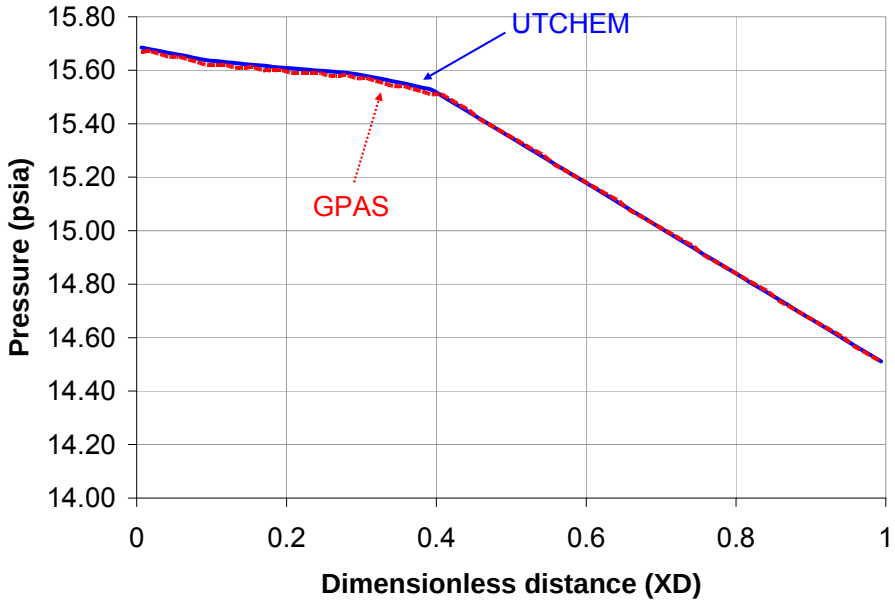

Figure 7.52: Comparison of pressure profiles at 0.5 PVs (1.06 days).

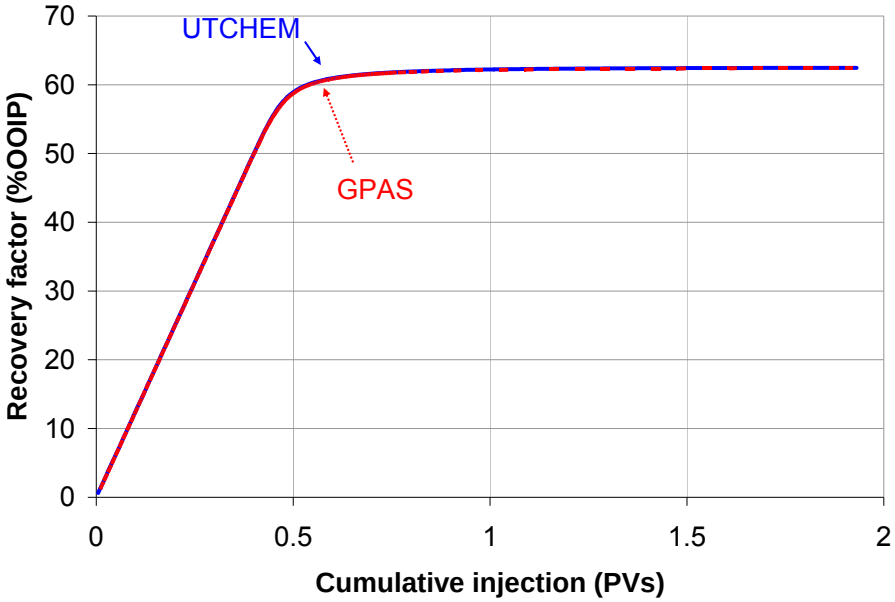

Figure 7.53: Comparison of waterflood recovery factors for 2D case

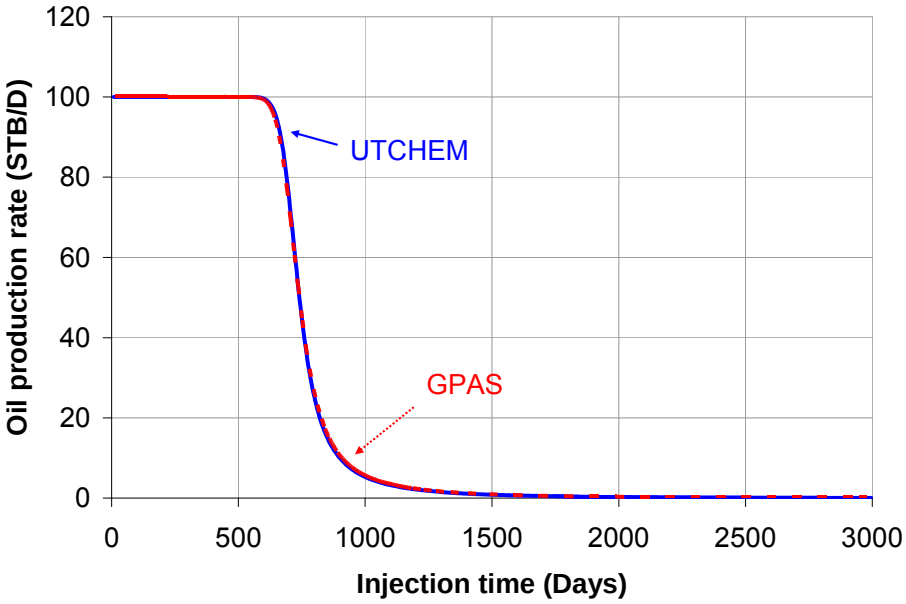

Figure 7.54: Comparison of 2D waterflood oil production rates.

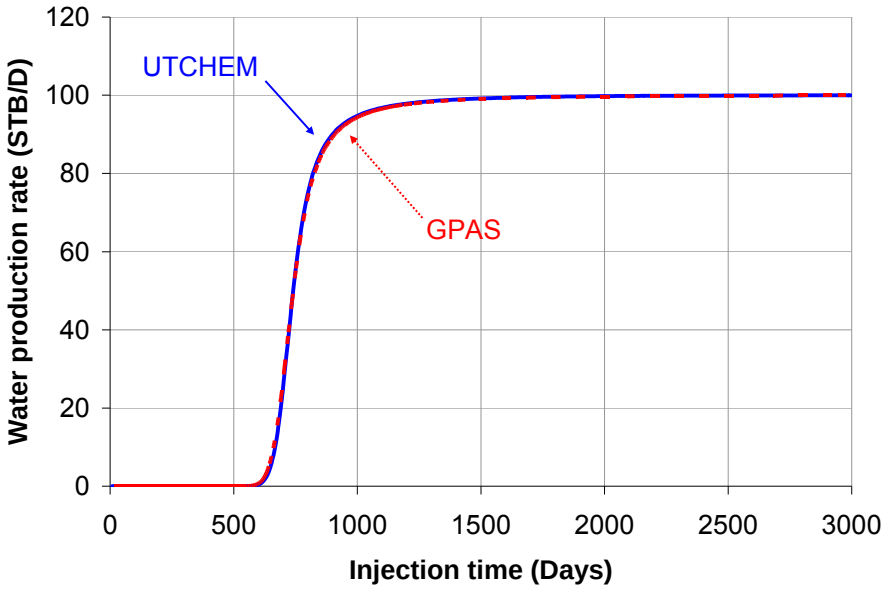

Figure 7.55: Comparison of 2D waterflood water production rates.

7.55

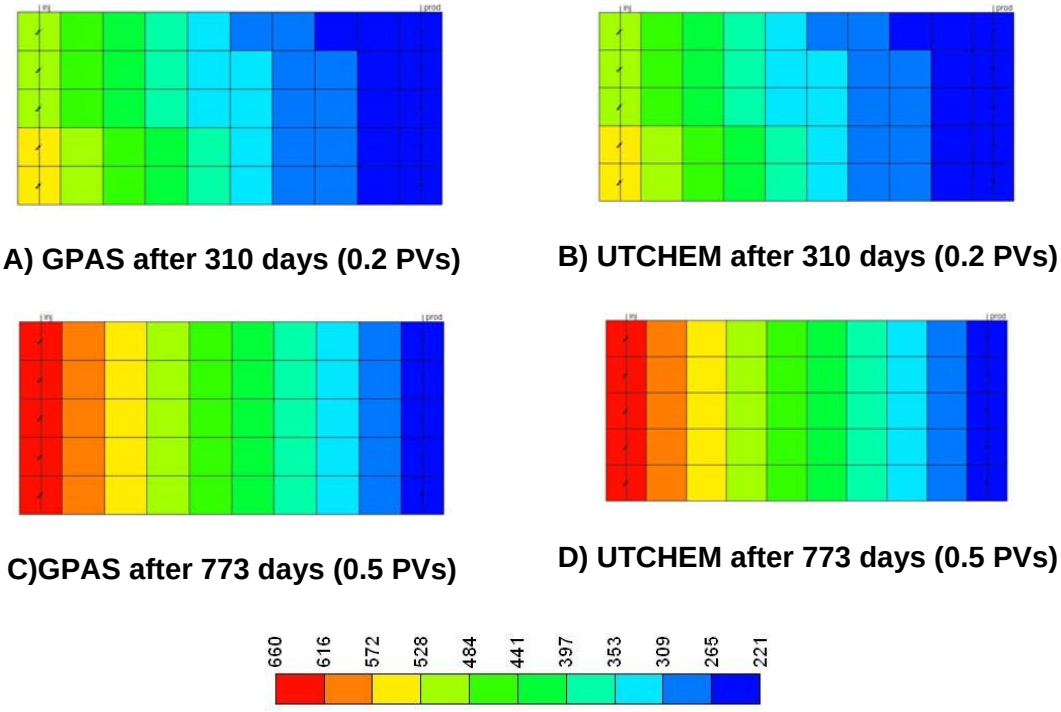

Figure 7.56: Comparison of pressure (psia) profiles for 2D waterflood.

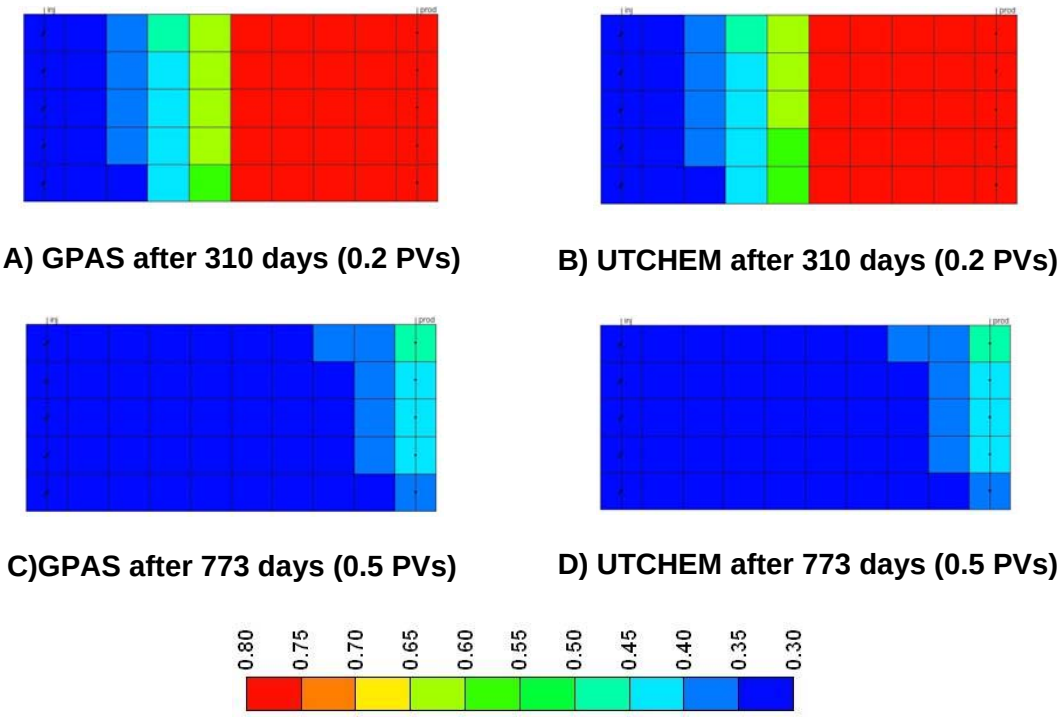

Figure 7.57: Comparison of oil saturation profiles for 2D waterflood r. 7.57

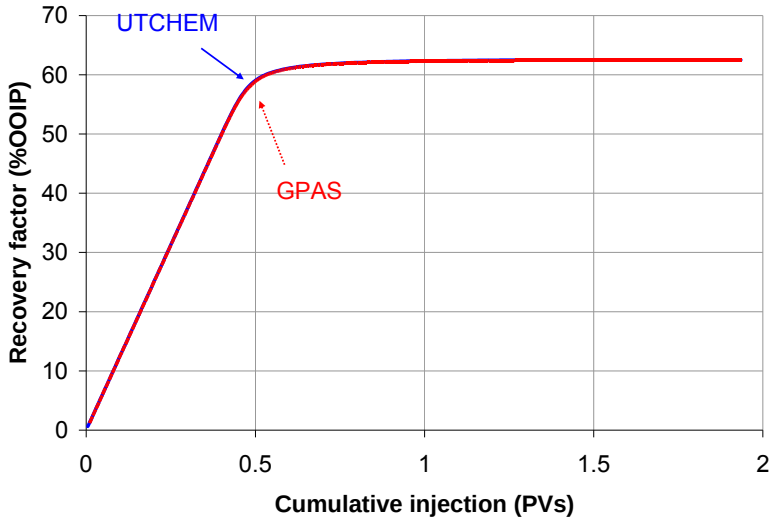

Figure 7.58: Comparison of 2D polymer flood recovery factors.

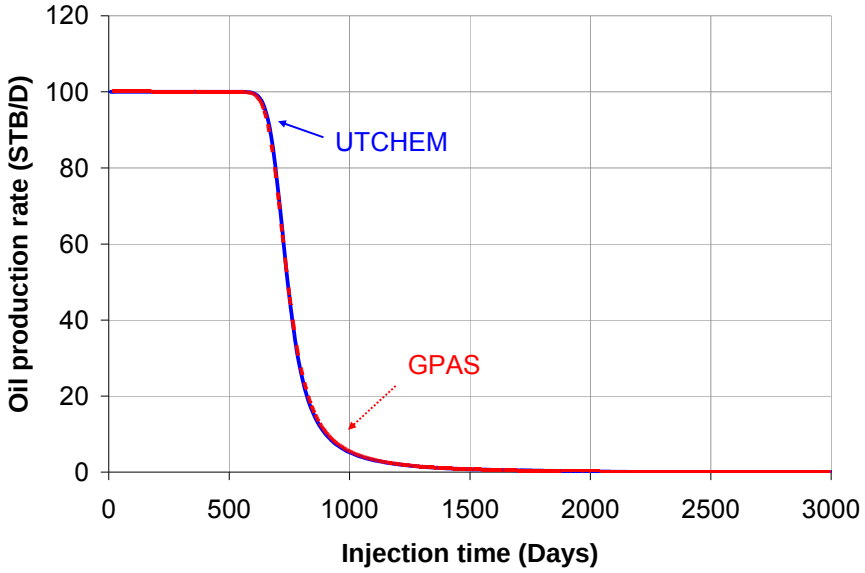

Figure 7.59: Comparison of 2D polymer flood oil production rates.

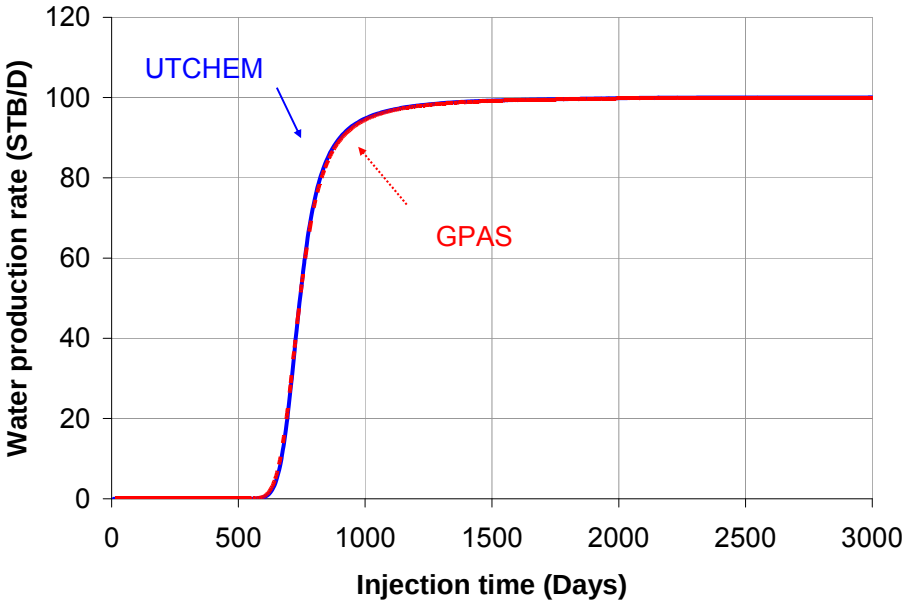

Figure 7.60: Comparison of 2D polymer flood water production rates.

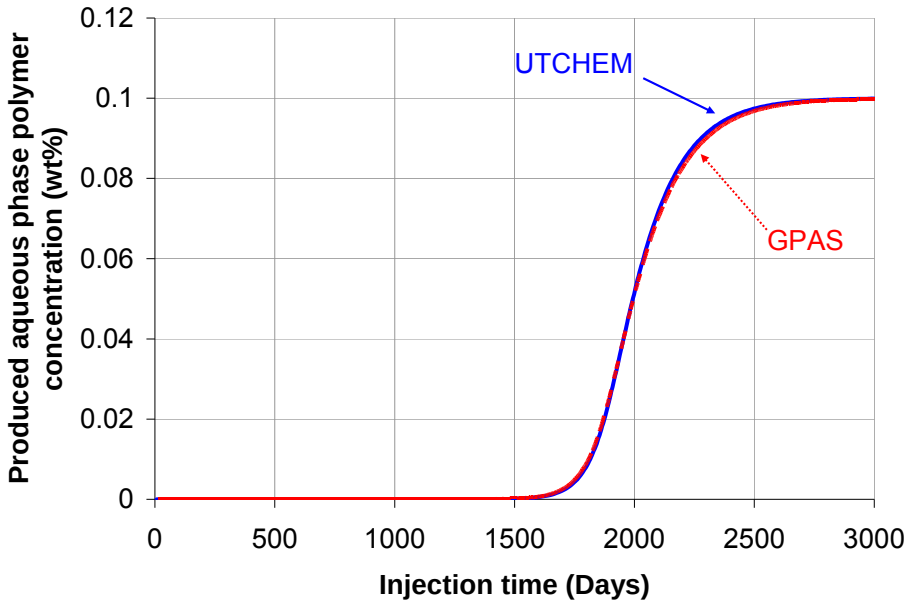

Figure 7.61: Comparison of 2D polymer flood effluent polymer concentration.

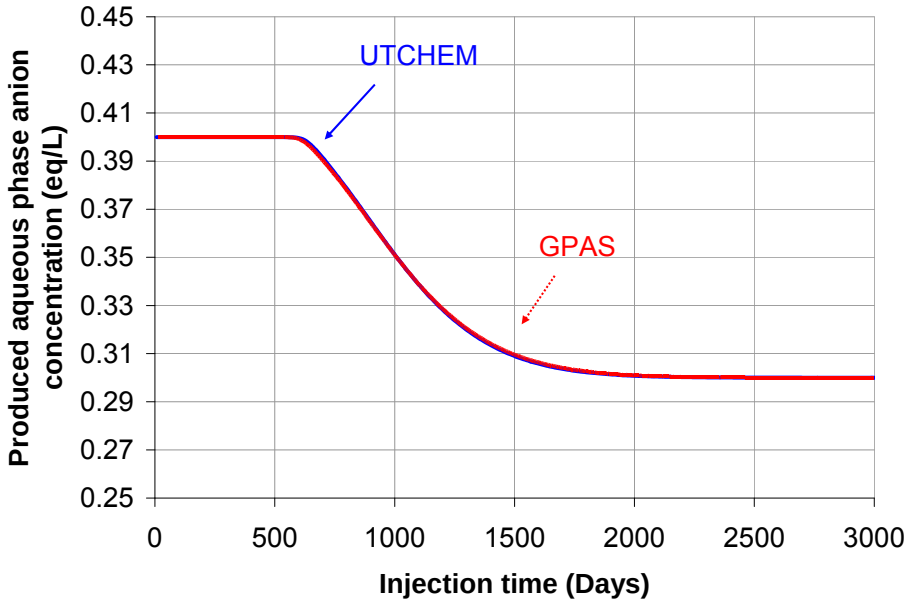

Figure 7.62: Comparison of 2D polymer flood effluent salt concentration.

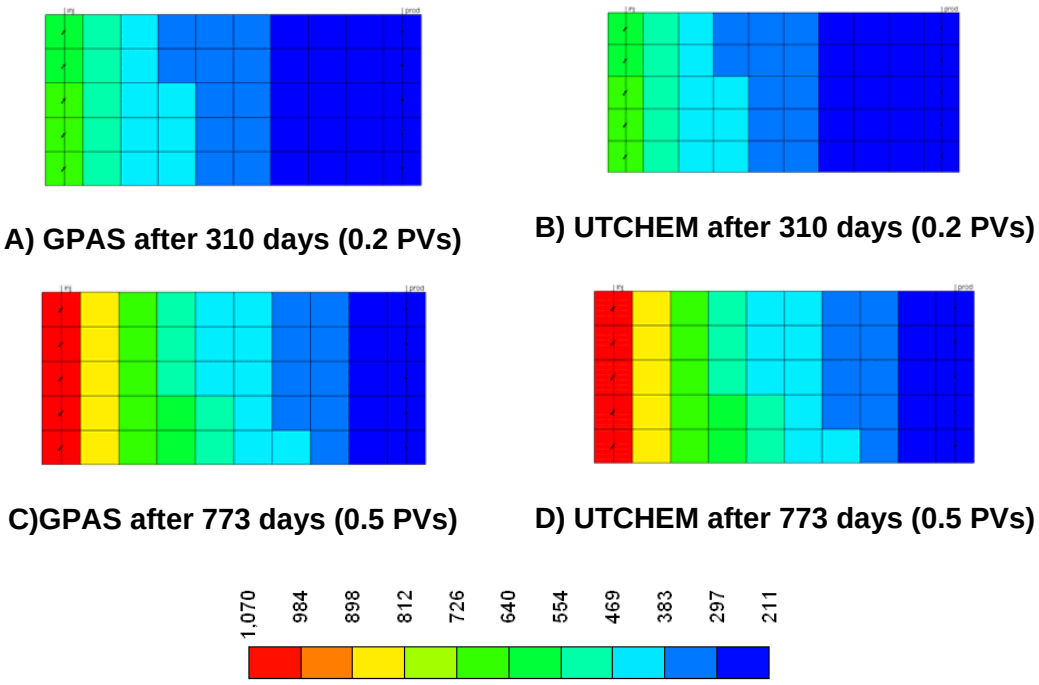

Figure 7.63: Comparison of pressure profiles (psia) for 2D polymer flood.

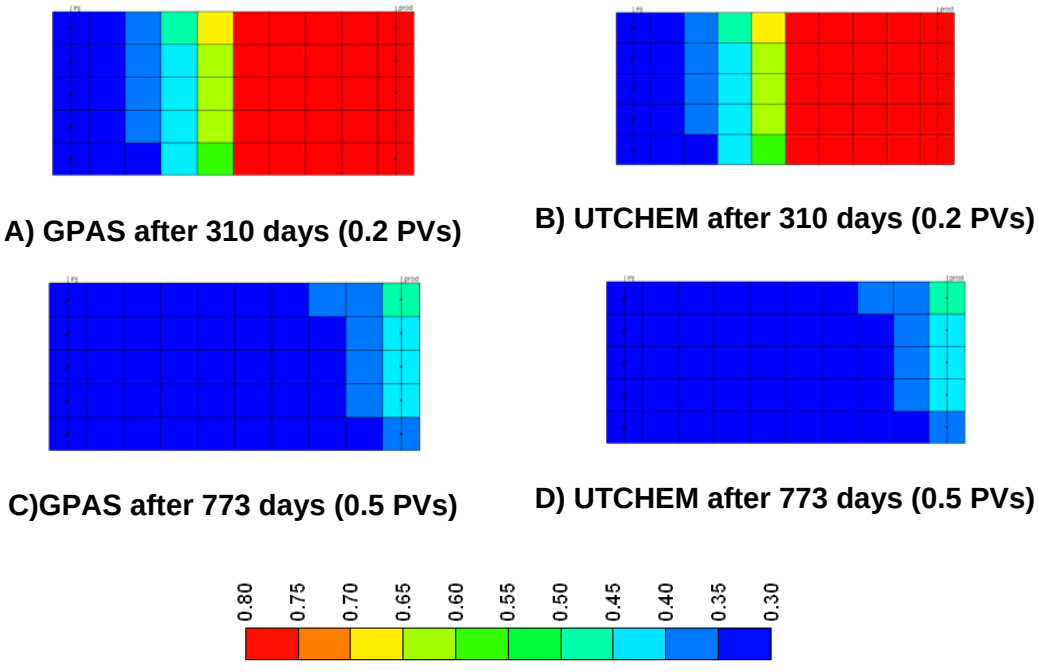

Figure 7.64: Comparison of oil saturation profiles for 2D polymer flood

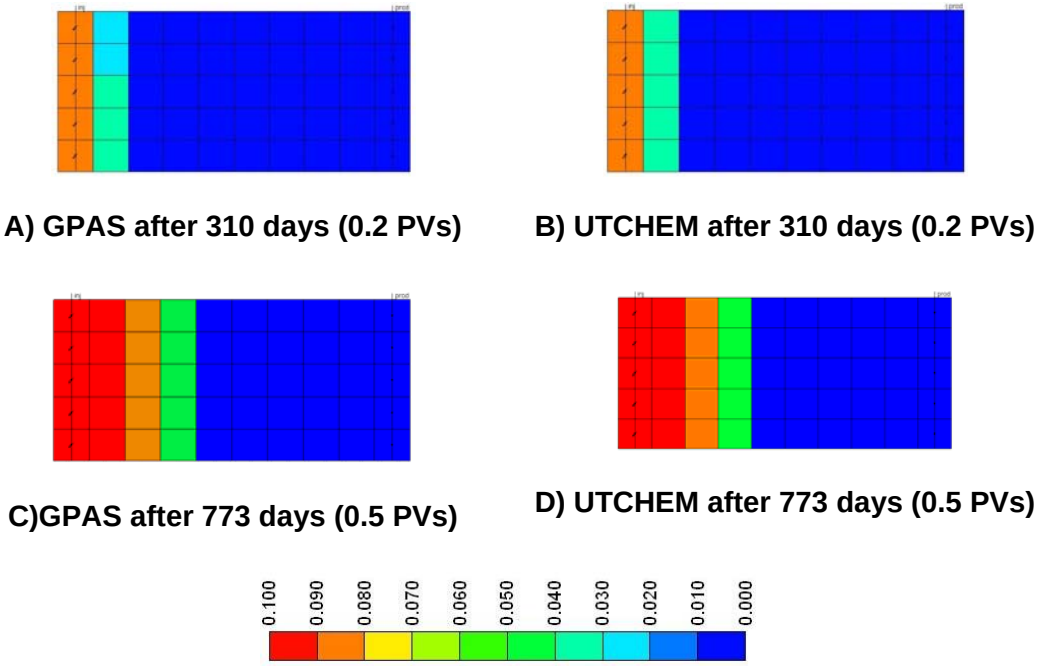

Figure 7.65: Comparison of polymer concentration (wt%) for 2D polymer flood.

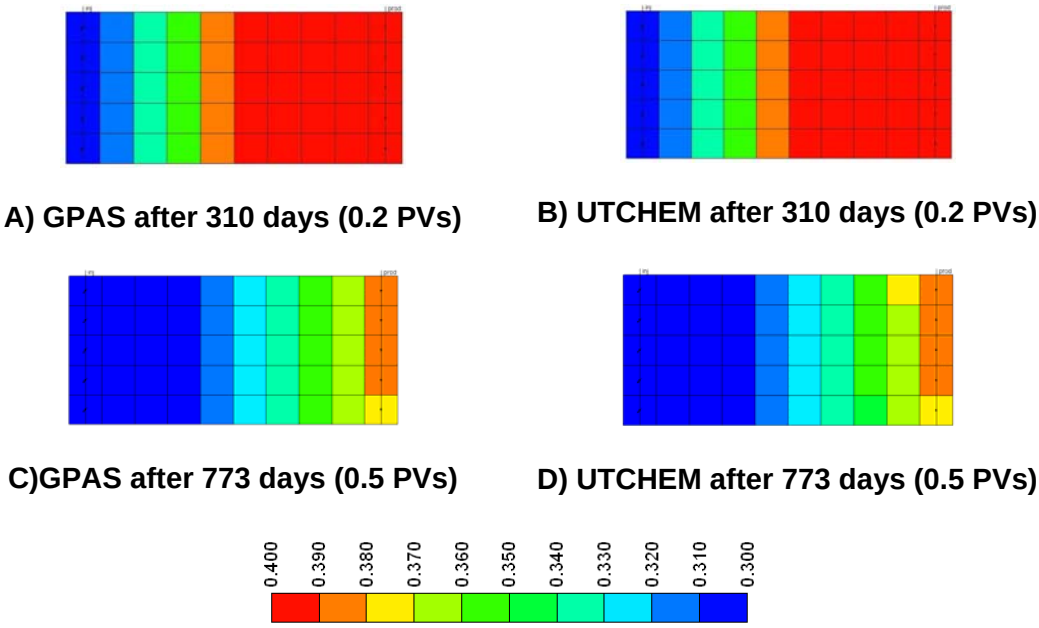

Figure 7.66: Comparison of salinity profiles (eq/L) for 2D polymer flood.

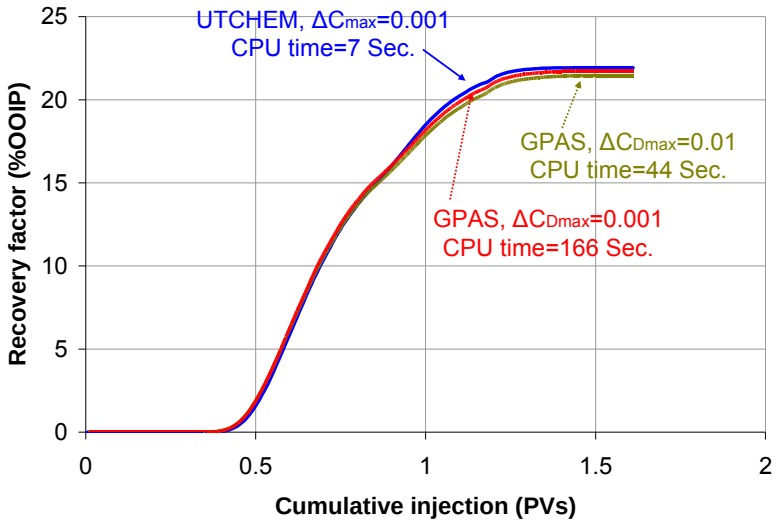

Figure 7.67: Comparison of 2D surfactant/polymer flood recovery factors.

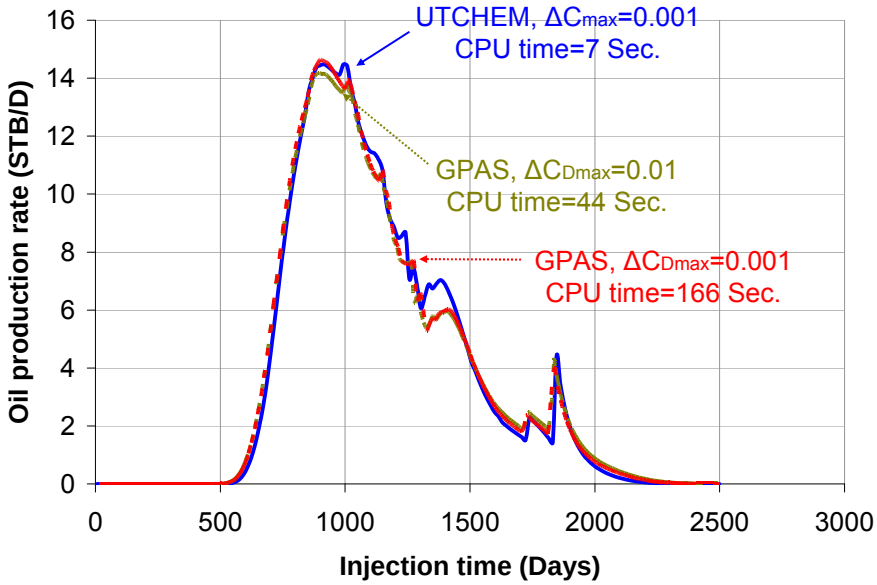

Figure 7.68: Comparison of 2D surfactant/polymer flood oil production rates.

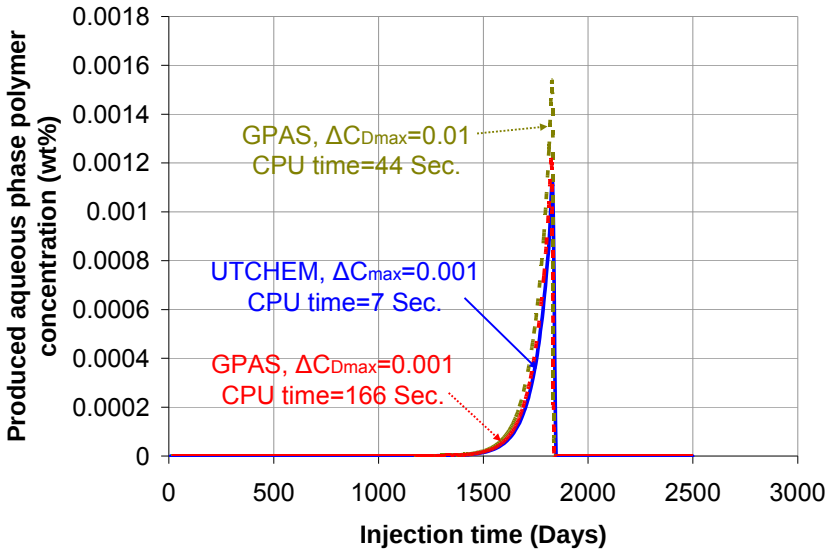

Figure 7.69: Comparison of aqueous phase polymer concentration for 2D surfactant/polymer flood.

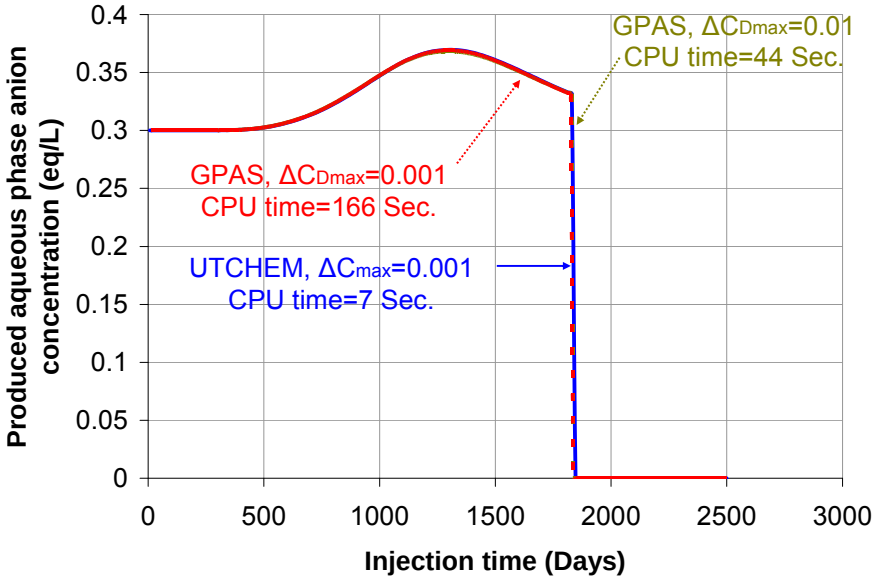

Figure 7.70: Comparison of aqueous phase salinity for 2D surfactant/polymer flood.

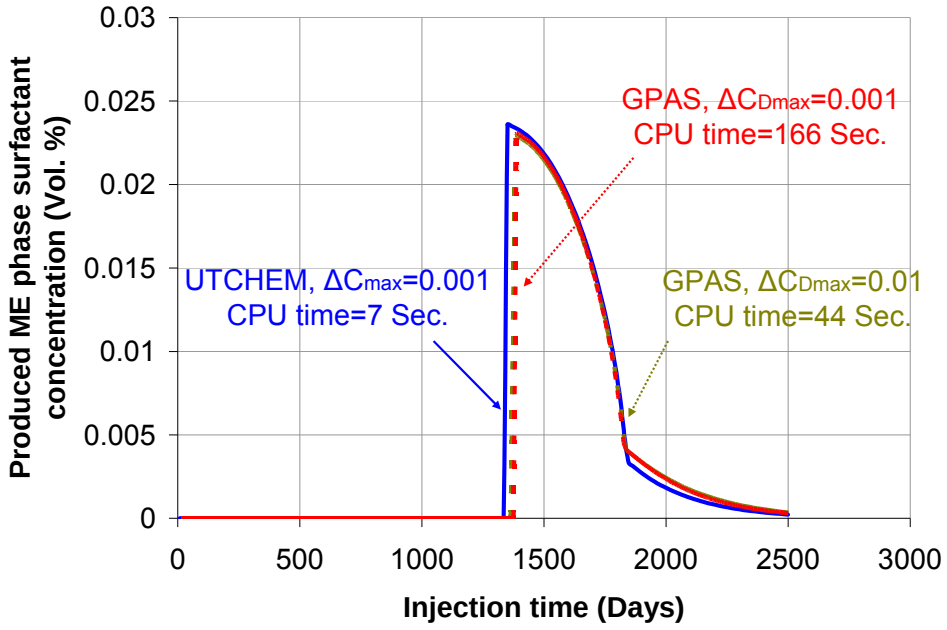

Figure 7.71: Comparison of ME phase surfactant effluent for 2D surfactant/polymer flood.

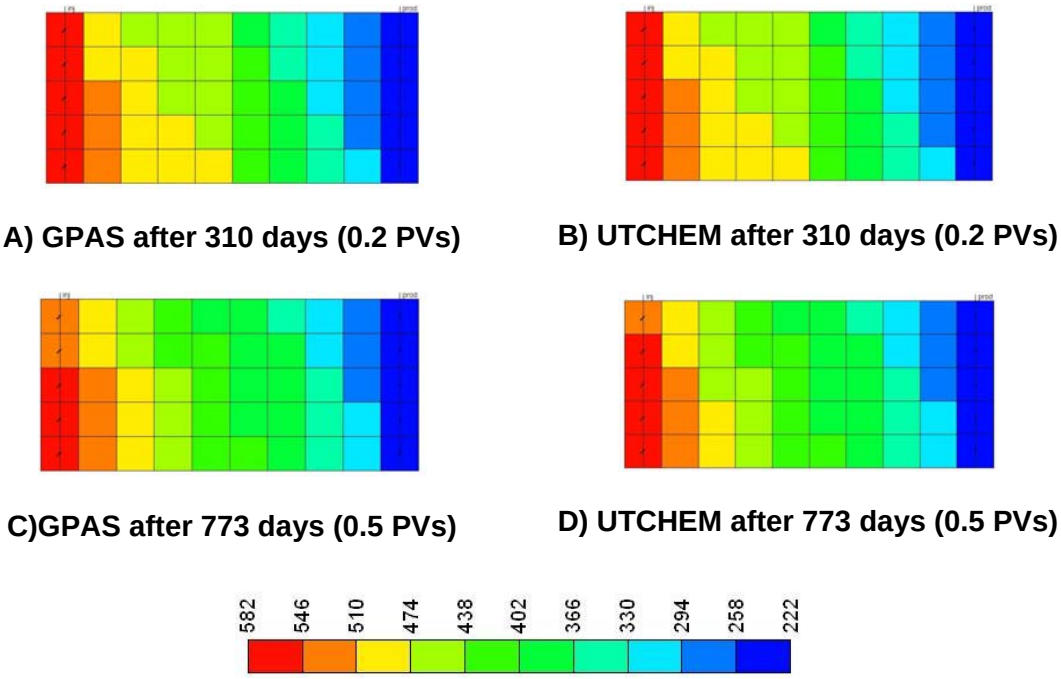

Figure 7.72: Comparison of pressure profiles (psia) for 2D surfactant/polymer flood.

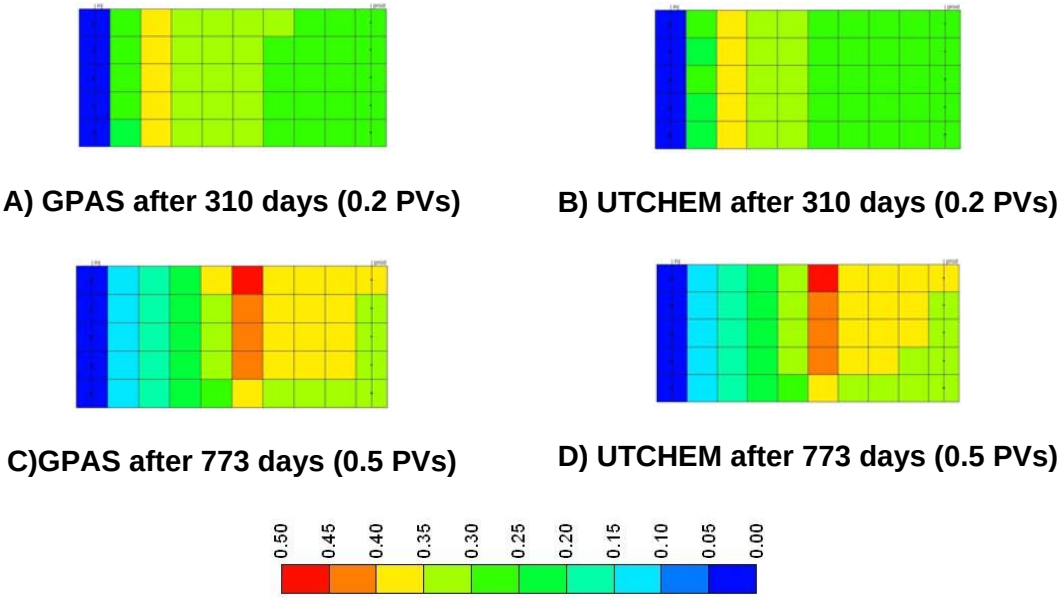

Figure 7.73: Comparison of oil saturation profiles for 2D surfactant/polymer flood.

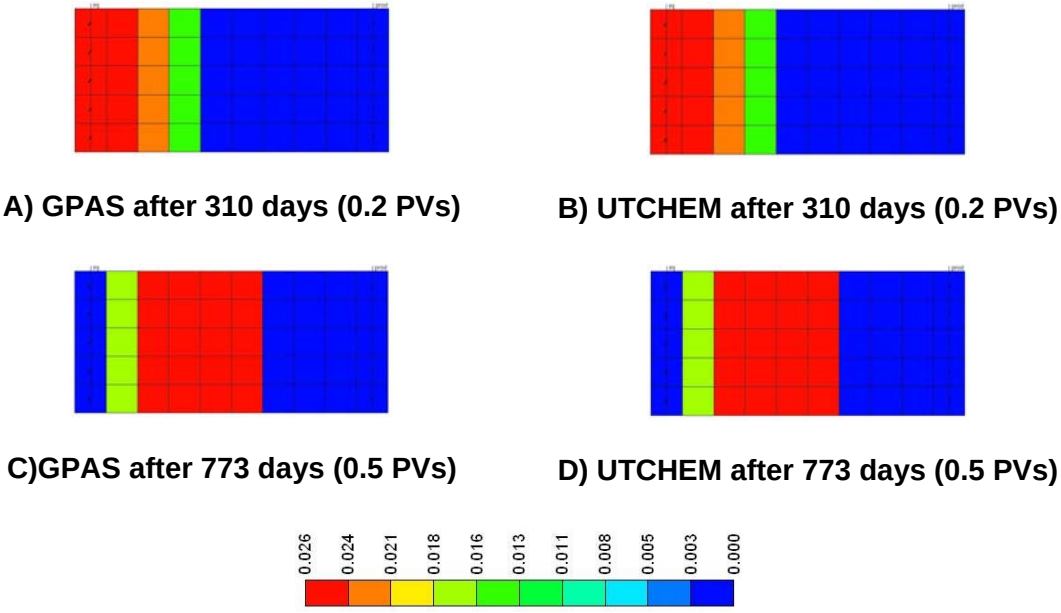

Figure 7.74: Comparison of surfactant concentration (Vol.%) profiles in ME phase for 2D surfactant/polymer flood.

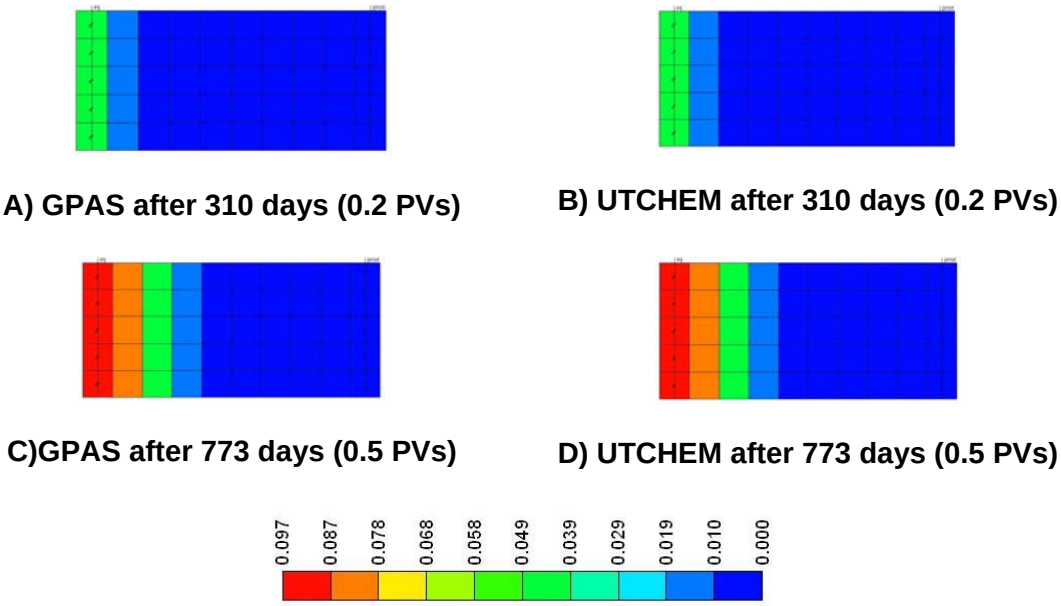

Figure7.75: Comparison of polymer concentration (wt. %) profiles in ME phase for 2D surfactant/polymer flood.

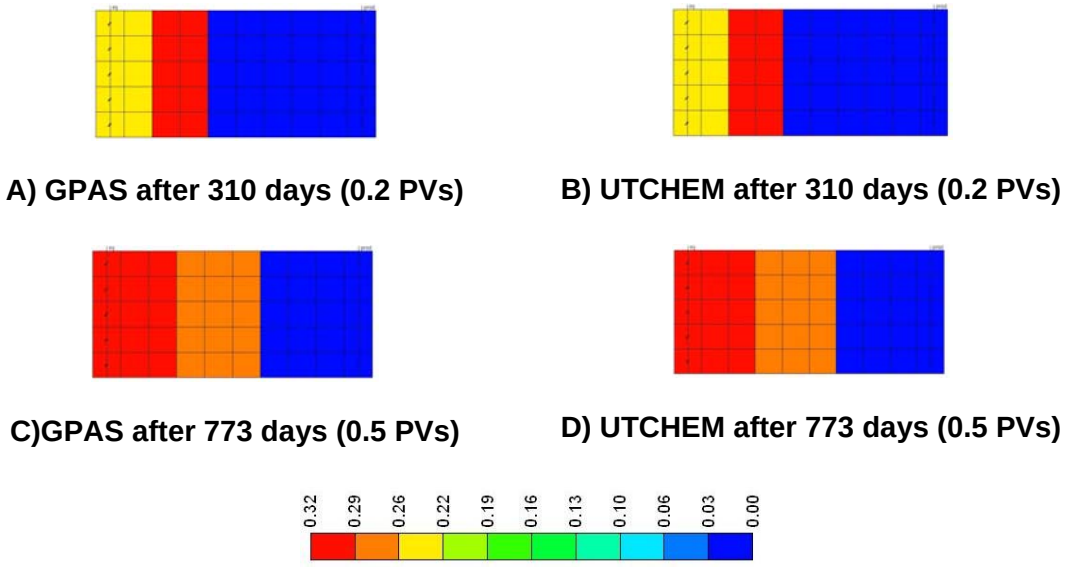

Figure7.76: Comparison of anion concentration (eq/L) profiles in ME phase for 2D surfactant/polymer flood.

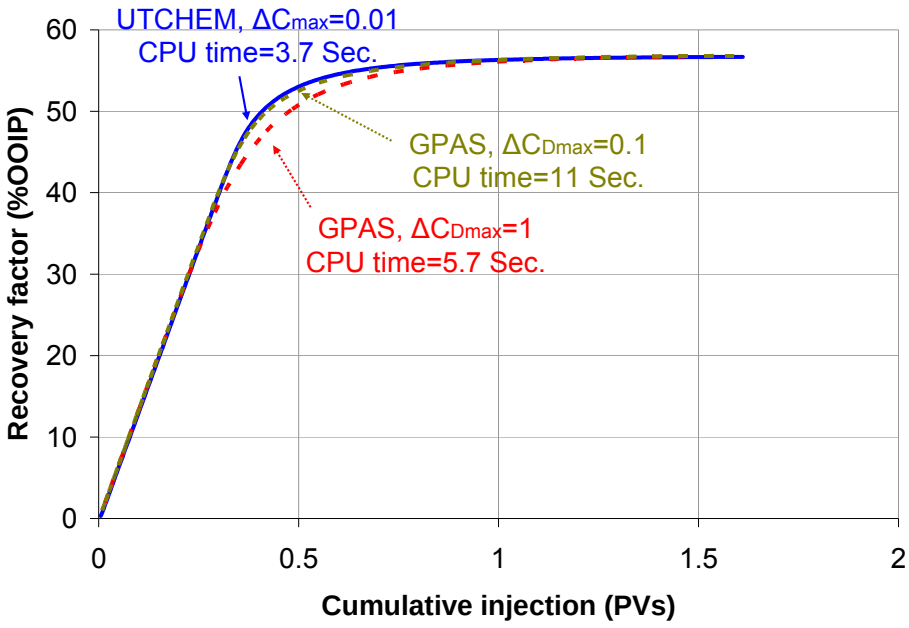

Figure 7.77: Comparison of 3D waterflood recovery factors.

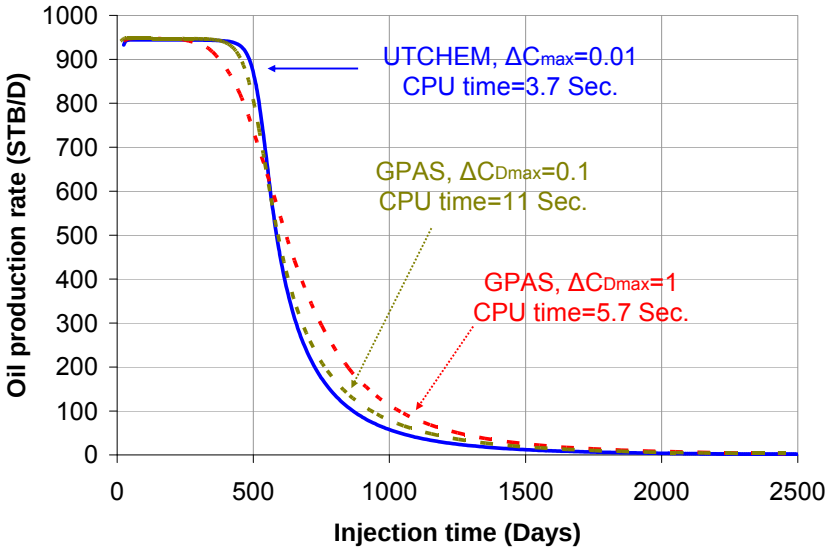

Figure7.78: Comparison of 3D waterflood oil production rates.

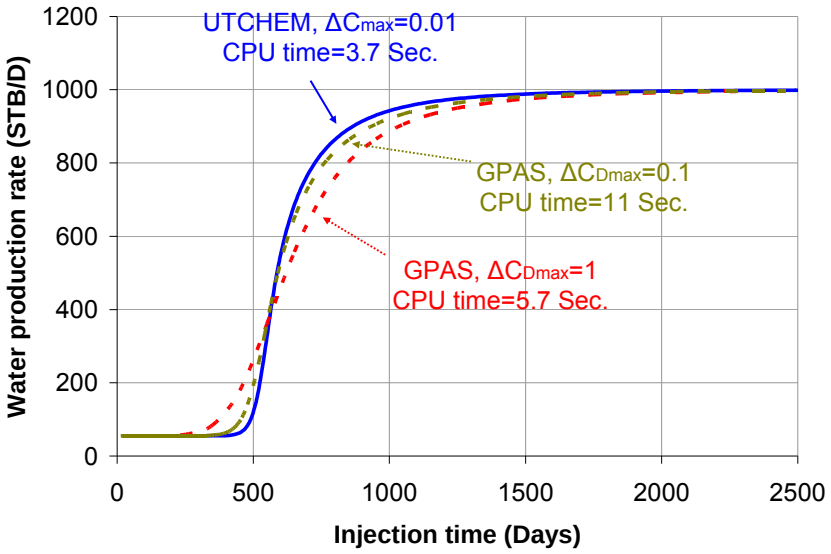

Figure7.79: Comparison of 3D waterflood water production rates.

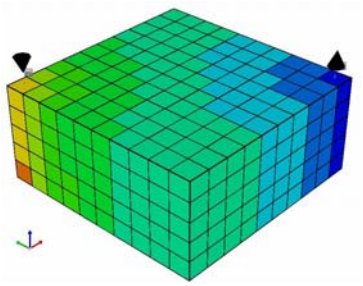

A) GPAS after 358 days (0.226 PVs)

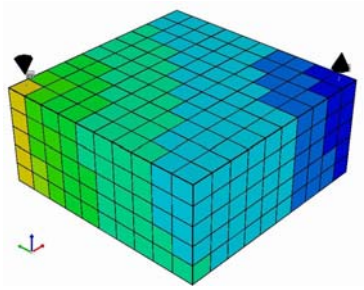

B) UTCHEM after 358 days (0.226 PVs)

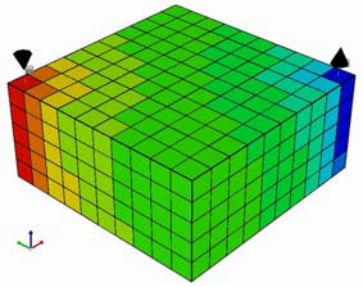

C)GPAS after 854 days (0.55 PVs)

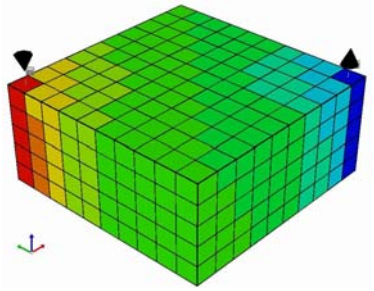

D) UTCHEM after 854 days (0.55 PVs)

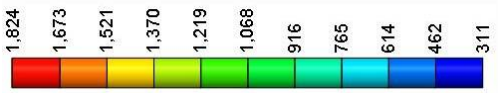

Figure 7.80: Comparison of pressure profiles (psia) for 3D waterflood. GPAS with $\Delta C_{Dmax}= 1$

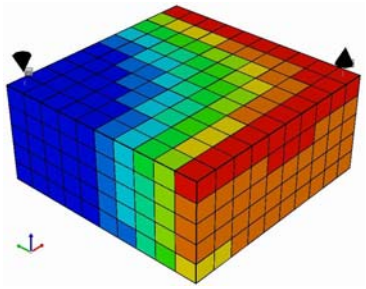

A) GPAS after 358 days (0.226 PVs)

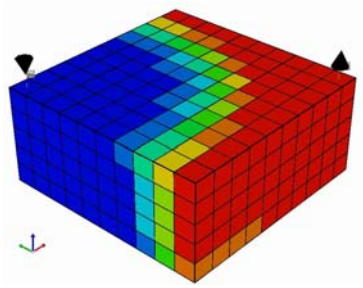

B) UTCHEM after 358 days (0.226 PVs)

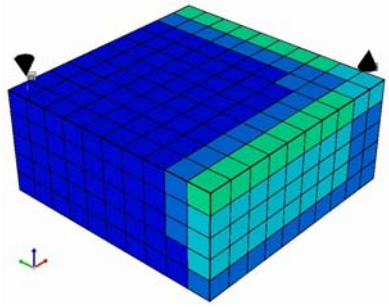

C)GPAS after 854 days (0.55 PVs)

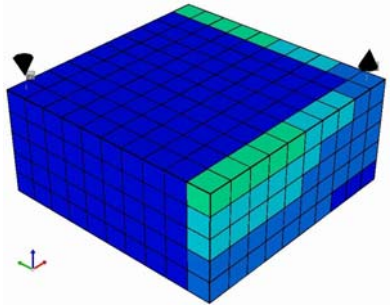

D) UTCHEM after 854 days (0.55 PVs)

Figure 7.81: Comparison of oil saturation profiles for 3D waterflood. GPAS with $\Delta C_{Dmax} = 1$.

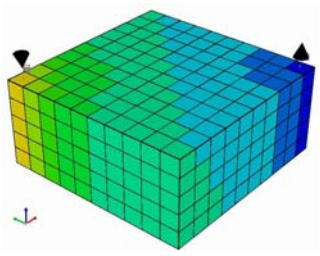

A) GPAS after 318 days (0.2 PVs)

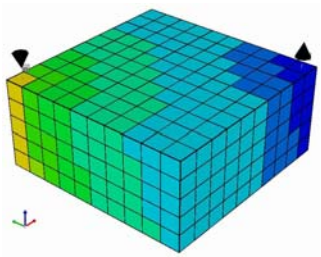

B) UTCHEM after 318 days (0.2 PVs)

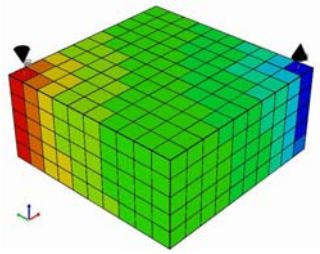

C)GPAS after 854 days (0.55 PVs)

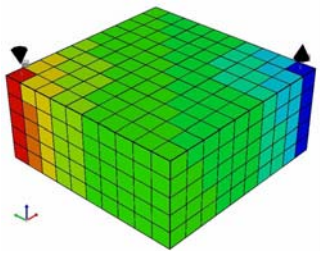

D) UTCHEM after 854 days (0.55 PVs)

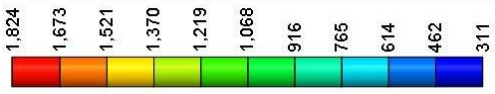

Figure7.82: Comparison of pressure profiles (psia) for 3D waterflood. GPAS with ΔC_{Dmax}= 0.1

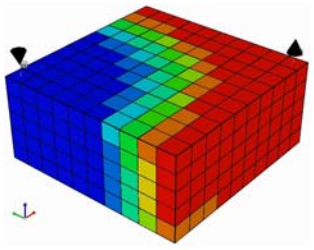

A) GPAS after 318 days (0.2 PVs)

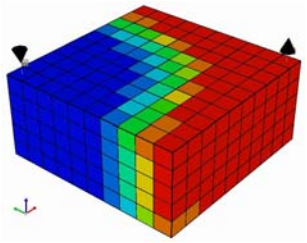

B) UTCHEM after 318 days (0.2 PVs)

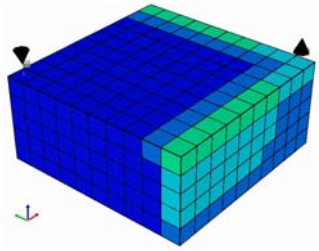

C)GPAS after 854 days (0.55 PVs)

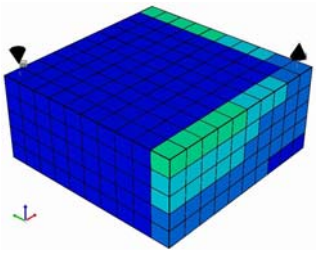

D) UTCHEM after 854 days (0.55 PVs)

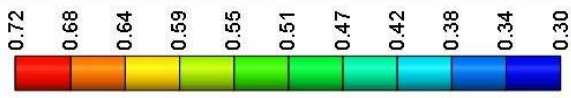

Figure7.83: Comparison of oil saturation profiles for 3D waterflood. GPAS with ΔC_{Dmax}= 0.1.

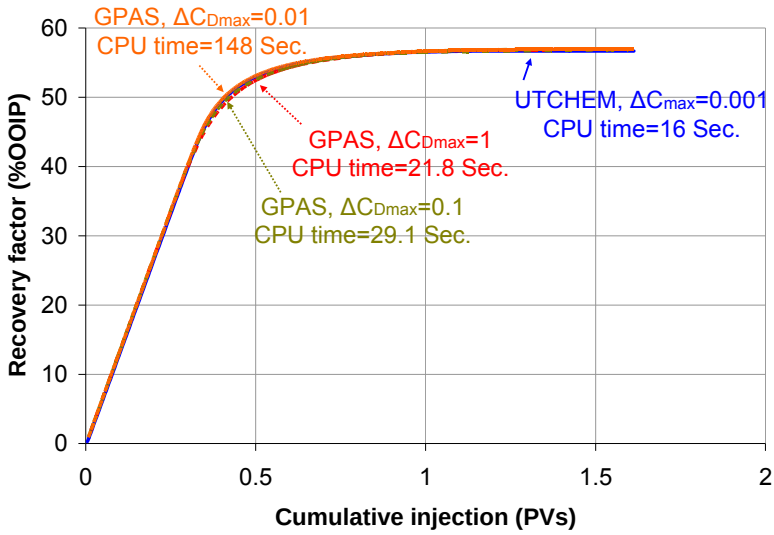

Figure 7.84: Comparison of 3D polymer flood recovery factors.

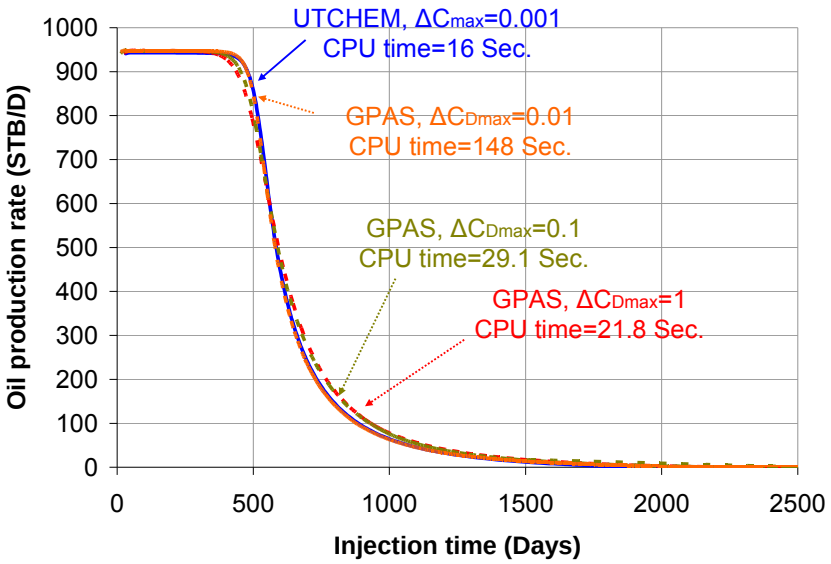

Figure 7.85: Comparison of 3D polymer flood oil production rates.

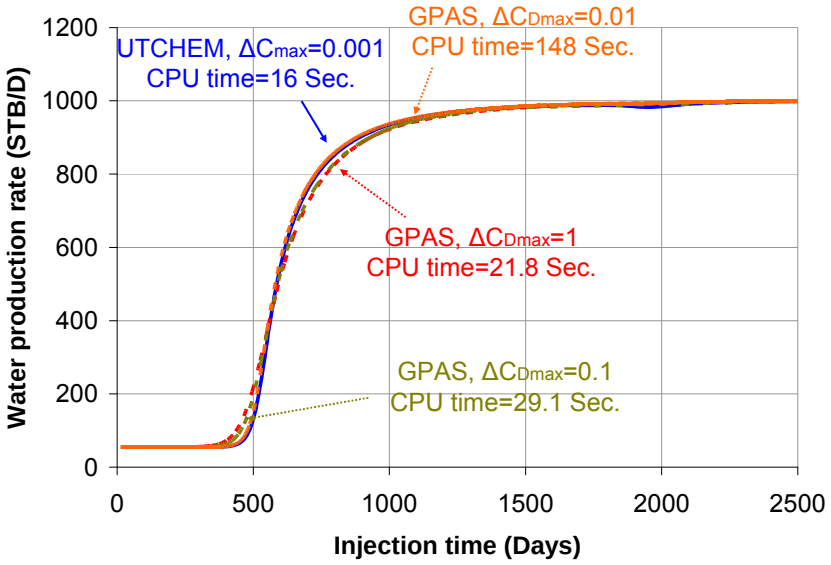

Figure 7.86: Comparison of 3D polymer flood water production rates.

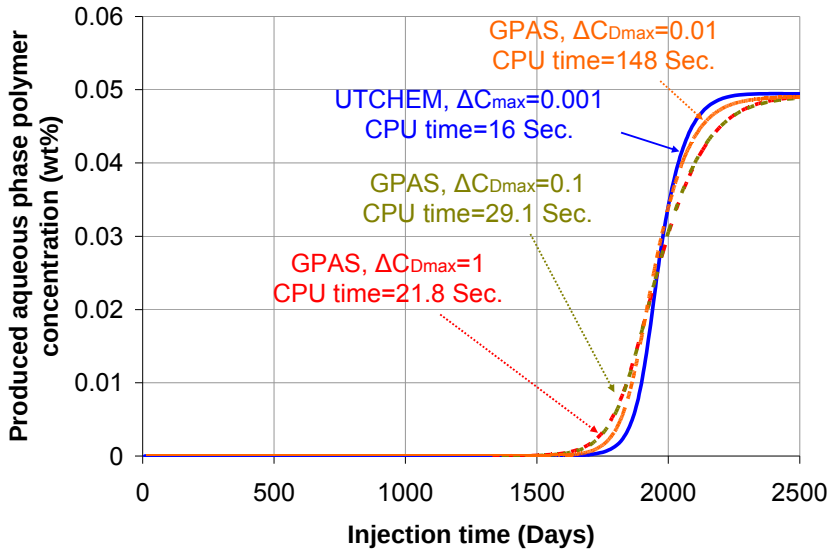

Figure 7.87: Comparison of produced aqueous phase polymer concentration for 3D polymer flood.

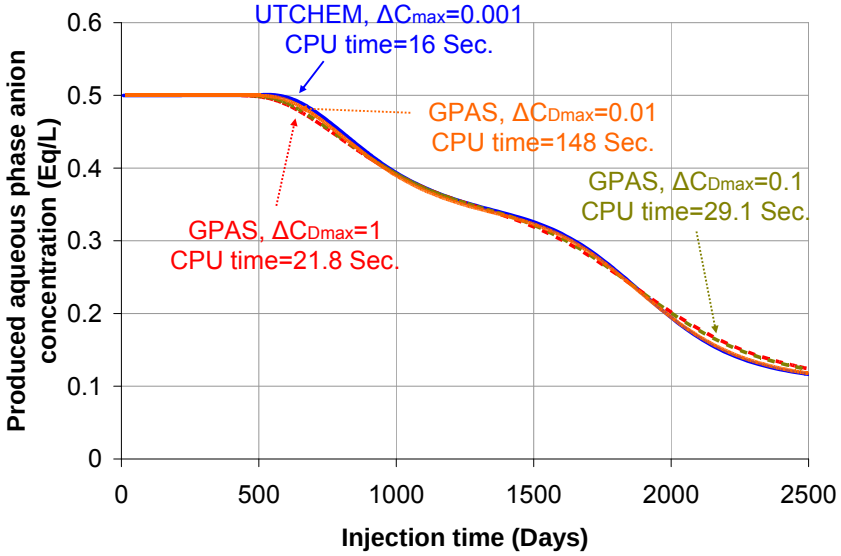

Figure 7.88: Comparison of produced aqueous phase anion concentration for 3D polymer flood.

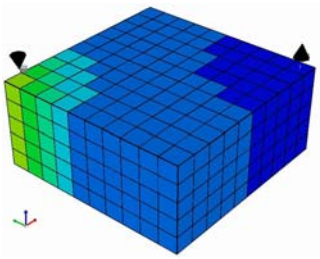

A) GPAS after 310 days (0.2 PVs)

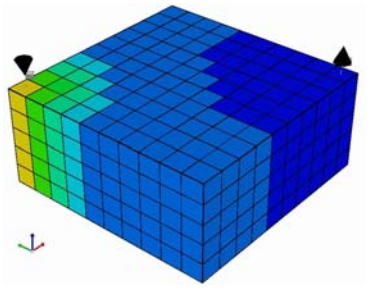

B) UTCHEM after 310 days (0.2 PVs)

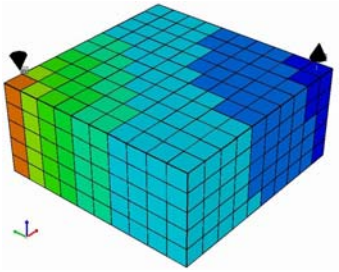

C)GPAS after 930 days (0.6 PVs)

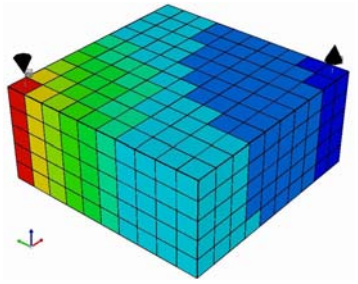

D) UTCHEM after 930 days (0.6 PVs)

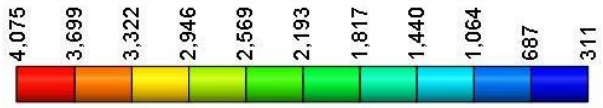

Figure 7.89: Comparison of pressure (psia) profiles predicted for 3D polymer flood. GPAS with ΔC_{Dmax}=1.0.

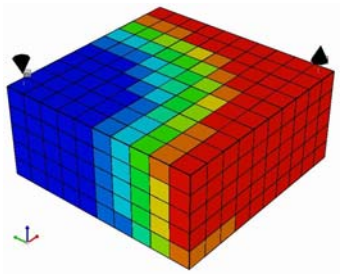

A) GPAS after 310 days (0.2 PVs)

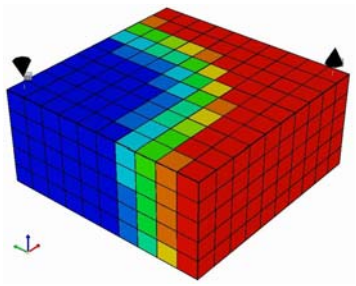

B) UTCHEM after 310 days (0.2 PVs)

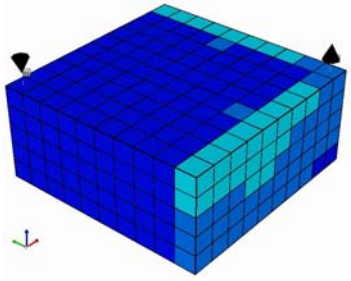

C)GPAS after 930 days (0.6 PVs)

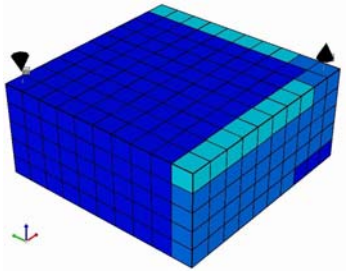

D) UTCHEM after 930 days (0.6 PVs)

Figure 7.90: Comparison of oil saturation profiles for 3D polymer flood. GPAS with ΔC_{Dmax}=1.0.

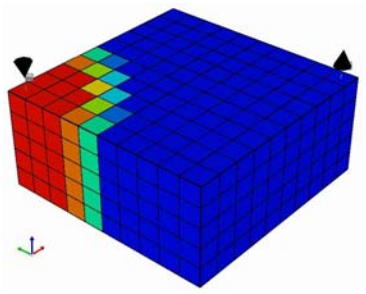

A) GPAS after 310 days (0.2 PVs)

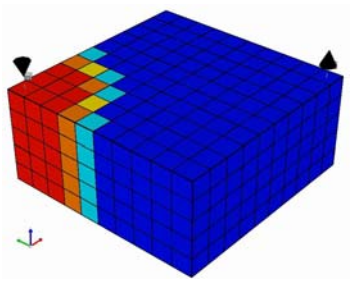

B) UTCHEM after 310 days (0.2 PVs)

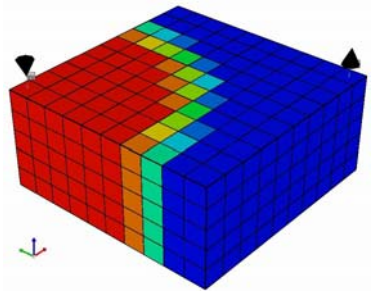

C)GPAS after 930 days (0.6 PVs)

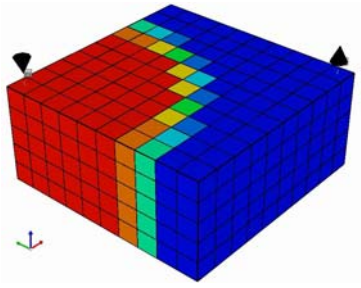

D) UTCHEM after 930 days (0.6 PVs)

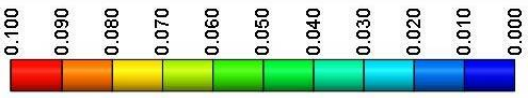

Figure 7.91: Comparison of polymer concentration profiles for 3D polymer flood. GPAS with ΔC_{Dmax}=1.0.

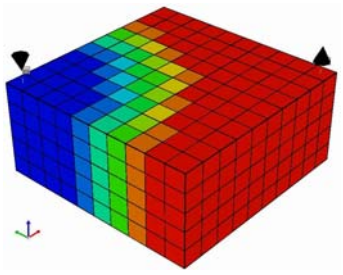

A) GPAS after 310 days (0.2 PVs)

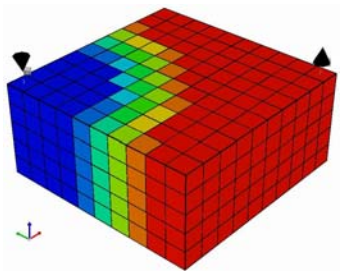

B) UTCHEM after 310 days (0.2 PVs)

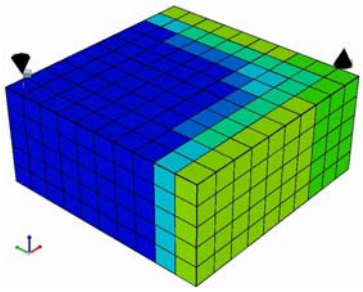

C)GPAS after 930 days (0.6 PVs)

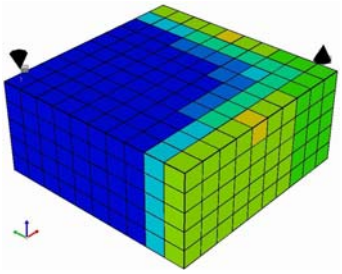

D) UTCHEM after 930 days (0.6 PVs)

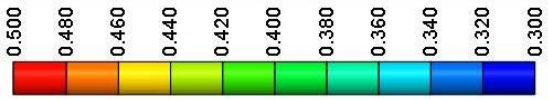

Figure 7.92: Comparison of anion concentration profiles for 3D polymer flood. GPAS with ΔC_{Dmax}=1.0.

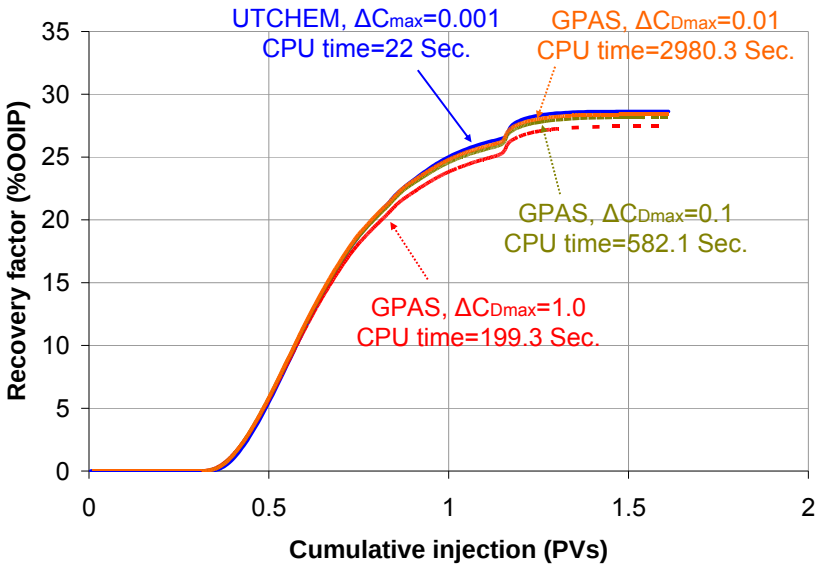

Figure 7.93: Comparison of recovery factors for 3D surfactant/polymer flood

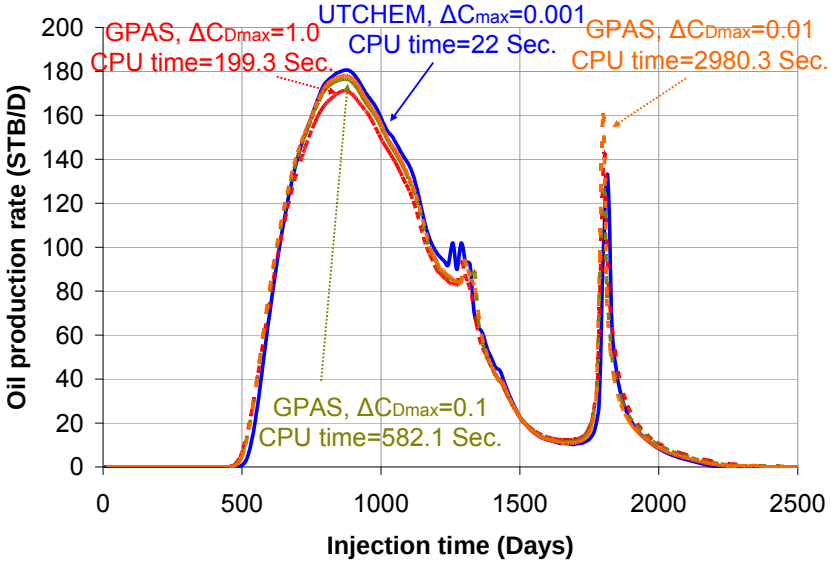

Figure 7.94: Comparison of oil production rates for 3D surfactant/polymer flood.

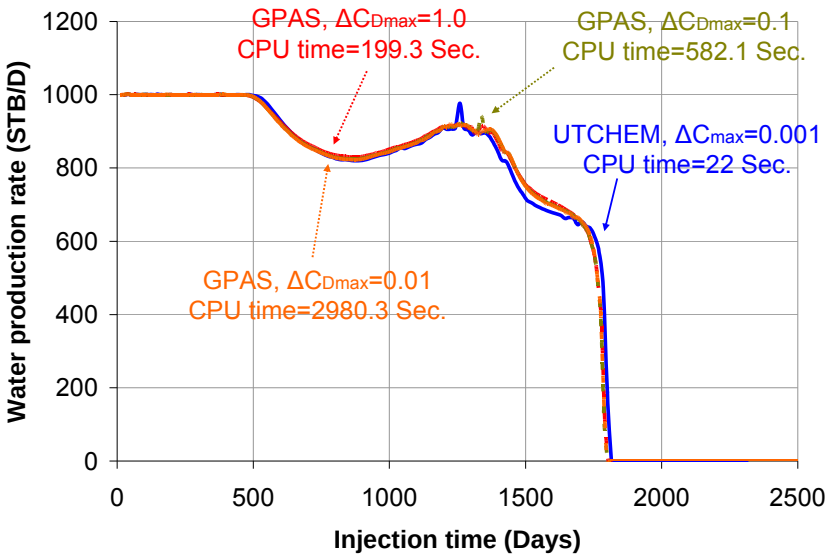

Figure 7.95: Comparison of water production rates for 3D surfactant/polymer flood.

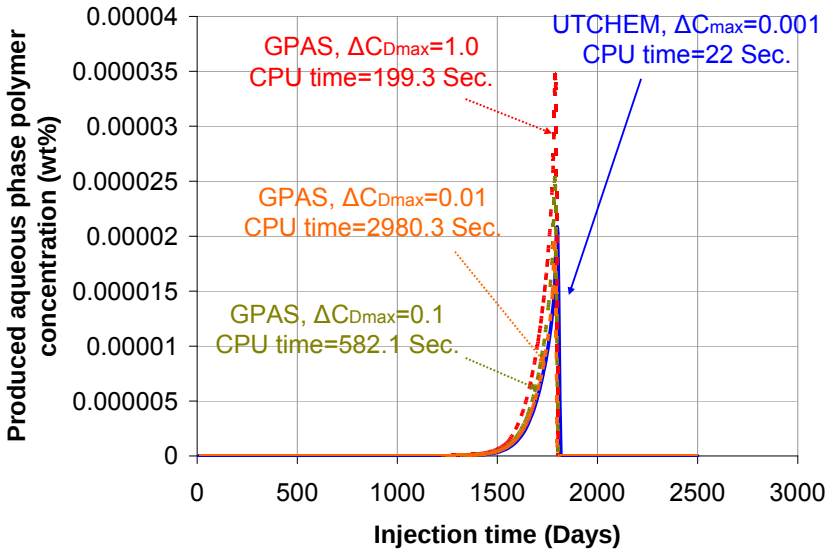

Figure 7.96: Comparison of produced aqueous phase polymer concentration for 3D surfactant/polymer flood.

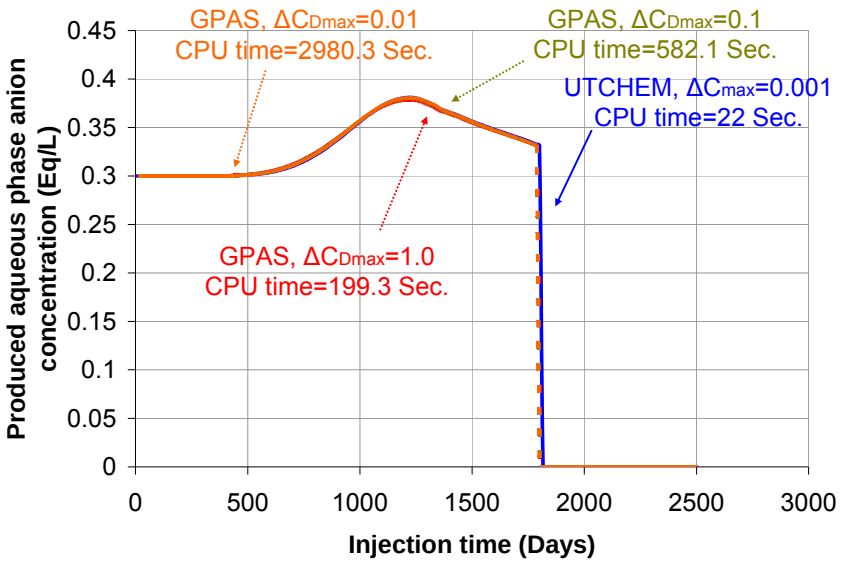

Figure 7.97: Comparison of produced aqueous phase anion concentration for 3D surfactant/polymer flood.

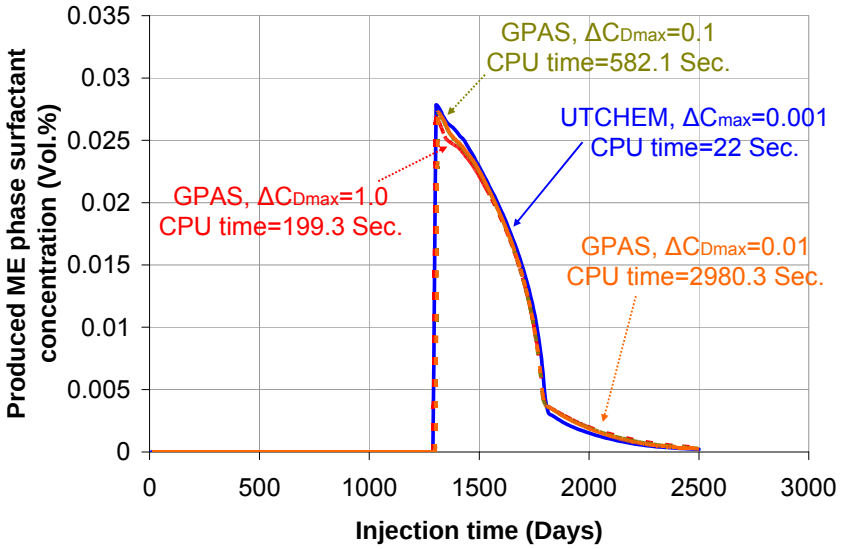

Figure 7.98: Comparison of produced ME phase surfactant concentration for 3D surfactant/polymer flood.

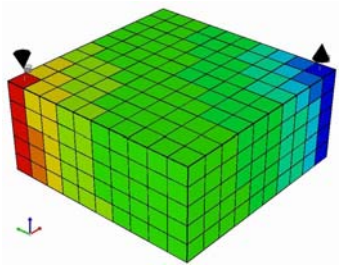

A) GPAS after 310 days (0.2 PVs)

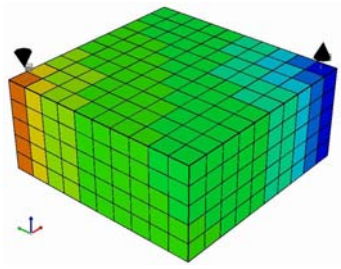

B) UTCHEM after 310 days (0.2 PVs)

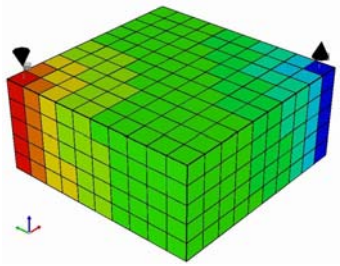

C)GPAS after 773 days (0.5 PVs)

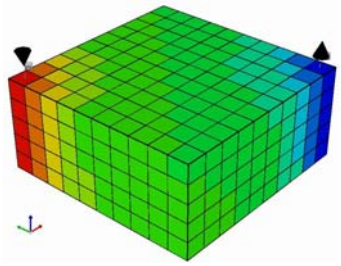

D) UTCHEM after 773 days (0.5 PVs)

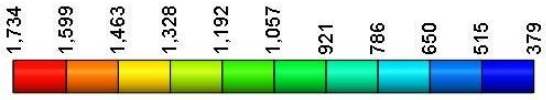

Figure 7.99: Comparison of pressure profiles for 3D surfactant/polymer flood.

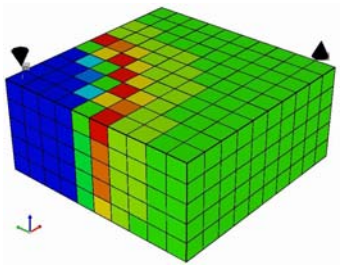

A) GPAS after 310 days (0.2 PVs)

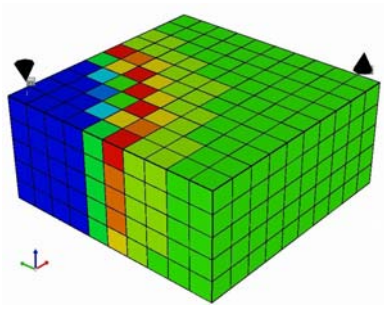

B) UTCHEM after 310 days (0.2 PVs)

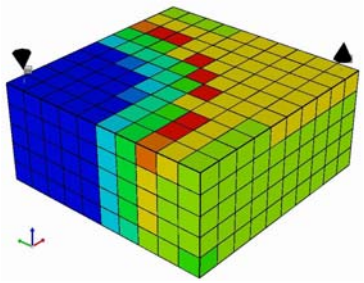

C)GPAS after 773 days (0.5 PVs)

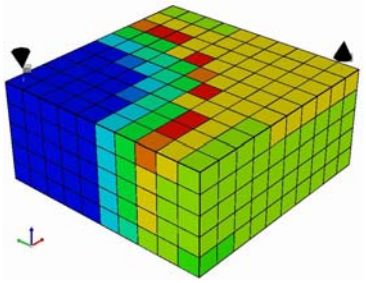

D) UTCHEM after 773 days (0.5 PVs)

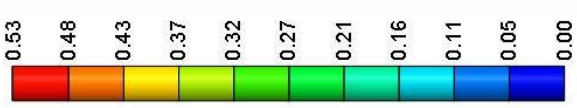

Figure 7.100: Comparison of oil saturation profiles for 3D surfactant/polymer flood

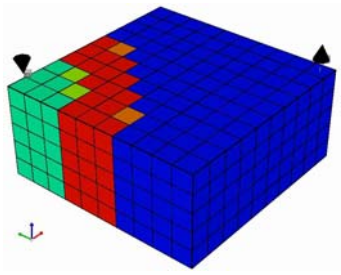

A) GPAS after 310 days (0.2 PVs)

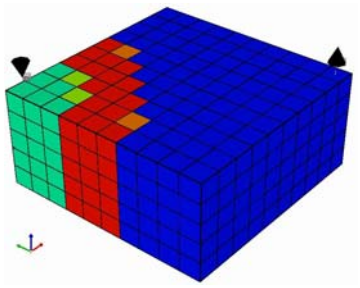

B) UTCHEM after 310 days (0.2 PVs)

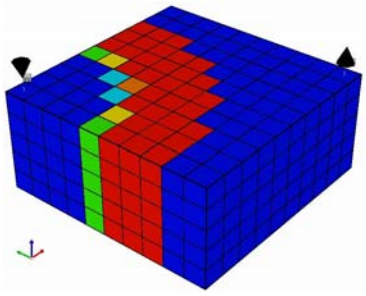

C)GPAS after 773 days (0.5 PVs)

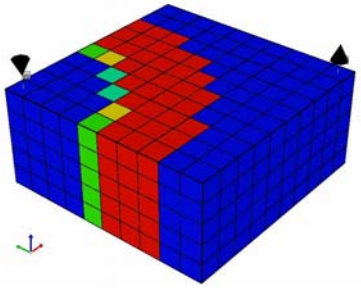

D) UTCHEM after 773 days (0.5 PVs)

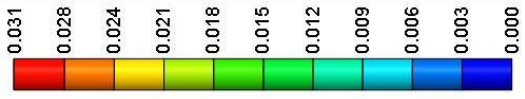

Figure 7.101: Comparison of ME phase surfactant concentration profiles (Vol.%) for 3D surfactant/polymer flood.

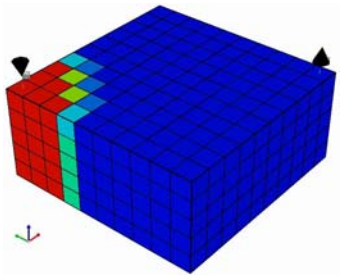

A) GPAS after 310 days (0.2 PVs)

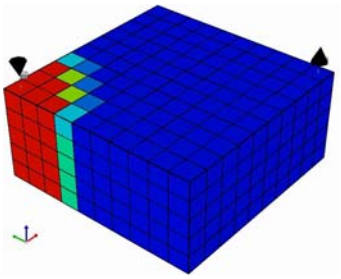

B) UTCHEM after 310 days (0.2 PVs)

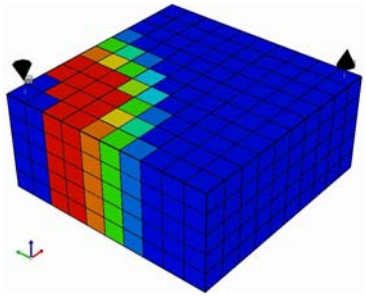

C)GPAS after 773 days (0.5 PVs)

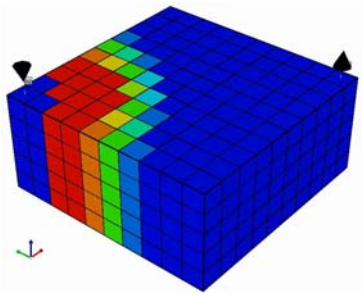

D) UTCHEM after 773 days (0.5 PVs)

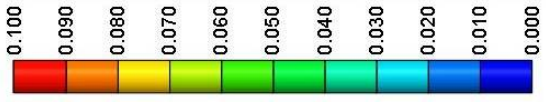

Figure 7.102: Comparison of ME phase polymer concentration profiles (wt. %) for 3D surfactant/polymer flood.

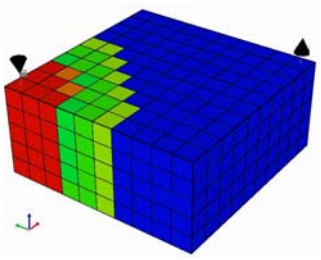

A) GPAS after 310 days (0.2 PVs)

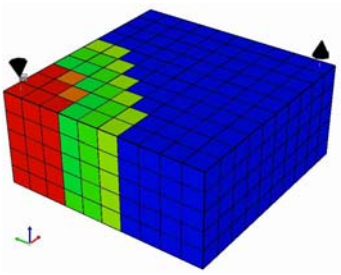

B) UTCHEM after 310 days (0.2 PVs)

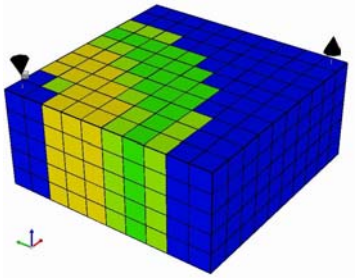

C)GPAS after 773 days (0.5 PVs)

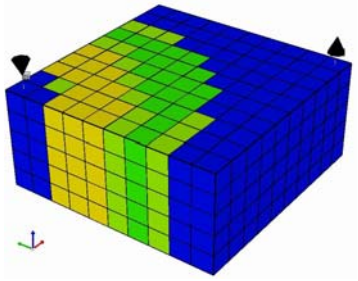

D) UTCHEM after 773 days (0.5 PVs)

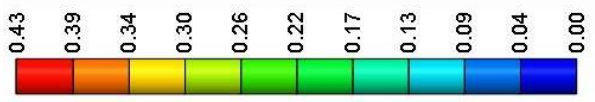

Figure 7.103: Comparison of ME phase anion concentration profiles (eq/L) for 3D surfactant/polymer flood.

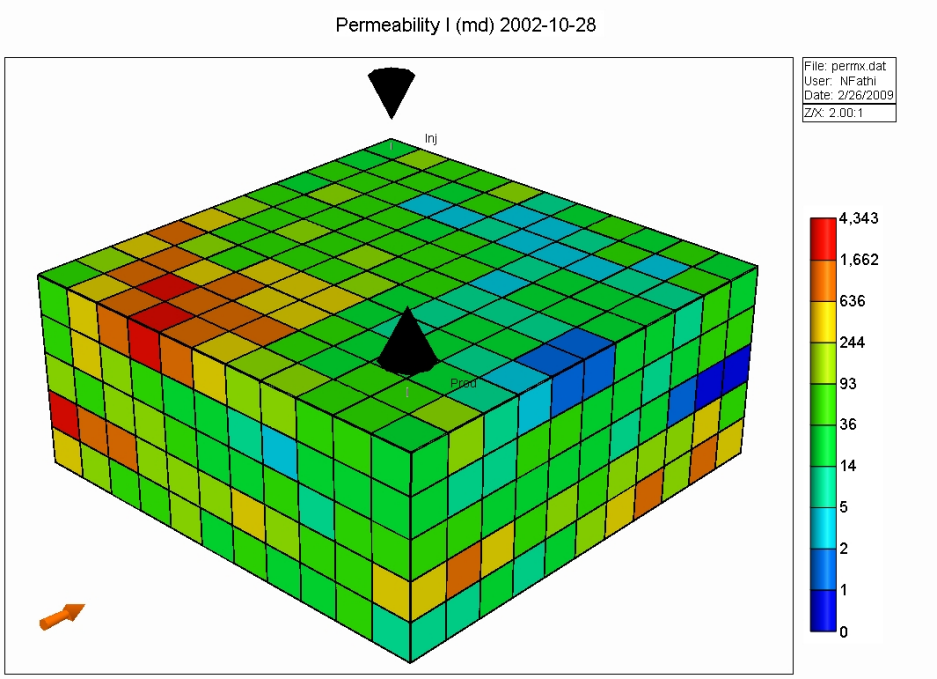

Figure 7.104: Permeability (md) distribution for 3D heterogeneous case

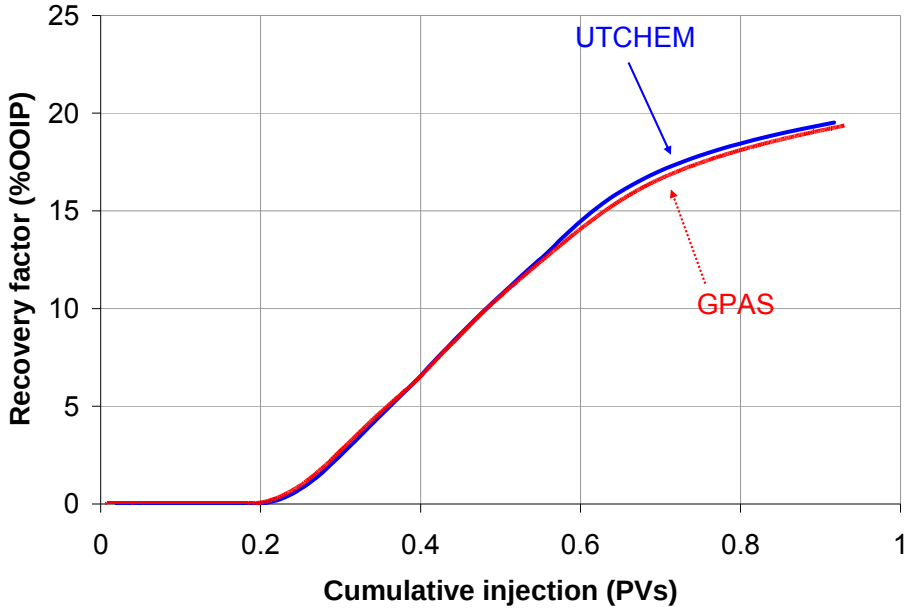

Figure 7.105: Comparison of recovery factors for 3D surfactant/polymer flood in a heterogeneous reservoir.

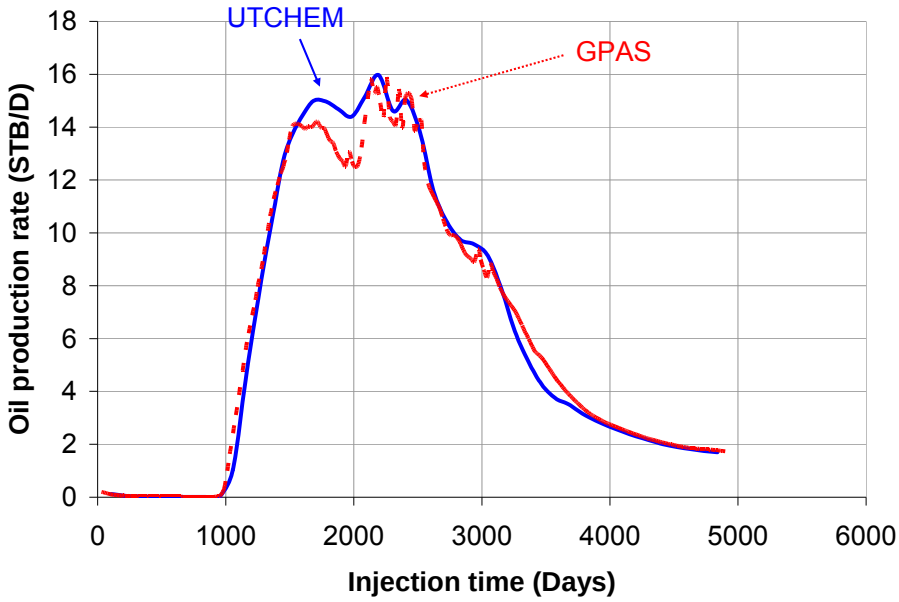

Figure 7.106: Comparison of oil production rate for surfactant/polymer flood in a 3D heterogeneous reservoir.

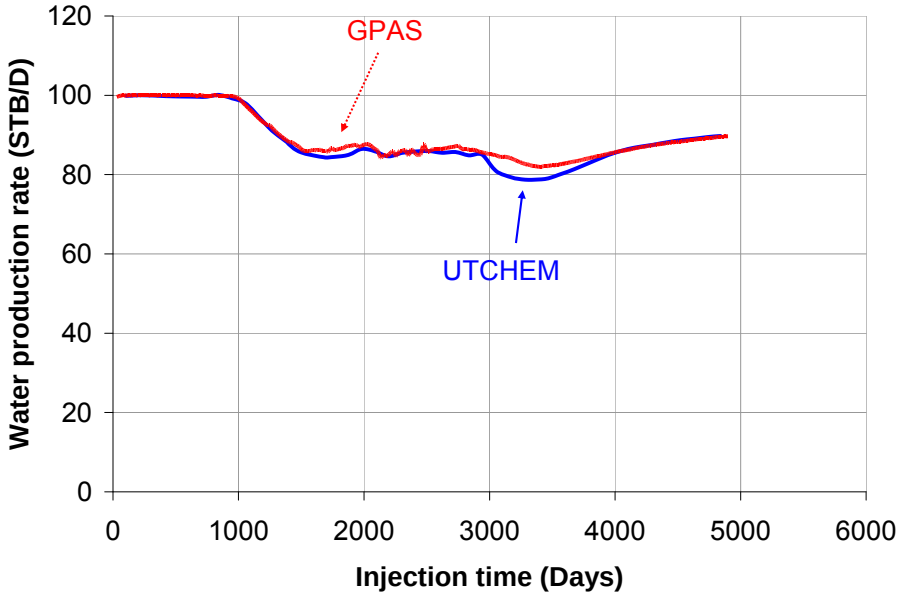

Figure 7.107: Comparison of water production rates for surfactant/polymer flood in a 3D heterogeneous reservoir.

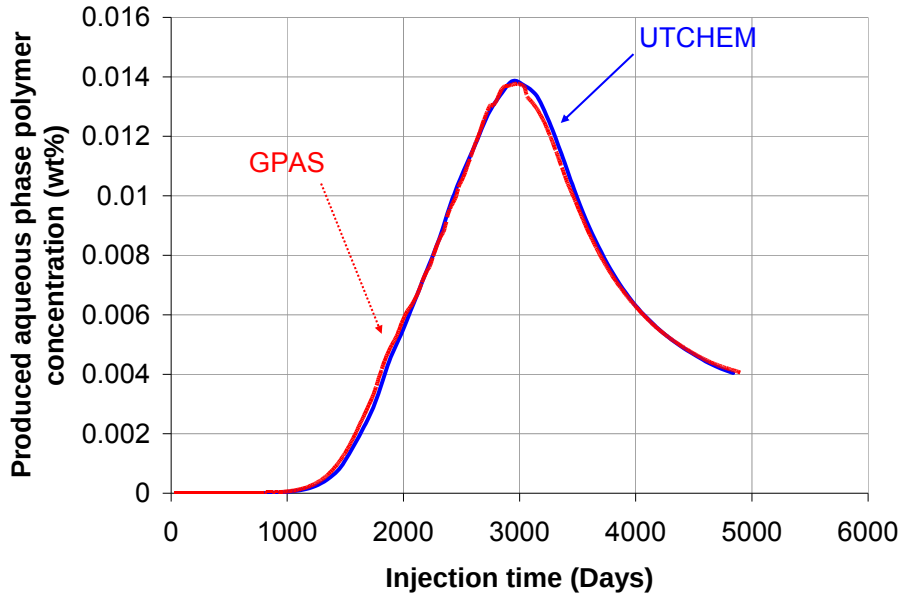

Figure 7.108: Comparison of produced aqueous phase polymer concentration for surfactant/polymer flood in a 3D heterogeneous reservoir

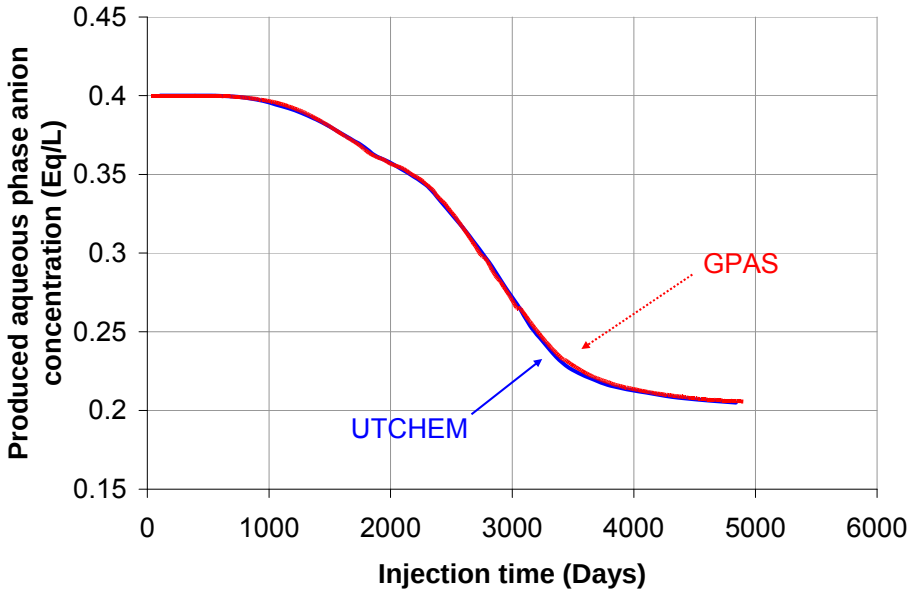

Figure 7.109: Comparison of produced aqueous phase anion concentration for surfactant/polymer flood in a 3D heterogeneous reservoir.

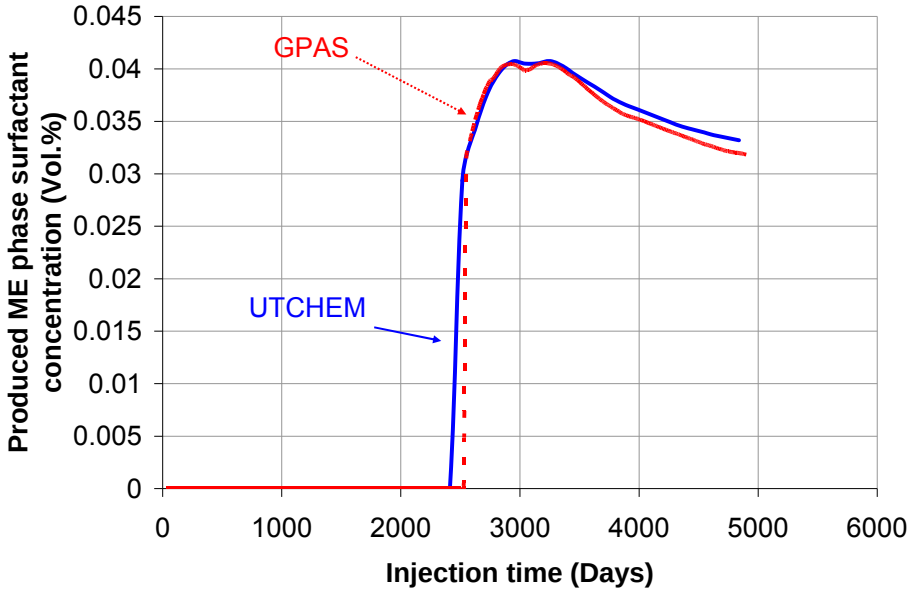

Figure 7.110: Comparison of produced ME phase surfactant concentration (for surfactant/polymer flood in a 3D heterogeneous reservoir.

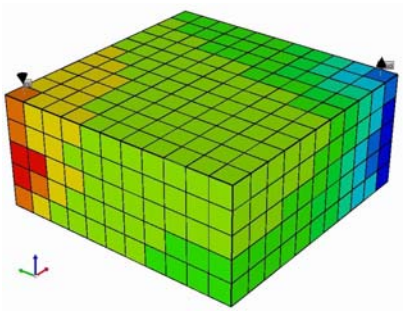

A) GPAS after 1055 days (0.2 PVs)

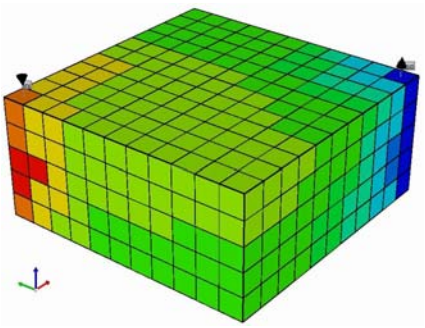

B) UTCHEM after 1055 days (0.2 PVs)

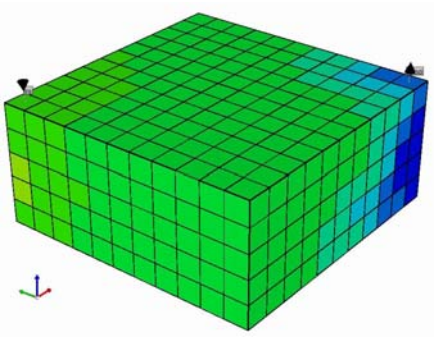

C)GPAS after 2622 days (0.5 PVs)

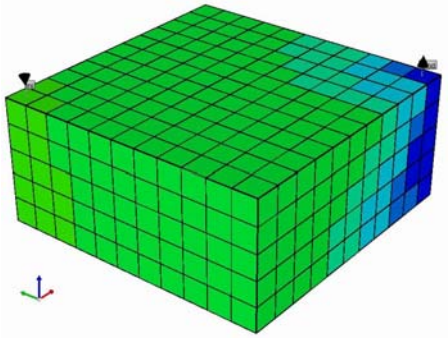

D) UTCHEM after 2622 days (0.5 PVs)

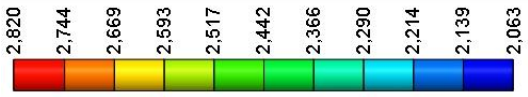

Figure 7.111: Comparison of reservoir pressure (psia) for surfactant/polymer flood of a 3D heterogeneous reservoir.

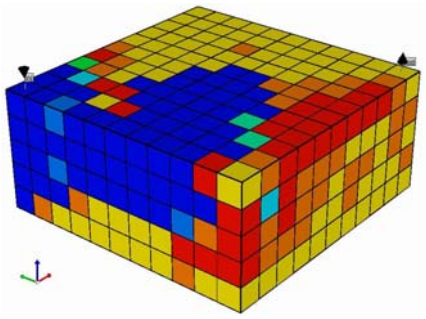

A) GPAS after 1055 days (0.2 PVs)

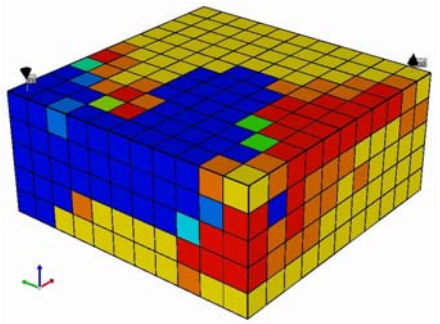

B) UTCHEM after 1055 days (0.2 PVs)

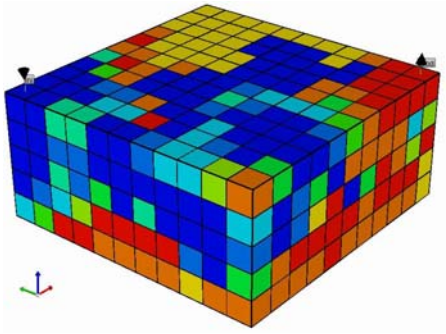

C)GPAS after 2622 days (0.5 PVs)

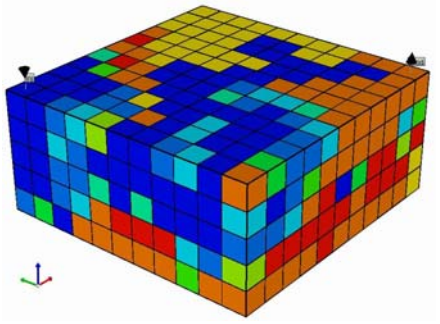

D) UTCHEM after 2622 days (0.5 PVs)

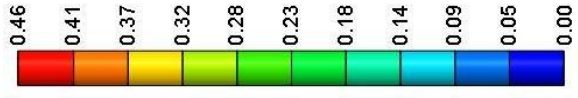

Figure 7.112: Comparison of oil saturation profiles for surfactant/polymer flood of a 3D heterogeneous reservoir.

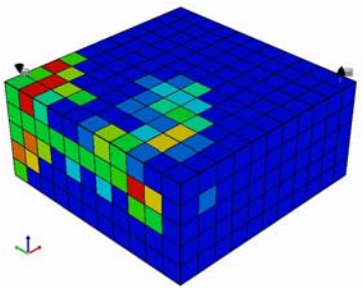

A) GPAS after 1055 days (0.2 PVs)

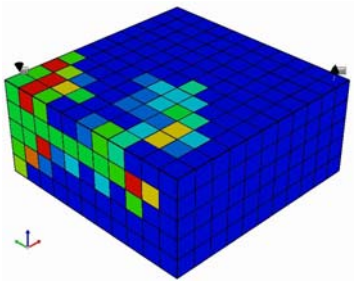

B) UTCHEM after 1055 days (0.2 PVs)

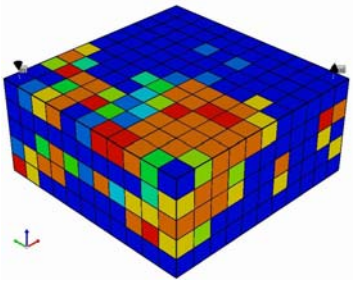

C)GPAS after 2622 days (0.5 PVs)

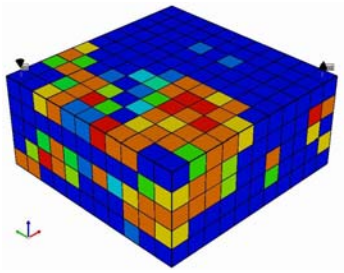

D) UTCHEM after 2622 days (0.5 PVs)

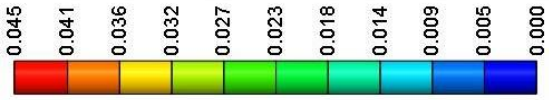

Figure 7.113: Comparison of surfactant concentration profiles in the ME phase (Vol. %) for surfactant/polymer flood of a 3D heterogeneous reservoir.

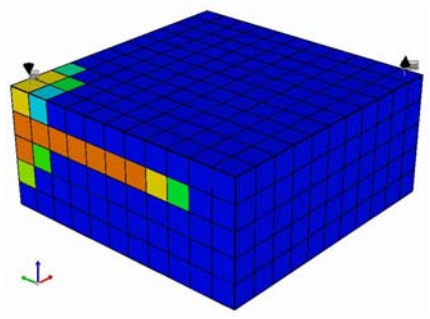

A) GPAS after 1055 days (0.2 PVs)

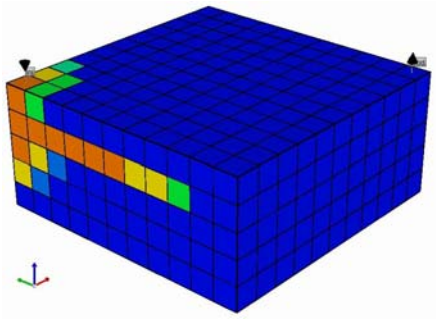

B) UTCHEM after 1055 days (0.2 PVs)

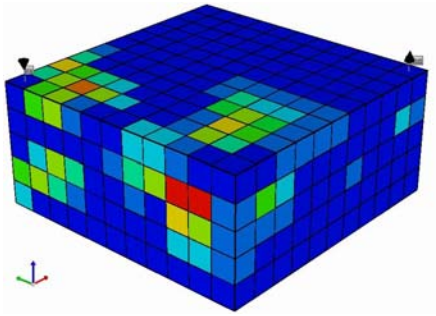

C)GPAS after 2622 days (0.5 PVs)

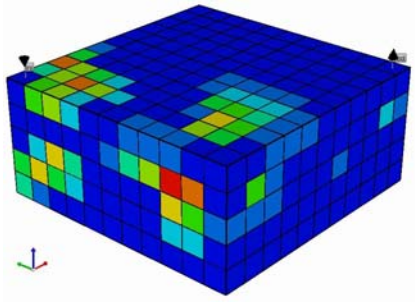

D) UTCHEM after 2622 days (0.5 PVs)

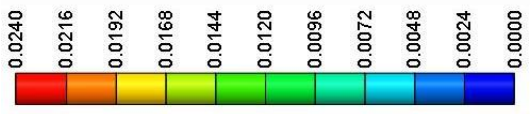

Figure 7.114: Comparison of polymer concentration profiles in the ME phase (wt. %) for surfactant/polymer flood in a 3D heterogeneous reservoir.

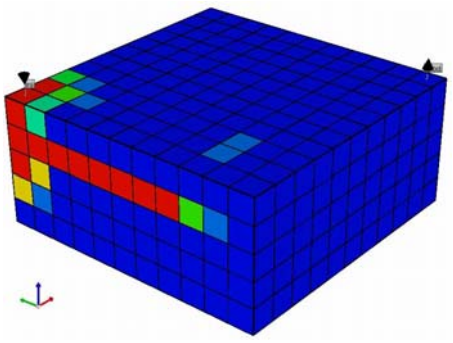

A) GPAS after 1055 days (0.2 PVs)

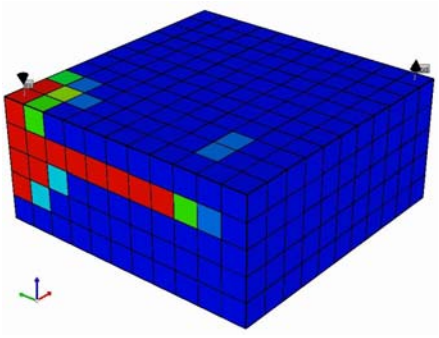

B) UTCHEM after 1055 days (0.2 PVs)

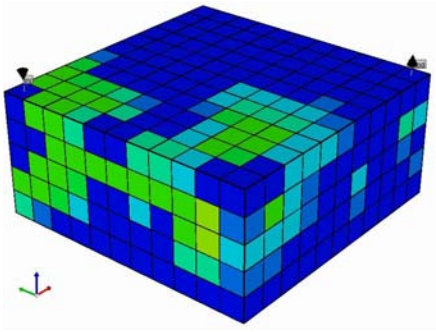

C)GPAS after 2622 days (0.5 PVs)

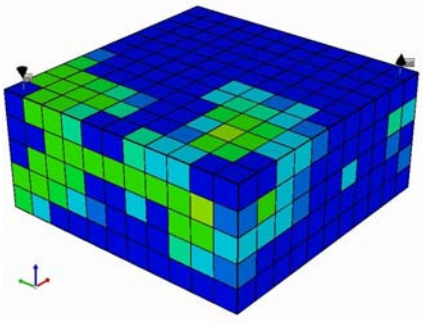

D) UTCHEM after 2622 days (0.5 PVs)

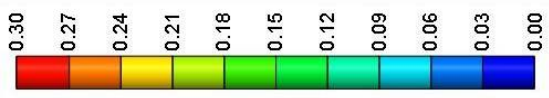

Figure 7.115: Comparison of anion concentration profiles in the ME phase (eq/L) for surfactant/polymer flood in a 3D heterogeneous reservoir.

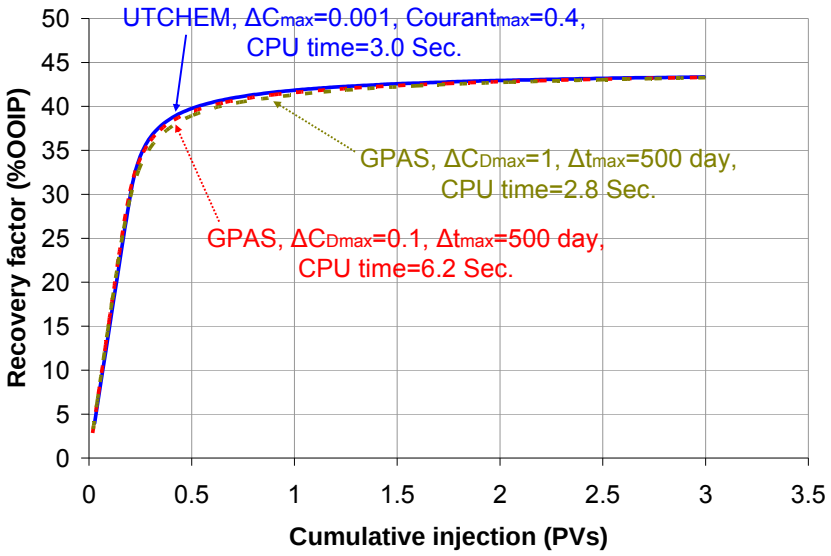

Figure 7.116: Comparison of waterflood recovery factors predicted by UTCHEM and GPAS for the base case benchmark.

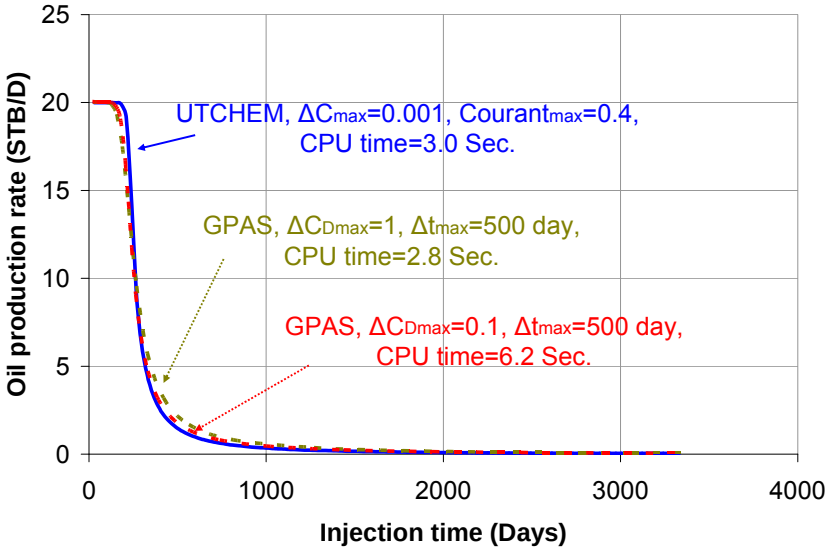

Figure 7.117: Comparison of waterflood oil production rates for the base case benchmark.

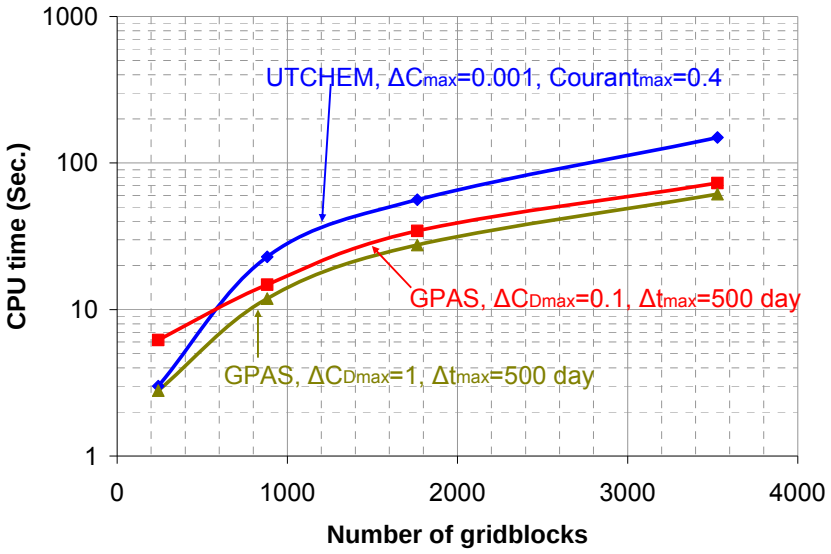

Figure 7.118: Comparison of waterflood CPU times as a function of number of cells.

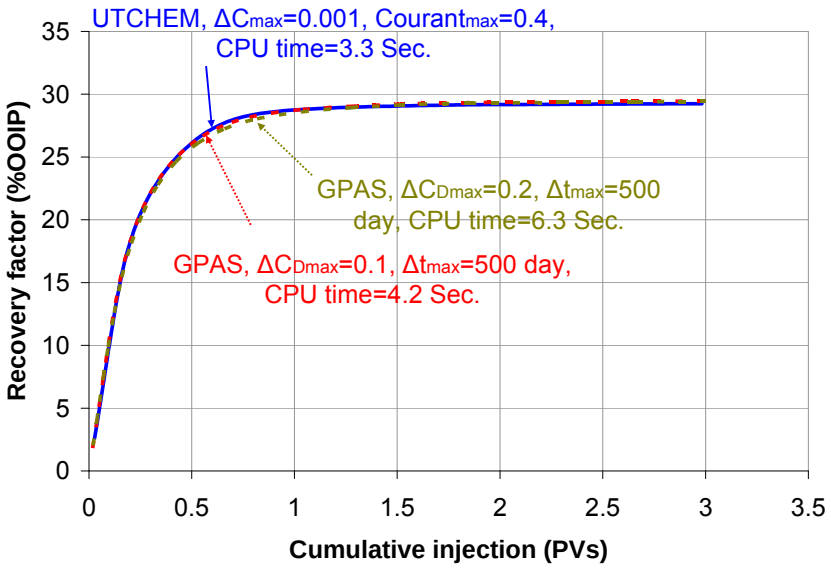

Figure 7.119: Comparison of polymer flood recovery factors for the base case benchmark.

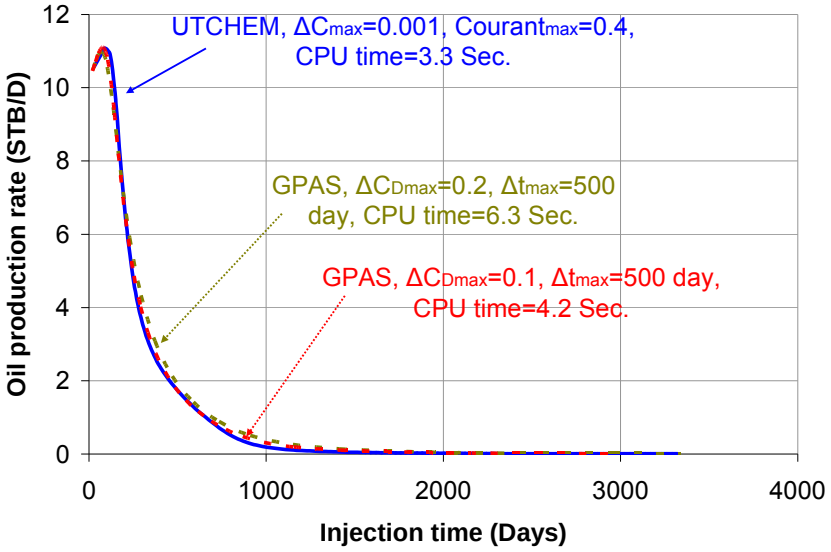

Figure 7.120: Oil production rates for the base case polymer flood benchmark.

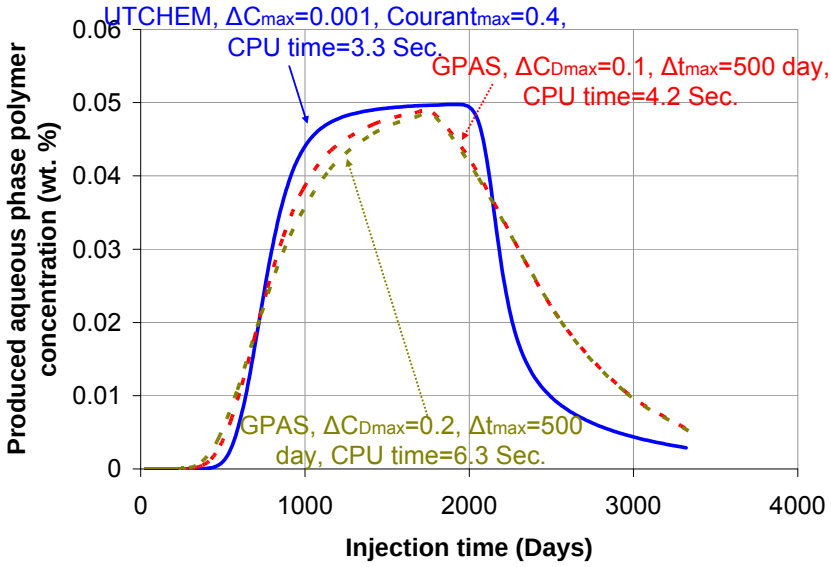

Figure 7.121: Produced aqueous phase polymer concentration for the base case benchmark.

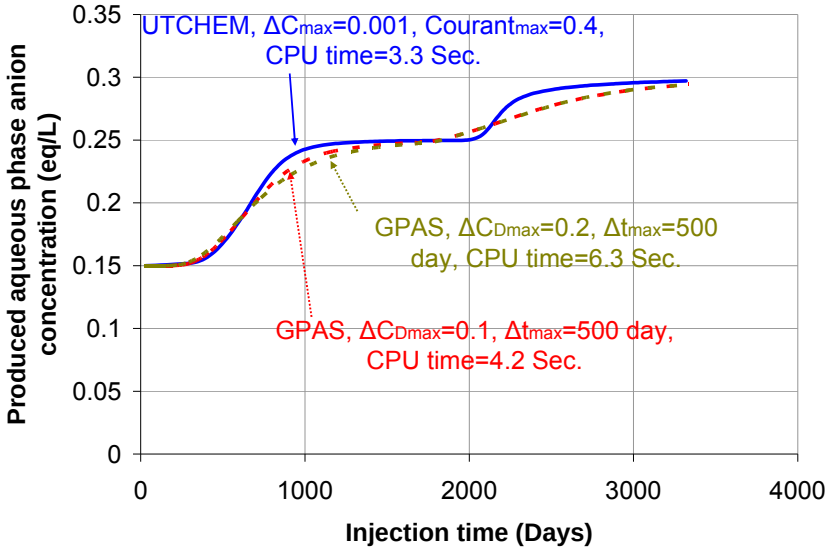

Figure 7.122: Comparison of produced aqueous phase anion concentration for the base case benchmark.

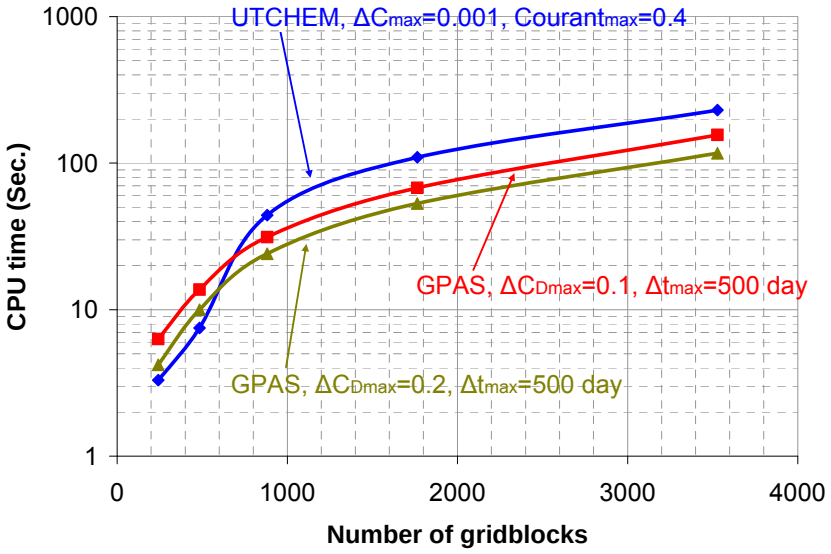

Figure 7.123: Comparison of CPU times for polymer flood in a homogeneous reservoir as a function of number of gridblocks.

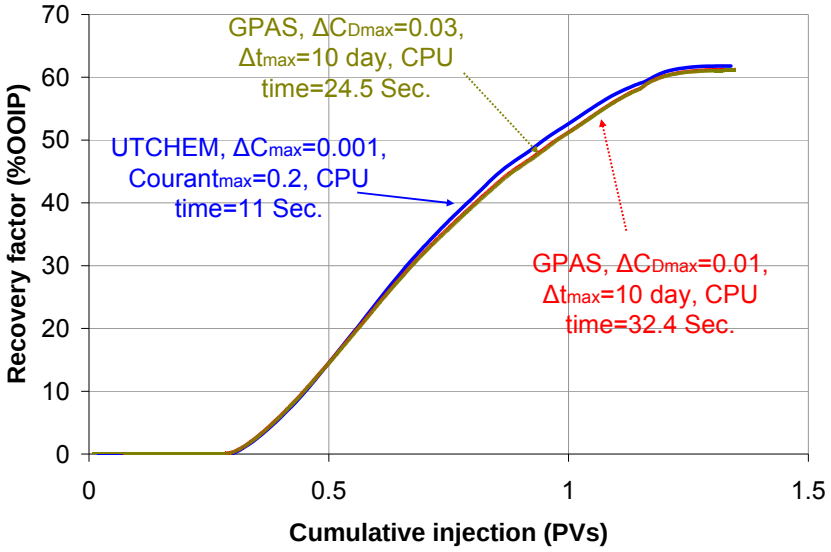

Figure 7.124: Comparison of surfactant/polymer flood recovery factors for the base case benchmark.

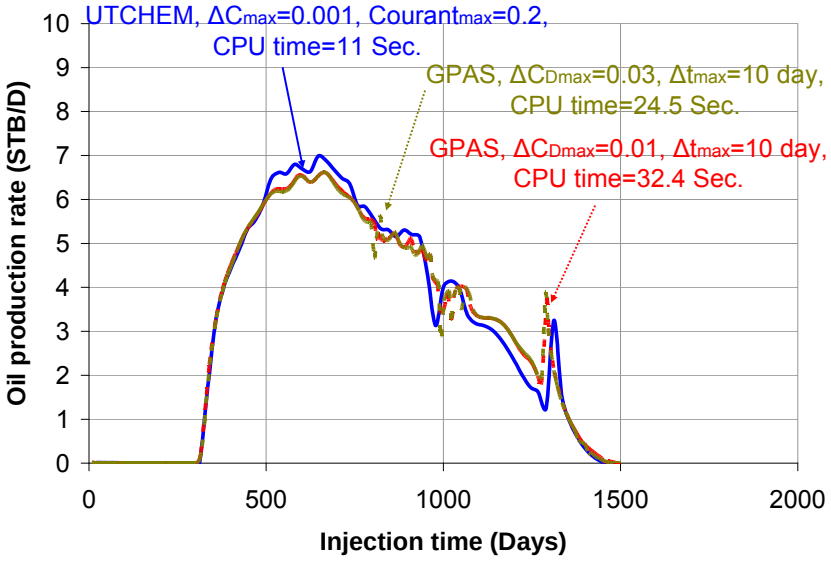

Figure 7.125: Comparison of oil production rates for the base case surfactant/polymer flood benchmark.

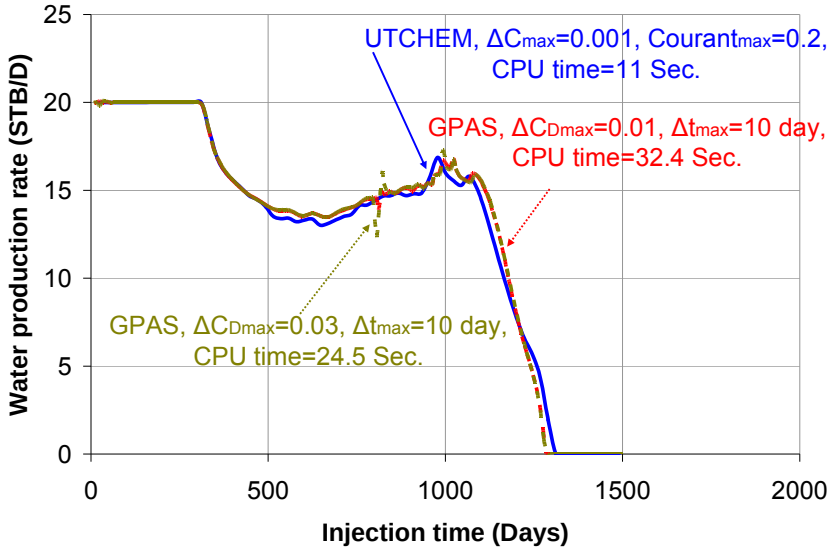

Figure 7.126: Comparison of water production rates for the base case surfactant/polymer flood benchmark.

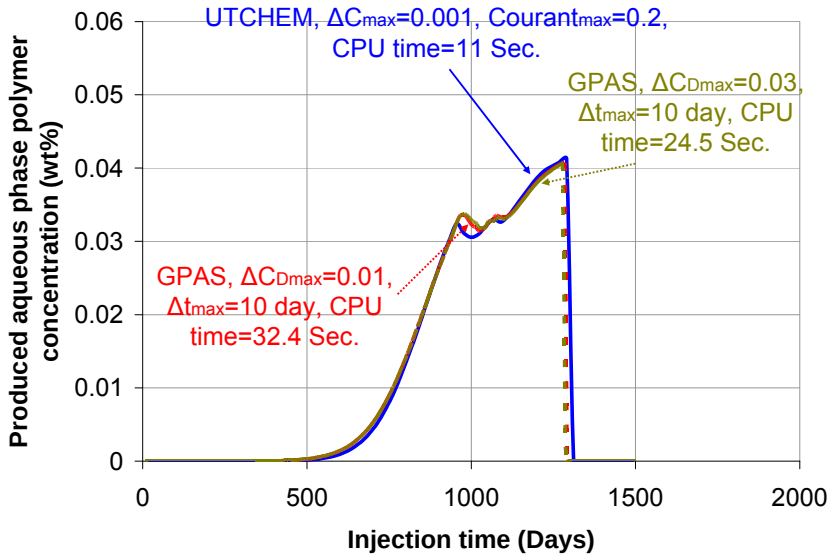

Figure 7.127: Comparison of produced aqueous phase polymer concentration for the base case surfactant/polymer benchmark.

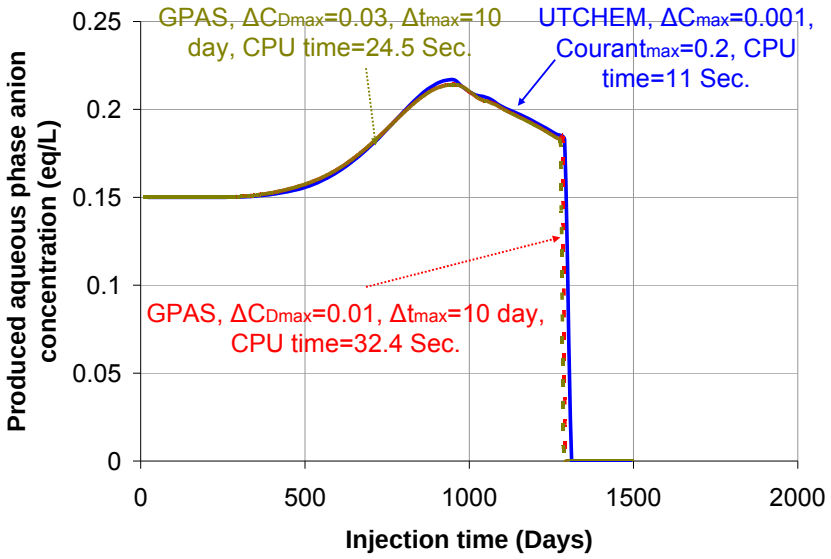

Figure 7.128: Comparison of produced aqueous phase anion concentration for the base case surfactant/polymer benchmark.

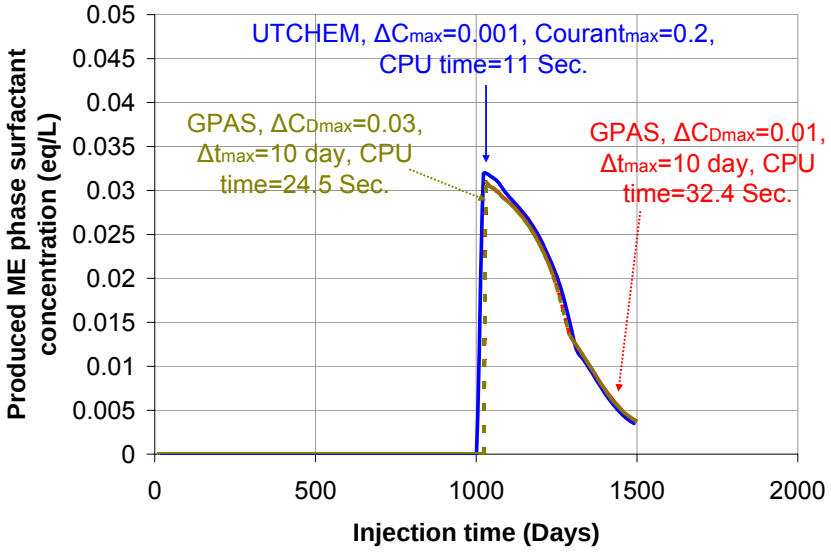

Figure 7.129: Comparison of produced ME phase surfactant concentration for the base case surfactant/polymer benchmark.

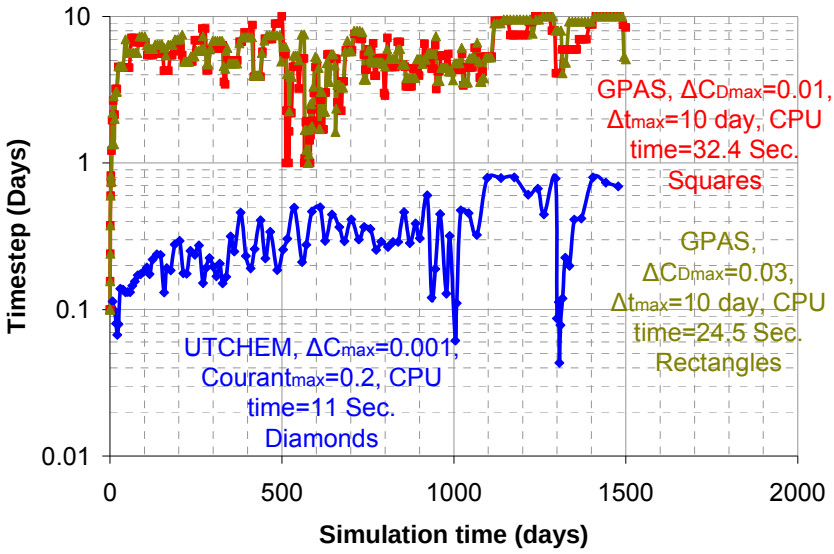

Figure 7.130: Comparison of actual timesteps taken by UTCHEM and GPAS for the base case surfactant/polymer flood benchmark.

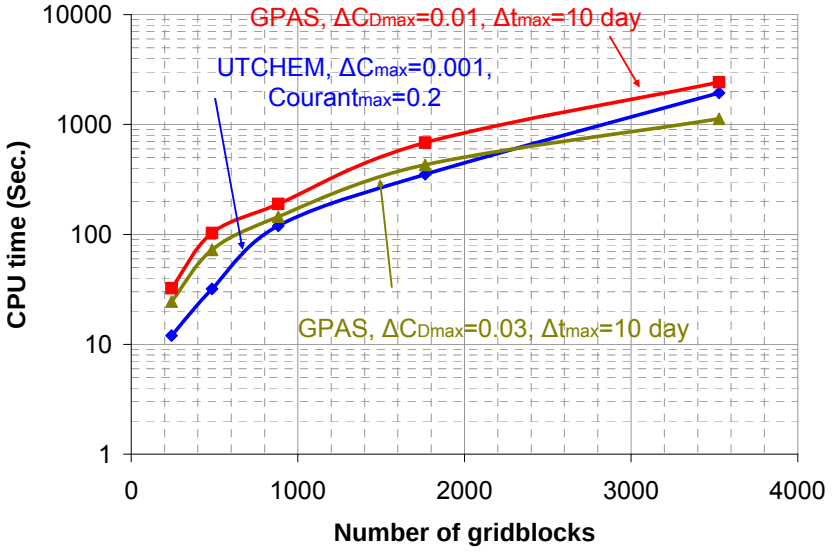

Figure 7.131: Comparison of CPU times for surfactant/polymer flood in a homogeneous reservoir as a function of number of gridblocks.

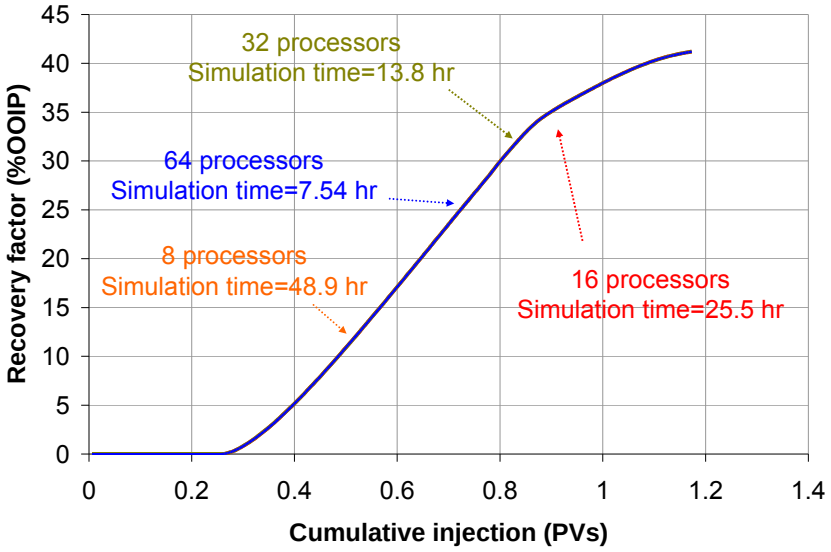

Figure 7.132: Surfactant/polymer flood oil recoveries and computation times for several processor configurations.

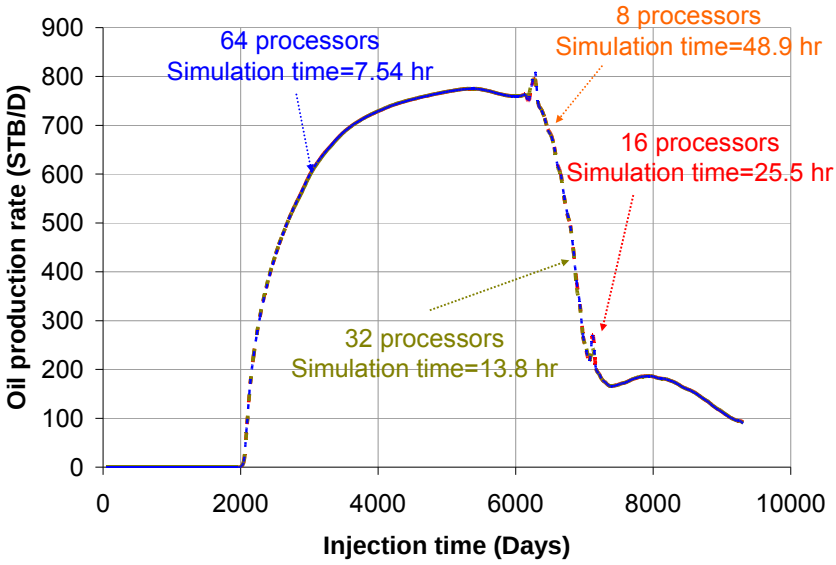

Figure 7.133: Surfactant/polymer oil production rate for parallel simulations.

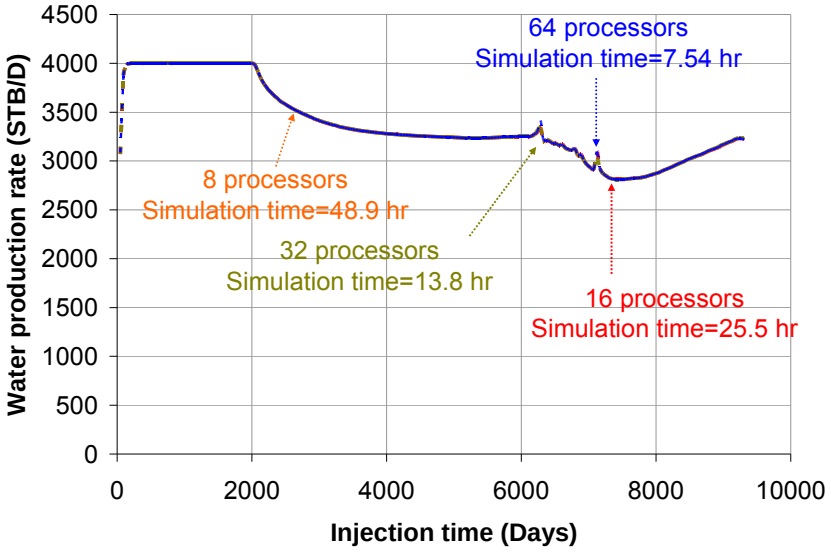

Figure 7.134: Water production rate for surfactant/polymer parallel simulations.

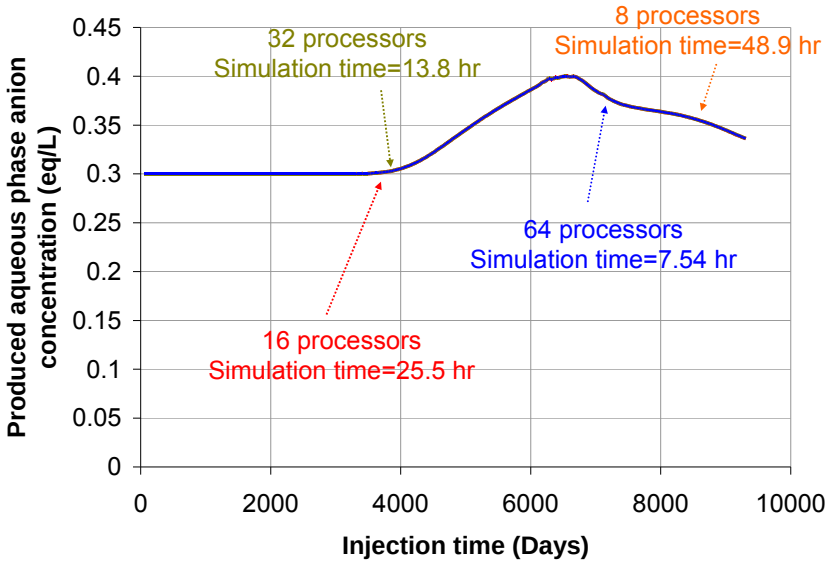

Figure 7.135: Effluent anion concentration for surfactant/polymer parallel simulations.

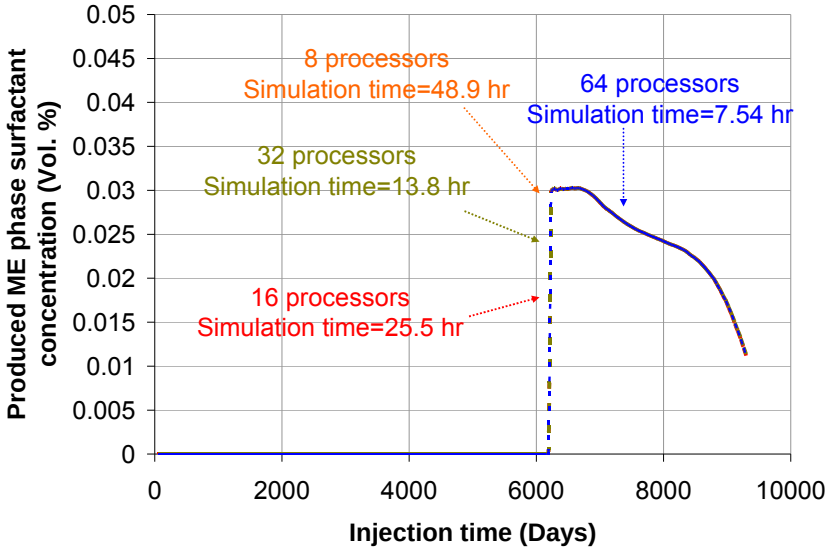

Figure 7.136: Effluent surfactant concentration in the microemulsion phase for parallel simulations.

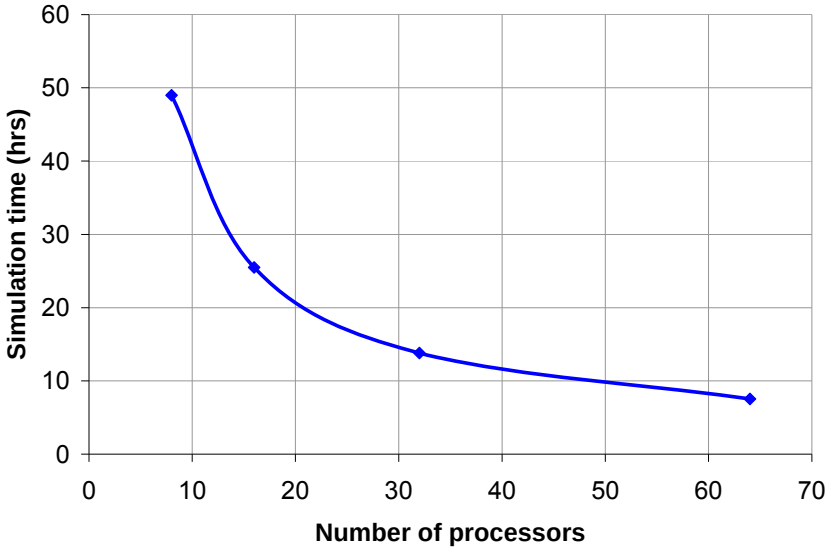

Figure 7.137: Surfactant/polymer flood simulation time vs. number of processors.

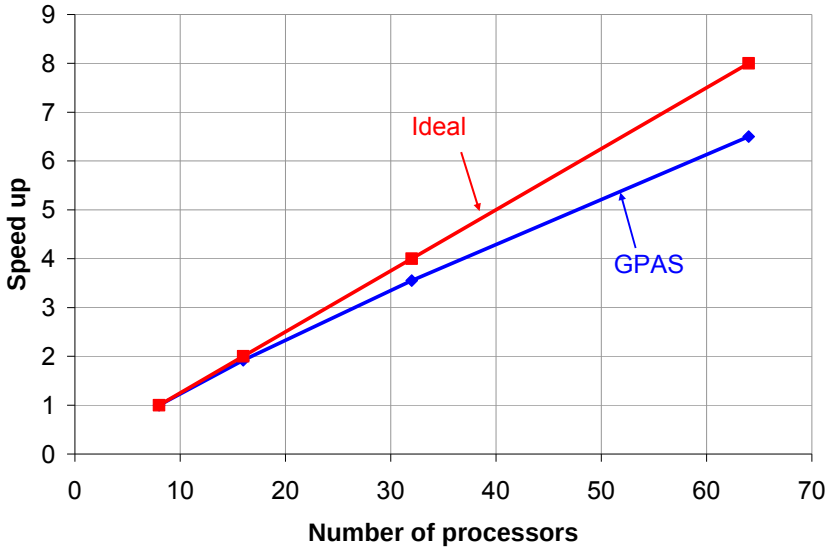

Figure 7.138: Speedup as a function of number of processors.

Chapter 8: Summary and Conclusions

This work consisted of two major parts. The first part of the research focused on the development, implementation, and validation of a wettability alteration module in UTCHEM simulator. The wettability alteration model was validated against two laboratory experiments. The recovery mechanisms were very different in these two experiments. An attempt was also made to scale up the static imbibition test and dynamic fractured block experiments to larger matrix blocks. Based on the results of this study, it was confirmed that viscous gradient has a significant effect on the oil recovery from NFRs and cannot be neglected in the laboratory results. Therefore, experiments under dynamic conditions give better insights about the recovery mechanisms involved in chemical flooding of NFRs compared to static imbibition experiments. Mobility control such as foam is required to increase the sweep efficiency of the injected chemicals in large matrix blocks. The most important conclusions are as follows:

- Wettability modification of mixed or oil wet matrix rocks to water-wet conditions using chemicals such as alkali or surfactant has great potentials in producing oil from naturally fractured carbonate reservoirs.
- The time of recovery for static experiment where gravity is the dominating recovery mechanism scales linearly with matrix height. The process is very slow and takes many years before any recovery enhancements is observed.
- Due to complexity of the mechanisms involved in the fractured block dynamic experiment, the existing scaling groups failed to predict the time of oil recovery for all of the three stages of the experiment in larger matrix blocks. A new scaling group is needed to predict the time of the recovery for field scale applications where gravity, capillarity, and viscous gradient play a role.

The second contribution of this research is the implementation and validation of a comprehensive oil/brine/surfactant phase behavior in a fully implicit and parallel reservoir simulator, GPAS. This development was performed and validated as follows:

- A new phase was added to the simulator to account for the ME phase. The chemical flooding module can now handle up to three liquid phases and the transition of phase behavior with salinity.
- The material balance equations of aqueous components were modified to allow for partitioning of aqueous components in the aqueous and ME phases.
- A new variable was added for interfacial tension between water/ME. This new IFT is calculated based on the phase environment and presence of both water and ME phases.
- Oil/brine/surfactant phase behavior calculations were extended to all possible phase environments in a chemical flood. Depending on the surfactant and anion concentrations, there may be 5 different phase environments.
- The relative permeability of water, oil and, ME phases as a function of trapping number was added for all possible phase environments.
- Polymer adsorption calculations, shear rate dependency of polymer viscosity and permeability reduction effects of polymer were corrected and validated against UTCHEM.
- The Jacobian of the system was modified to account for the newly added phase and partitioning of aqueous components in the aqueous and ME phases.
- The wettability alteration model of UTCHEM for surfactants was successfully added to GPAS.
- Several test cases of water, polymer, and surfactant/polymer floods were successfully compared with UTCHEM. These test cases included 1D corefloods, 2D vertical cross-sections and 3D homogeneous cases.
- Results of surfactant polymer flood in a 3D reservoir with heterogeneous permeability field were successfully compared to UTCHEM.
- Performed a systematic comparison of the efficiency on a single processor computer between UTCHEM and GPAS. The timesteps in GPAS are much larger than UTCHEM as expected. However, this study shows that there is a large overhead associated with the calculations in GPAS for each timestep. One of the reasons for this is the PETSc solver performs poorly as number of

gridblocks increases. The other reason is that the automatic timestep control option of GPAS is not optimized for chemical flooding.

- The results of GPAS are very sensitive to timestep size. Hence, it is a matter of judgment on how to compare GPAS and UTCHEM with respect to the simulators' computational time and accuracy. The larger the timesteps of GPAS and its concentration tolerances are, the faster it runs. But this comes with the price of losing the accuracyof the simulation results due to increased truncation errors.
- UTCHEM runs faster compared to GPAS for small size problems. However, as the number of gridblocks increases, GPAS becomes faster.
- Parallel simulations showed a close to ideal speedup for chemical flooding module of GPAS. A chemical flood simulation in a reservoir with 81920 gridblocks takes 48.9 hrs on 8 processors. This time is reduced to 7.5 hrs when 64 processors are used.

Recommendations for future work can be divided into two categories; implementation of new physical models and recommendations for improving the numerical computation.

Recommendations regarding implementation of different physical models are as follows:

- One of the most important limitations of the current formulation of GPAS is the assumption of no free gas at the time of chemical flooding. This limits the application of the simulator to waterflooded reservoirs only where the oil is almost free of gas. Since GPAS uses an EOS, it may be a good research idea to try and couple the EOS module with the chemical flooding module to remove this limitation.
- The wettability alteration model of UTCHEM can be coupled with the dual porosity model to allow for better modeling of NFRs.
- The effect of hardness on both polymer and surfactant phase behavior is significant and it is recommended to implement an additional component to represent the hardness (total divalent cations as an equivalent of calcium concentration).

- Cosolvents are needed in many chemical flooding formulations for phase stability and removing viscous gels. Cosolvents also affect the oil/brine/surfactant phase behavior. It is recommended to add the effect of cosolvents on phase behavior.
- GPAS has a thermal flooding module but this module is not coupled with the chemical flooding module at this time. It is recommended to couple these modules to be able to model surfactant polymer floods at elevated temperatures.
- Interest in alkali/surfactant/polymer (ASP) flooding is increasing nowadays due to its interesting features such as in-situ soap generation and low surfactant adsorption. It is recommended to add the capability of modeling ASP floods to GPAS by coupling a geochemical module with the chemical flooding module.
- Deviated and horizontal wells are very popular at the present time and it is recommended to add this capability to GPAS.

Recommendations regarding improvement of numerical computation are as follows:

- IMPES and fully implicit schemes have their advantages and disadvantages. Adaptive implicit methods may be used to have the advantages of both of these methods at the same time and improve the computation time to a great extent.
- Efficiency of the PETSc solver decreases as the problem size increases (the Jacobian matrix becomes larger). It is recommended to use more efficient solvers in GPAS to improve the CPU time for larger data sets.
- The timestep control of GPAS is not optimized for chemical flooding. It is recommended to conduct more research on optimization of the automatic time step control for chemical flooding. The timestep selection needs to be based on either flux or relative changes in the residuals of the material balance equations in the previous timesteps. It is also recommended to take the number of iterations in the previous two timesteps into account and prevent timestep enlargements when the number of iterations is increasing.

Nomenclature

$A_{p1}, A_{p2}, A_{p3}, S_p$	Polymer viscosity model parameters
A_0, A_1, A_2	Parameters used for calculation of Height of bimodal curve in Hand's rule
a, c	Chun-Huh IFT correlation parameters
a_{i1}, a_{i2}, b_i	Adsorption model parameters for component *i*
C_i	Volume of component *i* in fluid per fluid volume, fraction
$\tilde{C}_i$	Overall volume of component *i* per pore volume, fraction
$\hat{C}_i$	Adsorbed volume of component *i* per pore volume, fraction
C_i^f	Volume of component *i* in fluid per pore volume, fraction
C_{ij}	Volume of component *i* in phase *j* per volume of phase *j*, fraction
C_{SE}	Effective salinity, meq/ml
C_{SEL}, C_{SEU}	Lower and upper limits of effective salinity respectively, meq/ml
C_{SEOP}	Optimum salinity, meq/ml
C_{41}, C_{43}	Concentration of polymer in aqueous and ME phases respectively, wt%
$C_{3\max,s}$	Maximum height of binodal curve at salinity *s*
CMC	Critical micelle concentration
c_i^o	Compressibility of component *i* at reference pressure, psi^{-1}
$c_{i,inj}$	Injected concentration of component *i* in aqueous phase Surfactant: vol. fraction

Polymer: wt%

Salt: meq/ml

Tracer: lbmole/L

c_f Rock compressibility

D Depth, ft

g Acceleration of gravity

$\bar{\bar{k}}$ Absolute permeability tensor

k_{rj} Relative permeability of phase *j*, fraction

k_x, k_y, k_z Absolute permeability in x, y and z directions respectively, md

M_i Molecular weight of component *i*, lbmole/lb

N_i Moles of component *i* per pore volume, lbmole/ft^3

N_i^f Moles of component *i* in fluid per pore volume, lbmole/ft^3

$N_{i,j}$ Moles of component *i* in phase *j* per pore volume , lbmole/ft^3

$N_{T,j}$ Total number of moles of phase *j* per pore volume, lbmole/ft^3

N_{T_j} Trapping number of phase *j*

n_a Total number of aqueous components except water

n_b Total number of gridblocks

n_c Total number of oleic components

n_j Relative permeability exponent of phase *j*

P_α Model parameter for shear rate dependency of polymer viscosity

P^o	Reference pressure, psi
P_j	Fluid pressure of phase *j*, psi
P_{wf}	Well bottomhole pressure, psi
q_i	Sink or source of component *i*, lbmole/day
$\vec{R}$	Residual vector
$\vec{R}_I$	Residual vector for gridblock *I*
$R_{\ell 3}$	Solubilization ratio of phase ℓ
R_V	Residual of volume constraint
r_o	Equivalent well radius, ft
r_w	Well radius, ft
S_j	Saturation of phase *j*, fraction
S_{jr}	Residual saturation of phase *j*, fraction
T_j	Trapping number model parameter of phase *j*
t	Time, day
V_b	Bulk volume, ft^3
$\vec{X}$	Solution vector
$\vec{X}_I$	Solution vector for gridblock *I*
x_{ij}	Mole fraction of component *i* in phase *j*, fraction
$\Delta x, \Delta y, \Delta z$	Gridblock length in x, y and z directions respectively, ft

z_t, z_b	Top and bottom wellblock respectively
$\alpha_1, \alpha_2, \alpha_3, \alpha_4, \alpha_5$	Microemulsion viscosity correlation parameters
$\dot{\gamma}$	Shear rate, sec^{-1}
γ_j	Specific gravity of phase *j*, psi/ft
μ_j	Viscosity of phase *j*, cp
μ_p	Viscosity of water with polymer, cp
μ_w	Viscosity of pure water, cp
ξ_i	Molar density of component *i*, $lbmole/ft^3$
ξ_i^o	Molar density of component *I* at reference pressure, $lbmole/ft^3$
ξ_j	Molar density of phase *j*, $lbmole/ft^3$
ρ_j	Mass density of phase *j*, lb/ft^3
$\sigma_{\ell 3}$	Interfacial tension between phase ℓ and the ME phase, mN/m
σ_{OW}	Interfacial tension between oil and aqueous phase
τ_j	Trapping number model parameter of phase *j*
φ	Porosity, fraction
φ_r	Porosity at reference pressure, fraction

Superscripts and Subscripts

High	High trapping number
Low	Low trapping number
O	End point

i	Index for component
	For $C_i, \tilde{C}_i, \hat{C}_i, C_i^f$ and C_{ij}
	1:water
	2: oil
	3: surfactant
	4: polymer
	For other symbols
	1 to n_c: oleic component
	$n_c + 1$ to $n_c + n_a$: aqueous component except water
	water: water
	oil: oil
	poly: polymer
	salt: salt
	trac: tracer
j	Index for phase
	1: aqueous
	2: oleic
	3: ME
j'	Conjugate phase
z	Well gridblock

Appendix A: Effect of Temperature on Reservoir Fluid Properties and Surfactant Solutions

The effect of temperature on surfactant phase behavior is not general and can be very different for different surfactant molecules or the mixture of different surfactants.

A1.1.1. Phase Transition

An increase in temperature would normally shift the phase equilibrium of anionic surfactant solutions towards the lower phase microemulsions. This means that the anionic surfactants normally become more water-soluble and less oil-soluble as temperature increases. Figure A.1 illustrates this effect for an anionic surfactant (PDM 337) studied by Novosad (1982). He found that a middle phase microemulsion of the above mentioned anionic surfactant becomes lower phase microemulsion as temperature is increased.

A1.1.2. Solubilization Parameters

Healy and Reed (1976) observed that for a constant salinity, increasing the temperature would result in a decrease in solubilization of oil and an increase in solubilization of water in the microemulsion phase. *Solubilization ratio* or *solubilization parameter* of oil is defined as the ratio of volume of oil in the microemulsion phase to volume of surfactant in that phase, V_o/V_s. A similar definition is used for solubilization parameter of water as V_w/V_s. *Optimum salinity* is defined as the salinity in which the IFT of both microemulsion/oil and microemulsion/water interfaces is equal.

This is consistent with the observation of Novosad (1982) mentioned in the previous section. Figure A.2 shows solubilization ratios measured by Healy and Reed (1976) for an anionic surfactant at two different temperatures and a range of salinities. The surfactant studied was a monoethanol amine salt of dodecyl-orthoxylene sulfonic acid. **Table A.1** summarizes the surfactants used in the work of each of the authors mentioned in this dissertation. Looking at Figure A.2 suggests that solubilization ratio at optimum

salinity decreases with increasing temperature. This is confirmed by work of Puerto and Reed (1983) presented in Figure A.3. As shown in this figure, the systems studied by Puerto and Reed (1983) also show a similar trend, i.e. the optimum solubilization parameter decreases with temperature. Figure A.4 shows the results of a study by Aoudia and Wade (1995). They studied propoxylated C14 alcohol sodium sulfates. As shown in Figure A.4, the trend of the data is the same as suggested by other authors. Figure A.5 shows the correlation presented by Austad and Skule (1996). They also suggest that optimum solubilization ratio decreases with increasing temperature. Dwarakanath and Pope (2000) studied phase behavior of sodium dihexyl sulfosuccinate and Dense None Aqueous Phase Liquids (DNAPL) and found that although optimum salinity increases with temperature, the solubilization ratio versus normalized salinity (salinity divided by optimum salinity) remains the same for a range of temperatures. Figure A.6 shows their volume fraction diagram for four different temperatures.

A.1.1.3. IFT

Healy and Reed (1976) presented measured IFTs for different temperatures and a range of salinities (Fig. A.7). Ziegler (1988) presented a similar plot (Figure A.8). As seen in both of these figures, for both of the microemulsion/oil and microemulsion/water interfaces, the IFT increases as temperature is increased at a constant salinity. Based on these results, the IFT at the optimum salinity also increases with increasing temperature. As shown in Fig. A.4, Healy and Reed (1976) found that as temperature is doubled (from 74 ºF to 150 ºF) IFT at the optimum salinity is almost increased by a factor of 2.6 (from 0.0009 dyne/cm to 0.0024 dyne/cm).

A.1.1.4. Optimal Salinity

As shown in Fig. A.9, the optimum salinity normally increases with increasing temperature. This figure shows results from four different references and all of these results suggest that salinity at optimum conditions increases linearly with temperature.

A.1.1.5. Surfactant Retention

Novosad (1982) investigated effect of temperature on adsorption and retention of two anionic surfactants in Berea cores. Surfactant retention and adsorption tend to decrease with increasing temperature from 25 to 70 ºC for both of the surfactants studied. The decrease in surfactant retention could be explained by the shift in the phase transition with temperature. As mentioned in Section A1.1.1, increasing the temperature would shift the phase behavior towards lower microemulsions. This means that surfactant concentration in the trapped oil phase decreases with increasing temperature and thus surfactant retention is reduced.

A1.1.6. Critical Micelle Concentration

Noll (1991) measured CMC of three different commercial sulfonate surfactants used for foam creation and suggested that CMC increases with temperature. Bourrel and Schechter (1988) show some of the results of Flokhart (1957) where CMC of sodium dodecyl sulfate is plotted as function of temperature. These data suggest linear dependency of CMC on temperature in the temperature range of interest. These data are plotted in Fig. A.10.

A1.1.7 Oil Viscosity

The results presented here are based on the data of Miadcnye *et al.* (1993). They report viscosity data for North Sea crude oil measured by Ahrabi *et al.* (1987). They also report viscosity measurements for three different oil samples that they call light, medium and heavy oils respectively, taken from Al-Besharah *et al.* (1989). These data are plotted in Fig. A.11. As shown in this figure, oil viscosity could be reduced by orders of magnitude with few degrees increase in temperature. This is one of the most important driving forces of thermal oil recovery.

A1.1.8. Water Viscosity

Viscosity of reservoir brine is also a function of temperature. Temperature dependency of a brine containing 4 wt% NaCl is presented in Fig. A.12. This data is obtained from Mc Cain's reservoir fluid properties book (McCain, 1989).

A1.1.9. Density

Phase densities are functions of the component densities and the density of all of reservoir fluids is temperature dependant. It is desired to look at temperature dependency of reservoir fluids in this work.

A2. Revisiting Temperature Dependency of Phase Behavior and Fluid Properties in UTCHEM

A2.1. Effective salinity

As mentioned in Section 1.1.4., increasing the temperature would normally increase the optimum salinity of a crude oil/brine/surfactant formulation for anionic surfactants. This means that the effective salinity is decreased as temperature is increased. This is modeled in UTCHEM as described by Eq.A.1.

$$C_{SE} = \frac{C_{51}}{1+\beta_T\left(T-T_{ref}\right)} \qquad \text{Eq.A.1}$$

It should be noted that this equation introduces a nonlinear relationship between the effective salinity and temperature. Figure A.13 shows the quality of the fit to experimental data of Fig. A.9 using Eq.A.1. It seems the data have linear trend, and the existing correlation seems to be off for some of the data, especially for the data from Healy and Reed (1976). To see the performance of a linear correlation, Eq.A.2 was also examined.

$$C_{SE} = C_{51}\left[1-\beta_T^{'}\left(T-T_{ref}\right)\right] \qquad \text{Eq.A.2}$$

Figure A.14 compares the fits using UTCHEM model with linear fits to the data. One could see that for the data of Healy and Reed (1976), the linear fit seems to be better, whereas the existing correlation in UTCHEM seems to be a better fit for the Ziegler (1988) data and the existing correlation and the linear fit almost overlap for the data of Audia and Wade (1995). The relative error for these correlations are compared and values are summarized in **Table A.2**. As shown in this table, existing UTCHEM correlation works better for the Ziegler (1988) data by having a relative error of 5.31% compared to the linear correlation which has 15% error. On the other hand, the linear correlation works better for the data of Healy and Reed (1976) with a relative error of 2.5% compared to the existing UTCHEM correlation which has 7.8% error. The proposed model also predicts the Dwarakanath and Pope data with a smaller error (1.32%) compared to the existing model (8.22%). As expected, both of the correlations give reasonable estimates of the Audia and Wade (1995) data. Based on this analysis, it was decided to add the correlation of Eq.A.2 to UTCHEM to improve its ability in predicting phase behavior changes with temperature.

A2.2. Height of Binodal Curve

In UTCHEM we model the heights of binodal curves as linear functions of temperature. Eq.A.3 shows the correlation used in UTCHEM:

$$C_{3,\max} = H_{BNC,m} + H_{BNT,m}\left(T-T_{ref}\right), m = 0,1 or 2 \qquad \text{Eq.A.3}$$

where $C_{3,max}$ is the height of binodal curve at temperature T, $H_{BNC,m}$ is height of binodal curve at reference temperature for m times optimum salinity, $H_{BNT,m}$ is slope of binodal curve versus temperature for m times optimum salinity and T_{ref} is the reference temperature. To see if this correlation is good enough to represent the behavior of surfactants as function of temperature, the data from Puetro and Reed (1983) and Aoudia and Wade (1995) was used. Solubility parameters measured by these researchers at optimum salinity (presented in Figs. A.3 and A.4) were converted to heights of binodal curve using Eq.A.4.

$$C_{3,\max} = \frac{1}{2\sigma^*} \qquad \text{Eq.A.4}$$

It should be mentioned that this equation works in limiting case of very small surfactant concentrations. The results of this conversion are presented in Figs. A.15 and A.16 for Puetro and Reed and Aoudia and Wade data respectively. As shown in these figures, the dependency of height of binodal curve on temperature at optimum salinity has a linear trend for all of the data and therefore the correlation used in UTCHEM is adequate.

A2.3. Oil and Water Viscosities

The correlation used for temperature dependency of phase viscosities in UTCHEM is as of Eq.A.5.

$$\mu_k = \mu_{k,ref} \exp\left(b_x \left[\frac{1}{T} - \frac{1}{T_{ref}} \right] \right) for \quad \kappa = water, oil \quad or \quad air \qquad \text{Eq.A.5}$$

Oil viscosities measured by Ahrabi *et al.* (1987) and Al-Besharah *et al.* (1989) are plotted in Fig. A.8 and were matched with Eq.A.5 shown in Fig. A.17. As shown in this figure, Eq.A.5 is able to match the data to a good extent. Figure A.18 shows the match obtained with the water viscosity data from McCain (1989) using Eq.A.5. This figure shows that although Eq.A.5 can not match the data of water viscosity as good as the oil viscosity, but the match is still good enough and no more correlations are required.

A2.4. Critical Micelle Concentration of Surfactants

CMC was treated as a constant in UTCHEM. After finding some data on the dependency of CMC on temperature, a linear correlation was implemented in the code to represent this dependency. The user requires giving two additional parameters for this correlation: the slope of CMC as a function of temperature and the temperature at which the initial CMC is measured. The good thing about such a model is that one can easily go back to a constant CMC just by inputting a slope of zero to the simulator. The correlation implemented is as of Eq.A.6:

$$CMC = S_{CMC}\left(T - T_{ref}\right) + CMC_{ref} \qquad \text{Eq.A.6}$$

where CMC is the critical micelle concentration at elevated temperature, S_{CMC} is the slope of CMC as function of temperature, CMC_{ref} is the CMC at reference temperature denoted as T_{ref}.

A2.5. Density

There is no temperature dependency of component densities in UTCHEM at the present time, but it is desired to have such correlations in the simulator.

Table A.1:List of surfactants used in each of the references.

Reference	Surfactant used
Flokhart (1957)	sodium dodecyl sulfate
Healy and Reed (1976)	monoethanol amine salt of dodecyl-orthoxylene sulfonic acid
Novosad (1982)	PDM 337 (a synthetic sulfonate)
Puetro and Reed (1983)	alkylarylsulfonate: bl-C12BTXSNa
Zelegler (1988)	synthetic alkylaryl sulfonate (AAS)
Noll (1991)	DDTAB and three sulfonate surfactants
Audia and Wade (1995)	propxylated C14 alcohol sodium sulfates (C14EX(PO)n)
Austad and Skule (1996)	C12-o-xylene sulfonate
Dwarakanath and Pope (2000)	sodium dihexyl and sodium diamyl sulfosuccinate

Table A.2: Comparison of relative errors for the two correlations used to model temperature dependency of effective salinity.

Relative error (%)	Healy and Reed (1976)	Zelegler (1988)	Audia and Wade (1995)	Dwarakanath and Pope (2000)
UTCHEM correlation	7.80	5.31	1.12	8.22
Linear correlation	2.50	15.00	3.77	1.32

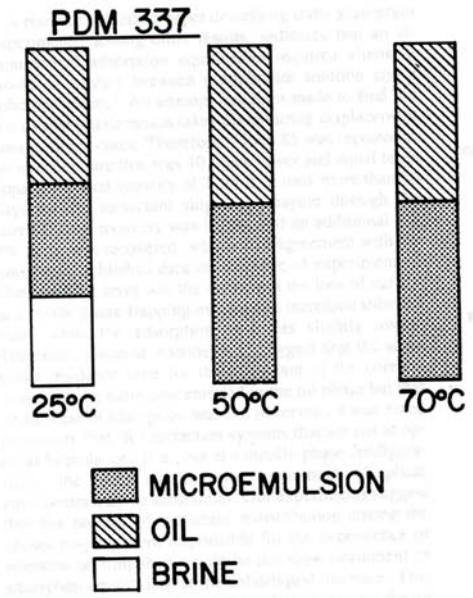

Figure A.1: Effect of temperature on phase transition of an anionic surfactant (Novosad, 1982).

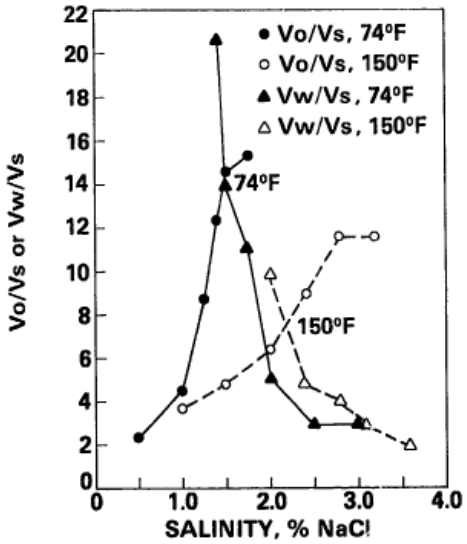

Figure A.2: Effect of temperature on solubilization ratio of an anionic surfactant, (Healy and Reed, 1976).

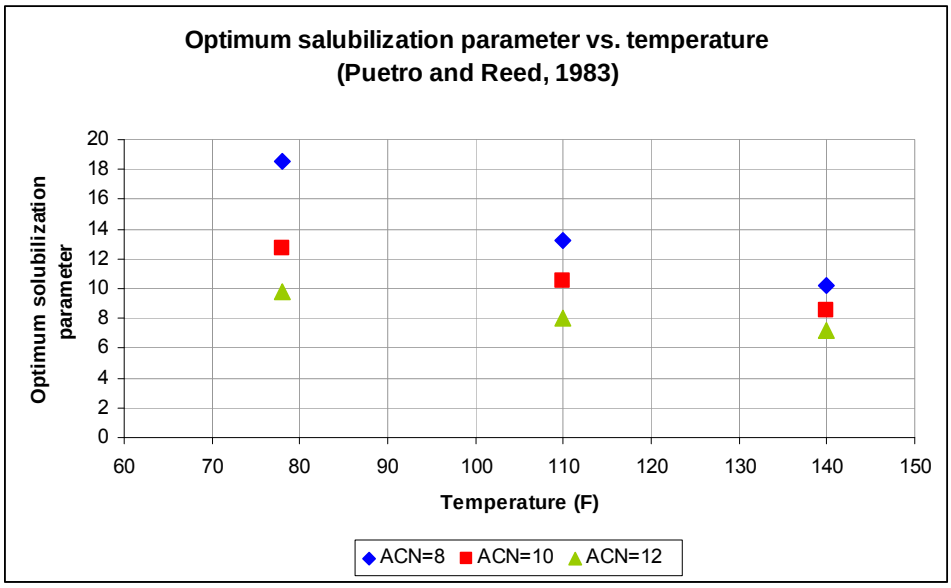

Figure A.3: Effect of temperature on optimum solubilization ratio of an anionic surfactant (Poetro and Reed, 1983).

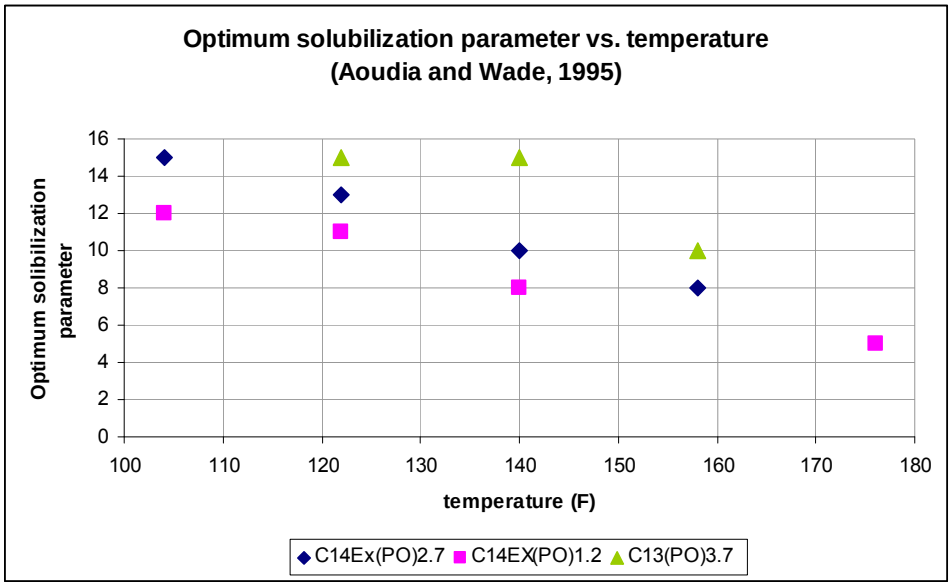

Figure A.4: Effect of temperature on optimum solubilization ratio of three different anionic surfactants and octane (Aoudia and Wade, 1995).

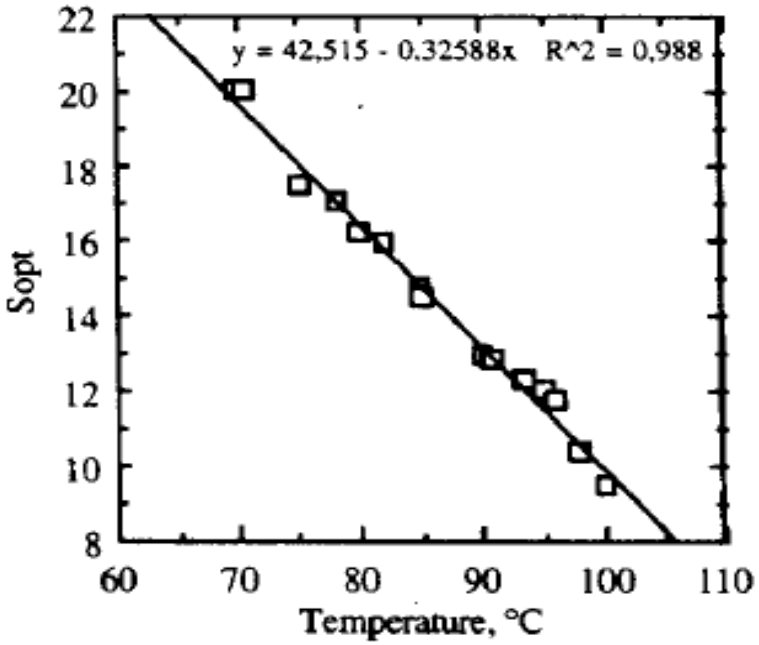

Figure A.5: Effect of temperature on optimum solubilization ratio for C12-o-xylene sulfonate and live crude oil (Austad and Skule, 1996).

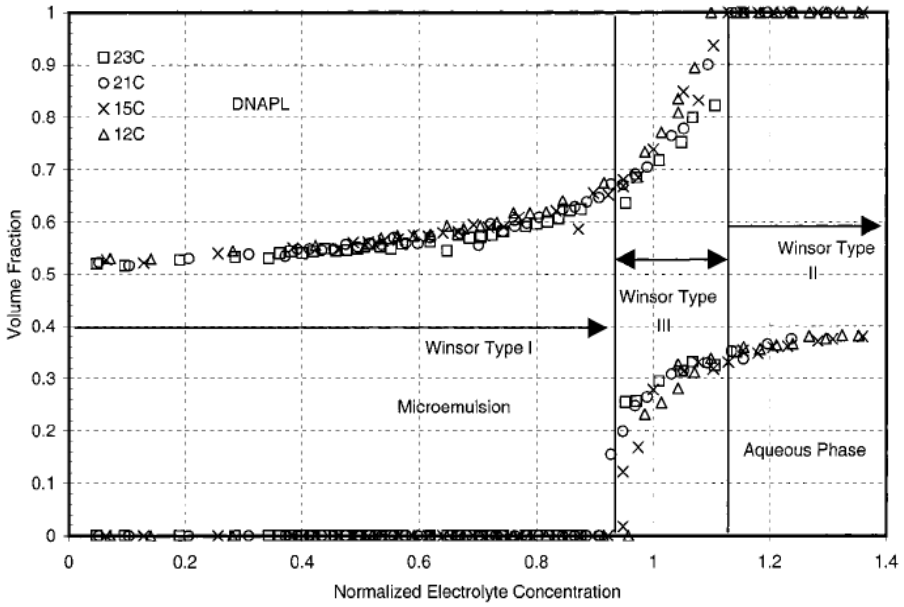

Figure A.6: Volume fraction diagram for a mixture of 2-Propanol and sodium dihexyl sufosuccinate at different temperatures (Dwarakanath and Pope, 2000).

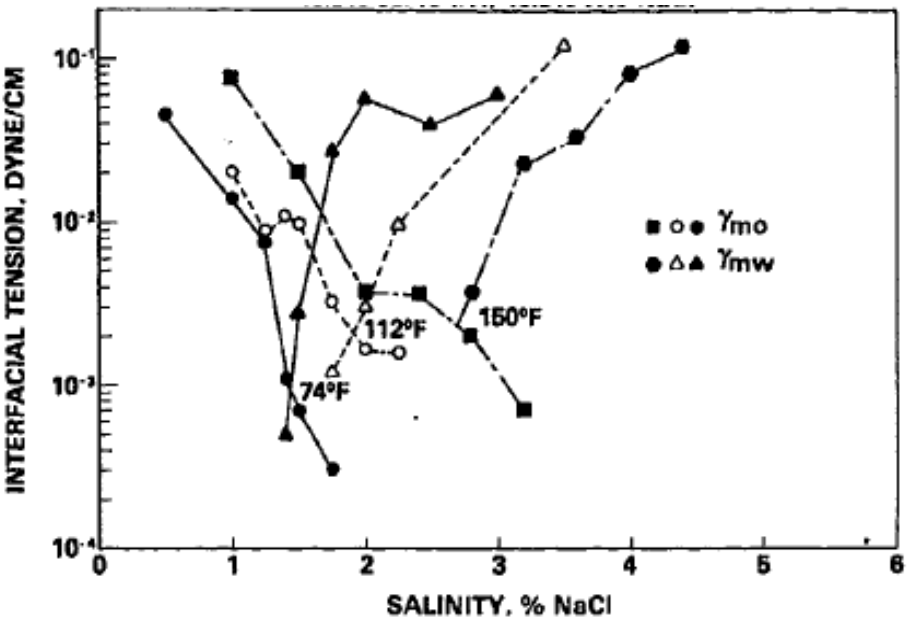

Figure A.7: Effect of temperature on IFT of microemulsions created by anionic surfactants (Healy and Reed, 1976).

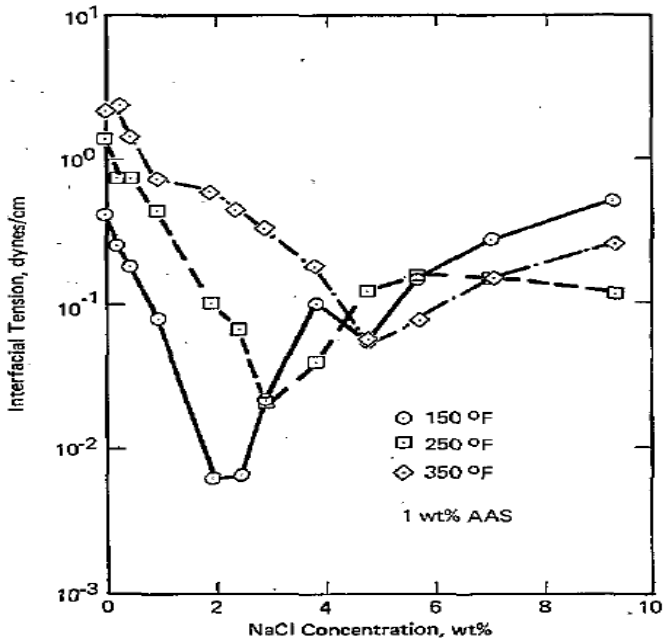

Figure A.8: Effect of temperature on IFT of microemulsions created by anionic surfactants (Ziegler, 1988).

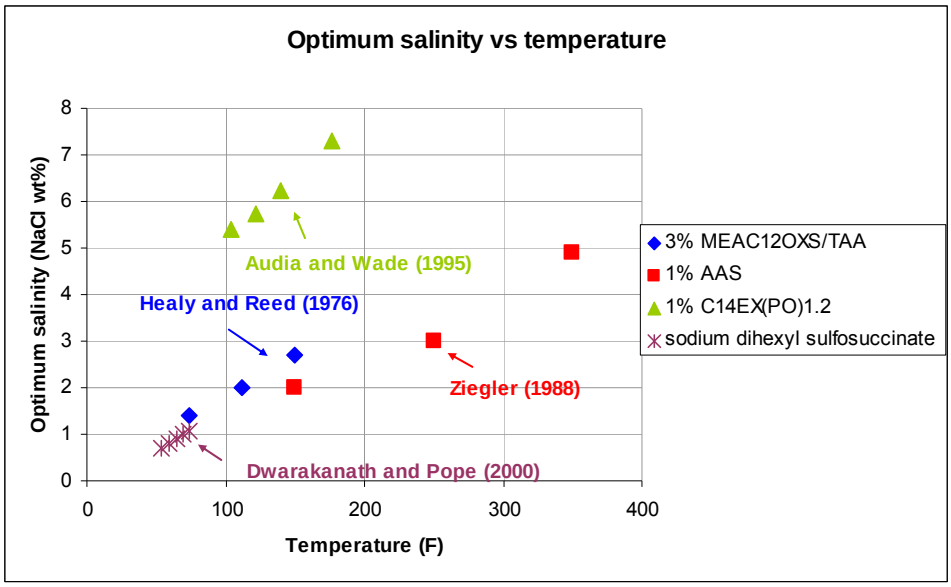

Figure A.9: Effect of temperature on optimum salinity.

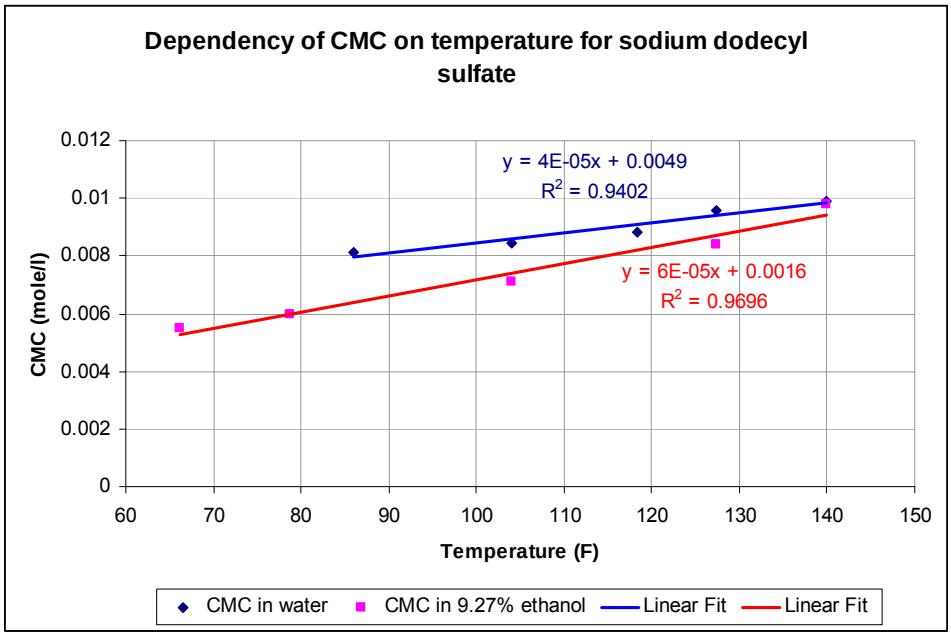

Figure A.10: Temperature dependency of CMC for sodium dodecyl sulfate (Bourrel and Schechter, 1988).

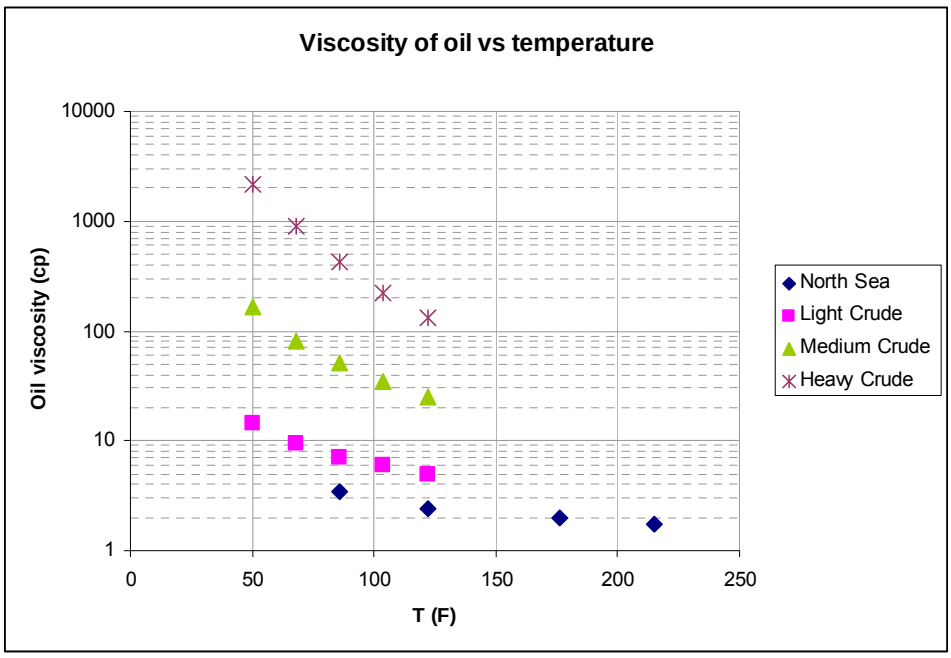

Figure A.11: Effect of temperature on oil viscosity, based on Ahrabi et al. (1987) and Al-Besharah et al. (1989).

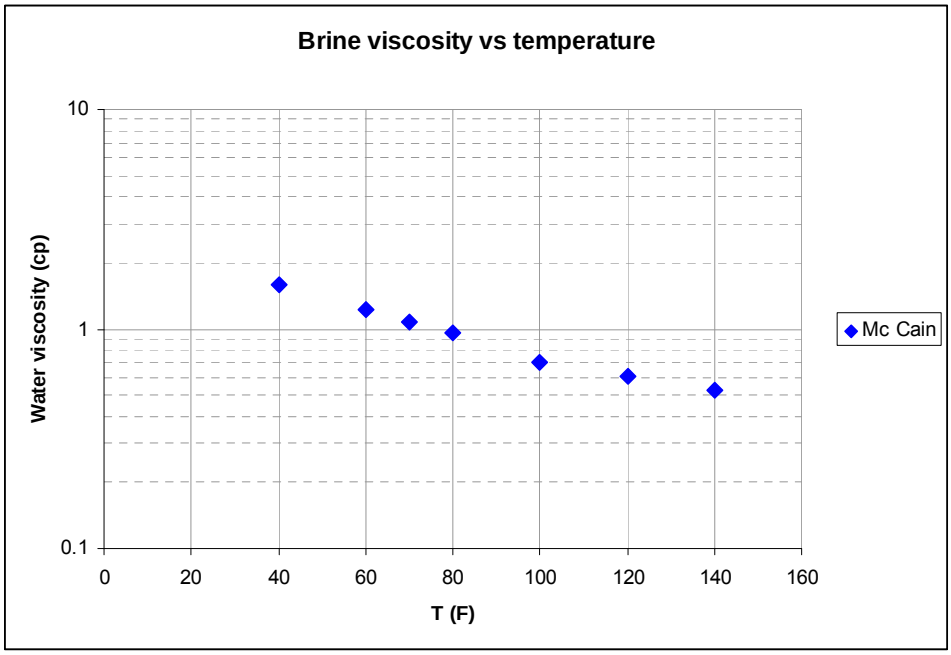

Figure A.12: brine viscosity as a function of temperature (McCain, 1989).

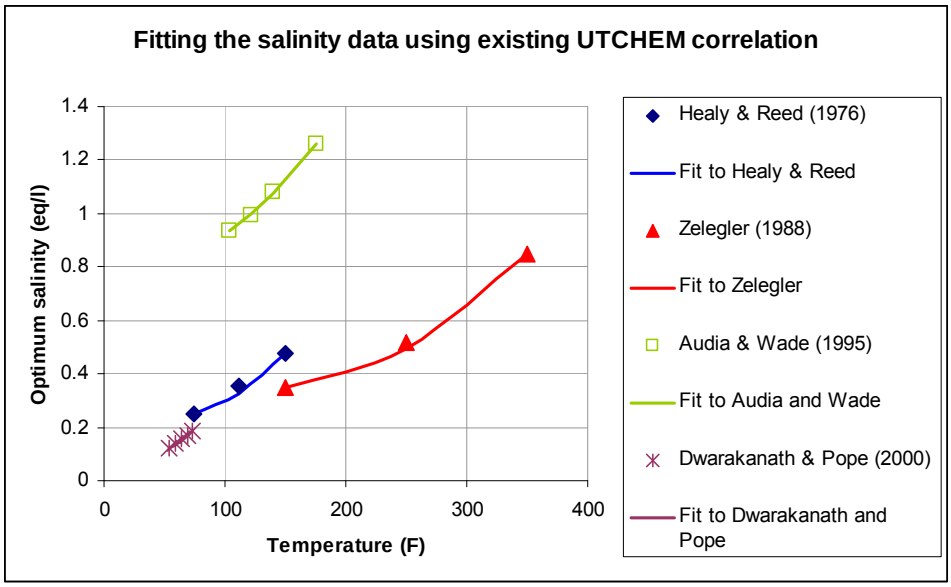

Figure A.13: Using UTCHEM effective salinity correlation to fit optimum salinity data found in the literature.

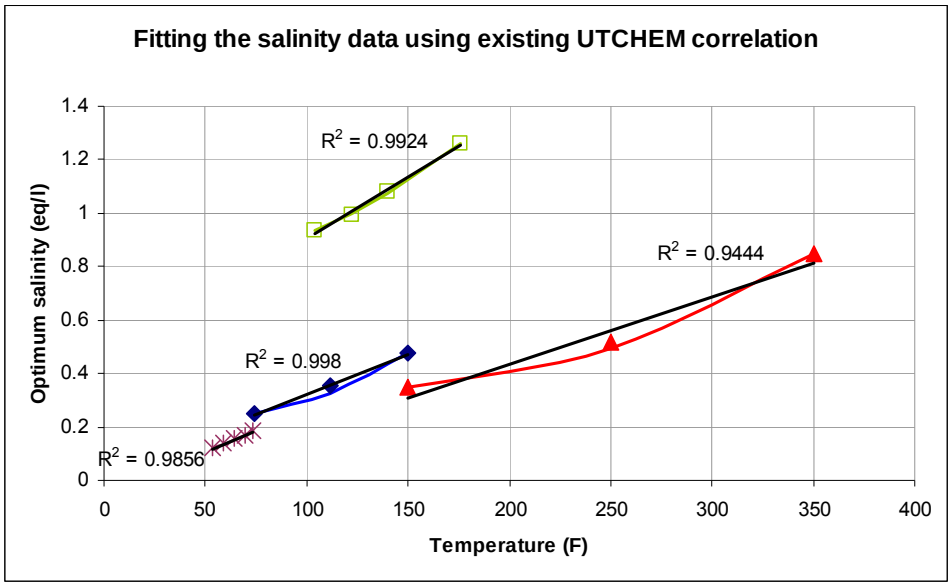

Figure A.14: Comparing the existing and proposed correlations for temperature dependency of effective salinity (Data from Fig. A.9).

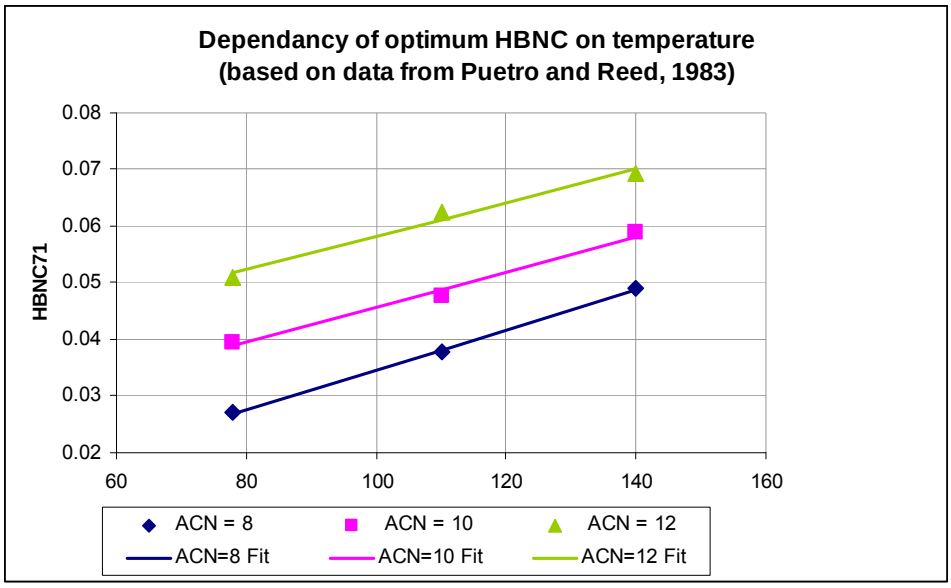

Figure A.15: Confirmation of linear dependency of HBNC on temperature (based on Puetro and Reed, 1983).

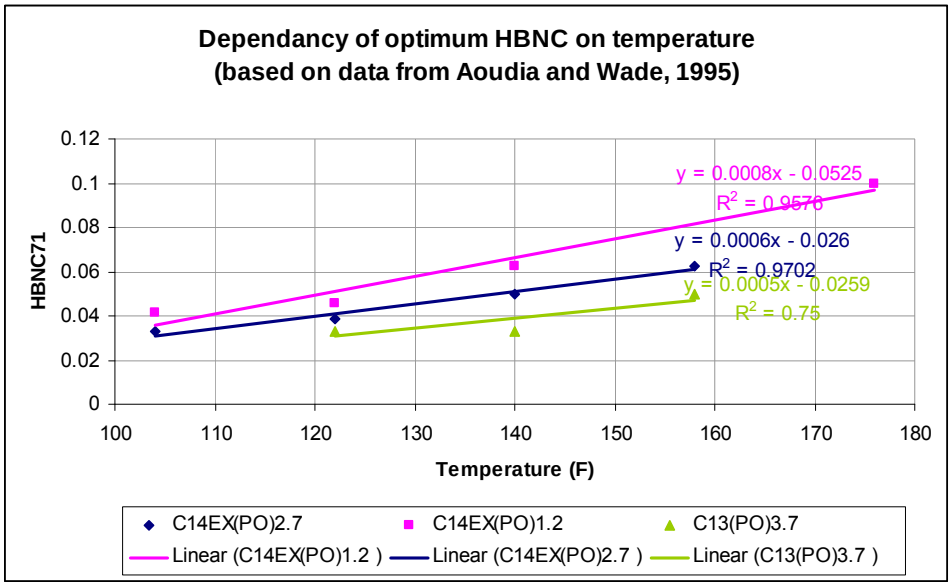

Figure A.16: Confirmation of linear dependency of HBNC on temperature (based on Aoudia and Wade, 1995).

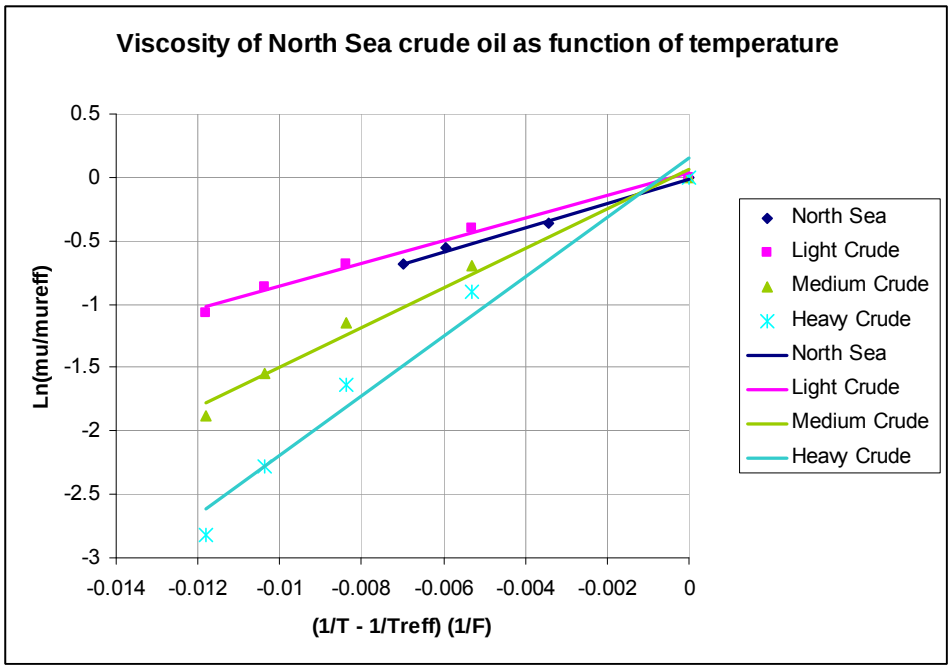

Figure A.17: Comparison of computed oil viscosity and measured data.

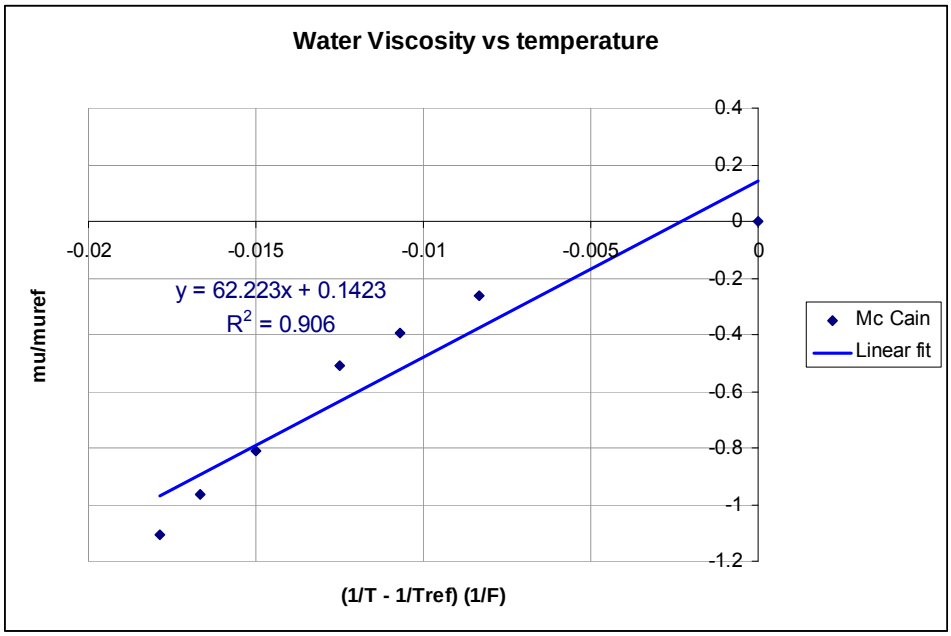

Figure A.18: Comparison of computed water viscosity and measure data of McCain (Fig. A.12)

Appendix B: Derivation of Equations of Chapter 6

B1 The Adsorption Isotherm

The adsorbed concentration of surfactant and polymer components is specified by Langmuir isotherms. Dividing the adsorbed concentration by overall water concentration, Eq.6.74 can be rewritten as follows

$$\frac{\hat{C}_\kappa}{\tilde{C}_1}=\frac{a_\kappa\left(\frac{\tilde{C}_\kappa}{\tilde{C}_1}-\frac{\hat{C}_\kappa}{\tilde{C}_1}\right)}{1+b_\kappa\left(\frac{\tilde{C}_\kappa}{\tilde{C}_1}-\frac{\hat{C}_\kappa}{\tilde{C}_1}\right)}\quad \kappa=3\quad or\quad 4 \qquad \text{Eq.B.1}$$

Equation B.1 can then be rewritten as follows knowing that the total in-fluid concentration of each component is its overall concentration less its adsorbed concentration

$$\frac{\tilde{C}_\kappa}{\tilde{C}_1}-\frac{\hat{C}_\kappa}{\tilde{C}_1}=\frac{a_\kappa\left(\frac{C_\kappa^f}{\tilde{C}_1}\right)}{1+b_\kappa\left(\frac{C_\kappa^f}{\tilde{C}_1}\right)}\quad \kappa=3\quad or\quad 4 \qquad \text{Eq.B.2}$$

We can now rename the variables of Eq.B.2 as follows:

$$\frac{C_\kappa^f}{\tilde{C}_1}=X\quad and\quad \frac{\tilde{C}_\kappa}{\tilde{C}_1}=\alpha \qquad \text{Eq.B.3}$$

Now Eq.B.2 can be rewritten as

$$b_i X^2+\left(a_i+1-\alpha b_i\right)X-\alpha=0 \qquad \text{Eq.B.4}$$

Eq.B.4 has only one physically reasonable root (since the adsorbed concentration can not be negative), which is

$$X=\frac{1}{2b_i}\left(-a_i-1+\alpha b_i+\sqrt{\left(a_i+-\alpha b_i\right)^2+4\alpha b_i}\right) \qquad \text{Eq.B.5}$$

Changing the variables of Eq.B.3 back to original variables, one can rewrite Eq.B.5 as shown in Eq.6.76.

B.2 Mole Fraction of Hydrocarbon Components in Oleic Phase

We would like to derive Eq.6.224 which states that the mole fraction of hydrocarbon components in the oleic phase does not change although some of the oil is solubilized in the ME phase. The mole fraction of each component in the ME phase is written as:

$$x_{i3} = \frac{N_{i,3}}{N_{T,3}} \qquad \text{Eq.6.205}$$

where

$N_{i,3}$: moles/PV of component i in ME phase

$N_{T,3}$: Total number of moles of ME phase

Our main assumption is that the mole fraction of component i in the oleic phase is the same as that of the ME phase

$$\frac{N_{i,2}}{N_{oil,2}} = \frac{N_{i,3}}{N_{oil,3}} \qquad \text{Eq.B.6}$$

where

$$N_{oil,j} = \sum_{i=1}^{n_c} N_{i,j} \qquad \text{Eq.B.7}$$

Eq.B.6 can be rewritten as

$$N_{i,2}N_{oil,3} = N_{i,3}N_{oil,2} \qquad \text{Eq.B.8}$$

Since hydrocarbon components are only present in the ME and oleic phases, we know that

$$N_i = N_{i,2} + N_{i,3} \qquad \text{Eq.B.9}$$

Combining Eq.B.8 and Eq.B.9 would result in

$$N_{i,2} = \frac{N_i N_{oil,2}}{N_{oil,2} + N_{oil,3}} = \frac{N_i N_{oil,2}}{\sum_{i=1}^{n_c} N_i} \qquad \text{Eq.B.10}$$

Therefore for a hydrocarbon component, we can write Eq.B.11 that is used in Eq.6.224:

$$x_{i,2} = \frac{N_{i,2}}{N_{oil,2}} = \frac{N_i}{\sum_{i=1}^{n_c} N_i} \qquad \text{Eq.B.11}$$

References

Adibhatla, B. and Mohanty, K. K.: "Oil Recovery from Fractured Carbonates by Surfactant-Aided Gravity Drainage: Laboratory Experiments and Mechanistic Simulations," *SPE Res. Eva. & Eng.,* Vol.11, No.1, 119-130, February 2008.

Adibhatla, B., Sun, X. and Mohanty, K. K.: "Numerical Studies of Oil Production From Initially Oil-Wet Fracture Blocks By Surfactant Brine Imbibition," Paper SPE 97687, presented at SPE International Improved Oil Recovery Conference in Asia Pacific, Kuala Lumpur, Malaysia, 5-6 December, 2005.

Akstinat, M. H.: "Surfactants for EOR Process in High-Salinity Systems: Product Selection and Evaluation," *Enhanced Oil Recovery*, F. J. Fayers (ed.) New York: Elsvier, 1981.

Al-Besharah, J. M., Akashah, S.A., Mumford, C.J.: "The effect of Temperature and Pressure on the Viscosities of Crude Oils and Their Mixtures," Ind. Eng. Chem. Res., 28, 213-21, 1989.

Aldejain, A.: "Implementation of a Dual Porosity Model in a Chemical Flooding Simulator," Ph.D. dissertation, The University of Texas, Austin, TX (1989).

Al-Hadherami, H., Blunt, M. J.: "Thermally induced Wettability Alteration to Improve Oil Recovery in Fractured Reservoirs," Paper SPE 59289, first presented at SPE/DOE Improved Oil Recovery Symposium, Tulsa, Oklahoma, 3-5 April 2000.

Ahrabi, F., Ashcroft, S. J., Shearn, R. B.: "High Pressure Volumetric, Phase Composition and Viscosity data for a North Sea Crude Oil and NGL," Chemical Engineering Research Design, 65(1), 63-73, 1987.

Al-Maamari, R.S.H. and Buckley, J. S.: "Asphaltene Precipitation and Alteration of Wetting: the Potential of Wettability Changes during Production," Paper SPE 59292, first presented at the SPE/DOE Improved Oil Recovery Symposium, Tulsa, Oklahoma, 3-5 April 2000.

Amaefule, J. O., Handy, L. L.: "The Effect of Interfacial Tension on Relative Oil/Water Permeabilities of Consolidated Porous Media," Paper SPE 9783, first presented at the SPE/DOE Enhanced Oil Recovery Symposium, Tulsa, April 5-8, 1982.

Anderson, G. A.: "Simulation of Chemical Flood Enhanced Oil Recovery Processes Including the Effects of Reservoir Wettability," Master's Thesis, The University of Texas at Austin, 2006.

Anderson, G. A., Delshad, M., King, C. B., Mohammadi, H. and Pope, G. A: "Optimization of Chemical Flooding in a Mixed-Wet Dolomite Reservoir," Paper SPE 100082, presented at SPE/DOE symposium on Improved Oil Recovery, Tulsa, Oklahoma, 22-26 April, 2006.

Anderson, W. G.: "Wettability Literature Survey-Part 1: Rock/Oil/Brine Interactions and the Effect of Core Handling in Wettability," *JPT*, 1125-1144, October 1986.

Anderson, W.G: "Wettability Literature Survey-Part 5: The effects of Wettability on Relative Permeability," *JPT*, 1453-1468, November 1987.

Anthony, D. K., Au, A. B., Rubin, B. and Vinsome, K.: "Techniques for Fully Implicit Reservoir Simulation," Paper SPE 9302, presented at 55th Annual Fall Technical Conference and Exhibition of Society of Petroleum Engineers of AIME, Dallas, Texas, 21-24 September, 1980.

Aoudia, M., Wade, W. H.: "Optimum microemulsions formulated with propoxylated Guerbet alcohol and propoxylated tridecyl alcohol sodium sulfates," Journal of Dispersion Science and Technology, 16(2), P. 115-35, 1995.

Austad, T., Milter, J.: "Spontaneous Imbibition of Water into Low Permeable Chalk at Different Wettabilities Using Surfactants," Paper SPE 37236, presented at the International Symposium of Oilfield Chemistry, Huston, Texas. 18-21 February, 1997.

Austad, T, Matre, B., Milter, J., Svareid, A. and Oyno, L: "Chemical Flooding of Oil Reservoirs. 8. Spontaneous Oil Expulsion from Oil- and Water-wet Low Permeability Caulk Material by Imbibition of Aqueous Surfactant Solutions," *Colloids and Surfaces A: Physicochemical and Engineering Aspects*, **137**, No. 1-3, 117, 15 June 1998.

Austad, T. and Skule, S.: "Chemical flooding of oil reservoirs 4. Effects of temperature and pressure on the middle phase solubilization parameters close to optimum flood conditions," Colloids and Surfaces, A: Physicochemical and Engineering Aspects, 108(2/3), P. 243-52, 1996.

Austad, T., Strand, S., Høgnesen and Zhang, P.: "Seawater as IOR Fluid in Fractures Chalk," Paper SPE 93000 presented at SPE International Symposium on Oilfield Chemistry, Houston, Texas, February 2005.

Austad, T., Strand, S., Madland, M. V., Puntervold, T. and Kornes, R. I.: "Seawater in Chalk: An EOR and Compaction Fluid," Paper IPTC 11370 presented at International Petroleum Technology Conference, Dubai, U.A.E., December 2007.

Babadagli, T.: "Capillary Imbibition for Surfactant and Polymer Injection in Naturally Fractured Reservoirs," *SPEJ*, 465-478, December 2001.

Babadagli, T.: "Analysis of Oil Recovery by Spontaneous Imbibition of Surfactant Solution," Paper SPE 84866, first presented at the SPE International Improved Oil Recovery Conference in Asia Pacific, Kuala Lumpur, Malaysia, 20-21 October, 2003.

Balay, S., Gropp, W. D., McInnes, L. C. and Smith, B. F.: "Effective Management of Parallelism in Object Oriented Numerical Software Libraries," *Modern Software Tools in Scientific Computing*, Arge *et al*. (eds.), Birkhauser Press, 1997.

Bhuyan, D.: "Development of an Alkaline/Surfactant/Polymer Compositional Reservoir Simulator," PhD dissertation, The University of Texas at Austin, Texas, December 1989.

Brownell, L. E., Katz, D. L.: "Flow of fluids through Porous Media, Part II," Chemical Engineering Process, 43, 601-612, 1949.

Castillo C. L.: "Modeling Wettability Alteration, Using a Chemical Compositional Simulator, UTCHEM," Masters report, University of Texas at Austin, August 2003.

Chen, H. L., Lucas L. R., Nogaret L. A. D., Yang H. D., Kenyon D. E., "Laboratory Monitoring of Surfactant Imbibition Using Computerized Tomography," Paper SPE 59006, first presented at the SPE International Petroleum Conference and Exhibition, Villahermosa, Mexico, 1-3 February, 2000.

Chilinger, G. V. and Yen, T. F.: "Some Notes on Wettability and Relative Permeability of Carbonate Reservoir Rocks, II," *Energy Sources*, 1983, **7**, No.1, 67-75.

Clementz, D., M.: "Alteration of Rock Properties by Adsorption of Petroleum Ends: Implications for Enhanced Oil Recovery," Paper SPE/DOE 10683, presented at the SPE/DOE Third Joint Symposium oh Enhanced Oil Recovery, Tulsa, OK, April, 4-7,1982 .

Craig, F. F: "The Reservoir Engineering Aspects of Waterflooding," Society of Petroleum Engineers of AIME, New York, 1971.

Cuiec, L. Bourbiaux, B. and Kalaydjian, K.: "Oil Recovery by Imbibition in Low-Permeability Chalk," SPE Formation Evaluation, September 1994.

Delshad, Mohammad: "Trapping of Micellar Fluids in Berea Sandstone," Ph.D. dissertation, The University of Texas at Austin, 1990.

Delshad, M., Pope, G. A., and Sepehrnoori, K.: "A Compositional Simulator for Modeling Surfactant Enhanced Aquifer Remediation, 1 Formulation" Journal of Contaminant Hydrology, 23, 303-327, 1996.

Delshad, M., Fathi Najafabadi, N., Anderson, G. A., Pope, G. A. and Sepehrnoori, K.: "Modeling Wettability Alteration in Naturally Fractured Reservoirs," Paper SPE 100081 presented at SPE/DOE Symposium on Improved Oil Recovery, Tulsa, Oklahoma, April 2006.

Delshad, M., Pope, G.A., and Sepehrnoori, K.: "Modeling Wettability Alteration Using Chemical EOR Processes in Naturally Fractured Reservoirs." Final report, DOE No. DE-FC26-04NT15529, NETL, University of Texas at Austin, Austin, Texas. 2007.

Delshad, M., Fathi Najafabadi, N. and Sepehrnoori, K.: "Scale up Methodology for Wettability Alteration in Fractured Carbonates," Paper SPE 118915, presented at SPE Reservoir Simulation Symposium, Woodlands, Texas, Feb 2-4, 2009.

Downs, H. H., and Hoover, P. D.: "Oil Field Chemistry: Enhanced Recovery and Production Stimulation," J. K. Borchardt & T. F. Yen editors, ACS Symposium series 396, Washington DC: American Chemical Society, 1989.

Dwarakanath, V., Pope, G. A.: "Surfactant Phase Behavior with Field Degreasing Solvent," Environmental Science and Technology, 34(22), P. 4842-8, 2000.

Fathi Najafabadi, N., Delshad, M., Sepehrnoori, K., Nguyen, Q. P., and Zhang, J.: "Chemical Flooding of Fractured Carbonates Using Wettability Modifiers," Paper SPE 113369, presented at SPE Symposium on Improved Oil Recovery, Tulsa, Oklahoma, 19-23 April, 2008.

Fathi Najafabadi, N., Delshad, M., Sepehrnoori, K.: "Development of a Three Phase, Fully Implicit, Parallel, Chemical Flooding Simulator," Paper SPE 119002, presented at SPE Reservoir Simulation Symposium, Woodlands, Texas, Feb 2-4, 2009.

Fathi Najafabadi, N.: "Modeling Wettability Alteration in Naturally Fractured Reservoirs," Masters Thesis, The University of Texas at Austin, December 2005.

Fazelipour, W., Pope, G. A. and Sepehrnoori K.: "Development of a Fully Implicit, Parallel EOS Compositional Simulator to Model Asphaltene Precipitation in Petroleum Reservoirs," Paper SPE 120203, 2008 SPE Annual Technical Conference and Exhibition, Denver, CO, September 21-24, 2008.

Flaaten, A. K., Nguyen, Q. P., Pope, G. A. and Zhang, J.: "A systematic Laboratory Approach to Low-Cost, High-Performance Chemical Flooding," Paper SPE 113469, presented at SPE/DOE symposium on Improved Oil Recovery, Tulsa, Oklahoma, 19-23 April, 2008.

Glover, C. J., Puerto, M. C., Maerker, J. M. and Sandvik, E. L.: "Surfactant Phase Behavior and Retention in Porous Media," *SPEJ*, 183-93, June 1979.

Gorrop, W., Lusk, E. and Skjellum, A.: *Using MPI: Portable Parallel Programming with Message Passing Interface*, MIT Press, Cambridge, Massachusetts, 1994.

Han, C., Delshad, M., Sepehrnoori, K. and Pope G. A.: "A Fully Implicit, Parallel, Compositional Chemical flooding Simulator," *SPEJ*, **12**, 322-338, September 2007.

Hand, F. B.: "Dineric Distribution: I. The Distribution of a Consolute Liquid Between Two Immiscible Liquids," *J. of Physics and Chem.*, **34**, 1961-2000, 1939.

Hatibogglu, C. U., Babadagli T.: "Experimental Analysis of Primary and Secondary Oil Recovery from Matrix by Counter-Current Diffusion and Spontaneous Imbibition," Paper SPE 90312, first presented at SPE Annual Technical Conference, Huston, Texas, 26-29 September, 2004.

Healy, R. N., Reed, R. L.: "Physicochemical Aspects of Microemulsion Flooding," *SPEJ*, **14,** 491-505, 1974.

Healy, R. N., Reed, R. L.: "Multiphase Microemulsion Systems," *SPEJ*, 174-160, June 1976.

Hirassaki, G. J.: "Application of the Theory of Multicomponent, Multiphase Displacement to Three-Component, Two-Phase Surfactant Flooding," *SPEJ*, 191, 1981.

Hirasaki, J. G., Miler, C. A., Pope, G. A., Jackson, R. E.: "Surfactant Based Enhanced Oil Recovery and Foam Mobility Control," 2nd Annual Technical Report, DE-FC26-03NT15406, July 2004.

Hirasaki, G. and Zhang, D. L.: "Surface Chemistry of Oil Recovery from Fractured, Oil-Wet Carbonate Formations," *SPE Journal*, June 2004.

Huh, C.: "Interfacial Tension and Solubilization Ability of a Microemulsion Phase That Coexists with Oil and Brine," *J. Colloid Interface Sci.*, **71**, 408-428, 1979.

Huh. C. and Pope, G. A.: "Residual Oil Saturation from Polymer Floods: Laboratory Measurements and Theoretical Interpretation," Paper SPE 113417, presented at SPE/DOE symposium on Improved Oil Recovery, Tulsa, Oklahoma, 19-23 April, 2008.

Jadhunandan, P. P. and Morrow, N. R.: "Effect of Wettability on Waterflood Recovery for Crude-Oil/Brine/Rock Systems," Paper SPE 22597, presented at the Annual Technical Conference and Exhibition, Dallas, TX, October 6-9, 1992.

Jain, V., Chattopadhyay S., and Sharma, M. M.: "Effect of Capillary Pressure, Salinity, and Aging on Wettability Alteration in Sandstones and Limestones," Paper SPE 75189, presented at the SPE/DOE Improved Oil Recovery Symposium, Tulsa, Oklahoma, April 13-17, 2002.

Jin, M.: "A Study of Nonaqueous Phase Liquid Characterization and Surfactant Remediation," PhD dissertation, The University of Texas at Austin, 1994.

John, A., Han, C., Delshad, M., Pope, G. A. and Sepehrnoori, K.: "A New Generation Chemical-Flooding Simulator," *SPEJ*, 206, June 2005.

Kamath, J., Meyer, R. F.: "Understanding Waterflood Residual Oil Saturation of Four Carbonate Rock Types," Paper SPE 71505, first presented at SPE Annual and Technical Conference, and Exhibition, New Orleans, Louisiana, 30 September-3 October 2001.

Kazemi, H., Gilman, J. R., and Elsharkawy, A. M.: "Analytical and Numerical Solution of Oil Recovery from Fractured Reservoirs with Empirical Transfer Functions," *SPERE*, 219, May 1992.

Kim, S. T., Boudh-Hir, M-E., and Mansoori, G. A.: "The Role of Asphaltene in Wettability Reversal," Paper SPE 20700, presented at the Annual Technical Conference and Exhibition, New Orleans, LA, September 23-26, 1990.

Lake, L. W.: *Enhanced Oil Recovery*, Prentice Hall Inc., Englewood Cliffs, 1989.

Lam, A. and Schechter, R. S.: "Theory of Diffusion in Microemulsion," *Journal of Colloid and Interface Science*, **120** (1), 56-63, 1987.

Levitt, D. B. and Pope, G. A.: "Selection and Screening of Polymers for Enhanced-Oil Recovery," Paper SPE 113845, presented at SPE/DOE symposium on Improved Oil Recovery, Tulsa, Oklahoma, 19-23 April, 2008.

Li, K. and Horne, R. N.: "Generalized Scaling Approach for Spontaneous Imbibition: An Analytical Model," Paper SPE 77544, first presented at SPE Annual Technical Conference and Exhibition, San Antonio, Texas, September 29-October 2, 2002. Paper peer approved February 26, 2006.

Lin, J.: "A study of Micellar/Polymer Flooding Using a Compositional Simulator," PhD dissertation, The University of Texas at Austin, 1981.

Liu, J.: "High Resolution Methods for Enhanced Oil Recovery Simulation," PhD dissertation, The University of Texas, Austin, TX, 1993.

Liu, J., Delshad, M., Pope, G. A., and Sepehrnoori, K.: "Application of Higher Order Flux-Limited Methods in Compositional Simulations," *J. of Transport in Porous Media*, **16**, 1-29, 1994.

Liu, S., Zhang, D. L., Yan, W., Puerto, M., Hirasali, G. J. and Miller, C.: "Favorable Attributes of Alkaline-Surfactant-Polymer Flooding," *SPEJ*, 5-16, March 2008.

Ma, S., Morrow, N. R., and Zhang, X.: "Generalized Scaling of Spontaneous Imbibition Data for Strongly Water-Wet Systems," J. Pet. Sci. and Tech., 18, 165, 1997.

Marcondes, F., Han, C. and Sepehrnoori, K. "Implementation of Corner Point Mesh Into a Parallel, Fully Implicit, Equation of State Compositional Reservoir Simulator," 18th International Congress of Mechanical Engineering, Ouro Preto, Minas Gerais, Brazil, November 6-11, 2005.

Marcondes, F., Han, C. and Sepehrnoori, K.: "Effect of Cross Derivatives in Discretization Schemes in Structured Non-Orthogonal Meshes for Compositional Reservoir Simulation." *JPSE*, **63**, 53-60, 2008.

Mattax, C.C., and Dalton, R. L.: *Reservoir Simulation*, Monograph Series, Society of Petroleum Engineers, Richardson, TX, **13**, 1990

Mattax, C. C. and Kyte, J. R.: "Imbibition Oil Recovery from Fractured, Water-Drive Reservoir," Paper SPE 187, first presented at 36th Annual Fall Meeting of PSE, Dallas, TX, October 8-11, 1961.

McCain, W. D.: *The Properties of Petroleum Fluids*, PennWell Corporation, 1989.

Miadcnye, A., Singh, B., Puttagunta, R. V.: "One-Parameter Correlation in the Estimation of Crude Oil Viscosity," Paper SPE 26206, 1993.

Meter, D., M. and Bird, R., B.: "Tube Flow of Non-Newtonian Polymer Solutions, Parts I and II- Laminar Flow and Rheological Models," *AIChE J.*, 878-881, 1143-1150, Nov. 1964.

Mohanty, K. K., Salter, S. J.: "Multiphase Flow in Porous Media III: Oil Mobilization, Transverse Dispersion and Wettability," Paper SPE 12127, first presented at 58th SPE Annual Technical Conference, and Exhibition, San Francisco, California, October 5-8, 1983.

Morrow, N. R., Lim, H. T., and Ward, J.S.: "Effect of Crude-Oil-Induced Wettability Changes on Oil Recovery," Paper SPE 13215, SPE Formation Evaluation, 89-103, February 1986.

Morrow, N.R: "Wettability and its Effect on Oil Recovery," *JPT*, 1476-1484, December 1990.

Naimi-Tajdar, R., Delshad, M., and Sepehrnoori, K.: "Matrix Subgridding and Its Effects in dual Porosity Simulators," Paper IPTC 11195, Proceeding at the International Petroleum Technology Conference, Dubai, UAE, December 4-6, 2007.

Nelson, R. C. and Pope, G. A.: "Phase Relationships in Chemical Flooding," *SPEJ*, 18, No. 5, 325-338, October 1978.

Noll, L. A.: "The Effect of Temperature, Salinity, and Alcohol on the Critical Micelle Concentration of Surfactants," SPE 21032, presented at the SPE International Symposium on Oil Field Chemistry, Anaheim, California, February 20-22, 1991.

Novosad, J.: "Surfactant Retention in Berea Sandstone- Effect of Phase Behavior and Temperature," SPEJ, 962-70, December 1982.

Olsen, D. K.: "Effect of Wettability on light Oil Steam Flooding," Technical Report No. NIPER-552, USDOE, December 1991.

Osterloh, W. T. and Jante, M. J.: "Surfactant-Polymer Flooding with Anionic PO/EO Surfactant Microemulsions Containing Polyethylene Glycol Additives," Paper SPE 24151, presented at SPE/DOE Symposium on Enhanced Oil Recovery, Tulsa, Oklahoma, April 22-24, 1992.

Pan, F., Sepehrnoori, K., and Chin, L. Y.: "Development of a Coupled Geomechanics Model for a Parallel Compositional Reservoir Simulator," Paper SPE 109867, 2007 SPE Annual Technical Conference and Exhibition (ATCE), Anaheim, CA, November 2007.

Pan, F. and Sepehrnoori, K., and Chin, L. Y.:"A New Solution Procedure for a Fully Coupled Geomechanics and Compositional Reservoir Simulator," Paper SPE 119029, 2009 SPE Reservoir Simulation Symposium, The Woodlands, TX, February 2-4, 2009.

Parashar, M., Wheeler, J. A., Pope, G. A., Wang, K. and Wang, P.: "A New Generation EOS Compositional Simulator: Part II- Framework and Multiprocessing," Paper SPE 37977 presented at the SPE Reservoir Simulation Symposium, Dallas, TX, June 8-11, 1997.

Pope, G. A. and Nelson, R.C.: "A Chemical Flooding Compositional Simulator," Soc. Pet. Eng. J, 339-354, October 1978.

Pope, G. A., Wu, W., Narayanaswamy, G., Delshad, M., Sharmah, M. M. and Wang, P.: "Modeling Relative Permeability Effects in Gas-Condensate Reservoirs with a New Trapping Number," *SPE Res. Eval. & Eng.*, **3**, No. 2, 171-178, April 2000.

Pourafshary, P., Sepehrnoori, K., Varavei, A. and Podio, A. L.: "A Compositional Wellbore/Reservoir Simulator to Model Multiphase Flow and Temperature Distribution," Paper SPE 12115, 2008 International Petroleum Technology Conference, Kuala Lumpur, Malaysia, December 3-5, 2008.

Puerto, M. C. and Reed, R. L.: "A Three Parameter Representation of Surfactant/Oil/Brine Interaction," *SPEJ*., **23**, 669-682, 1983

Radke, C.J., Kovscek, A.R., and Wong H.: "A Pore-Level Scenario for the Development of Mixed Wettability in Oil Reservoirs," Paper SPE 24880, presented at the Annual Technical Conference and Exhibition, Washington, October 4-7, 1992.

Robbins, M. L.: "Theory of the Phase Behavior of Microemulsions," Paper SPE 5839, 1976.

Roehl, P. O. and Choquette, P. W.: *Carbonate Petroleum Reservoirs*, New York, Springer-Verlag, 1985.

Saad, N.: "Field Scale Studies with a 3-D Chemical Flooding Simulator," Ph.D. dissertation, The University of Texas at Austin, 1989.

Salathiel, R. A.: "Oil Recovery by Surface Film Drainage in Mixed-Wettability Rocks", *JPT*, 1216-1224, October 1973.

Satio, H. and Shinoda, J.: "The Stability of W/O Type Emulsions as a Function of Temperature and the Hydrophilic Chain Length," *Journal of Colloid Interface Science*, 32, 647-51, 1970.

Satoh, T.: "Treatment of Phase Behavior and Associated Properties Used in Micellar-Polymer Flood Simulator," Master's Thesis, The University of Texas at Austin, 1984.

Skauge, A. and Fotland, P.: "Effect of Pressure and Temperature on the Phase Behavior of Microemulsions," *SPERE*, 601-8, November 1990.

Somasuundaran, P., and Zhang, L.: "Adsorption of surfactant on minerals for wettability control in Improved Oil Recovery Processes," presented at the 8th Symposium on Wettability, Houston, Texas, 16-18, May, 2004.

Sorbie, K., S.: *Polymer Improved Oil Recovery*, CRC Press, Inc., Boca Raton, Florida, 1991.

Tarahhom, T., Sepehrnoori, K., and Marcondes, F.: "A Novel Approach to Integrate Dual Porosity Model and Full Permeability Tensor Representation in Fractures," Paper SPE 119001, 2009 SPE Reservoir Simulation Symposium, The Woodlands, TX, February 2-4, 2009.

Thomas, L. K., Dixon, T. K., Evans, C. E., and Vienot, M. E.: "Ekofist Waterflood Pilot," JPT, Trans., AIME, 283, 221-232, 1987.

Tie, H. and Morrow, N. R.: "Low Flood Rate Residual Saturations in Carbonate Rocks," IPTC 10470, first presented at the International Petroleum Technology Conference, Doha, Qatar, 21-23 November, 2005.

Treiber, L. E., Archer, D.L., and Owens, W.W.: "Laboratory Evaluation of the Wettability of 50 Oil Producing Reservoirs," SPE J, 12, 1972, 531.

Treybal, R. E., *Liquid Extraction*, McGraw-Hill, New York, 1963.

Wang, D. M., Liu, C. D., Wu, W. X. and Wang, G.: "Development of an Ultra-Low Interfacial Tension Surfactant in a System with No-Alkali for Chemical

Flooding," Paper SPE 109017, presented at SPE/DOE symposium on Improved Oil Recovery, Tulsa, Oklahoma, 19-23 April, 2008.

Varavei, A. and Sepehrnoori, K.: "An EOS-Based Compositional Thermal Reservoir Simulator," Paper SPE 119154, 2009 SPE Reservoir Simulation Symposium, The Woodlands, TX, February 2-4, 2009.

Wang, F.H.: "Effect of Wettability Alteration on Water/Oil Relative Permeability, Dispersion, and Flowable Saturation in Porous Media," Paper SPE 15019, first presented at the SPE Permian Basin Oil & Gas Recovery Conference, Midland, Texas, March 13-14, 1986.

Wang, P., Balay, S., Sepehrnoori, K., Wheeler, J., Abate, J., Smithe, B., and Pope, G. A.: "A Fully Implicit Parallel EOS Compositional Simulator for Large Scale Reservoir Simulation," Paper SPE 51885, Fifteenth Symposium on Reservoir Simulation, Houston, TX, February 1999.

Wang, P., Yotov, I., Wheeler, M., Arbogast, T., Dawson, C., Parashar, M. and K. Sepehrnoori: "A New Generation EOS Compositional Reservoir Simulator: Part I - Formulation and Discretization," Paper SPE 37979, SPE Reservoir Simulation Symposium, Dallas, TX, June 1997.

Willhite, G. P.: *Waterflooding*, Society of Petroleum Engineers textbook series volume 3, Richardson, Texas, 1986.

Winsor, P. A.: *Solvent Properties of Amphiphillic Compounds*, Butterworth's Scientific Publication, London, 1954.

Wreath, D., Pope, G. A. and Sepehrnoori, K.: "Dependence of Polymer Apparent Viscosity on the Permeable Media and Flow Conditions," *In Situ*, **14**(3), 263-284, 1990.

Yang, H. D. and Wadleigh, E. E.: "Dilute Surfactant IOR Design Improvement for Massive Fractured Carbonate Applications," Paper SPE 59009 presented at 2000 SPE International Petroleum Conference and Exhibition, Mexico, 1-3 Feb., 2000.

Ziegler, V. M.: "Laboratory Investigation of High Temperature Surfactant Flooding," *SPERE*, 586-96, May 1988.

Zhang, X., Morrow, N. R., and Ma, X.: "Experimental Verification of a Modified Scaling Group for Spontaneous Imbibition," SPERE, November , 280, 1996.

Zhang, J., Nguyen, Q. P., Flaaten, A. K. and Pope, G. A.: "Mechanisms of Enhanced Natural Imbibition with Novel Chemicals," Paper SPE 113453, presented at SPE/DOE symposium on Improved Oil Recovery, Tulsa, Oklahoma, 19-23 April, 2008.

Zhao, P., Jacson, A. C., Britton, C., Kim, D. H., Britton, L. N., Levitt, D. B. and Pope, G. A.: "Development of High-Performance Surfactants for Difficult Oils," Paper SPE 113432, presented at SPE/DOE symposium on Improved Oil Recovery, Tulsa, Oklahoma, 19-23 April, 2008.

VITA

Nariman Fathi Najafabadi attended Alborz High School, Isfahan, Iran. In 1998 he entered Petroleum University of Technology, Ahwaz, Iran, where he was awarded the degree of B. Sc. in Petroleum Engineering in August 2002. He was admitted to The University of Texas at Austin in fall 2003 where he was awarded the degree of M. S. in Petroleum Engineering in December 2005. He continued his studies at The University of Texas at Austin and started his Ph. D. in spring 2006.

Email address is nariman@mail.utexas.edu.

This Manuscript was typed by Nariman Fathi Najafabadi.